

Faculdade de Engenharia da Universidade do Porto



Structural Simulation of Proximal Femoral Tumors Using Meshless Methods

Raquel Claro Silva Carvalho Sousa

Dissertation carried out under the
Master in Biomedical Engineering

Supervisor: Professor Jorge Américo Oliveira Pinto Belinha
Co-supervisor: Professor Renato Manuel Natal Jorge

June 2019

© Raquel Claro Silva Carvalho Sousa, 2019

Abstract

Bone sarcomas are one of the most common childhood malignancies. These rare and heterogeneous group of tumors jeopardize the longevity and health of the cancer survivors. However, the absence of initial symptoms delays the diagnosis and the beginning of the treatment, which has a negative impact, not only in terms of the health of the patient, but also on a social and economic aspect. As literature shows, there are still several unanswered questions related to this subject, which makes it crucial to understand the biomechanical effect of these tumors on the bone.

In this work, a bibliographic review with all the necessary information for the accomplishment of the dissertation is presented. First, the study focused on the physiology and structure of bone tissue, followed by a detailed survey on bone sarcomas and its mechanical properties. A theoretical approach on the numerical methods that will be used and on the fundamentals of solid mechanics is also performed.

A preliminary work with a healthy proximal femur bone was performed in order to acquire the necessary competences in computational tools, namely image processing and numerical simulation software using advanced discretization techniques (finite element methods and meshless methods). The results obtained allowed to understand the methodologies of the numerical analysis and to identify its limitations.

In addition, the structural response of bone sarcomas was simulated on 2D and 3D femur bone model. Four different clinical cases and different sarcomas sizes were analyzed with meshless methods, namely Radial Point Interpolation Method (RPIM) and Natural Neighbour Radial Point Interpolation Method (NNRPIM), and with Finite Element Method (FEM). The results obtained in this work demonstrate that bone sarcomas have an impact on the femoral structure, affecting mostly the femoral neck. Finally, it is possible to conclude that the effect of bone sarcomas can be predicted with FEM and meshless methods, demonstrating a satisfactory degree of assertiveness.

Resumo

Os sarcomas ósseos são uma das malignidades infantis mais comuns. Este grupo de tumores raros e heterógenos comprometem a longevidade e a saúde dos sobreviventes de cancro. No entanto, a ausência de sintomas iniciais atrasa o diagnóstico e o início do tratamento, o que afeta negativamente, não só na saúde do paciente, mas também em termos sociais e económicos. Tal como observado na literatura, ainda existem muitas questões por responder relativamente a este assunto, sendo, assim, importante entender o efeito biomecânico desses tumores no osso.

Neste trabalho é apresentado uma revisão bibliográfica com toda a informação necessária para a realização desta dissertação. Em primeiro lugar, o estudo incidiu sobre a estrutura e fisiologia do tecido ósseo, seguido de uma descrição detalhada sobre os sarcomas ósseos e as suas propriedades mecânicas. Uma abordagem teórica sobre os métodos numéricos que irão ser utilizados e sobre os fundamentos de mecânica dos sólidos é também realizada.

De seguida, um trabalho preliminar com um fémur proximal saudável foi realizado com o intuito de adquirir competências nas ferramentas computacionais, nomeadamente em softwares de processamento de imagem e simulação numérica utilizando técnicas de discretização avançadas (método dos elementos finitos e métodos sem malha). Os resultados obtidos permitiram compreender as metodologias de análise numérica e identificar as suas limitações.

Posteriormente, foi avaliado o efeito de sarcomas ósseos na estrutura do fémur proximal em modelos 2D e 3D. Quatro casos clínicos e diferentes tamanhos de tumores foram simulados, utilizando os métodos sem malha, nomeadamente Radial Point Interpolation Method (RPIM) e Natural Neighbour Radial Point Interpolation Method (NNRPIM), e com Finite Element Method (FEM). Os resultados demonstraram que os sarcomas ósseos têm um impacto negativo na estrutura do fémur, afetando principalmente o pescoço femoral. Por último é possível concluir que o efeito dos sarcomas ósseos pode ser previsto com recurso ao FEM e métodos sem malha, demonstrando um grau de assertividade satisfatório.

Acknowledgments

Este último ano foi repleto de novos desafios, que teriam sido impossíveis de ultrapassar sem o apoio e colaboração de várias pessoas. Por isso, a todos os que direta ou indiretamente participaram neste trabalho, desejo expressar o meu profundo agradecimento.

Em primeiro lugar, gostaria de agradecer ao meu orientador, o Professor Jorge Belinha, por todo o apoio, prestabilidade e conhecimentos adquiridos ao longo do desenvolvimento da dissertação. Gostava também de agradecer ao meu co-orientador, o Professor Renato Natal, pelo acompanhamento e disponibilidade.

Às duas pessoas mais importantes da minha vida, os meus queridos PAIS, Graça e Jorge, quero agradecer imenso pelos 22 anos da minha vida, pelo amor incondicional, por todo o carinho, motivação, força, e paciência (e por todos os pastéis de nata), tanto nos bons momentos como nos de maior frustração. Esta etapa concluída com sucesso é graças a vocês por tudo o que me ensinaram ao longo da vida e por me motivarem a estudar, a ir mais longe, a dar o melhor de mim e nunca desistir.

À minha querida amiga Tânia, quero agradecer imenso pelas nossas tardes, por todos os momentos de riso, por todos os momentos em que nos perdemos na rua e, principalmente, por todos os lattes, que me ajudaram a concentrar e arranjar a motivação necessária para concluir esta etapa da minha vida.

Aos meus Pinkie-Winkies, Ana, Cátia, João, Mariana e Tiago, que me acompanham há 6 anos, mesmo quando o tempo não era muito. Por todos os momentos e experiências incríveis que partilhei convosco e que recordarei para sempre.

Institutional Acknowledgments

The author truly acknowledges the work conditions provided by the Applied Mechanics Division (SMAp) of the department of mechanical engineering (DEMec) of Faculty of Engineering of the University of Porto (FEUP), and by the MIT-Portugal project “MIT-EXPL/ISF/0084/2017”, funded by Massachusetts Institute of Technology (USA) and “Ministério da Ciência, Tecnologia e Ensino Superior - Fundação para a Ciência e a Tecnologia” (Portugal).

Additionally, the authors gratefully acknowledge the funding of Project NORTE-01-0145-FEDER-000022 - SciTech - Science and Technology for Competitive and Sustainable Industries, cofinanced by Programa Operacional Regional do Norte (NORTE2020), through Fundo Europeu de Desenvolvimento Regional (FEDER).

Furthermore, the author acknowledges the inter-institutional collaboration with the orthopaedics service of Central Hospital of Porto - Hospital de Santo António - and its director, Prof.Dr. António Fonseca Oliveira. Thus, the author acknowledges the support and guidance provided by Prof.Dr. António Fonseca Oliveira from Hospital de Santo António (Porto) and Dr. Vânia Oliveira from Hospital de Santo António (Porto).

Finally, the author acknowledges the synergetic collaboration with the collaborators of “Computational Mechanics Research Laboratory CMech-Lab” (ISEP/FEUP/INEGI), and its director, Prof.Dr. Jorge Belinha, and its senior advisors, Prof.Dr. Renato Natal Jorge and Prof.Dr. Lúcia Dinis.

“Nothing in life is to be feared, it is only to be understood. Now is the time to understand more, so that we may fear less.”

Marie Curie

Contents

Abstract.....	iv
Resumo	vi
Acknowledgments	viii
Institutional Acknowledgments	x
Contents	xiv
List of Figures	xvii
List of Tables	xxiii
List of Abbreviations and Symbols.....	xxiv
Chapter 1.....	1
Introduction.....	1
1.1 - Motivation.....	2
1.2 - Objective.....	3
1.3 - Document Structure.....	3
Chapter 2.....	4
Bone 4	
2.1- Skeletal System	4
2.2- Bone Morphology	5
2.3- Bone Structure.....	7
2.4- Bone Cells	8
2.5 - Bone Matrix	9
2.6- Bone Development	10
2.6.1- Bone Formation	10
2.6.2- Bone Growth and Remodeling	11
2.7- Trabecular and Cortical Bone	12
2.8 - Femur Anatomy	14
2.9 - Bone Quality	16
2.10 - Bone Mechanical Properties.....	17
2.11 - Bone Remodeling Process.....	20
2.11.1 - Mechanical Models	21
2.11.2 - Biological Models	21

2.11.3 - Mechanobiological Models	22
Chapter 3	23
Bone Sarcomas	23
3.1 - Socioeconomic Analysis	23
3.2 - Types of Sarcomas.....	27
3.3 - Staging, Grading and Development	29
3.4 - Imaging Methods	30
3.5 - Mechanical Properties of Bone Sarcomas	31
3.5.1 - Mechanical Properties of Trabecular Bone with Metastatic Lesions	31
3.5.2 - Mechanical Properties of Cortical Bone with Metastatic Lesions	34
Chapter 4.....	36
Numerical Methods	36
4.1 - Finite Element Method (FEM)	36
4.2 - Meshless Methods.....	38
4.2.1 - Meshless Generic Procedure	38
4.2.2 - Nodal Connectivity	39
4.2.2.1 - RPIM	39
4.2.2.2 - NNRPIM	40
4.2.3 - Numerical Integration.....	41
4.2.3.1 - RPIM	41
4.2.3.2 - NNRPIM	42
4.2.4 - Interpolation Functions.....	43
Chapter 5.....	46
Solid Mechanics	46
5.1 - Fundamentals	46
5.2 - Weak Form	48
5.2.1 - Galerkin Weak Form	48
5.3 - Discrete Equation System.....	50
Chapter 6.....	52
Numerical Methods in Bone Biomechanics	52
6.1 - FEM	52
6.1.1 - FEM and Bone	53
6.1.1.1 - Fracture Prediction	53
6.1.1.2 - Analysis of Stress and Strain	58
6.1.1.3 - Study of Bone Remodeling Process.....	59
6.1.2 - FEM and Sarcoma	59
6.1.2.1 - FEM and Bone Sarcomas	60
6.1.2.1 - FEM and Bone Metastatic Lesions.....	61
6.2 - Meshless Methods.....	62
6.2.1 - Meshless Methods and Bone	63
6.2.2 - Meshless Methods and Sarcomas	64
Chapter 7	65
Preliminary Work	65
Chapter 8.....	70
Numerical Analysis of Bone Sarcomas in the Proximal Femur	70
8.1 - Numerical Analysis of Two-dimensional Femur Models with Bone Sarcomas ..	70
8.2 - Numerical Analysis of Three-dimensional Femur Models with Bone Sarcomas	92
Chapter 9.....	118

Conclusions and Future Work	118
References	120

List of Figures

Figure 1.1 - Number of documents published through the years, in the subjects indicated. The data was obtained through a research on Scopus database (www.scopus.com) assuming as keywords the subjects indicated in the graph.	2
Figure 2.1 - Bone shape major groups. Adapted from [9].	5
Figure 2.2 - Parts of a long bone: epiphysis, metaphysis and diaphysis; Representation of a partially dissected humerus. Adapted from [6].	6
Figure 2.3 - Hierarchical structure of the bone. Adapted from [20].	7
Figure 2.4 - Sequential phases of the normal bone remodeling cycle. Adapted from [8].	9
Figure 2.5 - Sequential phases of the normal bone remodeling cycle. Adapted from [8].	12
Figure 2.6 - Osteons in compact bone. Adapted from [9].	13
Figure 2.7 - Lateral and posterior view of the femur. Adapted from [4].	15
Figure 2.8 - Muscles in the thigh: medial and lateral view [7].	16
Figure 2.9 - Representation of a stress-strain curve.	17
Figure 2.10 - Elasticity modulus in axial direction. Comparison between experimental data from Ziopous work, Lotz law for cortical and trabecular bone, and mathematical model proposed by Belinha. Adapted from [5].	20
Figure 2.11- (a) Elasticity modulus in transversal direction. (b) Ultimate compressive stress in axial direction. (c) Ultimate compressive stress in transversal direction. Adapted from [5].	20
Figure 3.1 - Global map representing the National Ranking of Cancer as a cause of death at ages below 70 years in 2015. Adapted from [23].	24
Figure 3.2 - Incidence rate of bone sarcomas in Europe. Adapted from [22].	24
Figure 3.3 - Primary malignant bone tumor incidence in the world. Adapted from [11].	25
Figure 3.4 - Distribution of new cases by histology, in 2008. Adapted from [12].	26
Figure 3.5 - X-ray of OS lesion on the femur. Adapted from [21].	27

Figure 3.6 - Comparison between imaging techniques from a young man with left knee pain for 1 month. (A) radiograph of distal femur shows aggressive tumor. (B) MRI of the distal femur. (C) PET/CT scan of left femur. Adapted from [2].	31
Figure 3.7 - Linear regression models of (A) modulus of elasticity and (B) yield strength of noncancer and cancer specimens in function of BV/TV_{min} . Linear regression models of (A) modulus of elasticity and (B) yield strength of noncancer and cancer specimens in function of $vBMD$. Adapted from [24].	33
Figure 3.8 - Linear regression for elasticity modulus in function of ρQCT . Adapted from [17].	35
Figure 4.1 - Creation of a mesh and demonstration of its influence on the discretization error. Adapted from [34].	37
Figure 4.2 - FE models of the 2D and 3D human femur. Adapted from [10].	37
Figure 4.3 - Nodal discretization of the domain of the problem: (a) solid domain with the natural and essential boundaries; (b) regular nodal discretization; (c) irregular nodal discretization. Adapted from [5].	39
Figure 4.4 - Examples of different types of influence-domains: (a) influence-domain with fixed size and rectangular shape; (b) influence-domain with fixed size and circular shape; (c) influence-domain with variable size and circular shape. Adapted from [5].	40
Figure 4.5 - (a) Second degree influence cell of interest point x_i ; (b) Representation of the sub-cells forming the Voronoï cell; (c) Schematic representation of 4×4 integration points inside a sub-cell. Adapted from [5].	41
Figure 4.6 - (a) Gaussian integration mesh and (b) transformation of the initial quadrilateral into an isoparametric square shape and application of the 2×2 quadrature point rule. Adapted from [5].	41
Figure 4.7 - (a) Initial Voronoï diagram; (b) Delaunay triangulation. Adapted from [5].	43
Figure 4.8 - (a) Voronoï cell and respective intersection points, P_{ij} ; (b) Middle points, M_{ij} , and the respective generated triangles; (c) Triangular. (d) Voronoï cell and respective intersection points, P_{ij} ; (e) Middle points, M_{ij} , and the respective generated triangles; (f) Quadrilateral. Adapted from [5].	43
Figure 6.1 - Number of documents published through the years, in the subjects indicated. The data was obtained through a research on Scopus database (www.scopus.com) assuming as keywords the subjects indicated in the graph.	52
Figure 6.2 - Percentage of hip fracture in the femoral neck, trochanter region and femoral shaft.	53
Figure 6.3 - Failure location computed for the stance loading condition (top) and fall condition (bottom) for a matched pair of femora. Adapted from [13].	54
Figure 6.4 - Typical QCT-FE model of proximal femur, showing 3D (A) and 2D sectional (B) views. The color-coding shows the spatial variation of material strength assigned to the individual finite element. Adapted from [1].	55
Figure 6.5 - (Left) Location of the midfemoral neck in stance; schematic diagram showing cortical thickness at the midfemoral neck at 25 and 85 years. Adapted from [19].	56
Figure 6.6 - Examples of typical Von Mises stress distribution from A, B, C, D, E, F and control group during fall simulation. H-I represents high-impact, O-I represents odd-	

impact, H-M represents high-magnitude, R-I represents repetitive-impact and R-NI represents repetitive non-impact. Adapted from [3].	57
Figure 6.7 - Principal strains ϵ_1 (maximal) and ϵ_1 (minimal) along the human femur at 45% gait cycle with all thigh muscles included (dark lines). A representation for the simplified load regimes are also included (light lines). Adapted from [15].	58
Figure 6.8 - Number of documents published through the years, in the subjects indicated. The data was obtained through a research on Scopus database (www.scopus.com) assuming as keywords the subjects indicated in the graph.	60
Figure 6.9 - Number of documents published through the years concerning bone metastatic lesions. The data was obtained through a research on Scopus database (www.scopus.com) assuming as keywords bone metastatic lesion and FEM.	61
Figure 6.10 - Compressive principal strain illustrate different failure locations (shown in black) for the proximal femur (A) in the intact state, (B) with an inferomedial femoral neck defect, and (C) with a defect in the anteromedial corner at the level of the lesser trochanter. Adapted from [18].	62
Figure 6.11 - Number of documents published through the years, in the subjects indicated. The data was obtained through a research on Scopus database (www.scopus.com) assuming as keywords the subjects indicated in the graph.	63
Figure 7.1 - (a) Final femur model with cortical (purple) and trabecular (blue) bone; (b) Points of interest selected for the study to analyze the strain and the von Mises stress.	66
Figure 7.2 - Loads of the different cases. (a) First mechanical case, (b) Second mechanical case, (c) Third mechanical case.	66
Figure 7.3 - Six numerical models resulting from the use of FEM in each load case. Three models present the equivalent von Mises stress and three others present the equivalent strain applied for the different load cases. Representation of the maximum stress and strain for each case.	67
Figure 7.4 - Graphical representation of the values obtain for the equivalent von Mises stress, for each load case. The stress is represented in function of distance between nodes (dx), in millimeters (mm).	68
Figure 7.5 - Bar graphs for displacement field, in millimeters (mm), of point A and point B, for each load case. The u represents the x component of the displacement vector and v represents y component of displacement field.	69
Figure 8.1 - (a) Anteroposterior radiograph of the femur on the right side of the patient; (b) Representation of the geometric femur model with a bone sarcoma located on the shaft.	70
Figure 8.2 - Representation of the 12 two-dimensional models of bone sarcomas in the proximal femur.	71
Figure 8.3 - Discretization of the problem domain: (a) nodal mesh; (b) element mesh.	72
Figure 8.4 - Representation of the natural and essential boundary conditions: (a) load case described by Beaupré <i>et.al.</i> [14]; (b) load case described by Lutz <i>et. al.</i> [16] and Kersh <i>et. al.</i> [25]; (c) loads applied to the femur models with bone sarcomas.	73
Figure 8.5 - Color maps of the von Mises effective stress (σ_{ser}) of the 12 two-dimensional models, using FEM.	74

Figure 8.6 - Color maps of the von Mises effective stress (σ_{sef}) of the 12 two-dimensional models, using RPIM.	75
Figure 8.7 - Color maps of the von Mises effective stress (σ_{sef}) of the 12 two-dimensional models, using NNRPIM.	76
Figure 8.8 - Color maps of the principal stress 1 (σ_{11}) of the 12 two-dimensional models, using FEM.	77
Figure 8.9 - Color maps of the principal stress 1 (σ_{11}) of the 12 two-dimensional models, using RPIM.	78
Figure 8.10 - Color maps of the principal stress 1 (σ_{11}) of the 12 two-dimensional models, using NNRPIM.....	79
Figure 8.11 - Color maps of the principal stress 2 (σ_{22}) of the 12 two-dimensional models, using FEM.	80
Figure 8.12 - Color maps of the principal stress 2 (σ_{22}) of the 12 two-dimensional models, using RPIM.	81
Figure 8.13 - Color maps of the principal stress 2 (σ_{22}) of the 12 two-dimensional models, using NNRPIM.....	82
Figure 8.14 - Generic representation of the selected nodes (black line) for all clinical cases: (a) Case A; (B) case B; (c) Case C and (d) Case D.....	83
Figure 8.15 - Graphical representation of the von Mises stress distribution obtained through FEM for the cases of bone sarcomas studied in the four areas of interest.	84
Figure 8.16 - Graphical representation of the von Mises stress distribution obtained through RPIM for the cases of bone sarcomas studied in the four areas of interest.	84
Figure 8.17 - Graphical representation of the von Mises stress distribution obtained through NNRPIM for the cases of bone sarcomas studied in the four areas of interest. .	85
Figure 8.18 - Graphical representation of the principal stress 1 and 2 obtained through FEM for the cases of bone sarcomas studied in the four areas of interest.	86
Figure 8.19 - Graphical representation of the principal stress 1 and 2 obtained through RPIM for the cases of bone sarcomas studied in the four areas of interest.	87
Figure 8.20 - Graphical representation of the principal stress 1 and 2 obtained through NNRPIM for the cases of bone sarcomas studied in the four areas of interest.	88
Figure 8.21 - Graphical representation of the maximum von Mises effective stress obtained through FEM, RPIM and NNRPIM for all clinical cases of bone sarcomas.	89
Figure 8.22 - Graphical representation of the maximum principal stress 1 obtained through FEM, RPIM and NNRPIM for all clinical cases of bone sarcomas.	89
Figure 8.23 - Graphical representation of the maximum principal stress 2 obtained through FEM, RPIM and NNRPIM for all clinical cases of bone sarcomas.	90
Figure 8.24 - Generic representation of the location of maximum values of the von Mises effective stress obtained through FEM, RPIM and NNRPIM, for size 1, 2 and 3 of all clinical cases analyzed.	90

Figure 8.25 - Generic representation of the location of maximum values of the principal stress 2 obtained through FEM, RPIM and NNRPIM, for size 1, 2 and 3 of all clinical cases analyzed.	91
Figure 8.26 - Generic representation of the location of maximum values of the principal stress 1 obtained through FEM, RPIM and NNRPIM, for size 1, 2 and 3 of all clinical cases analyzed.	91
Figure 8.27 - (a) Element mesh (b) Representation of the geometric three-dimensional femur model with a bone sarcoma located on the femoral head.	92
Figure 8.28 - Representation of the 8 three-dimensional models of bone sarcomas in the proximal femur.	93
Figure 8.29 - Representation of the natural and essential boundary conditions: (a) load case described by Beaupré <i>et.al.</i> [14]; (b) load case described by Lutz <i>et. al.</i> [16] and Kersh <i>et. al.</i> [25]; (c) loads applied to the femur models with bone sarcomas.	94
Figure 8.30 - Color maps of the von Mises effective stress (σ_{sef}) in the cortical and trabecular bone of the 8 three-dimensional models, using FEM.	95
Figure 8.31 - Color maps of the von Mises effective stress (σ_{sef}) in the cortical and trabecular bone of the 8 three-dimensional models, using RPIM.	96
Figure 8.32 - Color maps of the von Mises effective stress (σ_{sef}) in the cortical and trabecular bone of the 8 three-dimensional models, using NNRPIM.	97
Figure 8.33 - Color maps of the principal stress 1 (σ_{11}) in the cortical and trabecular bone of the 8 three-dimensional models, using FEM.	98
Figure 8.34 - Color maps of the principal stress 1 (σ_{11}) in the cortical and trabecular bone of the 8 three-dimensional models, using RPIM.	99
Figure 8.35 - Color maps of the principal stress 1 (σ_{11}) in the cortical and trabecular bone of the 8 three-dimensional models, using NNRPIM.	100
Figure 8.36 - Color maps of the principal stress 3 (σ_{33}) in the cortical and trabecular bone of the 8 three-dimensional models, using FEM.	101
Figure 8.37 - Color maps of the principal stress 3 (σ_{33}) in the cortical and trabecular bone of the 8 three-dimensional models, using RPIM.	102
Figure 8.38 - Color maps of the principal stress 3 (σ_{33}) in the cortical and trabecular bone of the 8 three-dimensional models, using NNRPIM.	103
Figure 8.39 - Representation of the zones (red circles) where the points of interest were selected.	104
Figure 8.40 - Graphic representation of the von Mises effective stress obtained through FEM, RPIM and NNRPIM, for all clinical cases studied in zone of interest 1.	105
Figure 8.41 - Graphic representation of the von Mises effective stress obtained through FEM, RPIM and NNRPIM, for all clinical cases studied in zone of interest 2.	105
Figure 8.42 - Graphic representation of the von Mises effective stress obtained through FEM, RPIM and NNRPIM, for all clinical cases studied in zone of interest 3.	106
Figure 8.43- Graphic representation of the von Mises effective stress obtained through FEM, RPIM and NNRPIM, for all clinical cases studied in zone of interest 4.	106

Figure 8.44 - Graphic representation of the principal stress 1 and 3 obtained through FEM, RPIM and NNRPIM, for all clinical cases studied in zone of interest 1.	107
Figure 8.45 - Graphic representation of the principal stress 1 and 3 obtained through FEM, RPIM and NNRPIM, for all clinical cases studied in zone of interest 2.	108
Figure 8.46 - Graphic representation of the principal stress 1 and 3 obtained through FEM, RPIM and NNRPIM, for all clinical cases studied in zone of interest 3.	109
Figure 8.47 - Graphic representation of the principal stress 1 and 3 obtained through FEM, RPIM and NNRPIM, for all clinical cases studied in zone of interest 4.	110
Figure 8.48 - Generic representation of the selected nodes (black line) for all clinical cases: (a) Case A; (B) case B; (c) Case C and (d) Case D.	111
Figure 8.49 - Graphical representation of the von Mises effective stress obtained through FEM for the cases of bone sarcomas studied in the four areas of interest.	112
Figure 8.50 - Graphical representation of the von Mises effective stress obtained through RPIM for the cases of bone sarcomas studied in the four areas of interest.	112
Figure 8.51 - Graphical representation of the von Mises effective stress obtained through NNRPIM for the cases of bone sarcomas studied in the four areas of interest.	113
Figure 8.52 - Graphical representation of the principal stress 1 and 3 obtained through FEM for the cases of bone sarcomas studied in the four areas of interest.	114
Figure 8.53 - Graphical representation of the principal stress 1 and 3 obtained through RPIM for the cases of bone sarcomas studied in the four areas of interest.	115
Figure 8.54 - Graphical representation of the principal stress 1 and 3 obtained through NNRPIM for the cases of bone sarcomas studied in the four areas of interest.	116

List of Tables

Table 2.1 - Coefficients of Lotz law.	18
Table 2.2 - Coefficients of Belinha law.	19
Table 3.1 - The tumor, node and metastasis (TNM) system.	29
Table 3.2 - The Enneking system.	30
Table 3.3 - Material and structural properties for cancer and noncancer specimens (mean ± standard deviation) [24].	32
Table 3.4 - Material properties of trabecular bone with metastatic lesions. NA indicates not available. Adapted from [84].	32
Table 3.5 - Material property of cortical bone with metastatic lesions [17].	34
Table 8.1 - Mechanical Properties of the materials [14, 24].	72
Table 8.2 - Mechanical Properties of the materials [14, 24].	93

List of Abbreviations and Symbols

Abbreviations

2D	<i>Two-dimensional</i>
3D	<i>Three-dimensional</i>
ATV	<i>Absolute Tumor Volume</i>
BMD	<i>Bone Mineral Density</i>
BMU	<i>Basic Multicellular Unit</i>
BV/TV	<i>Bone Volume Fraction</i>
CT	<i>Computed Tomography</i>
DEM	<i>Diffuse Element Method</i>
DICOM	<i>Digital Imaging and Communications in Medicine</i>
DXA	<i>Dual-energy X-ray Absorptiometry</i>
EFGM	<i>Element Free Galerkin Method</i>
FEM	<i>Finite Element Method</i>
FEMAS	<i>Finite Element and Meshless Method Analysis Software</i>
FEUP	<i>Faculdade de Engenharia da Universidade do Porto</i>
HA	<i>Hydroxyapatite</i>
MRI	<i>Magnetic Resonance Imaging</i>
MSL	<i>Moving Least Square</i>
NCD	<i>Noncommunicable Disease</i>
NCP	<i>Non-collagenous Protein</i>
NEM	<i>Natural Element Method</i>
NIH	<i>National Institute of Health</i>
NNFEM	<i>Natural Neighbor Finite Element Method</i>
NNRPIM	<i>Natural Neighbour Radial Point Interpolation Method</i>
OS	<i>Osteosarcoma</i>
PET	<i>Positron Emission Tomography</i>
PIM	<i>Point Interpolation Method</i>

PSFE	<i>Patient-specific Finite Element</i>
PTH	<i>Parathyroid Hormone</i>
QCT	<i>Quantitative Computed Tomography</i>
RBF	<i>Radial Basis Function</i>
RKPM	<i>Reproducing Kernel Particle Method</i>
RPIM	<i>Radial Point Interpolation Method</i>
SED	<i>Strain Energy Density</i>
SPH	<i>Smoothed-Particle Hydrodynamics</i>
TMN	<i>Tumor, Metastasis and Node</i>
WHO	<i>World Health Organization</i>

Symbols

E	Young's Modulus
ν	Poisson ratio

Chapter 1

Introduction

Over the last few decades, the socioeconomic development has led to the increase of life expectancy and of population growth worldwide. As a result, both aging and rapid population growth are associated with a higher cancer incidence and mortality. Nowadays, the negative impact of cancer on society is compromising the increase of life expectancy across the world. According to the World Health Organization (WHO), cancer is the first or the second leading cause of death in 91 of 172 countries. Also, recent estimations predict 18.1 million new cancer cases and 9.6 million deaths in 2018 [23].

The most common types of cancer are lung cancer (11,6% of the total cases and 18.4% of cancer deaths), followed by female breast cancer (11,6% of the total cases and 6,6% of all cancer deaths), prostate cancer (7,1% of the total cases and 3,8% of all cancer deaths) and colorectal cancer (6,1% of the total cases and 5,8% of all cancer deaths). Contrarily, bone sarcomas are among the rarest type of cancers, accounting for only 2% of all cancer related deaths and 1% of all newly diagnosed cancers [26].

Despite being very uncommon, bone sarcomas have a major impact on the health of young adults and elderly, which have the higher incidence rate for this type of cancer. Adults, however, are more affected by metastatic bone cancer [27], which is caused by metastases from other types of cancers. In fact, about 30% of all cancers (particularly lung and breast cancer) metastasize to bone [28].

As the cancer cells proliferate within the bone, the natural bone architecture is disrupted, which compromises its stability and weakens it. Ultimately, these pathological changes in bone anatomy increase the bone susceptibility for fracture [27]. Because bone cancer affects mainly the long bones of the lower limb [29], the effects of surgeries and chemotherapy have a negative impact on the physical performance of patients [30].

Over the past 25 years, changes in treatments have led to a steadily increase of the survival rates from most bone tumors [29]. Despite these improvements, diagnosis is still delayed [31]. As a result, at the time of diagnosis, up to one fifth of the patients will present a pathological fracture [32], reducing the chances of survival up to 20% when compared with patients without fracture [33].

Numerical methods have an important role in biomechanical simulations of biological structures. These methods allow to obtain results faster than in vitro studies without the invasive nature and less time-consuming [34].

In the current project, it is proposed to study the structure of proximal femoral tumors. A 2D and 3D models of the proximal femur with and without tumors will be created based on X-ray and CT images. In the end, both models will be studied using finite element method and meshless methods, which will allow to obtain and analyze the stress distribution on a global and local scale. Several locations and sizes of tumors will be considered, allowing to study their influence on the bone structure.

1.1 - Motivation

Bone sarcomas have a large impact on the patient health and social life. A compromised bone structure results from an aggressive tumor growth, which limits the physical performance of the patient. Even after the tumor removal, the late effects can still lead to a pathological fracture of the reconstructed bone. On the other hand, late diagnosis caused by lack of distinct initial symptoms has a negative influence on the patient prognosis due to the extension of bone damage. All these factors have an impact on the bone anatomy and can result in pathological changes that, ultimately, makes the bone more prone to fracture. Thus, one of the motivations of this work is to study and analyze the effect of bone sarcomas on the femoral structure.

Biomechanical simulations allow to solve complex problems faster. In particular, these numerical methods can be used to simulate and study bone tumors and its consequences on bone anatomy. One of the most common method is the Finite Element Method (FEM), but there are other methods, such as the meshless methods. As it can be seen in Figure 1.1 (the data presented was previously obtained through a research on Scopus database: www.scopus.com), the number of published papers related to the numerical analysis of bone sarcomas is reduced. Also, the search has revealed that meshless methods have not yet been used in this scientific area. Therefore, another motivation of this work was to understand the level of performance of these methods regarding the structural analysis of bone tumors and to expand the state-of-art of meshless methods.

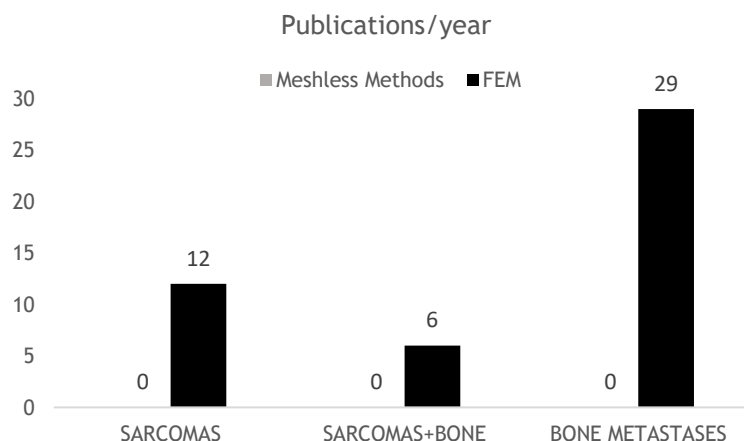


Figure 1.1 - Number of documents published through the years, in the subjects indicated. The data was obtained through a research on Scopus database (www.scopus.com) assuming as keywords the subjects indicated in the graph.

1.2 - Objective

The main goal of this dissertation is to study the effect of size and location of bone sarcomas in the femoral bone structure. For that reason, a detailed survey was performed in bone structure and bone tissue (physiology), bone sarcomas (physiology and mathematical models to describe it) and discrete numerical techniques (mathematical formulation and state-of-the-art). In this dissertation, the discrete numerical methods used are FEM, RPIM and NNRPIM.

Another major goal is to validate the meshless methods as a way of simulating and studying the effect of bone sarcomas on the proximal femur. In order to achieve these main goals, other secondary goals have been established:

- Simulate the overall femur/tumor system;
- Simulate tumors with different sizes and in different locations of the femur;

In the end, the results obtained *in silico* will be compared to the information available in the literature.

1.3 - Document Structure

The dissertation was organized in nine chapters. Chapter 1 begins with a brief description of the theme in study, followed by the objectives and structure of the present document. In chapter 2, it is presented a physiological and anatomical description of the bone, particularly, the femur. Also, the chapter includes an overview of bone growth and remodeling. At last, it is presented the material laws as well as biological, mechanical and mecanobiological models of bone remodeling. Chapter 3 focuses on a physiological description of bone sarcomas and the imaging technologies used for tumors detection and staging. In chapter 4, the numerical methods used in mechanical computation are described, namely the finite element method and meshless methods with emphasis on the natural neighbour radial point interpolation method (NNRPIM) and radial point interpolation method (RPIM). Chapter 5 describes the basic fundamentals of solid mechanics. In chapter 6, a review of the state-of-art is conducted concerning the different numerical methods used to analyze the proximal femur, bone sarcomas and bone metastatic lesions. Chapter 7 describes the preliminary work developed previously to the analyses of femoral bone sarcomas. In Chapter 8, the numerical studies to evaluate the effect of bone tumors on the proximal femur are presented, considering different clinical cases. At last, in chapter 9, it is presented the overall conclusions of this dissertation. Additionally, some limitations and forecasts of future work are mentioned.

Chapter 2

Bone

The human skeleton comprises all the bones, ligaments and tendons of the human body. The bones, the hardest tissue in the human body [5], have a characteristic physiological structure capable to adapt to the mechanical demands of the daily life [35]. However, in the events of a pathological change induced by a disease, bone structure is compromised and more susceptible to fracture.

In this chapter, anatomical and biological concepts of the bone are presented, followed by a detailed description of the femur anatomy. Furthermore, the material laws of the bone tissue are described, which correlate the apparent local density with the mechanical bone properties. Lastly, it is presented a description of numerical approaches able to predict bone remodeling, including biological, mechanical and mechanobiological models.

2.1- Skeletal System

The adult skeleton contains 206 bones, excluding the sesamoid bones [4]. Younger individuals contain a higher number of bones, as they fuse together to form an adult bone [9]. The skeleton can be subdivided into: axial skeleton and appendicular skeleton. The axial skeleton has 80 bones which comprise the vertebral column, skull, sternum and ribs. The appendicular skeleton, composed by 126 bones, includes all the bones in the limbs [4]. This system presents several functions which can be either mechanical or biochemical:

1. **Support:** the rigid structure allow to support the body and contains attachment points for muscles;
2. **Protection:** provide protection to the vital internal organs;
3. **Body movement:** the bones act as levers for the muscles which generate forces that permits body movement and locomotion;
4. **Mineral homeostasis:** the bones store mainly calcium and phosphate which are release to the blood in order to maintain mineral homeostasis;
5. **Blood cell production:** provides the required environment to allow hematopoiesis to occur within the marrow;

6. **Storage of triglycerides:** the yellow bone marrow is responsible for the storage of triglycerides.

2.2- Bone Morphology

Individual bones can be divided into four categories, according to their shape: long, short, flat and irregular [36]. The different bone types are represented in the diagram of Figure 2.1.

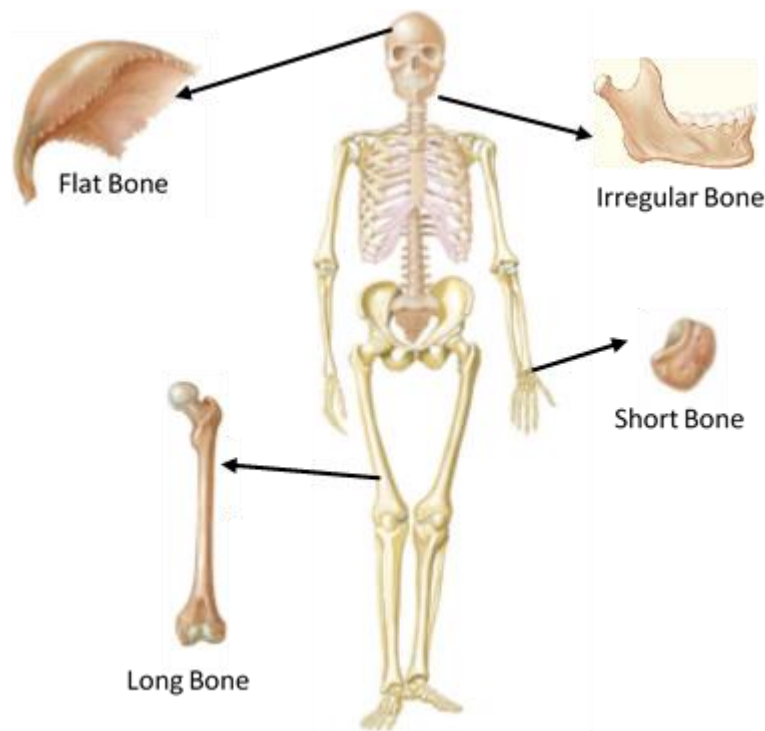


Figure 2.1 - Bone shape major groups. Adapted from [9].

Long bones are located in the limbs. These bones are curved with a length greater than the width. The curve occupies two different planes, which provides more strength to the bone [4]. At the extremities of the bone are located the epiphyses. These areas are mainly composed by cancellous bone surrounded by a thin layer of cortical bone. The long bones present in the arms, forearms, thighs and legs have one or more epiphyses on each end. However, the long bones of the hand and foot only have one epiphysis located on the distal or proximal end of the bone. The connection between the diaphysis and epiphysis occurs in the metaphysis through the epiphyseal plate, or growth plate. The diaphysis is the body of the bone mainly composed by compact bone. It is the largest area with a long and cylindrical shape. Within the diaphysis, there is a hollow center which contains the medullary cavity, filled with marrow. Bone marrow can be divided into yellow and red marrow. The red bone marrow is the site where hematopoiesis occurs, while the yellow marrow is composed mostly by adipose tissue. In the long bones, the yellow marrow completely replaces the red marrow with exception of the arm and thigh bones. In other bone types, the proportion of red and yellow marrow are variable. A thin layer of hyaline cartilage, named articular cartilage, covers the extremities of long bones where joints are formed. The cartilage, which has no periosteum, blood vessels or nerves, is important to reduce the friction between bones and to absorb shocks (Figure 2.2). Some examples of long bones are femur, humerus and tibia.

The outer surface of the bone is covered by a membrane of connective tissue named periosteum. The periosteum is composed by an outer layer of dense collagenous connective tissue with blood vessels and nerves, and an inner layer with bone cells, responsible for bone growth in thickness. The collagen fibers of the tendons and ligaments attach to the bones through a continuous connection with those of the periosteum [9]. The medullary cavity and the small cavities of the cancellous and cortical bone are covered by a layer of connective tissue, the endosteum, which contains different bone cells [37].

Short bones can be found in areas of limited movement and are characterized for being as thick and broad as they are long. These bones are composed by a thin cortical layer surrounding a cancellous tissue layer with marrow. Contrarily to long bones, short bones have no diaphysis. Examples of short bones are carpals and tarsals.

Flat bones serve mainly to protect or to provide a surface for muscle attachment. These bones have a relatively flattened and curved shape and have no diaphysis or epiphysis. Two thin cortical layers surround a variable cancellous tissue layer filled with red marrow. The flat bones are: cranial bones, sternum, ribs and scapulae.

Finally, due to their peculiar form, the irregular bones are all the bones without the characteristics referred previously. They are composed by a thin cortical layer filled with cancellous bone. The vertebrae and some of the bones in the face, like the jaw, are examples of irregular bones [9].

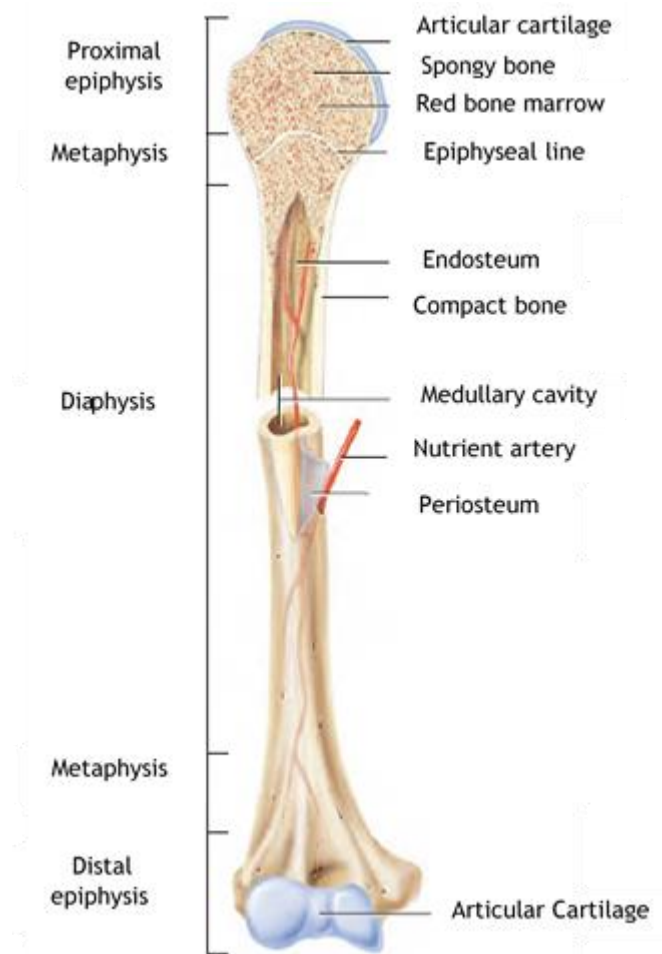


Figure 2.2 - Parts of a long bone: epiphysis, metaphysis and diaphysis; Representation of a partially dissected humerus. Adapted from [6].

2.3- Bone Structure

The bone tissue is composed by: an organic matrix (mostly collagen type I), calcium phosphate in the form of hydroxyapatite (HA) and water (Figure 2.3). The bone minerals are responsible for mechanical rigidity and load-bearing strength of the bone while the organic matrix provides flexibility and elasticity [36].

The different bone components are assembled in a complex arrangement of structures at different scales, ranging from the nanoscale up to the macroscale. These structures work together to perform a variety of mechanical, biological and chemical functions that contribute to the mechanical properties of the bone, such as its strength, stiffness, energy absorption and light weight. At a microscopic level, bone tissue is composed by collagen molecules. These molecules self-assemble into collagen fibrils of approximately 100 nm in diameter that are mineralized by HA. Between the collagen and minerals, pores are formed which are filled with non-collagenous proteins (NCPs) and water, creating the mineralized collagen fibril, the basic building block of bone. The fibrils are arranged unidirectionally into sheet-like structures, named lamellae with 3-7 μm thick, approximately. Lamellae bone is composed by a strong inorganic matrix (HA crystals) reinforced with a flexible and resistant organic matrix (collagen fibrils). Later, the lamellae assembles into different structures that constitute the cortical and trabecular bone. In the cortical bone, the lamellae organizes into concentric cylinders of approximately 200-300 μm in diameter and several millimeters long, forming the osteons. Each osteon aligns along the bone's long axis and contains a canal in its center, called Haversian canal, where blood vessels run. In the trabecular bone, the lamellae forms rods or struts with a crescent shape of 50 μm thick and 1 mm long.

At a macroscopic level, the osteons and trabeculae give rise to two different bone types: cortical bone and the trabecular bone, respectively. The cortical bone corresponds to 80% of the human skeleton mass and it is denser than trabecular bone. The cortical bone has microscopic blood vessels and no marrow. Contrarily, trabecular bone, which covers 20% of the skeleton mass, has many small blood vessels and marrow in between the trabeculae [20].

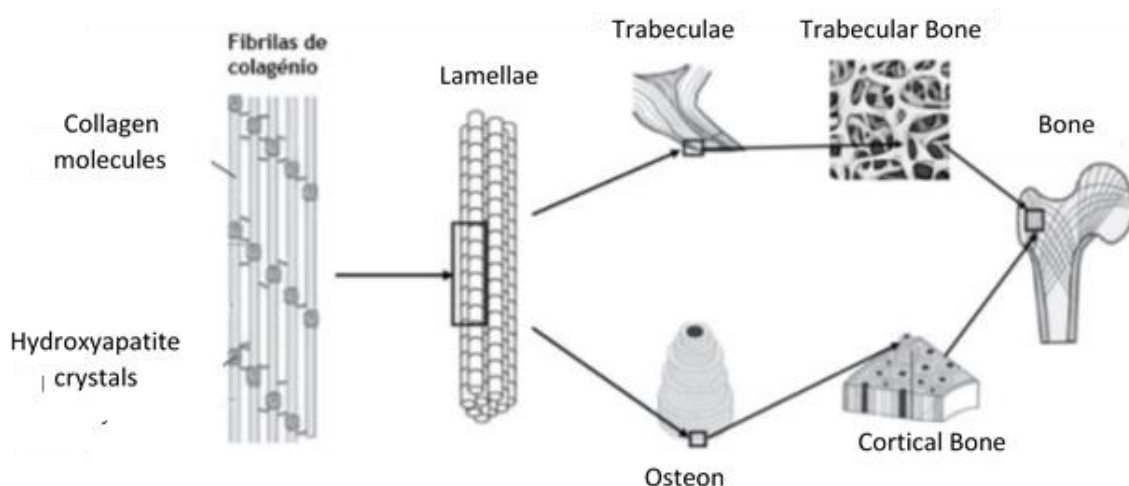


Figure 2.3 - Hierarchical structure of the bone. Adapted from [20].

2.4- Bone Cells

Bone tissue is composed by three types of cells - osteoclasts, osteoblasts and osteocytes. Bone cells are originated from mesenchymal stem cells. A small population of mesenchymal stem cells can be found in the bone marrow. Under the correct environmental conditions, these stem cells can give rise to osteochondral progenitor cells, the stem cells capable to originate and maintain the osteoblasts. Osteochondral progenitor cells are located in the endosteum and periosteum of the bone, providing a viable new source for osteoblasts [9].

The osteoblasts are responsible for the synthesis of new organic bone matrix on bone-forming surfaces. According to their activity, osteoblasts acquire different shapes. The immature and inactive osteoblasts have a spindle shape, while active and mature osteoblasts, capable to synthesize new bone matrix, have a circular shape with large nuclei [36]. These cells are capable to synthesize and secrete type I collagen, proteoglycans and glycoproteins which are released into the bone surface. Also, osteoblasts can participate in the mineralization of the matrix through the release of matrix vesicles packed with high concentrations of calcium and phosphate. When the concentration of these minerals in the matrix reach a critical level, crystals of hydroxyapatite are formed, further stimulating the formation of new hydroxyapatite crystals [9].

The osteoblasts activity is regulated by various hormonal, mechanical and cytokine signals. Different subpopulations of osteoblasts express different gene sets. As a consequence, different osteoblasts have heterogeneous responses to the various stimulus. Several studies indicate that the osteoblasts from the appendicular and axial bone respond differently to the biochemical and mechanical signals. Also, the heterogeneity within the osteoblast lineage may explain the different trabecular microarchitecture at different skeletal sites [36].

When an osteoblast becomes surrounded by bone matrix the cell is referred to as osteocyte. In fact, 15% of active osteoblasts differentiate into osteocytes [38]. With an estimated lifespan of 10-20 years, osteocytes account roughly 10 000 cells per mm³ in humans, making them the most abundant cell in the bones. Osteocytes present a shape typical of inactive cells, such as small Golgi structures, reduced endoplasmic reticulum and small nuclei. Though inactive when compared to osteoblasts, osteocytes are still capable to produce the components required to maintain the bone matrix. In the bone matrix, the osteocytes cell bodies occupied spaces without matrix called lacunae. Also, osteocytes are considered to be mechanosensor, playing a crucial role in the detection of mechanical signals and their transformation to biochemical stimulus. In the bone matrix, the osteocytes cell bodies occupied spaces without matrix called lacunae [35]. Inside each lacunae, there is only one osteocyte, on contrary to cartilage where more than one chondrocyte can be found per lacunae. Even though trapped in the matrix, the osteocytes still maintain contact with neighboring osteocytes through cell extensions that allow the diffusion of nutrients and gases among the cells. The canaliculi are the name of the spaces in the matrix occupied by these extensions and act as a mold for the formation of bone matrix [37].

Finally, osteoclasts are multinucleated cells responsible for bone reabsorption (Figure 2.4). As oppose to osteoblasts and osteocytes, osteoclasts originate from mononuclear precursors present in the red bone marrow, which also differentiate into monocytes (also named macrophages in tissues). These precursors, which are attached to the bone matrix, need direct contact with osteoblasts in order to mature into functional osteoclasts [9].

Like the osteoblasts, the osteoclasts activity is also coordinated by cytokines, hormones such as calcitonin and parathyrin as well as mechanical signals [37].

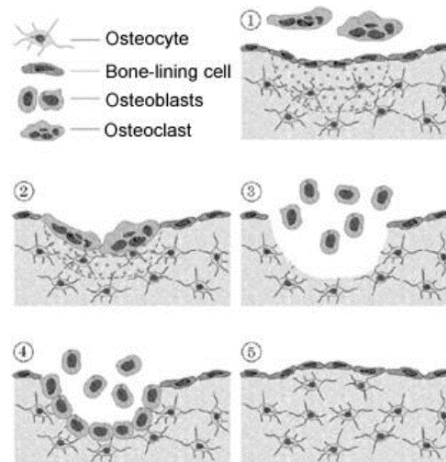


Figure 2.4 - Sequential phases of the normal bone remodeling cycle. Adapted from [8].

2.5 - Bone Matrix

The bone matrix contains organic and inorganic material with 5 to 10% water and less than 3% lipids. The organic portion of the bone matrix comprises 20 to 40% of bone volume and is composed mainly by type I collagen fibers (approximately 85 to 90%) as well as noncollagenous proteins. Osteoblasts produce collagen fibers and noncollagenous proteins in the same amount.

The flexibility and elasticity of the organic matrix is due to the prevalent collagen fibers. The type I collagen fibers have several crosslinks that increases the bone strength. Therefore, the bone resistance to biomechanical forces is dependent on the amount of collagen fibers. Also, their orientation and size influence the direction and magnitude of microcracks that arise in a stressed bone [8].

The noncollagenous proteins comprise several categories of proteins, including glycosylated proteins, proteoglycans and γ -carboxylated proteins. Around 25% of all noncollagenous proteins are not endogenously derived, which includes serum albumin and α 2-HS-glycoprotein. The noncollagenous proteins derived from the serum are important to regulate the mineralization of the matrix, while α 2-HS-glycoprotein is thought to regulate the proliferation of bone cells. Osteonectin is the most abundant noncollagenous protein in the matrix, representing 2% of total protein in the growing bone. This protein is believed to influence the growth of osteoblasts and the mineralization of the matrix. Alkaline phosphatase (AP) is the main glycosylated protein in the organic matrix. Bound to osteoblasts, AP performs an important yet un-defined role in the bone mineralization [36].

Approximately 50 to 70% of the bone volume corresponds to the inorganic matrix which is constituted by minerals. The more abundant mineral in the bone is hydroxyapatite $[\text{Ca}_{10}(\text{PO}_4)_6(\text{OH})_2]$. Other minerals can be found in the bone matrix in smaller amounts such as carbonate, magnesium and acid phosphate. The bone's hydroxyapatite crystals are much smaller than the geologic ones, measuring only 200 Å. Due to a lower solubility than the geologic crystals, these poorly crystalline and small crystals are able to support mineral metabolism. When deposited in the collagen fibers, the bone minerals provide mechanical rigidity, strength and hardness of the bone [36]. The average degree of mineralization differs from one skeletal region to another. However, an excessive mineralization makes the bone stiffer and more prone

to fracture. Also, larger crystals increases the brittleness of the bone, leading to a higher risk of fracture [8].

2.6- Bone Development

Bone tissue is a metabolically active organ that continuously undergoes modeling and remodeling in order to maintain its frame and mineral homeostasis. The different processes that occur during bone development are reviewed in the following sections.

2.6.1- Bone Formation

Ossification, or osteogenesis, is the process of bone formation by osteoblasts that occurs during fetal development and bone healing. The bone tissue is formed by intramembranous ossification or endochondral ossification. Intramembranous ossification occurs from highly vascularized membranes of connective tissue. However, in endochondral ossification, which is the main process of bone formation, bone is formed from a preexisting cartilage template [8].

The woven bone is the first type of bone tissue formed by osteoblasts during intramembranous and endochondral ossification. This weak bone has collagen fibers randomly oriented in different directions. During bone remodeling, osteoclasts remove the old bone (woven bone) and add new bone to the matrix called lamellar bone. This mature bone is organized into concentric layers of approximately 3-7 μm thick. Contrarily to woven bone, the collagen fibers in lamellar bone are oriented in parallel to one another [37].

The intramembranous ossification begins at the eighth week of fetal development and will only be completed after, approximately, two years. The frontal, parietal, and parts of the occipital bones as well as the upper and lower jaw are formed by this ossification process. In the membrane of the connective tissue, the ossification begins in the centers of ossification. In these centers, embryonic mesenchymal cells differentiate into osteochondral progenitor cells that later will origin osteoblasts. Osteoblasts produce an organic and non-mineralized matrix called osteoid, which is later mineralized, ossifying the membrane. Therefore, new woven bone is created that will radially expand throughout the centers of ossification. As a result of this process, osteoblasts become entrapped in the matrix and become osteocytes. The new woven bone develops into small trabeculae that becomes gradually larger and longer due to additional osteoblasts present at the surfaces of the trabeculae. This process forms a network of trabeculae and spaces, creating the trabecular bone. The spaces between the trabeculae are penetrated by blood vessels and the cells present in this cavities differentiate to form red bone marrow. The periosteum is formed by the osteoblasts that surround the bone in development. These osteoblasts will then produce the compact bone around the trabecular bone.

The endochondral ossification begins at the fourth week of fetal development. However, contrarily to intramembranous ossification, in endochondral bone formation, some cartilage starts to ossify at the end of the fourth week, while other cartilage may not begin this process until 18-20 years of age. This process happens in the majority of the skeletal system and is responsible for the formation of long and short bones [37].

Endochondral ossification begins with the differentiation of embryonic mesenchymal cells into osteochondral progenitor cells that give rise to chondroblasts. The chondroblasts form a hyaline cartilage template surrounded by a perichondrium and with a shape similar to the bone

that will be formed. As the matrix develops, the chondroblasts become entrapped and create chondrocytes. Afterwards, the perichondrium is penetrated by blood vessels and osteochondral progenitor cells present in the perichondrium differentiate into osteoblasts. With the production of bone matrix by the osteoblasts, the perichondrium becomes periosteum and the surface of cartilage begins to calcify into compact bone, creating a bone collar. During this process, the chondrocytes hypertrophied, releasing matrix vesicles into the cartilage which leads to the formation of hydroxyapatite crystals. As a result, the cartilage becomes calcified and the chondrocytes in this area die, leaving empty lacunae in the calcified matrix. The osteoblasts migrate into the calcified matrix and create bone on the surface of the cartilage, forming trabeculae. This area of trabeculae bone is called the primary center of ossification. In long bones, the primary ossification center forms in the diaphysis and, as the bone formation proceeds, the bone collar thickens and secondary ossification centers are formed in the epiphyses. The process in the secondary centers of ossification is the same as those in the primary ossification center. However, primary ossification centers only appear during embryonic development, whereas the secondary centers of bone formation are only created in the epiphyses of the tibia, humerus and femur within 1 month before birth. The last secondary ossification center will form in the medial epiphysis of the clavicle at the 18-20 years of age. At the end of this process, the cartilage is fully replaced by bone, except in the epiphyseal plate and on articular surfaces. The epiphyseal plate exists while the bone is actively growing. Once it stops growing, this plate regresses into the epiphyseal line [9].

2.6.2- Bone Growth and Remodeling

Throughout life, bone develops through longitudinal and radial growth, modeling and remodeling. Intramembranous and endochondral ossification lead to radial and longitudinal bone growth, which occurs until, approximately, 20 years of age, depending on the bone and individual. After bone formation, long bones are capable to grow in length and width. Until adolescence, growth in bone length occurs through the formation of new cartilage at the epiphyseal plate [8]. This cartilage is later calcified and ossified by the same process that occurs during endochondral ossification. With aging, the thickness of the epiphyseal plate decreases and becomes the epiphyseal line, in a process called epiphyseal plate closure. As a result, bone stops growing in length. Long bones can also grow in width through appositional growth by the addition of new bone due to osteoblasts present in periosteum. As the osteoblasts produce more matrix, the bone ridges increase in size and extend to each other, creating a tunnel surrounding a blood vessel. Then, the lamellae with a circumferential shape is remodeled and becomes an osteon.

The structure and shape of the bones in an adult skeleton are genetically determined, but other factors such as hormones and nutrition can modify the expression of those genes, thus influencing bone growth [9].

As a highly active organ, bone can progressively adjust its shape and size through bone modeling and remodeling, as a response to biomechanical forces. In bone modeling, the process of bone removal by osteoclasts and bone formation by osteoblasts are independent. Thus, bone resorption and bone formation do not occur at the same site. With aging, skeletal modeling becomes less frequent than bone remodeling [8, 36].

Approximately 10% of the human skeleton is renewed each year due to bone remodeling. Bone remodeling is a perennial and coordinated process prevalent in the adult skeleton. This

process is crucial to maintain the bone mass, to repair microscopic damage in specific regions (with the purpose to prevent accumulation of damage and, consequently, fracture), and to preserve mineral homeostasis. In a homeostatic equilibrium, old bone is removed and new tissue is formed at the same skeletal site due to a response to mechanical and biochemical stimuli. An increase of the mechanical stress leads to an increase in osteoblastic activity and decrease in the osteoclastic activity, resulting in bone formation. Contrarily, as the mechanical stress decreases, the osteoblastic activity also decreases while osteoclastic activity is increased, which leads to bone resorption. However, if there is an imbalance between bone resorption and bone formation, the structure of the bone is compromised and several bone diseases can arise, such as osteoporosis [39, 40].

The remodeling process depends on the temporary interaction between the osteoclasts and osteoblasts, which are organized into basic multi-cellular units (BMU's). The organization of the BMU's is different in the cortical and trabecular bone and is estimated that $1-2 \times 10^6$ of these units exist in the human skeleton [40]. Each year, between 2% and 5% of cortical bone is renewed. However, trabecular bone has a larger surface and, therefore, is more frequently remodeled than cortical bone.

Bone remodeling is a cyclic process composed by three sequential phases: reabsorption, reversion and formation (Figure 2.5). During the first phase, the mononuclear pre-osteoclasts migrate to the bone surface, where occurs the formation of multinucleated osteoclasts. Thereafter, mononuclear cells arise in the bone surface, preparing it for bone formation and to provide signals for the migration and differentiation of osteoblasts. Finally, osteoblasts are responsible for bone formation, which occurs in two stages: matrix synthesis (osteoid) and extracellular mineralization. The activity of these cells is regulated by a set of hormones, cytokines, as well as mechanical loading, and there is a systemic and local regulation of bone cell function [38].

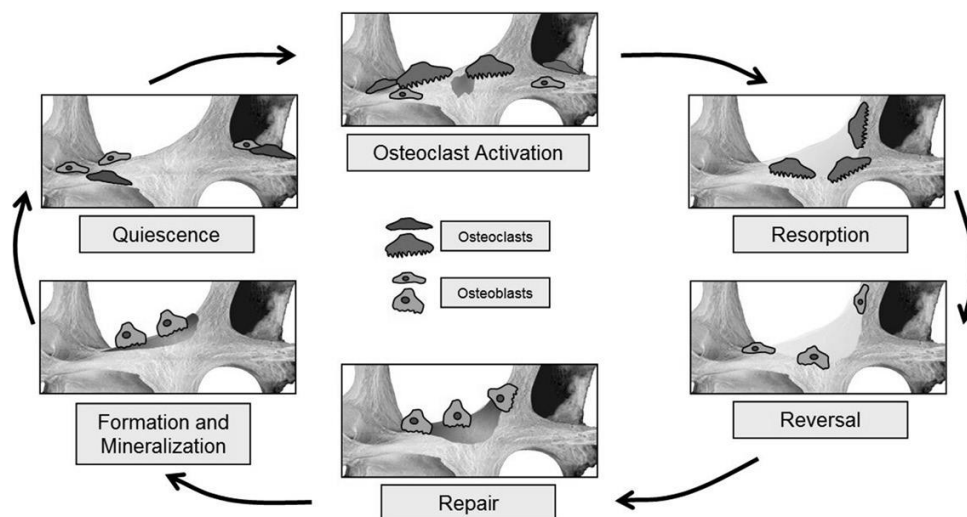


Figure 2.5 - Sequential phases of the normal bone remodeling cycle. Adapted from [8].

2.7- Trabecular and Cortical Bone

The human skeleton is composed by two different bone types: the cortical and trabecular bone. Overall, the cortical tissue accounts for 80% of the bone mass and the remaining 20% match the trabecular tissue. Depending on the bone and skeletal site, the ratio between

trabecular and cortical bone is different. The cortical bone is composed by osteons while the trabecular bone is composed by trabeculae [36].

Cortical bone is dense and compact and is typically found in the surface of bones (Figure 2.6). The main functions of the cortical bone is to provide protection and mechanical strength, but it can contribute to mineral homeostasis in the cases of severe mineral deficit. Compared to trabecular bone, cortical bone has a slow turnover rate and, as a result, its porosity is usually less than 5%. An increase in cortical remodeling leads to an increase in porosity and decrease of the cortical bone mass. With aging, the porosity of the cortical bone increases [38].

In a healthy human, it is estimated to exist 21×10^6 cortical osteons, named Haversian systems, which constitutes, approximately, $3,5 \text{ m}^2$ of total remodeling area [36]. Each Haversian system contains a central canal (Haversian canal) where blood vessels, nerves and lymphatic vessels run. The osteons are aligned parallel to each other and across the bone longitudinally. Within the osteon, there are lacunae where osteocytes are to be found. From each lacunae, a network of canaliculi spread throughout the osteon. These network connects the vessels and nerves in the medullary canal, Haversian canal and in the Volkman's canal (perforating canals where the blood vessels and nerves enter the cortical bone in the periosteum), allowing for the distribution of nutrients and oxygen, as well as the disposal of waste throughout the bone. Between each osteon, there are remnants of old Haversian systems called interstitial bone, with a structure similar to the osteons but with a higher mineralization degree. These secondary Haversian systems are formed during bone remodeling and contain a boundary between the osteon and the interstitial bone named cement lines. The osteons that have not being remodeled are called primary osteons and do not have cement lines [20].

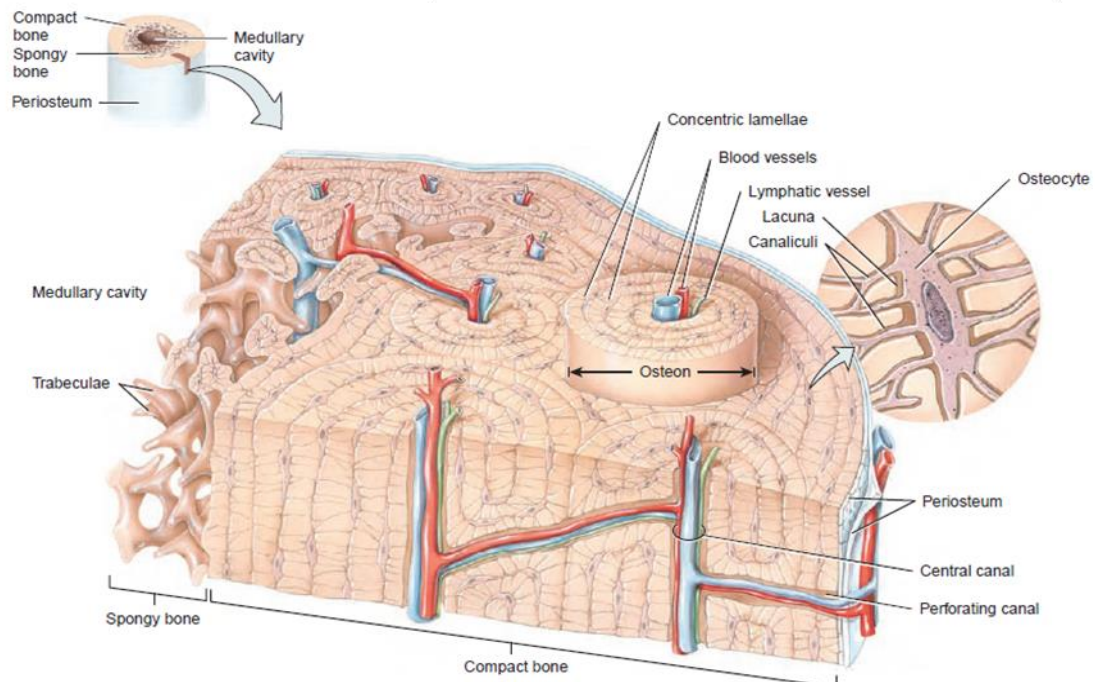


Figure 2.6 - Osteons in compact bone. Adapted from [9].

The cortical bone is composed by two different surfaces: an outer periosteal surface and an inner endosteal surface. Appositional growth and fracture repair occur in the periosteal surface. On the periosteal surface, bone formation prevails inducing an increase in diameter with aging. The inner surface has a higher remodeling activity than periosteal surface due to

greater biomechanical and biochemical signals. With aging, the marrow space in the endosteal surface is expanded due to an exceeding bone resorption [36].

Despite constituting only one fifth of the bone mass, trabecular bone accounts for 80% of the bone surface. Trabecular bone is composed by rods and studs interconnected to form the trabeculae. In a healthy human, there are approximately 14×10^6 trabeculae that constitutes 7m^2 of the total trabecular area [36]. Between each trabeculae are spaces, which are filled with bone marrow and blood vessels. This bone type is more elastic and porous with a higher turnover rate than cortical bone. For that reason, trabecular bone plays a crucial metabolic role in maintaining mineral homeostasis [38, 41].

2.8 - Femur Anatomy

The longest and strongest bone in the adult human skeleton is the femur with an average length of 48 cm (Figure 2.7). Located in the thigh, the femur extends from the hip to the knee and as the ability to support as far as 30 times the weight of an adult [41]. It is a slightly curved bone with a variable degree of inclination among different people. In the female, the femur has a higher degree of inclination due to a greater breadth of the pelvis. Like other long bones, the femur can be divided into a body and two extremities [9].

The proximal femur, or upper extremity, is composed by a head, a neck, a greater and a lesser trochanter. The prominent and rounded head has a smooth surface covered with cartilage, except in the fovea, an ovoid depression located below and behind the head. The fovea acts as an attachment point for the ligament of the head of the femur (or ligamentum teres). This ligament provides support for the hip joint and transports an artery that supplies the femur's head. The head of the femur is connected to the body through the neck, structurally weak area prone to fractures. This flattened bone forms an angle opening medialward with the body. The widest angle is formed during infancy and diminish during growth. In adulthood, the angle between the neck and the body is 125° . This angle can vary in inverse proportion to the development of the pelvis and the stature. Also, the angle is different between female and male, due to differences in the width of the pelvis.

Lastly, there are two trochanters in the femur- the lesser and greater trochanters- that act as levers to the muscles, allowing the rotation of the thigh on its axis. The lesser trochanter is a conical eminence located in the inferior and posterior part of the neck. The size of the lesser trochanter is variable among different people. A single muscle is attached to the lesser trochanter. Located at the junction with the neck and the body of the femur, the greater trochanter is an irregular and large eminence. The trochanters provide an attachment point for muscles that secure the hip to the thigh. At the union between the greater trochanter and the upper part of the neck, a protuberance of variable size called tubercle of the femur can be found. Like the trochanters, the tubercle of the femur is an attachment site for muscles. On the anterior side of the femur, there is the intertrochanteric line between the trochanters. On the posterior side of the femur, the intertrochanteric crest connects the trochanters.

The body, or shaft, has a cylindrical shape with a slight curvature. At the proximal end of the shaft, a roughened crest named linea aspera is the site of attachment for multiple muscles of the hip and thigh [4].

The distal femur, or lower extremity, contains medial and lateral condyles which articulate with the tibia to form the knee joint. The medial and lateral epicondyles are located proximally to the condyles and form an attachment point for muscles and ligaments. Proximal to the

medial epicondyle, an adductor tubercle can be found and is, also, a site of attachment for muscles. The articulation between the femur and patella in the knee is established by a wide groove formed between the condyles named patellar surface [9].

The inner and outer structure of the femur are defined by the mechanical conditions that exist in every point in the bone. Overall, the femur is composed by an outer shell of cortical bone surrounding cancellous bone. The ratio of cortical to trabecular bone varies throughout the femur; in the head, the ratio is 50:50 and 95:5 in the shaft [36]. Also, the femur contains a medullary cavity with red and yellow marrow, an endosteum and a periosteum as well as articular cartilage in the hip and knee joint [41].

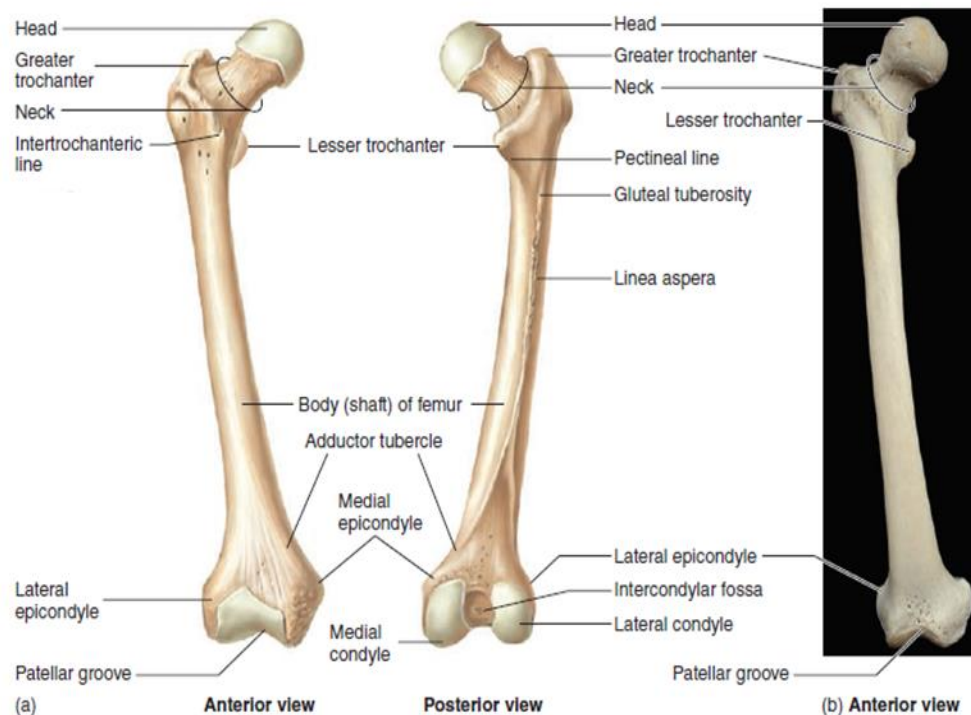


Figure 2.7 - Lateral and posterior view of the femur. Adapted from [4].

The femur performs several daily movements, which requires the action of multiple muscles (Figure 2.8). The 22 muscles that act on the femur provide, not only stability, but also the necessary force to perform these movements. [42]. These muscles can be subdivided in different ways. Based on their function, the muscles can be divided into: flexors, extensors, abductors, adductors, external and internal rotators.

Each subdivision contains different muscles [4, 9]:

- **Flexors:** *iliopsoas*, *rectus femoris*, *tensor fasciae latae* and *pectineus*;
- **Extensors:** *gluteus maximus*, *semimembranosus*, *semitendinosus* and *biceps femoris*;
- **Abductores:** *gluteus medius* (the main abductor of the hip articulation) and *gluteus minimus*;
- **External Rotators:** *piriformis*, *quadratus femoris* and *obturatorius internus externus*;
- **Internal rotators:** *gluteus minimus*, with the help of *tensor fasciae latae*, *semitendinosus*, *semimembranosus* and *gluteus medius*.

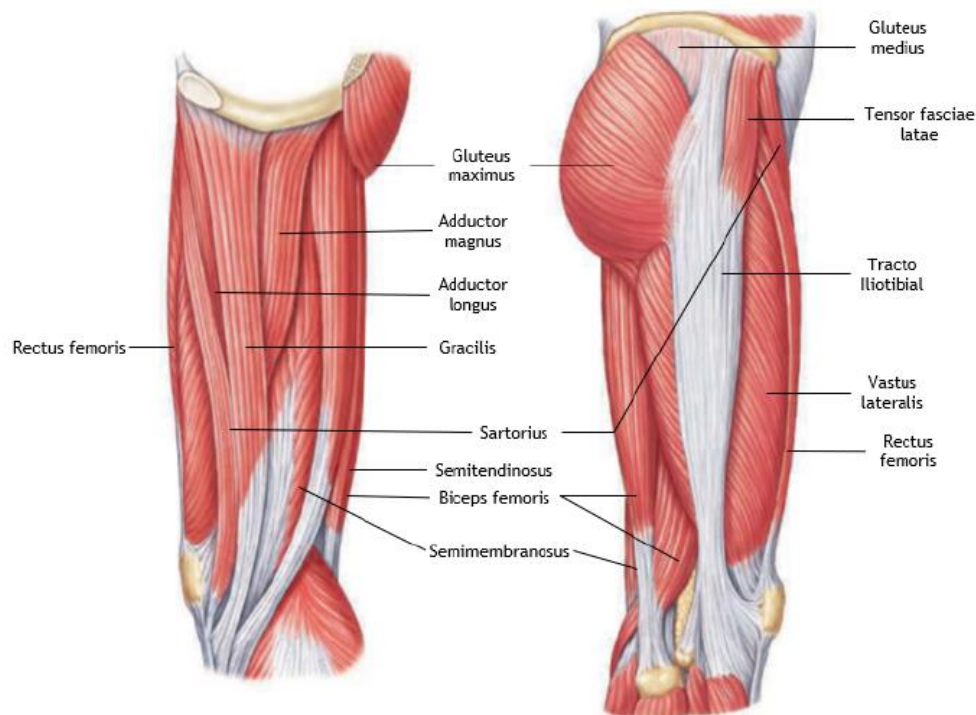


Figure 2.8 - Muscles in the thigh: medial and lateral view [7].

2.9 - Bone Quality

As the main support system in the human body, bones are constantly submitted to a mechanical stress under different loading conditions. The maximal amount of load endured by the bone without causing structural failure defines its strength. Bone strength depends on bone mass, geometry and quality in order to dissipate the stress generated within the bone and to prevent the formation of micro-cracks [43].

The term bone quality is related to several aspects of the bone structure and architecture, which comprises microarchitecture, the degree of mineralization, bone turnover, fatigue damage, composition of the matrix and geometry [44]. When the quality of the bone is compromised, bone strength decreases and the bone becomes more fragile with a higher risk of fracture. The assessment of bone quality *in vitro* is most commonly associated with the determination of the bone turnover [45]. Higher turnover rates eliminate microdamages which, in return, lead to an improvement of the bone quality [44].

In the femoral bone, the assessment of bone quality is important to evaluate the risk of fracture but also to determine therapeutic options in implantology. Dorr et al. developed an X-ray classification system based on the femoral shape and cortical thickness [46]. Three different structural patterns were identified, based on X-ray images, and labelled as A, B and C. A bone classified as type A has dense and thick cortices with a narrow and funnel shape of the proximal femur canal. This bone type is more commonly found in men and in younger people. A type B bone prevails in men and presents a moderate cortices with higher porosity and irregular endosteal surfaces. Lastly, a type C bone contains a wide and cylindrical shaped canal in the

proximal femur with dramatically thin walls. This bone type is more common in older women due to a more compromised structure [47].

2.10 - Bone Mechanical Properties

The bones experience a set of forces, or loads, with external and internal origins. The external forces can occur due to an impact during a fall or during walking, whereas the internal forces are caused by contact forces between bones, muscle contraction and tension from ligaments. While the forces are acting, stress develops in the bone. The deformation caused by the action of the external forces leads to strains, which defines the relative volume/shape change of the domain.

In structural engineering, it is common to depict the load-deformation curve of material or structure [48]. The stress-strain curve replicates the material behavior of the bone (Figure 2.9) and the curve slope represents the elasticity modulus (Young's Modulus). The Young's modulus is a measure of the bone stiffness. The area under the curve denotes the amount of energy per unit of bone volume required to induce a fracture in the bone [8].

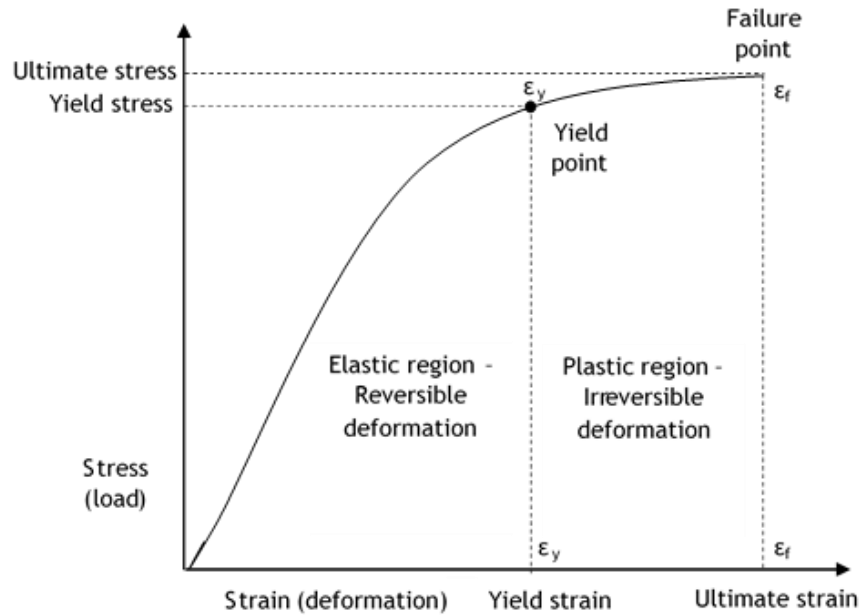


Figure 2.9 - Representation of a stress-strain curve.

The bone's capacity to sustain loads is dependent on its mechanical properties. In order to perform numerical and experimental analysis, it is important to determine these properties [49]. The bone is composed by a dense and compact tissue, the cortical tissue, and by the trabecular tissue, which has a smaller apparent density. The apparent density, ρ_{app} , is determined by the wet mineralized mass of hydrated tissue (w_{sample}), over the volume of sampled tissue (V_{sample}).

$$\rho_{app} = \frac{w_{sample}}{V_{sample}} \quad (2.1)$$

However, the apparent density is dependent on the bone porosity, p , as demonstrated by the following expression,

$$p = \frac{V_{holes}}{V_{sample}} \quad (2.2)$$

The porosity differs between the trabecular and cortical bone. The trabecular bone is more porous with a porosity that varies between 30% up to 90%. On the other hand, cortical bone is more compact and, ergo, with a reduced porosity that varies between 5% up to 30%.

Based on the compact bone density ($\rho_0 = 2,1 \text{ g / cm}^3$), it is possible to calculate the apparent density (ρ_{app}) through the expression,

$$\rho_{app} = \rho_0 \cdot (1 - p) \quad (2.3)$$

Many studies relate the bone mechanical properties with bone density [50-52]. One of these studies was performed by Carter e Hayes [53] that, while analyzing cortical and trabecular bone, discovered that the Young's modulus was proportional to the cube of apparent density:

$$E = 3790 \varepsilon^{0,06} \rho^3 \quad (2.4)$$

where E is the elastic modulus in MPa, ρ is the apparent density in g/cm³ and ε is the deformation rate per second. Despite being capable of predicting bone mechanical properties, this model does not consider the influence of bone microstructure and mechanical behaviors in different directions [5].

- **Lotz material law**

The bone orthotropic behavior was first considered in the work of Lotz [54], where it was suggested different material laws for the behavior of the cortical and trabecular bone. Thus, using the apparent density (ρ_{app}), it was possible to determine the elasticity modulus and the ultimate compressive stress for both the trabecular and cortical bone in the axial and transversal direction:

$$E_i = a_1 \cdot (\rho_{app})^{a_2} \quad (2.5)$$

$$\sigma_i^c = a_3 \cdot (\rho_{app})^{a_4} \quad (2.6)$$

Where E_i is the elasticity modulus and σ_i^c the ultimate compressive stress in direction i , expresses in MPa and the apparent density ρ_{app} in g /cm³. The coefficients for the trabecular and cortical bone are stated in Table 2.1, for both the axial and transversal direction [5].

Table 2.1 - Coefficients of Lotz law.

Bone tissue	Direction	a ₁	a ₂	a ₃	a ₄
Cortical	Axial	2,056E+03	3,090E+00	7,240E+01	1,880E+00
	Transversal	2,314E+03	1,570E+00	3,700E+01	1,510E+00
Trabecular	Axial	1,904E+03	1,640E+00	4,080E+01	1,890E+00
	Transversal	1,157E+03	1,780E+00	2,140E+01	1,370E+00

- **Belinha material law**

A new orthotropic law was proposed by Belinha *et. al.* [55] based on the experimental data obtained by Zioupos [56]. They concluded that the law governing the mechanical behavior is the same for both the cortical and the trabecular bone. With the work of Belinha *et. al.* [55], it is possible to classify the bone according to the apparent density (ρ_{app}), such that $\rho_{app} \leq 1,3 \text{ g/cm}^3$ corresponds to trabecular bone and corresponds to cortical bone. The minimum and maximum values found for the apparent density were $0,1 \text{ g/cm}^3$ and $2,1 \text{ g/cm}^3$, respectively.

Thus, based on the work of Zioupos [56] and Lotz [54], Belinha *et. al.* [55] proposed a new mathematical orthotropic law, unified for the trabecular and the cortical bone. Hence, the elasticity modulus in the axial direction (E_{axial}) is obtained by the following expression:

$$E_{axial} = \sum_{j=0}^3 a_j \cdot (\rho_{app})^j \text{ if } \rho_{app} \leq 1,3 \text{ g/cm}^3 \quad (2.7)$$

$$E_{axial} = \sum_{j=0}^3 b_j \cdot (\rho_{app})^j \text{ if } \rho_{app} > 1,3 \text{ g/cm}^3 \quad (2.8)$$

Where the coefficients a_j and b_j are represented on Table 2.2 Belinha *et. al.* also proposed mathematical curves for the elasticity modulus in the transversal direction (E_{trans}) and ultimate compressive stress in the axial (σ_{axial}^c) and transversal direction (σ_{trans}^c). The values for E_{trans} , σ_{axial}^c and σ_{trans}^c are calculated by the following expressions:

$$E_{trans} = \sum_{j=0}^3 c_j \cdot (\rho_{app})^j \quad (2.9)$$

$$\sigma_{axial}^c = \sum_{j=0}^3 d_j \cdot (\rho_{app})^j \quad (2.10)$$

$$\sigma_{trans}^c = \sum_{j=0}^3 e_j \cdot (\rho_{app})^j \quad (2.11)$$

Where the coefficients c_j , d_j and e_j are represented in Table 2.2.

Table 2.2 - Coefficients of Belinha law.

Coefficient	$j = 0$	$j = 1$	$j = 2$	$j = 3$
a_j	0,000E+00	7,216E+02	8,059E+02	0,000E+00
b_j	-1,770E+00	3,861E+05	-2,798E+05	6,836E+04
c_j	0,000E+00	0,000E+00	2,004E+03	-1,442E+02
d_j	0,000E+00	0,000E+00	2,680E+01	2,035E+01
e_j	0,000E+00	0,000E+00	2,501E+01	1,247E+00

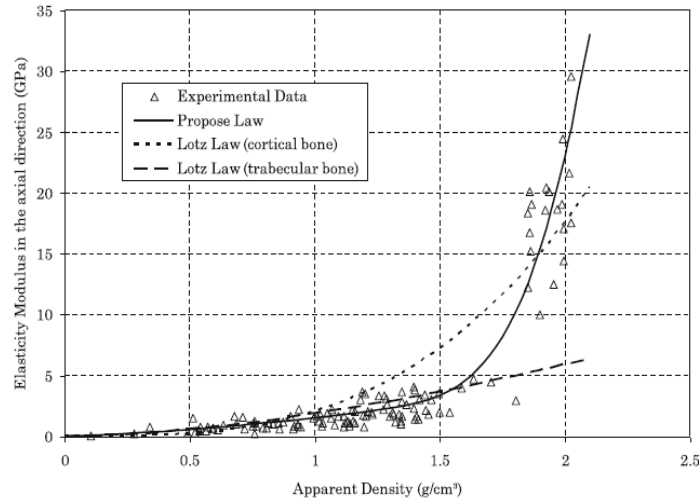


Figure 2.10 - Elasticity modulus in axial direction. Comparison between experimental data from Ziopous work, Lotz law for cortical and trabecular bone, and mathematical model proposed by Belinha. Adapted from [5].

The graphical representations for the elasticity modulus in the axial and transversal direction as well as for the ultimate compressive stress in the axial and transversal direction are represented in Figure 2.10 and Figure 2.11, respectively [5].

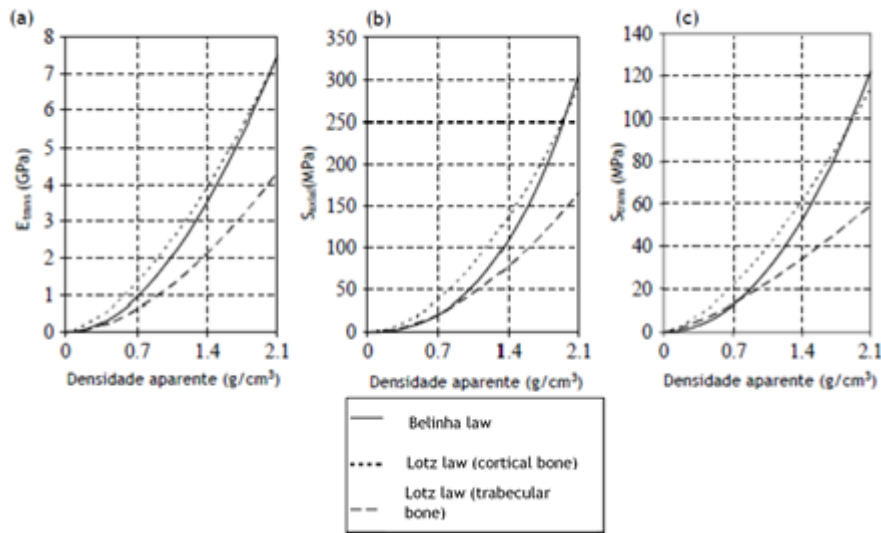


Figure 2.11- (a) Elasticity modulus in transversal direction. (b) Ultimate compressive stress in axial direction. (c) Ultimate compressive stress in transversal direction. Adapted from [5].

2.11 - Bone Remodeling Process

The remodeling bone phenomena leads to changes in the bone structure and, consequently, in the mechanical properties. In order to understand this complex process, several mathematical models of bone remodeling have been developed and proposed in the literature. These models are able to provide useful clinical information related to: therapeutic options for metabolic bone disorders, such as in osteoporosis; as well as predicting the distribution of tension and correlate it with bone remodeling in situations of implant placement. Next, a brief

overview over mechanical, biological and mecanobiological models proposed by several authors.

2.11.1 - Mechanical Models

The mechanical models are able to predict bone remodeling based on mechanical stimulus and bone structure, but do not consider actual biological processes. The first mathematical formulation of “Wolff’s Law” was developed by Pauwels [5]. After this, several authors developed and proposed different models of bone remodeling. Cowin [57] developed a theory named adaptive elasticity, describing the process of bone remodeling as a result of the sum of the chemical reactions between the bone matrix and extracellular fluids. Later, Cowin [58] created a model able to predict density changes and reorientation of trabecular architecture, through the stress applied to the bone and certain bone parameters. However, in order to describe the remodeling behavior, the model requires an elevated number of parameters needed for bone remodeling, which poses a significant disadvantage.

The concept of self-optimization was proposed by Carter and Fyhrie [59]. Then, they developed a model that is able to predict the apparent density of the bone and the trabecular orientation for a continuous description of the trabecular material. However, the model presented a disadvantage since the approach only considered a single load condition, which only occurs, for example, during the gait, in the posture phase of a single limb. Later, Carter [59, 60] expanded this approach and described a theory that considers the daily loading history. This condition is characterized in terms of stress magnitude, cyclic strain energy density and number of loading cycles.

Beaupré [14, 61] modified and extended ideas developed by other authors in order to develop a remodeling theory dependent on time. Later, Petermann [62] suggested an improved version of the Carter’s model which reported that the adaptation bone tissue may be described at a continuous level by using global parameters of the material and measures of stress/deformation. Also, Doblaré [63] developed a continuous damage repair algorithm grounded in the model of Carter.

2.11.2 - Biological Models

The biological models are important in order to predict the results of multiple and simultaneous actions of paracrine and autocrine factors in the process of bone remodeling. In recent years, it is possible to observe a growing interest in this approach.

The first mathematical model developed was created by Komarova [64] and demonstrates the effect of paracrine and autocrine signalization in the interaction between osteoclasts and osteoblasts, and, consequently, it describes the changes in the bone mass in a single site of bone remodeling. Also, the model is capable of predicting different modes of behavior: a bone remodeling in a healthy situation or in a pathological one, such as Paget’s disease. Based on this model, Komarova studied the regulation of bone remodeling through the administration of parathyroid hormone (PTH). The results obtained demonstrated that a continuous administration of PTH leads to bone loss as it activates the osteoclasts responsible for bone resorption [65].

Other studies have been developed to investigate the mechanism for different effects of PTH administration [64, 66]. Ayati *et. al.* developed a model based on Komarova [67], which studied the bone remodeling phenomena in an healthy and pathologic situation such as myeloma, which is an important tool to investigate new possible treatments [68].

2.11.3 - Mechanobiological Models

The mechanobiological models are a useful tool to predict bone remodeling since it takes in consideration the mechanical stimulus as well as the biological factors that influence this process. These models are recent and have been developed in order to fill the existing gaps related to the bone remodeling process.

The model created by Hambli describes the process of bone remodeling as a combination of the osteoclasts and osteoblasts activity with the bone mechanical behavior, considering the accumulation and mineralization of fatigue damages. This model was later applied in a model of proximal femur using finite element method (FEM) which demonstrated similar remodeling patterns observed in a human proximal femur [69].

Another model that simulates the bone remodeling process, was developed by Mercuri. The mathematical model describes the biological response to different mechanical stimulus, such as strain energy density (SED). The model was tested in a two-dimensional femur model developed by FEM. The results demonstrated that different mechanical stimulus can influence the bone homeostasis [70].

Chapter 3

Bone Sarcomas

The term neoplasia or tumor is defined as an abnormal mass of tissue resulting from an excessive, uncontrolled and autonomous growth of a group of cells. Based on their growth patterns, tumors can be classified as benign, when their growth occurs in a confined local area, or malignant, which are capable of invading surrounding tissues, entering the bloodstream and, ultimately, spreading to other parts of the body [71].

In this chapter, a socioeconomic analysis for bone sarcomas is presented, followed by a detailed description of the distinct types of sarcomas. Furthermore, the growth and staging of bone sarcomas are described as well as the imaging methods necessary to define them. Finally, the mechanical properties of bone sarcomas are introduced.

3.1 - Socioeconomic Analysis

Cancer is a noncommunicable disease (NCD) with a global impact. According to the World Health Organization (WHO), in the 21st century, cancer is the leading cause of death worldwide responsible for death of people before age 70 years in 91 of 172 countries. In fact, cancer incidence and mortality rates are rapidly increasing on a global scale and, as a result, it poses a significant obstacle to the increase of life expectancy. Based on the GLOBOCAN 2018 estimates, 18,1 million new cancer cases and 9,6 million cancer deaths are expected to occur in the year 2018 (Figure 3.1)[23].

Sarcomas are a rare heterogeneous group of tumors, accounting for less than 1% of all adult diagnosed cancers and nearly 21% of all pediatric malignant cancers [12]. Also, sarcomas are responsible for 2% of cancer deaths and the 5-year survival rate is 60% [26]. Sarcomas can be divided into soft-tissue sarcomas and bone sarcomas. Soft-tissue sarcomas are more frequent, representing nearly 87% of all diagnosed sarcomas, with the remaining 13% related to bone sarcomas.

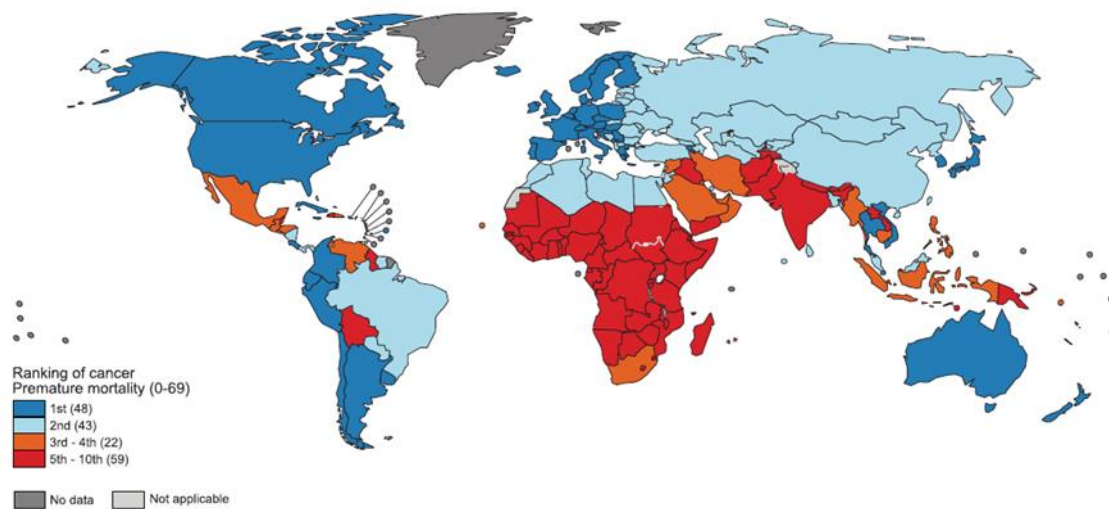


Figure 3.1 - Global map representing the National Ranking of Cancer as a cause of death at ages below 70 years in 2015. Adapted from [23].

Bone cancer can be classified as primary bone tumors (sarcomas), or secondary bone tumors. Bone sarcomas are rare primary malignant tumors that originate in the bone and are responsible for only 0,2% of all malignant tumors [29]. Although extremely rare, the incidence rate for these type of tumors is rising as life expectancy becomes higher in developed countries. However, improvements in chemotherapy treatment have led to a steadily increase of the survival rates over the past 25 years. The 5-year survival rate in Europe is 57% (Figure 3.2) [22]. Regardless of treatment improvements, the incidence of subsequent secondary malignancies within 2 to 3 years from the time of initial diagnosis ranges between 30 to 40%, with 90% being located in the lung [72].

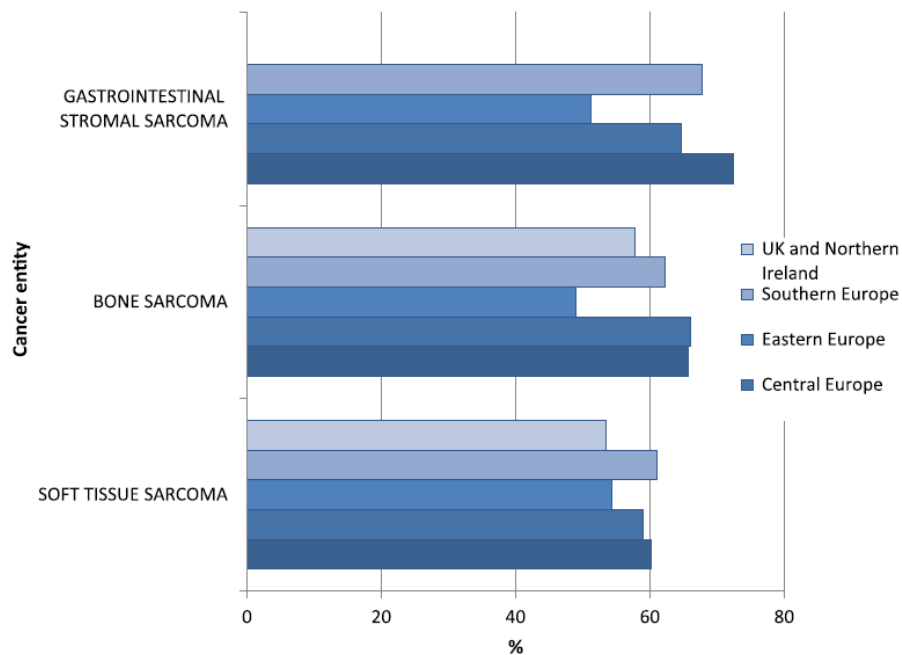


Figure 3.2 - Incidence rate of bone sarcomas in Europe. Adapted from [22].

Secondary bone tumors are caused by metastases from other cancers, such as lung cancer, breast cancer and prostate cancer. In fact, the bones are the third most common place for metastatic cancer of which the femur is among the most affected bones [73], with an incidence rate of up to 70% in patients with advanced breast and prostate cancer and 15 to 30% in patients with carcinoma of stomach, lung, rectum, colon, thyroid, kidney or bladder. In the United States alone, an estimation of 350 000 deaths occur due to bone metastasis. Furthermore, the survival rates for metastatic bone cancer are very low: the 5-year survival rate for a patient with breast cancer is only 20%. The frequency of bone metastasis is owed to the high blood flow in the areas of the red marrow [74].

Many factors can influence the risk of developing bone cancer, with age being one of the most important. These malignant tumors have a double peak of incidence in early adolescence and the elderly. Teenagers and young adults with ages between 15 -24 years are the most affected by this type of cancer, which is currently the third leading cause of death in this age group within developed countries, females have an earlier peak of incidence below 15 years whereas males have a peak after 15 years of age in all continents. This could be due to the growth spurt that occurs earlier in females during adolescence. As demonstrated by Figure 3.3, the incidence rate plateaus during the third and fourth decade, but begins to increase from the fifth decade onwards, reaching a peak at 70 years or later depending on life expectancy [11]. However, males are more affected by bone cancer than females, with a male/female ratio of 13:10 [29]. Secondary bone cancer is more common among adults [27].

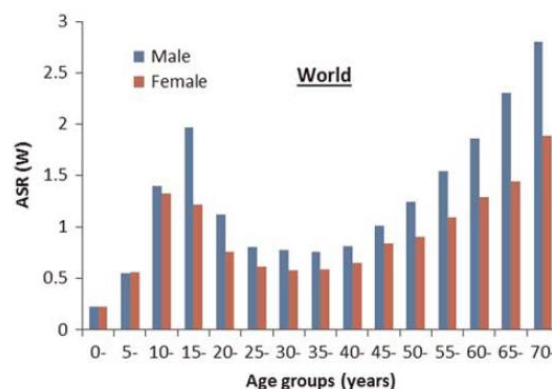


Figure 3.3 - Primary malignant bone tumor incidence in the world. Adapted from [11].

Bone sarcomas comprise a large and distinct group of tumors (Figure 3.4). The most common types are osteosarcoma, chondrosarcoma and Ewing's sarcoma. Osteosarcoma has an incidence rate of 32% and affects all age groups and is the second leading cause of death in young children [21]. Chondrosarcoma occurs mainly during adulthood and the incidence gradually increases with age. Ewing's sarcoma accounts for only 15% and affects mostly during the second decade of life. The other types of bone tumors comprise only 10% of bone sarcomas [11, 32].

Due to its heterogeneity, bone tumors can affect any bone or cartilage. However, the areas more affected are the metaphyses of long bones, where the growth rate is maximum. Osteosarcoma is mostly found in the distal femur (40%), tibia (20%), humerus (10%) and pelvis (8%). Chondrosarcomas can be found mainly in the axial skeleton, affecting the pelvis and ribs (45%), ilium (20%), femur (15%) and humerus (10%). Lastly, Ewing's sarcomas are more common in the diaphysis or metaphyseal-diaphyseal portion of long bones, pelvis and ribs [32].

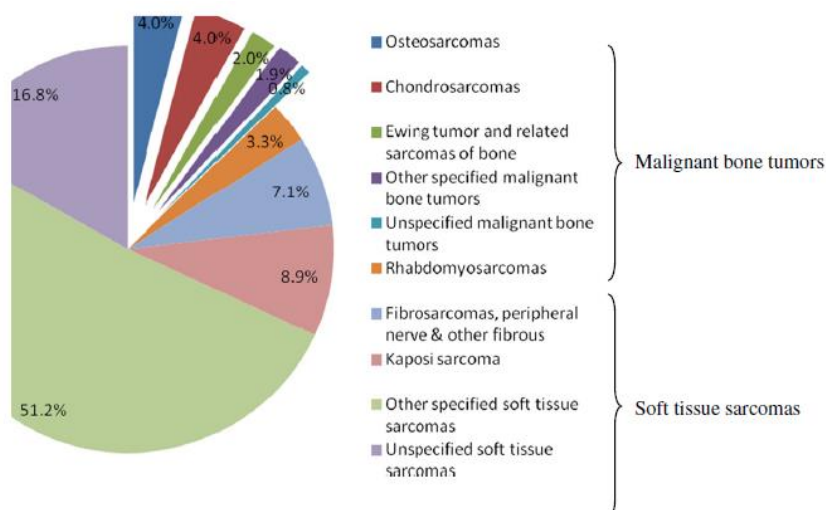


Figure 3.4 - Distribution of new cases by histology, in 2008. Adapted from [12].

Globally, malignant bone tumors are not as significant as other neoplasms, such as breast cancer. However, because bone sarcomas affect mostly young children and, thus their potential longevity, the long-term effects of this disease can have a severe impact on their lives. Therefore, recent studies have been conducted to evaluate the late effects of cancer treatments among children [21].

In the United States, approximately 1 of 640 individuals, between the ages of 20 and 39 years, is a survivor of childhood cancer. Despite having a 5-year survival rate higher than 70%, new attempts have been made to raise this values which lead to therapeutic options that resort to more intensive and painful therapy as well as radical surgeries, thus increasing the changes of long-term adverse outcomes in the patients [75].

About one third of childhood bone cancer survivors have stated late effects that restricted physical performance and participation in daily activities. The surgical procedures conducted result in damaged structures necessary to execute movement. In fact, limb-sparing surgery can result in frequent infection, delayed healing, nonhealing fractures and early immobility, all of which have a negative impact on the survivor's quality of life. Likewise, patients who underwent amputation or limb-sparing procedures had significant deficits in education, employment and insurance when compared with sibling controls and approximately 11% reported difficulties to attend work or school due to poor health restriction [30]. Also, up to 40% of survivors stated adverse general health and mental health [75]. Evidences indicate that females and patients who underwent limb-sparing surgery had impaired emotional and social functioning, symptoms of fatigue and a higher risk for poor quality of life [76].

Because bone sarcomas are extremely rare and lack initial symptoms, delayed diagnosis are very common, which affects the prognosis of the patient, making these type of malignancy quite deadly [31]. The time between initial symptoms and a correct diagnosis ranges between 4 months and 2 years depending on the site and type of tumor. The average size of a bone sarcoma at the time of presentation is 10 cm as opposed to less than 2,5 cm for breast cancer tumors [32]. Also, up to one fifth presented a pathological fracture at the time of diagnosis and approximately 80% of the patients with osteosarcomas present micrometastatic lung disease [77], which reduces their survival rates to less than 25% [32].

Delayed diagnosis are related to poor prognosis and require more intensive and expensive treatments. According to estimates by the National Institutes of Health (NIH), the overall cost

of cancer in 2005 was 210 billion dollars, with 74 billion dollars related to direct medical expenses, 17,5 billion dollars in indirect morbidity and 118 billion dollars due to indirect mortality. From that total amount, 9,7 million dollars are required for the lifetime treatment of childhood bone cancer survivors. In the cases of young people that need a prosthesis or implant, the treatment costs will be higher, because a constant substitution will be required during growth. For out-of-hospital costs, the expenditure is estimated to be 0,7 million dollars for men and 0,2 million dollars for female. Due to physical limitation and a compromised health, the workforce participation by the bone cancer survivors is reduced, costing close to 16,4 million dollars. On the other hand, premature mortality will also have a negative impact on economy, accounting for 17,5 million dollars, approximately, with 13,8 million dollars corresponding to male and 3,6 million dollars for female [78].

In United States, the national cost for patients with bone metastasis is estimated to be 12,6 billion dollars, which accounts for 17% of the 74 billion dollars in total direct medical cost estimated by NIH [79].

3.2 - Types of Sarcomas

Sarcomas are a heterogeneous group of malignant neoplasms that originate primarily from mesenchymal cells. There are several distinct histological categories comprised within sarcomas and the tumors can form in any anatomic site [22]. Mainly, sarcomas can be divided into soft-tissue and bone sarcomas. Bone sarcomas are classified based on the cytologic features or the recognizable products of the proliferating cells. The most common types of bone sarcomas are chondrosarcoma (33%), osteosarcoma (32%) and Ewing's sarcoma (15%).

Osteosarcomas (OS) are the most common type of primary malignant bone tumor, accounting for 150 cases per year in the UK and a 5-year survival rate of 65%. The mesenchymal malignant cells in OS produce osteoid (immature bone), but can also contain cartilage and fibrous tissue matrix. The radiological features of osteosarcomas indicate lytic, sclerotic or mixed lesions with aggressive characteristics that include a wide zone of transition, breach of the cortical tissues and periosteal reaction (Figure 3.5) [32].



Figure 3.5 - X-ray of OS lesion on the femur. Adapted from [21].

OS is composed by several morphological sub-types, which are classified based on anatomical location and grade. Central osteosarcomas, formed within medullary bone, constitute the majority of these tumors and are mainly classified as high-grade in nature. The

most common subtype of central sarcomas are conventional sarcomas which account for 75% of cases. Accounting for only 4% of OS, telangiectatic osteosarcoma is characterized by a large blood-filled spaces with lysis and no mineralization of the matrix, which represents a poor prognosis. Surface osteosarcomas occur in the cortex and are classified as low-grade. Parosteal osteosarcomas are more commonly found in young adults and occur in the bone surface, representing only 4% of osteosarcomas. Characterized by a well-defined lobulated mass, this sub-type of OS is usually formed in the posterior aspect of the distal femur or on the proximal humerus. The prognosis is more favorable than conventional osteosarcomas, with 91% survival at 5 years. Periosteal sarcomas accounts for less than 2% of osteosarcomas. The tumors are usually rich in cartilage and are formed in the deep surface of the periosteum of the long bones diaphysis, particularly the femur and tibia. Finally, high-grade surface osteosarcomas are very similar to conventional osteosarcomas and account for less than 1% of osteosarcomas [32].

OS has two age peaks: in the second decade of life, which coincides with the growth spurt, and over the fifth decade (likely due to other malignancies). OS affects more males than females (ratio 1,4:1), while females have an earlier peak of incidence due to an earlier onset of growth spurt. In fact, the higher incidence of OS in adolescence is observed during puberty, when the rate of bone growth is highest. Recent studies indicated that young patients with OS were taller than normal population of the same age group [21].

The most common sites for OS are the distal femur (40%) and the proximal tibia (20%), due to their large growth plates with high proliferative activity and bone turnover. For patients with OS in the tibia or femur, the prognosis is favorable and the 5-year survival rates are, approximately, 77,5% for the tibia, which is slightly better than the distal femur at 66%. However, Bieling *et. al.* noted that the tumors with an absolute tumor volume (ATV) greater than 150 cm³ where often found in the distal femur, contrarily to the smaller tumor group observed in the tibia [33]. A tumor with an ATV of less than 150 cm³ has a 92% 5-year metastasis-free survival rate, as oppose to the 58% in tumors with an ATV greater than 150 cm³ [21].

Chondrosarcomas is a malignant bone tumor that presents a cartilage matrix and account for approximately 180 new cases in the UK and present variable radiological features which may include calcified cartilaginous areas or fusiform cortical expansion and erosions. Based on morphology and cellularity, chondrosarcomas are sub-divided into conventional, de-differentiated, mesenchymal and clear cell. Conventional chondrosarcoma are the most frequent type with a higher incidence in female adults, usually in fourth and fifth decades of life. This sub-type of tumor is usually found in the pelvis and in metaphyseal area of long bones, especially in the femur and proximal humerus. These slow-growing tumors rarely metastize to other areas. Its radiological features usually indicates an expansive lesion in the medulla, with thickening of the cortex, endosteal scalloping and chondroid mineralization. Occasionally, a soft-tissue mass may be observed. De-differentiated chondrosarcomas are an aggressive tumor that account for 10% of all chondrosarcomas. Within this low-grade variant of chondrosarcoma, a high-grade sarcoma can usually form without chondroid formation and frequently mestastasises to the lungs. Representing only 0,7% of all bone tumors and 3-10% of all chondrosarcomas, mesenchymal chondrosarcomas occur in the earlier stages of life, usually in the second or third decade of life, and are commonly found in maxilla, mandible and ribs. Finally, clear cell chondrosarcomas are a rare low-grade variant of chondrosarcomas that commonly affect the epiphysis of long bones, particularly in the femur.

Ewing's sarcoma presents varying degrees of neuroectodermal differentiation and occurs mainly in patients younger than 20 years (80%). This type of malignancy is more commonly

found in male, accounting for a ratio male/female of 1,4:1. Unlike other bone sarcomas, Ewing's sarcoma has no osteoid or chondroid formation and usually presents undifferentiated small round cells with an indistinct pattern and a vascular network around the lesion. The majority of the lesions are mixed lytic-sclerotic (75%) with the remaining being purely lytic (25%). This type of malignancy affects the diaphysis or metaphyseal-diaphyseal area of long bones, pelvis and ribs [32].

3.3 - Staging, Grading and Development

All sarcomas have a characteristic pattern of biological behavior due to their common mesenchymal origin. These patterns allow to categorize the tumors according to their stage and grade, which is important to predict the prognosis and guide the treatment [77].

Staging systems categorize the tumors according to its extension in the body and are based in size of the tumor, existence of metastases and areas where it spread. For that reason, staging requires a local and systemic approach. Local staging provides information related to the tumor size and anatomical relationships (proximity to neurovascular bundles). Systemic staging is important to detect distant spread of the tumor. Grading systems classify cancer cells based on the cells activity and morphology when compared to normal healthy cells [32].

The tumor, node and metastasis (TNM) system contains both staging and grading, which makes it the most used system to classify all types of cancers (Table 3.1). These system is based on tumor grade, size and the presence of metastases.

However, the Enneking system is the most commonly used to classify bone tumors (Table 3.2). Stage IA is the most uncommon stage which confers a 5-year survival rate of nearly 100%. Stage IIB is the most common of all osteosarcomas presentations and with a 5-year survival rate of 40%. Stage III is defined by the presence of metastasis with a 5-survival rate of 68% in the patients with only lung metastasis [33].

Table 3.1 - The tumor, node and metastasis (TNM) system.

Stage	Tumor (T)	Node (N)	Metastasis (M)	Grade (G)
Stage IA	T1 (tumor 8 cm or less)	No	M0	G1, 2 low grade
Stage IB	T2 (tumor more than 8 cm)	No	M0	G1, 2 low grade
Stage IIA	T1	No	M0	G3, 4 high grade
Stage IIB	T2	No	M0	G3, 4 high grade
Stage III	T3 (discontinuous tumors in primary site)	No	M0	Any G
Stage IVA	Any T	No	M1a (lung)	Any G
	Any T	N1 (regional lymph nodes)	Any M	Any G
Stage IVB	Any T	Any N	M1b (other sites)	Any G

Bone sarcomas, as malignant tumors, are enclosed in a reactive zone called pseudocapsule. The thickness of the reactive zone is dependent on the histogenic type and grade of the tumor. In general, bone sarcomas grow within the anatomical site in which they arise. As the tumor continues to grow, the walls of the compartment are breached and the tumor extends into the

adjacent soft tissues. At time of diagnosis, most bone sarcomas are bi-compartmental [77]. However, the majority rarely expands to the marrow cavity. In the case of osteosarcomas, the tumor usually arises intramedullary and grows towards the cortex. The growth of this type of tumor is radial and forms a ball-like mass. As the tumor continues to expand, it compresses the surrounding muscles and can, ultimately, encircle the bone. Once the formation of soft-tissue masses occurs, pulmonary metastasis are very likely to develop [21].

Table 3.2 - The Enneking system.

Stage	Grade	Tumor	Metastasis
IA	G1 low grade	T1 (intracompartmental)	M0
IB	G1 low grade	T2 (extracompartmental)	M0
IIA	G2 high grade	T1 (intracompartmental)	M0
IIB	G2 high grade	T2 (extracompartmental)	M0
IIIA	G1 or G2	T1(intracompartmental)	M1
IIIB	G1 or G2	T2(extracompartmental)	M1

Contrarily to primarily malignant bone tumors, bone metastatic cancer arises in the bone marrow. The metastases can spread in a direct, arterial or venous way with the latter representing the most common form. The hematopoietically active bone marrow is highly vascularized and, due to the slow blood flow typical of the venous circulation, the entrance of cancer cells is facilitated. The tumor cells produce adhesion molecules that bind to the marrow stromal cells and bone matrix [80]. Furthermore, the cancer cells disrupt the normal bone remodeling process, usually causing major trabecular bone loss before cortical bone loss [28].

3.4 - Imaging Methods

In order to determine the stage and grade of a bone sarcoma, physical examination and imaging studies are required (Figure 3.6). The key imaging method in the evaluation of bone tumors is plain radiography and each patient should have X-rays images in two planes at presentation. Combined with physical examination, the final diagnosis has an accuracy of more than 80% of cases [77].

In the cases where diagnosis is uncertain, computed tomography (CT) images allow to evaluate the extent of bone destruction, such as areas of microcalcification, periosteal bone formation, cortical destruction and soft-tissue involvement. Also, CT images are the diagnostic technique of choice to evaluate the lungs for metastases.

Magnetic resonance imaging (MRI) is a method superior to CT and the best modality for local staging in the cases where the malignancy can be diagnosed on X-rays. This modality is also used to evaluate the intramedullary and extraosseous extension of the bone tumor. Contrast MRI is important to study the relationship of the tumor to adjacent blood vessels and nerves [77, 81]. Additional imaging studies are sometimes required for accurate staging of the tumor. Positron emission tomography (PET) imaging is a complementary modality used to determine the metabolic rates of tumors, monitor the therapy response of neoadjuvant therapies, differentiate viable sarcoma from post-treatment changes and to select biopsies sites [82]. Recently, fusion of PET images with CT scans or MRI has improved the accuracy of the diagnosis and the differentiation between benign and malignant primary bone tumors [2, 83].

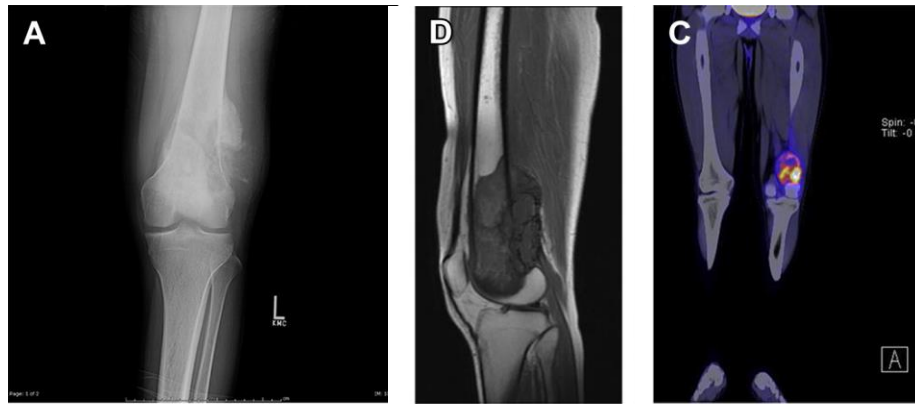


Figure 3.6 - Comparison between imaging techniques from a young man with left knee pain for 1 month. (A) radiograph of distal femur shows aggressive tumor. (B) MRI of the distal femur. (C) PET/CT scan of left femur. Adapted from [2].

3.5 - Mechanical Properties of Bone Sarcomas

Bone sarcomas and metastatic bone lesions disrupt the structural integrity of the bone. On account of a compromised structure, the pathologic changes affect the bone density and mechanical properties, making the bone weaker and more susceptible to fracture [84]. The fracture risk is dependent on the reduction in the load-bearing capacity of the bone, which is caused by the cancer and the loads applied to it. Studies suggest that the strength of the bone tissue adjacent to the lesions is diminished and the bone stress is increased during loading, resulting in an increased fragility of the bone [24].

However, it is important to mention that the articles found in literature were referred to the mechanical properties of metastatic bone cancer and not to primary bone tumors (bone sarcomas).

3.5.1 - Mechanical Properties of Trabecular Bone with Metastatic Lesions

A study conducted by Nazarian *et. al.* [24] on specimens with normal and metastatic trabecular bone demonstrated that the trabecular bone with the neoplasm is hypomineralized when compared with a normal noncancer bone. Furthermore, the average tissue density, ρ_{tissue} , and the bone volume fraction of the specimens with cancer was 11% and 33% lower than that of normal noncancer bone, respectively. Additionally, the mineral content of metastatic trabecular bone was 19% lower than the normal trabecular bone and, as a result, the tissue in the cancer specimens was 50% less hard and less rigid than normal noncancer specimens (Table 3.3). However, Nazarian *et. al.* concluded that metastatic cancer has an evident effect at the material level but it has a smaller influence on the mechanical properties of the trabecular bone.

They also observed that a single analytic function could predict the strength and stiffness of normal and metastatic trabecular bone by using bone mineral density (BMD) or bone volume fraction (BV/TV) as independent variables. Surprisingly, they verified that the bone mineral density was not able to predict the macroscopic behavior of trabecular bone as oppose to the

minimum bone volume fraction governed the mechanical behavior of the normal and metastatic trabecular bone.

Table 3.3 - Material and structural properties for cancer and noncancer specimens (mean \pm standard deviation) [24].

Variable	Unit	Metastatic cancer	Normal
Tissue density (ρ_{tissue})	g cm^{-3}	$1,68 \pm 0,22$	$1,82 \pm 0,12$
Average bone volume fraction (BV/TV_{AVG})	%	$24,29 \pm 12,26$	$36,46 \pm 15,38$
Hardness (H)	GPa	$0,24 \pm 0,03$	$0,52 \pm 0,09$
Tissue elastic modulus (E_{NANO})	GPa	$0,22 \pm 0,03$	$0,47 \pm 0,07$
Modulus of elasticity (E)	MPa	$201,5 \pm 59,68$	$356,2 \pm 89,7$
Yield strength (σ_y)	MPa	$40,4 \pm 10,1$	$100,5 \pm 21,8$

Therefore, it is possible to determine the elasticity modulus and yield strength of metastatic trabecular bone by the following expressions:

$$E_{\text{cancer}} = 1030 \cdot (BV/TV_{\text{MIN}}) + 19,7 \quad (3.1)$$

$$\sigma_y = 37,4 \cdot (BV/TV_{\text{MIN}}) - 1,81 \quad (3.2)$$

Where BV/TV_{min} is the bone volume fraction in mm^3/mm^3 , E_{cancer} is the elasticity modulus of metastatic trabecular bone in MPa and σ_y is the yield strength of metastatic trabecular bone in MPa. The linear regression models are represented in Figure 3.7 [24].

In another study, Kaneko *et. al.* [84] studied the effect of metastatic cancer on the material properties and quantitative tomography (QCT) data of trabecular bone. Three different types of bone metastases were considered: lytic, blastic and mixed, based on radiographic appearance. In lytic metastasis, bone resorption prevails around the tumor sites while bone formation barely occurs, which results in areas with profound osteopenia. Blastic lesions are characterized by an increase in bone formation and decrease of bone resorption with a sclerotic appearance. Mixed lesions are a combination of the lytic and blastic lesions. However, bone formation and resorption are unbalanced, changing the bone turnover. When the blastic component is prevalent, bone formation is increased, but in the cases where lytic activity is dominant, an increase in bone resorption leads to significant bone loss [74, 85]. Like Nazarian *et. al.*, Kaneko *et. al.* also observed that metastatic cancer has no significant impact on the relationships between the mechanical properties (E, S_y and S_u) and ρ_{ash} of distal femoral trabecular bone (Table 3.4).

Table 3.4 - Material properties of trabecular bone with metastatic lesions. NA indicates not available. Adapted from [84].

Material Property	L_{mixed}	L_{lytic}	L_{blastic}	Normal
E_{SI} (MPa)	$518 \pm 30,3$	$1030 \pm 77,5$	1240 ± 674	1110 ± 591
E_{AP} (MPa)	$204 \pm 31,4$	620 ± 184	828 ± 551	710 ± 371
E_{ML} (MPa)	$132 \pm 52,6$	353 ± 256	581 ± 348	457 ± 276
E_{MEAN} (MPa)	$284 \pm 17,1$	667 ± 121	915 ± 430	774 ± 360
S_y (MPa)	$3,93 \pm \text{na}$	$4,47 \pm 0,907$	$7,64 \pm 3,70$	$7,59 \pm 3,29$
S_u (MPa)	$4,04 \pm \text{na}$	$4,67 \pm 1,07$	$7,41 \pm 4,38$	$7,89 \pm 3,49$
Ash density (mg/cm^3)	$138 \pm 7,37$	$173 \pm 24,4$	$202 \pm 75,1$	$214 \pm 63,3$
QCT data (mg/cm^3)	$88,7 \pm 12,2$	$122 \pm 25,4$	$158 \pm 81,0$	$169 \pm 79,0$

They also determined that ρ_{ash} can be used to predict the mechanical properties of bone with and without cancer. Therefore, it is possible to determine the elasticity modulus and yield strength of metastatic trabecular bone by the following expressions:

$$E_{SI} = 0,161 \cdot \rho_{ash}^{1,61} \quad (3.3)$$

$$E_{AP} = 0,00578 \cdot \rho_{ash}^{2,15} \quad (3.4)$$

$$E_{ML} = 0,00155 \cdot \rho_{ash}^{2,30} \quad (3.5)$$

$$E_{Mean} = 0,0308 \cdot \rho_{ash}^{1,85} \quad (3.6)$$

$$S_y = 0,000831 \cdot \rho_{ash}^{1,68} \quad (3.7)$$

$$S_u = 0,000592 \cdot \rho_{ash}^{1,75} \quad (3.8)$$

Where E_{SI} , E_{AP} and E_{ML} are the moduli in the superior-inferior (SI), anterior-posterior (AP) and medial-lateral (ML) direction in MPa, E_{Mean} is the average of E_{SI} , E_{AP} and E_{ML} in MPa, S_y is the yield strength in MPa and S_u is the ultimate strength in MPa. Finally, the correlation between ρ_{ash} and ρ_{QCT} for metastatic cortical bone is calculated by the following expression:

$$\rho_{ash} = 57,7 + 0,917 \cdot \rho_{QCT} \quad (3.9)$$

Where ρ_{ash} is the apparent density in mg/cm^3 and ρ_{QCT} is the quantitative tomography density in mg/cm^3 .

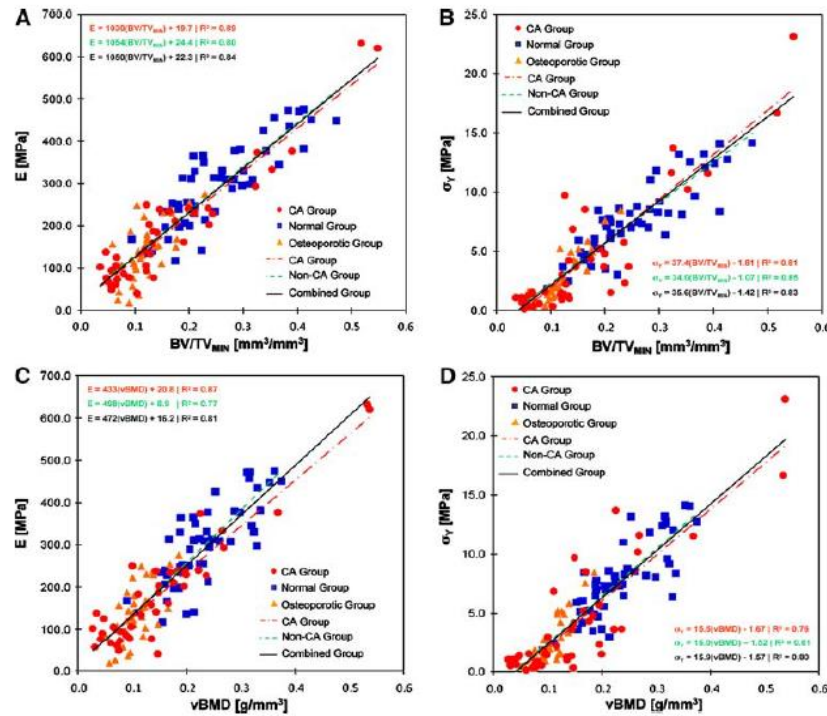


Figure 3.7 - Linear regression models of (A) modulus of elasticity and (B) yield strength of noncancer and cancer specimens in function of BV/TV_{min}. Linear regression models of (A) modulus of elasticity and (B) yield strength of noncancer and cancer specimens in function of vBMD. Adapted from [24].

3.5.2 - Mechanical Properties of Cortical Bone with Metastatic Lesions

The bone structural capacity is highly determined by the cortical tissue. Kaneko *et. al.* [17] studied the mechanical properties of cortical bone from femoral diaphysis with and without metastatic lesions (Table 3.5). The results demonstrated linear relationships between quantitative tomography (QCT) density and the elasticity modulus, strength, and ash density (ρ_{ash}) for metastatic cortical bone (Figure 3.8). The correlations between the mechanical properties of metastatic trabecular bone in tension and ρ_{QCT} are calculated by the following expressions:

$$E_t = -4,4 + 0,0201 \cdot \rho_{QCT} \quad (3.10)$$

$$S_{yt} = -15,8 + 0,0815 \cdot \rho_{QCT} \quad (3.11)$$

$$S_{ut} = -18,4 + 0,0941 \cdot \rho_{QCT} \quad (3.12)$$

$$\epsilon_{yt} = 0,00718 - 9,10 \times 10^{-7} \cdot \rho_{QCT} \quad (3.13)$$

Where E_t is the elastic modulus expressed in GPa, S_{yt} is the yield strength expressed in GPa, S_{ut} is the ultimate strength expressed in GPa and ϵ_{yt} is the yield strain expressed in mm/mm.

Table 3.5 - Material property of cortical bone with metastatic lesions [17].

Material Property	Metastatic	Normal
E_t (GPa)	$17,7 \pm 4,3$	$22,7 \pm 1,7$
E_c (GPa)	$18,0 \pm 4,3$	$23,0 \pm 1,8$
S_{yt} (MPa)	$74,9 \pm 15,7$	$83,9 \pm 8,8$
S_{yc} (MPa)	$106,6 \pm 34,6$	$153,0 \pm 16,5$
S_{ut} (MPa)	$86,2 \pm 18,7$	$95,6 \pm 10,9$
S_{uc} (MPa)	$115,5 \pm 34,1$	$161,8 \pm 5,9$
ϵ_{yt} (mm/mm)	$0,0062 \pm 0,0002$	$0,0057 \pm 0,0003$
ϵ_{yc} (mm/mm)	$0,0079 \pm 0,0007$	$0,0086 \pm 0,0008$
ϵ_{ut} (mm/mm)	$0,0168 \pm 0,0050$	$0,0129 \pm 0,0047$
ϵ_{uc} (mm/mm)	$0,0137 \pm 0,0027$	$0,0118 \pm 0,0019$
$\epsilon_{(u-y)t}$ (mm/mm)	$0,0106 \pm 0,0051$	$0,073 \pm 0,0043$
$\epsilon_{(u-y)c}$ (mm/mm)	$0,0058 \pm 0,0029$	$0,0033 \pm 0,0024$
Ash density (mg/cm ³)	1011 ± 139	1145 ± 20
QCT data (mg/cm ³)	1074 ± 162	1169 ± 32

The correlations between the mechanical properties of metastatic trabecular bone in tension and ρ_{QCT} are calculated by the following expressions:

$$E_c = -4,30 + 0,0203 \cdot \rho_{QCT} \quad (3.14)$$

$$S_{yc} = -54,8 + 0,150 \cdot \rho_{QCT} \quad (3.15)$$

$$S_{uc} = -46,1 + 0,150 \cdot \rho_{QCT} \quad (3.16)$$

$$\epsilon_{yc} = 0,00533 + 2,40 \times 10^{-6} \cdot \rho_{QCT} \quad (3.17)$$

$$\epsilon_{(u-y)c} = 0,0130 - 6,76 \times 10^{-6} \cdot \rho_{QCT} \quad (3.18)$$

Where E_c is the elastic modulus in compression expressed in GPa, S_{yc} is the yield strength in compression expressed in GPa, S_{uc} is the ultimate strength in compression expressed in GPa, ϵ_{yc} is the yield strain in compression expressed in mm/mm and $\epsilon_{(u-y)c}$ is the strain from yield to ultimate failure in compression expressed in mm/mm.

Finally, the correlation between ρ_{ash} and ρ_{QCT} for metastatic cortical bone is calculated by the following expression:

$$\rho_{ash} = 147 + 0,805 \cdot \rho_{QCT} \quad (3.19)$$

Where ρ_{ash} is the apparent density in mg/cm^3 and ρ_{QCT} is the quantitative tomography density in mg/cm^3 .

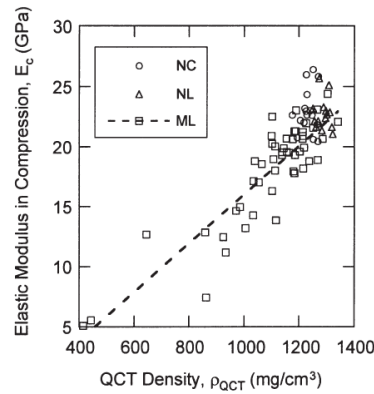


Figure 3.8 - Linear regression for elasticity modulus in function of ρ_{QCT} . Adapted from [17].

Chapter 4

Numerical Methods

Over the last years, computers have constantly evolved, increasing the processing speed and the capability to store information. These improvements have increased the use of numerical methods to simulate biological structures, allowing to build more robust and reliable models for the biomechanical analysis. As such, numerical methods have become a solid alternative for biomedical research, which is still expensive and ethically questionable, and is now considered an important tool in the diagnosis and treatment of diseases [86].

In this chapter, a brief explanation of FEM is introduced, presenting its advantages and disadvantages, followed by a detailed presentation of meshless methods, particularly on the RPIM and NNRPIM methods.

4.1 - Finite Element Method (FEM)

FEM is a numerical technique used in physics and engineering that provides the exact analytical solution to a complex mechanical problem. In order to find the right solution, the problem has to be defined in a geometrical shape (or domain) that, later, will be subdivided into multiple subdomains called finite elements. Each element has a certain number of vertices, called nodes, and both assemble into the finite element mesh (Figure 4.1). This process is denominated domain discretization and allows to split the complex problem into simpler and smaller regions. However, the accuracy of the results is dependent on the type, arrangement and total number of elements. Normally, the elements are shaped as triangles in 2D models, but, in 3D models, the elements assume a tetrahedral shape. On the other hand, the elements may also have different properties, which allows to simulate structures composed with different materials [5].

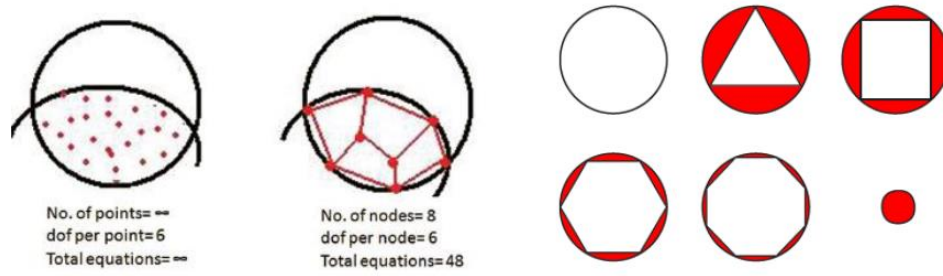


Figure 4.1 - Creation of a mesh and demonstration of its influence on the discretization error. Adapted from [34].

FEM can be combined with the theory of elasticity to obtain several variable fields, such as stress, strain and displacements. Shape functions are used to interpolate the field variables. Forces and constraints (boundary conditions) are applied to the nodes in order to simulate the loads that act on the body and to prevent nodal displacements, respectively. For each element, the forces and displacements at the nodes are related by the stiffness matrix, denoted K^e . Because each element is linked to other elements, the stiffness matrix of the whole structure (denoted K) is defined by the assembly of the individual matrixes. The global system of equations can be presented as:

$$KU = F \quad (4.1)$$

Where F represents all nodal forces, K is the stiffness matrix of the whole structure and U are the nodal displacements. Therefore, the entries for the matrix are known and, by solving equation 4.1 for U , it is possible to obtain all nodal displacements [87].

FEM was developed in 1956 for aerospace industry and was only applied in biomechanics in 1972, for the mechanical analysis of skeletal parts [34]. The first studies conducted with FEM started with 2D models (Figure 4.2) [10], later evolving for 3D models with more complex structures [88]. Over the past years, FEM has been used in the biomedical engineering field to study percutaneous heart valves, human lumbar spine, among others. Relatively to biomechanics, FEM has been used to analyze stress and strain, to predict bone fractures and to study the bone remodeling process.

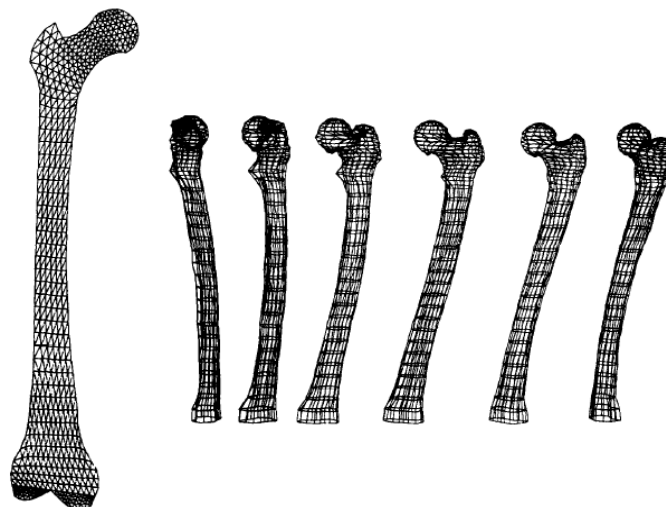


Figure 4.2 - FE models of the 2D and 3D human femur. Adapted from [10].

However, FEM is not without limitations. An interpolation based on a mesh is one of the main limitations of this method. The accuracy of the results is dependent on the quality of the mesh, therefore, high values of error occur for low quality meshes. Also, FEM is not capable of solving problems with discontinuities misaligned with element edges, because it is a mesh-based method [89].

4.2 - Meshless Methods

Meshless methods were created to overcome the limitations of FEM, mainly concerning the difficulties in the mesh generation [89].

In meshless methods, the problem domain is discretized in arbitrarily distributed nodes without any pre-established relation between them. Influence-domains establish the nodal connectivity, so the field functions are approximated within an influence-domain, rather than an element. However, influence-domains must overlap each other in meshless methods, contrarily to FEM [5].

Meshless methods can be divided into: approximation methods and interpolation methods. Approximation methods, the first meshless methods to be developed, use approximation functions to obtain smoother solutions. The influence-domains were implemented through fixed radial searches and the background integration scheme was nodal independent.

The Smoothed-Particle Hydrodynamics (SPH) was the first meshless approximation method to be created, initially developed for astronomy. This method was in the origin of the Reproducing Kernel Particle Method (RKPM) [90]. From the early 1990's, other meshless methods were developed. The Diffuse Element Method (DEM) [89] was the first meshless methods to use Moving Least Square approximants (MSL), proposed by Lancaster and Salkaukas, in the construction of approximation functions. Based on DEM, the Element Free Galerkin Method (EFGM) was, later, developed [89].

However, approximation methods lack the delta Kronecker property, which represents a limitation in the imposition of essential and natural boundary conditions. For that reason, several interpolation methods have been developed, which includes the Point Interpolation Method (PIM) [89], the Radial Point Interpolation Method (RPIM) [89], the Natural Neighbour Finite Element Method (NNFEM) [89] and the Natural Element Method (NEM) [89]. The combination between NEM and RPIM originated the NNRPIM [5].

In this work, the meshless methods used are the RPIM and the NNRPIM. A brief introduction of both techniques is presented in the next subsections.

4.2.1 - Meshless Generic Procedure

The generic procedure of meshless methods consists of three basic steps: nodal connectivity, numerical integration scheme and shape functions. The first step consists on the study of the problem's geometry and establish a solid domain with its boundaries and boundary conditions. However, it is important to mention that the nodal distribution does not form a mesh, because no previous information about the relation between each node is required to construct the approximation or interpolation functions of unknown variable field functions. The process of nodal discretization is presented in Figure 4.3.

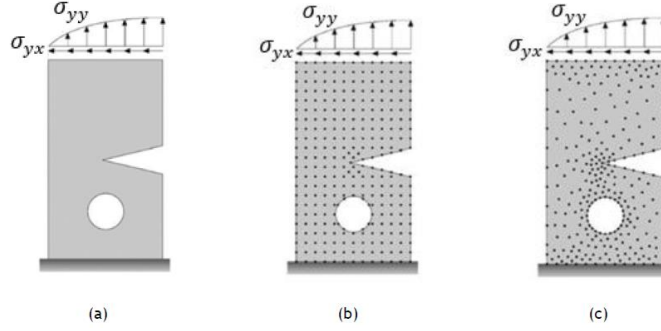


Figure 4.3 - Nodal discretization of the domain of the problem: (a) solid domain with the natural and essential boundaries; (b) regular nodal discretization; (c) irregular nodal discretization. Adapted from [5].

Then, using influence-domains or Voronoï diagrams, nodal connectivity is established, followed by the construction of a background integration mesh. With the use of Gaussian integration meshes, the background mesh is adjusted to the problem domain, as in FEM. However, other methods that use nodal integration, require Voronoï diagrams to obtain the integration weight on each node.

After the imposition of nodal connectivity, an equation system is established using approximation or interpolation functions, based on the combination of RBFs with polynomial basis functions. The interpolation functions have an important property, namely the delta Kronecker property, so the obtained function passes through all nodes inside the influence-domain. With this property, the same simple FEM techniques can be used to impose boundary conditions.

Next, an explanation of the generic procedure for both RPIM and NNRPIM will be presented. However, only 2D cases will be described for both methods, since it is simpler to represent 2D domains, the sections regarding the nodal connectivity, numerical integration and interpolation functions [5].

4.2.2 - Nodal Connectivity

4.2.2.1 - RPIM

In order to obtain the discrete equation system, RPIM uses the Galerkin weak form formulation. After the nodal discretization, nodal connectivity in RPIM is obtained by the overlap of the influence domain of each node.

Influence-domains are found by searching enough nodes inside a certain area or volume, and can have a fixed or a variable size, as well as may take different shapes. RPIM, contrarily to other meshless methods, uses a fixed number of neighbor nodes. In Figure 4.4 are represented two types of fixed size domains, a rectangular and a circular, respectively. Based on these figures, it is possible to observe that different nodal connectivity is obtained for influence-domains with different shapes and sizes. In addition, depending on the initial nodal spatial distribution, influence-domains obtained can be unbalanced without containing an approximated equal number of nodes. These factors can affect the final solution of the problem and reduce the accuracy in the numerical analysis.

For that reason, in order to overcome these problems, RPIM depends on influence-domains with variable size, but with a constant number of nodes within the domain, as represented in Figure 4.4. Thus, a radial search is performed and the interest point x_i is used as center in order to find the n closest nodes. The process is illustrated in 4.4c, resulting in a constant nodal connectivity [5].

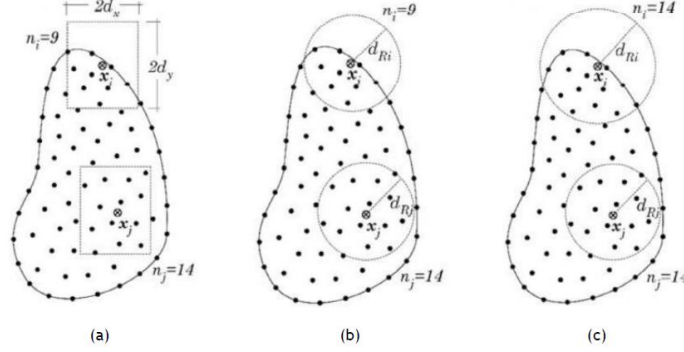


Figure 4.4 - Examples of different types of influence-domains: (a) influence-domain with fixed size and rectangular shape; (b) influence-domain with fixed size and circular shape; (c) influence-domain with variable size and circular shape. Adapted from [5].

4.2.2.2 - NNRPIM

In NNRPIM, the nodal connectivity is obtained by using the natural neighbor concept with the partition of the discretized domain into a set of Voronoï cells [91]. A node is associated with each one of these cells.

Considering a problem domain $\Omega \subset \mathbb{R}^2$, bounded by a physical boundary $\Gamma \in \Omega$, discretized in several randomly distributed nodes $N = \{n_0, n_1, \dots, n_N\} \in \mathbb{R}^2$ with the following coordinates $X = \{x_0, x_1, \dots, x_N\}$ with $x_i \in \mathbb{R}^2$, the Voronoï cell is defined by

$$V_i = \{x_i \in \Omega \subset \mathbb{R}^d: \|x_i - x_i\| < \|x_j - x_j\|, \forall i \neq j\} \quad (4.2)$$

Where x_i is an interest point of the domain and $\|\cdot\|$ the Euclidian metric norm. Therefore, the Voronoï cell V_i is the geometric place where all points in the interior V_i are closer to the node n_i than to any other node. The Voronoï diagram is defined by the assemble of the Voronoï cells. Thus, the Voronoï diagram of N is the partition of the domain defined by Ω into sub regions V_i , closed and convex, as represented in Figure 4.5.

Therefore, in NNRPIM, the influence cells are built based on the information from the Voronoï diagram, making them dependent on the nodal mesh arrangement. Influence cells can be divided in two types: first-degree-cells and second-degree cells.

The first-degree influence-cells, represented in Figure 4.5(a), are established when a point of interest x_i begins to search the direct neighboring nodes, following the Natural Neighbour Voronoï Construction. The second-degree influence-cells, shown in Figure 4.5(b), are established when a point of interest searches neighboring nodes similarly to first degree influence-cells and, then, taking into account the Voronoï diagram, the natural neighbour of the first neighbour of x_i are attached to the influence-cell. Second-degree influence-cells have

a superior size than the first degree influence cells and, thus, it is expected to obtain more accurate approximations [5].

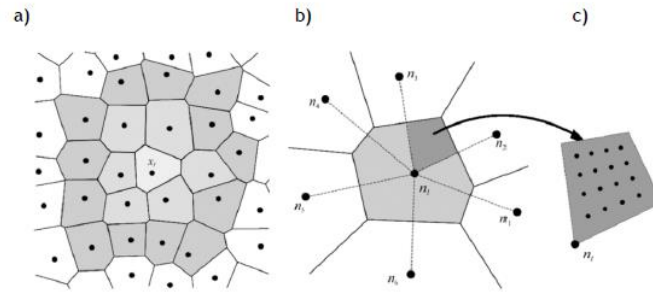


Figure 4.5 - a) Second degree influence cell of interest point x_i ; (b) Representation of the sub-cells forming the Voronoï cell; (c) Schematic representation of 4 x 4 integration points inside a sub-cell. Adapted from [5].

4.2.3 - Numerical Integration

4.2.3.1 - RPIM

For the numerical integration, RPIM uses the Gauss-Legendre quadrature scheme. Initially, the solid domain is divided in a regular grid as Figure 4.6a indicates. Then, each grid-cell is filled with integration points, respecting the Gauss-Legendre quadrature rule, as illustrated in Figure 4.6b.

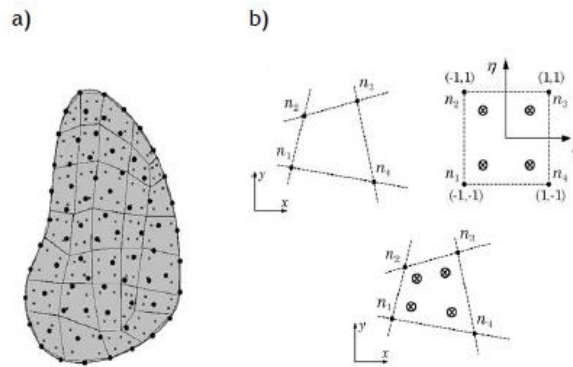


Figure 4.6 - (a) Gaussian integration mesh and (b) transformation of the initial quadrilateral into an isoparametric square shape and application of the 2 x 2 quadrature point rule. Adapted from [5].

The Cartesian coordinates of the quadrature points are obtained using isoparametric interpolation functions, N_i , present in Equations (4.3) and (4.4).

$$\begin{aligned}
N_1(\xi, \eta) &= \frac{1}{4}(1 - \xi)(1 - \eta) \\
N_2(\xi, \eta) &= \frac{1}{4}(1 - \xi)(1 + \eta) \\
N_3(\xi, \eta) &= \frac{1}{4}(1 + \xi)(1 + \eta) \\
N_4(\xi, \eta) &= \frac{1}{4}(1 + \xi)(1 - \eta)
\end{aligned} \tag{4.3}$$

$$\begin{aligned}
N_1(\xi, \eta) &= 1 - \xi - \eta \\
N_2(\xi, \eta) &= \eta \\
N_3(\xi, \eta) &= \xi
\end{aligned} \tag{4.4}$$

The Cartesian coordinates are given by

$$x = \sum_{i=1}^m N_i(\xi, \eta) \cdot x_i \tag{4.5}$$

$$y = \sum_{i=1}^m N_i(\xi, \eta) \cdot y_i \tag{4.6}$$

in which m is the number of nodes inside the grid-cell and x_i and y_i are the Cartesian coordinates of the cells nodes.

The integration weight of the quadrature point is obtained by multiplying the isoparametric weight of the quadrature point with the inverse of the Jacobian matrix determinant of the respective grid-cell, as described in the Equation (4.6) [5].

$$J = \begin{pmatrix} \frac{\partial x}{\partial \xi} & \frac{\partial x}{\partial \eta} \\ \frac{\partial y}{\partial \xi} & \frac{\partial y}{\partial \eta} \end{pmatrix} \tag{4.7}$$

4.2.3.2 - NNRPIM

NNRPIM uses the Galerkin weak form, which requires a background integration mesh. In this method, the integration mesh is obtained using directly and exclusively the nodal distribution, namely the previously constructed Voronoï diagram. Using the Delaunay triangulation, the area of each Voronoï cell is subdivided in several sub-areas, as represented in Figure 4.7.

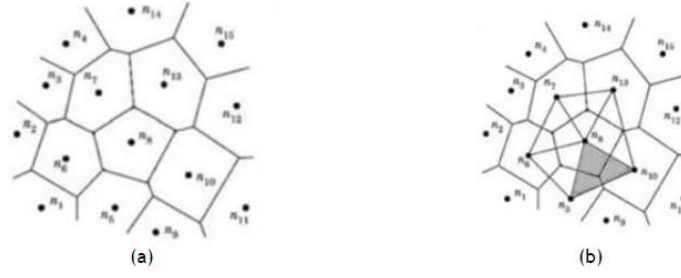


Figure 4.7 - (a) Initial Voronoï diagram; (b) Delaunay triangulation. Adapted from [5].

In each of the Voronoï cells are identified the corners of the polygon, P_{ij} , and the middle points, M_{ij} , between n_i and each neighbour node n_i are determined, as illustrated in Figure 4.8. The Voronoï cells are divided into k quadrilateral sub-cells, S_{ij} . The number of each quadrilateral sub-cell is equal to the number of natural neighbors of node n_i .

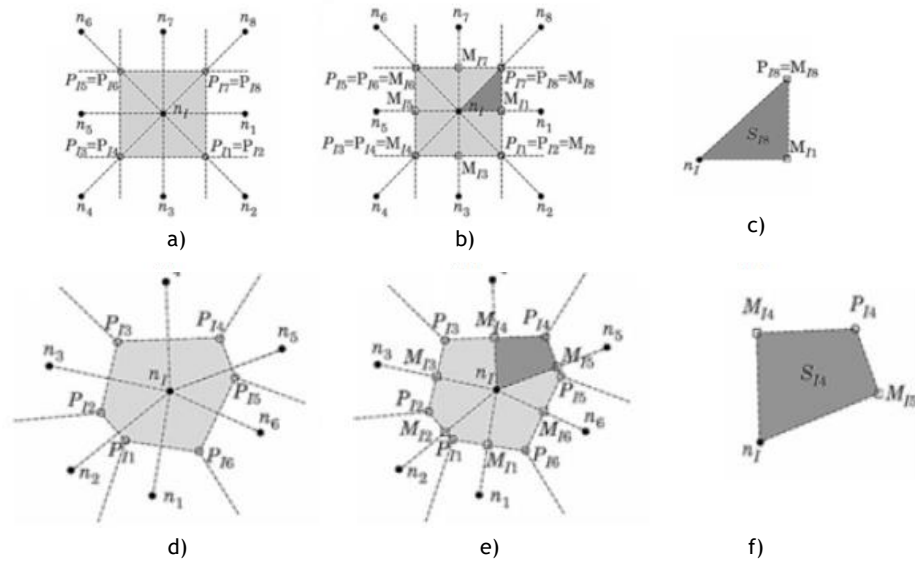


Figure 4.8 - (a) Voronoï cell and respective intersection points, P_{ii} ; (b) Middle points, M_{ii} , and the respective generated triangles; (c) Triangular. (d) Voronoï cell and respective intersection points, P_{ii} ; (e) Middle points, M_{ii} , and the respective generated triangles; (f) Quadrilateral. Adapted from [5].

The sub-cells created have a quadrilateral shape when the nodes N are distributed in an irregular way. If the nodes are distributed in a regular way, the sub-cells will have a triangular shape, as represented in Figure 4.8.

Thus, each area of the Voronoï cell of node x_i , A_{Vi} , is divided into k sub-areas $A_{S_{ii}}$. The area of the Voronoï cell is equal to the sum of the area of each sub-cell, as indicated by the following expression:

$$A_{Vi} = \sum_{i=1}^k A_{S_{ii}}, \quad \forall A_{S_{ii}} \geq 0 \quad (4.8)$$

Then, following the Gauss-Legendre quadrature rule, it is possible to distribute integration points inside each subarea $A_{S_{ii}}$ [5].

4.2.4 - Interpolation Functions

Both RPIM and NNRPIM use the same procedure for interpolation functions, using the radial point interpolator (RPI) technique, combining radial basis functions (RBF) and polynomial base

functions. The interpolation functions considering both methods, RPIM and NNRPIM, possess the delta Kronecker property, satisfying the following condition,

$$\varphi_i(\mathbf{x}_j) = \delta_{ij} \quad (4.9)$$

Where δ_{ij} is the delta Kronecker, for which $\delta_{ij} = 1$ if $i = j$ and $\delta_{ij} = 0$ if $i \neq j$. This property allows to use direct imposition techniques to numerically apply the essential boundary conditions in the stiffness matrix.

Considering a function $u(\mathbf{x}_I)$ defined in the domain Ω , which is discretized by a set of N nodes. It is assumed that only the nodes within the influence-cell of the point of interest considered have an effect on $u(\mathbf{x}_I)$. The value of the function $u(\mathbf{x}_I)$, defined in the domain $\Omega \subset \mathbb{R}^2$, at the point of interest \mathbf{x}_I , is given by the following expression:

$$u(\mathbf{x}_I) = \sum_{i=1}^n R_i(\mathbf{x}_I) \cdot a_i(\mathbf{x}_I) + \sum_{j=1}^m p_j(\mathbf{x}_I) \cdot b_j(\mathbf{x}_I) = \{\mathbf{R}(\mathbf{x}_I)^T, \mathbf{p}(\mathbf{x}_I)^T\} \begin{Bmatrix} \mathbf{a}(\mathbf{x}_I) \\ \mathbf{b}(\mathbf{x}_I) \end{Bmatrix} \quad (4.10)$$

Where $\mathbf{R}(\mathbf{x}_I)^T$ is the RBF, n the number of nodes inside the influence-cell of \mathbf{x}_I , $\mathbf{p}(\mathbf{x}_I)^T$ is the polynomial function and $\mathbf{a}(\mathbf{x}_I)$ and $\mathbf{b}(\mathbf{x}_I)$ are the constant coefficients associated with the respective functions mentioned.

Normally, $m < n$ to guarantee a stable function. The vectors in equation (4. 10) can be represented as:

$$\begin{aligned} \mathbf{R}(\mathbf{x}_I) &= \{R_1(\mathbf{x}_I), R_2(\mathbf{x}_I), \dots, R_n(\mathbf{x}_I)\}^T \\ \mathbf{P}(\mathbf{x}_I) &= \{p_1(\mathbf{x}_I), p_2(\mathbf{x}_I), \dots, p_m(\mathbf{x}_I)\}^T \\ \mathbf{a}(\mathbf{x}_I) &= \{a_1(\mathbf{x}_I), a_2(\mathbf{x}_I), \dots, a_n(\mathbf{x}_I)\}^T \\ \mathbf{b}(\mathbf{x}_I) &= \{b_1(\mathbf{x}_I), b_2(\mathbf{x}_I), \dots, b_m(\mathbf{x}_I)\}^T \end{aligned} \quad (4.11)$$

The distance between the relevant node \mathbf{x}_I and the neighbour node \mathbf{x}_i corresponds to the variable established in the RBF, given by $r_{ii} = \|\mathbf{x}_i - \mathbf{x}_I\|$. In this work, the RBF used is the Multiquadric RBF, $R_i(\mathbf{x}_I) = R(r_{ii}) = (r_{ii}^2 + c^2)^p$, in which shape parameter c takes a value close to zero, $c \cong 0$, and p close to one, $p \cong 1$. The general formulation of MQ-RBF is:

$$R(r_{ii}) = (r_{ii}^2 + c^2)^p \quad (4.12)$$

The non-constant coefficients \mathbf{a} and \mathbf{b} need to be determined. The polynomial basis functions used have the following monomial term as:

$$\mathbf{p}(\mathbf{x})^T = [1, x, y, x^2, xy, y^2, \dots] \quad (4.13)$$

Having in consideration equation (4. 10), for each node inside the influence-cell and admitting an extra equation, $\mathbf{p}(\mathbf{x}_I)\mathbf{a}(\mathbf{x}_I) = \mathbf{0}$, to guarantee a unique solution, a system of equations is obtained:

$$\begin{bmatrix} \mathbf{u}_s \\ 0 \end{bmatrix} = \begin{bmatrix} \mathbf{R} & \mathbf{P} \\ \mathbf{P}^T & \mathbf{0} \end{bmatrix} \begin{Bmatrix} \mathbf{a} \\ \mathbf{b} \end{Bmatrix} = \mathbf{M} \begin{Bmatrix} \mathbf{a} \\ \mathbf{b} \end{Bmatrix} \quad (4.14)$$

Where:

$$\mathbf{u}_s = \{u_1, u_2, \dots, u_n\}^T \quad (4.15)$$

$$\mathbf{R} = \begin{bmatrix} R(r_{11}) & R(r_{12}) & \dots & R(r_{1n}) \\ R(r_{21}) & R(r_{22}) & \dots & R(r_{2n}) \\ \vdots & \vdots & \ddots & \vdots \\ R(r_{n1}) & R(r_{n2}) & \dots & R(r_{nn}) \end{bmatrix} \quad (4.16)$$

The constant polynomial basis is defined as:

$$\mathbf{P} = [1 \quad 1 \quad \dots \quad 1]^T \quad (4.17)$$

For the 2D problem, the polynomial basis is represented as:

$$\mathbf{P} = \begin{bmatrix} 1 & 1 & \dots & 1 \\ x_1 & x_2 & \dots & x_n \\ y_1 & y_2 & \dots & y_n \end{bmatrix}^T \quad (4.18)$$

Therefore, is possible to determine the non-constant coefficients \mathbf{a} and \mathbf{b} with the following equation:

$$\begin{Bmatrix} \mathbf{a} \\ \mathbf{b} \end{Bmatrix} = \begin{bmatrix} \mathbf{R} & \mathbf{P} \\ \mathbf{P}^T & \mathbf{0} \end{bmatrix}^{-1} \begin{Bmatrix} \mathbf{u}_s \\ \mathbf{0} \end{Bmatrix} \Rightarrow \begin{Bmatrix} \mathbf{a} \\ \mathbf{b} \end{Bmatrix} = \mathbf{M}^{-1} \begin{Bmatrix} \mathbf{u}_s \\ \mathbf{0} \end{Bmatrix} \quad (4.19)$$

Replacing in equation (4. 10):

$$u(\mathbf{x}_I) = \{\mathbf{R}(\mathbf{x}_I)^T, \mathbf{p}(\mathbf{x}_I)^T\} \mathbf{M}^{-1} \begin{Bmatrix} \mathbf{u}_s \\ \mathbf{0} \end{Bmatrix} = \{\Phi(\mathbf{x}_I), \Psi(\mathbf{x}_I)\} \begin{Bmatrix} \mathbf{u}_s \\ \mathbf{0} \end{Bmatrix} \quad (4.20)$$

Thus, the shape function $\Phi(\mathbf{x}_I) = \{\varphi_1(\mathbf{x}_I), \varphi_2(\mathbf{x}_I), \dots, \varphi_n(\mathbf{x}_I)\}$ can be determined using [5]:

$$\begin{aligned} \{\Phi(\mathbf{x}_I), \Psi(\mathbf{x}_I)\} &= \{\mathbf{R}(\mathbf{x}_I)^T, \mathbf{p}(\mathbf{x}_I)^T\} \mathbf{M}^{-1} \\ &= \{\varphi_1(\mathbf{x}_I), \varphi_2(\mathbf{x}_I), \dots, \varphi_n(\mathbf{x}_I), \psi_1(\mathbf{x}_I), \psi_2(\mathbf{x}_I), \dots, \psi_m(\mathbf{x}_I)\} \end{aligned} \quad (4.21)$$

Chapter 5

Solid Mechanics

Solid Mechanics focus on the study of deformations and relative displacements of solids, caused by the action of loads or forces. Hence, for a given solid and boundary condition, this field of study attempts to understand the relationship between stress and strain and the relationship between strain and displacements [5].

In this chapter, a brief exposition of the used continuum formulation will be presented, introducing the concepts of stress and strain as well as an explanation of the considered equilibrium and constitutive equations.

5.1 - Fundamentals

The behavior of each solid is predicted based on the stress-strain curve, as previously mentioned in section 2.11. In this work only linear elastic materials are considered. In this case, the relationship between stress and strain is linear and, once the applied load is removed, the solid returns to its initial form. Contrarily, in the case of plastic materials, the deformation in the solid caused by loading remains after the removal of the applied load.

Materials can be defined as isotropic and anisotropic. Linear elastic isotropic materials only require two independent material properties to classify them, the Young's Modulus (E) and Poisson's ratio (ν). Anisotropic materials have distinct properties in each direction, which means that the deformation caused by a load applied in one direction is not equal to that caused by the same load in a different direction. In this work, only isotropic materials will be considered.

When a solid is subjected to a load or force, an internal distribution of stresses and strains is produced. The symmetric Cauchy stress tensor, Λ , represents the stresses of the current configuration. For a two-dimensional problem, the stress state is defined as:

$$\Lambda = \begin{bmatrix} \sigma_{xx} & \sigma_{xy} \\ \sigma_{yx} & \sigma_{yy} \end{bmatrix} \quad (5.1)$$

Voigt notation expresses tensors in column vectors, reducing their order. Thus, the stress tensor, (5.1), is transformed into stress vector, σ , [5]:

$$\sigma = \{\sigma_{xx} \quad \sigma_{yy} \quad \sigma_{xy}\}^T \quad (5.2)$$

Stresses can be classified as normal stress or shear stress. Normal stresses, such as tension and compression, develop perpendicularly to the plane of the applied force and are indicated by the letter σ , contrarily to shear stresses, which act parallel to that plane and are denoted by the letter τ [8].

Strain is also represented by two components. The normal strain, represented by the letter ε , denotes the relative change of the length of a certain line segment. The shear strain is denoted by the letter γ and represents the change in angle of two previously perpendicular line segments [92]. The strain tensor is reduced to the strain vector ε ,

$$\varepsilon = \{\varepsilon_{xx} \quad \varepsilon_{yy} \quad \varepsilon_{xy}\}^T \quad (5.3)$$

The relation between stress and strain of a solid domain is given by the constitutive equation, known as Hooke's law:

$$\sigma = c\varepsilon \quad (5.4)$$

In which, c is the constitutive matrix, given by $c = s^{-1}$, being the matrix s the compliance elasticity matrix. For 2D cases, considering a general anisotropic material and a plane stress formulation, matrix s is given by the following expression:

$$s_{plane}^{stress} = \begin{bmatrix} \frac{1}{E_{11}} & -\frac{\nu_{21}}{E_{22}} & 0 \\ -\frac{\nu_{12}}{E_{11}} & \frac{1}{E_{22}} & 0 \\ 0 & 0 & \frac{1}{G_{12}} \end{bmatrix} \quad (5.5)$$

While, when considering a plane strain formulation, matrix s is expressed as:

$$s_{plane}^{stress} = \begin{bmatrix} \frac{1 - \nu_{31}\nu_{31}}{E_{11}} & -\frac{\nu_{21} + \nu_{31}\nu_{23}}{E_{22}} & 0 \\ -\frac{\nu_{12} + \nu_{32}\nu_{13}}{E_{11}} & \frac{1 - \nu_{32}\nu_{23}}{E_{22}} & 0 \\ 0 & 0 & \frac{1}{G_{12}} \end{bmatrix} \quad (5.6)$$

Being E_{ij} the elasticity modulus, ν_{ij} the material Poisson coefficient and G_{ij} the distortion modulus in the material direction i and j .

Then, considering the displacement field, for each point of the solid:

$$\mathbf{u}(x, y, z) = \begin{pmatrix} u(x, y, z) \\ v(x, y, z) \\ w(x, y, z) \end{pmatrix} \quad (5.7)$$

The strain components can be calculated with the following expressions:

$$\begin{pmatrix} \varepsilon_{xx} \\ \varepsilon_{yy} \\ \varepsilon_{zz} \\ \varepsilon_{xy} \\ \varepsilon_{xz} \\ \varepsilon_{yz} \end{pmatrix} = \begin{pmatrix} \frac{\partial u}{\partial x} \\ \frac{\partial v}{\partial y} \\ \frac{\partial w}{\partial z} \\ \frac{\partial v}{\partial x} + \frac{\partial u}{\partial y} \\ \frac{\partial w}{\partial x} + \frac{\partial u}{\partial z} \\ \frac{\partial w}{\partial y} + \frac{\partial v}{\partial z} \end{pmatrix} \quad (5.8)$$

The strain vector can be obtained through the combination of a partial differential operator and the displacements field, \mathbf{u} :

$$\boldsymbol{\varepsilon} = \mathbf{L}\mathbf{u} \quad (5.9)$$

Where \mathbf{L} is given by:

$$\mathbf{L} = \begin{bmatrix} \frac{\partial}{\partial x} & 0 & 0 & \frac{\partial}{\partial y} & 0 & \frac{\partial}{\partial z} \\ 0 & \frac{\partial}{\partial y} & 0 & \frac{\partial}{\partial x} & \frac{\partial}{\partial z} & 0 \\ 0 & 0 & \frac{\partial}{\partial z} & 0 & \frac{\partial}{\partial y} & \frac{\partial}{\partial x} \end{bmatrix}^T \quad (5.10)$$

5.2 - Weak Form

The partial differential equation governing a physical phenomenon is defined as strong form equations. An exact solution is obtained with this formulation, but it has some limitations. This type of equations are very difficult to solve, particularly in complex practical engineering problems.

Therefore, a discrete system of equations based on the weak form is established, being stated for each integration point. Despite the lower consistency, this system has the ability to produce equations of more stable algebraic systems [5].

5.2.1 - Galerkin Weak Form

In this work, the Galerkin weak form, a variational method based on energy minimization, is applied to obtain the system of discrete equations.

Considering a body in a domain $\Omega \in \mathbb{R}^2$ and bounded by Γ , where $\Gamma \in \Omega: \Gamma_u \cup \Gamma_t = \Gamma \wedge \Gamma_u \cap \Gamma_t = \emptyset$, in which Γ_u corresponds to the essential boundary conditions and Γ_t to the natural boundary conditions, the equilibrium equations governing the linear elasto-static problem are defined as:

$$\nabla \Lambda + \mathbf{b} = 0 \quad (5.11)$$

In which, ∇ is the nabla operator, \mathbf{b} is the body force per volume unit and Λ is the Cauchy stress tensor, as defined previously. According to the Galerkin weak form, the real solution is the one that minimizes the Langrangian functional, L given by:

$$L = T - U - W_f \quad (5.12)$$

Being T the kinetic energy, U is the strain energy and W_f is the work produced by the external forces. The kinetic energy is defined as:

$$T = \frac{1}{2} \int_{\Omega} \rho \dot{\mathbf{u}}^T \dot{\mathbf{u}} d\Omega \quad (5.13)$$

Where Ω represents the solid volume, $\dot{\mathbf{u}}$ is the first derivative of displacement with respect to time and ρ is solid mass density. For elastic materials, the strain energy is given by:

$$U = \frac{1}{2} \int_{\Omega} \varepsilon^T \sigma d\Omega \quad (5.14)$$

Where ε is the strain vector and σ is the stress vector. The work performed by external forces is represented by:

$$W_f = \frac{1}{2} \int_{\Omega} \mathbf{u}^T \mathbf{b} d\Omega + \int_{\Gamma_t} \mathbf{u}^T \bar{\mathbf{t}} d\Gamma_t \quad (5.15)$$

Where \mathbf{u} corresponds to displacement, \mathbf{b} is the body forces and Γ_t is the traction boundary where forces \mathbf{t} are applied. Thus, Galerkin weak form is expressed as:

$$L = \frac{1}{2} \int_{\Omega} \rho \dot{\mathbf{u}}^T \dot{\mathbf{u}} d\Omega - \int_{\Omega} \varepsilon^T \sigma d\Omega + \int_{\Omega} \mathbf{u}^T \mathbf{b} d\Omega + \int_{\Gamma_t} \mathbf{u}^T \bar{\mathbf{t}} d\Gamma_t \quad (5.16)$$

Equation (5.16) can be minimized ($\delta L = 0$) and developed as in [5]. Thus, neglecting the dynamic term, the following expression is obtained:

$$- \int_{\Omega} (\delta \varepsilon^T \sigma) d\Omega + \int_{\Omega} \delta \mathbf{u}^T \mathbf{b} d\Omega + \int_{\Gamma_t} \delta \mathbf{u}^T \bar{\mathbf{t}} d\Gamma_t = 0 \quad (5.17)$$

Considering stress-strain relation, $\sigma = \mathbf{c}\varepsilon$, and strain-displacement relation, $\varepsilon = \mathbf{L}\mathbf{u}$, equation (5.) can be defined as [5]:

$$\int_{\Omega} (\delta \mathbf{L}\mathbf{u})^T \mathbf{c}(\mathbf{L}\mathbf{u}) d\Omega + \int_{\Omega} \delta \mathbf{u}^T \mathbf{b} d\Omega + \int_{\Gamma_t} \delta \mathbf{u}^T \bar{\mathbf{t}} d\Gamma_t = 0 \quad (5.18)$$

5.3 - Discrete Equation System

Based on the principle of virtual work, the discrete equation system for the finite elements method and for meshless methods is obtained. Through interpolation functions, mentioned in section 4.2.4, the field variables can be obtained. For a 2D case, the field of displacement \mathbf{u} can be defined as:

$$\delta \mathbf{u}(\mathbf{x}_I) = \delta \mathbf{u}_I = \mathbf{I} \begin{Bmatrix} \Phi(\mathbf{x}_I) \\ \Phi(\mathbf{x}_I) \end{Bmatrix} \mathbf{u}_s = \begin{bmatrix} \varphi_1(\mathbf{x}_I) & 0 & \dots & \varphi_n(\mathbf{x}_I) & 0 \\ 0 & \varphi_1(\mathbf{x}_I) & \dots & 0 & \varphi_n(\mathbf{x}_I) \end{bmatrix} \begin{Bmatrix} \delta u_I \\ \delta v_I \\ \vdots \\ \delta u_n \\ \delta v_n \end{Bmatrix} = \mathbf{H}_I \delta \mathbf{u}_s \quad (5.19)$$

being \mathbf{I} a 2x2 identity matrix and $\mathbf{u}_I = \{u_I, v_I\}$, having two degrees of freedom. Thus, simplifying the first term of Equation (5.18):

$$\begin{aligned} \int_{\Omega} (\delta \mathbf{L} \mathbf{u})^T \mathbf{c} (\mathbf{L} \mathbf{u}) d\Omega &= \int_{\Omega} (\mathbf{L} \mathbf{H}_I \delta \mathbf{u}_s)^T \mathbf{c} (\mathbf{L} \mathbf{H}_I \delta \mathbf{u}_s) d\Omega = \int_{\Omega} \delta \mathbf{u}_s^T \mathbf{B}_I^T \mathbf{c} \mathbf{B}_I \mathbf{u}_s d\Omega \\ &= \delta \mathbf{u}^T \int_{\Omega} \mathbf{B}_I^T \mathbf{c} \mathbf{B}_I d\Omega \mathbf{u} \end{aligned} \quad (5.20)$$

In which the deformability matrix \mathbf{B}_I for the n nodes constituting the influence-cell of interest point \mathbf{x}_I , can be defined as:

$$\mathbf{B}_I = \begin{bmatrix} \frac{\partial \varphi_1(\mathbf{x}_I)}{\partial x} & 0 & \frac{\partial \varphi_2(\mathbf{x}_I)}{\partial x} & 0 & \dots & \frac{\partial \varphi_n(\mathbf{x}_I)}{\partial x} & 0 \\ 0 & \frac{\partial \varphi_1(\mathbf{x}_I)}{\partial y} & 0 & \frac{\partial \varphi_2(\mathbf{x}_I)}{\partial y} & \dots & 0 & \frac{\partial \varphi_n(\mathbf{x}_I)}{\partial y} \\ \frac{\partial \varphi_1(\mathbf{x}_I)}{\partial y} & \frac{\partial \varphi_1(\mathbf{x}_I)}{\partial x} & \frac{\partial \varphi_2(\mathbf{x}_I)}{\partial y} & \frac{\partial \varphi_2(\mathbf{x}_I)}{\partial x} & \dots & \frac{\partial \varphi_n(\mathbf{x}_I)}{\partial y} & \frac{\partial \varphi_n(\mathbf{x}_I)}{\partial x} \end{bmatrix} \quad (5.21)$$

In an analogous way, the second and third terms of Equation (5.18) can be also simplified, obtaining the following expression:

$$\int_{\Omega} \delta \mathbf{u}^T \mathbf{b} d\Omega = \int_{\Omega} (\mathbf{H}_I \delta \mathbf{u}_s)^T \mathbf{b} d\Omega = \delta \mathbf{u}^T \int_{\Omega} \mathbf{H}_I^T \mathbf{b} d\Omega \quad (5.22)$$

$$\int_{\Gamma_t} \delta \mathbf{u}^T \bar{\mathbf{t}} d\Gamma_t = \int_{\Gamma_t} (\mathbf{H}_I \delta \mathbf{u}_s)^T \bar{\mathbf{t}} d\Gamma_t = \delta \mathbf{u}^T \int_{\Gamma_t} \mathbf{H}_I^T \bar{\mathbf{t}} d\Gamma_t \quad (5.23)$$

So, equation (5.18) can become the following:

$$\delta L = \delta \mathbf{u}^T \underbrace{\int_{\Omega} \mathbf{B}_I^T \mathbf{c} \mathbf{B}_I d\Omega \mathbf{u}}_{\mathbf{K}} - \delta \mathbf{u}^T \underbrace{\int_{\Omega} \mathbf{H}_I^T \mathbf{b} d\Omega}_{\mathbf{f}_b} - \delta \mathbf{u}^T \underbrace{\int_{\Gamma_t} \mathbf{H}_I^T \bar{\mathbf{t}} d\Gamma_t}_{\mathbf{f}_t} = 0 \quad (5.24)$$

The equilibrium is then obtained and defined as:

$$\mathbf{K} \mathbf{u} = \mathbf{f}_b + \mathbf{f}_t \quad (5.25)$$

Being K , the stiffness matrix, u , the displacement field, f_b , the body weight vector and f_t the external forces vector. Therefore, considering the vector $f = f_b + f_t$, as the sum vector of the forces applied, it is possible to solve the linear equation system $u = K^{-1}f$ and obtain the displacement field [5].

Chapter 6

Numerical Methods in Bone Biomechanics

6.1 - FEM

FEM is a numerical method developed in 1956 to solve problems in aerospace engineering. Over the last few decades, the growing computer capacities allowed to apply this method to the majority of scientific areas, which has helped to solve ever more complex problems with a reasonable degree of accuracy [34]. Based on a research on Scopus database using different keywords, the graph depicted in Figure 6.1 demonstrates the expansion of this method to bone mechanics, as the number of published papers follows a growing trend over the years. However, when the search was narrowed to a more specific area of bone mechanics (FEM+femur), it was also possible to verify an increase in the number of published papers.

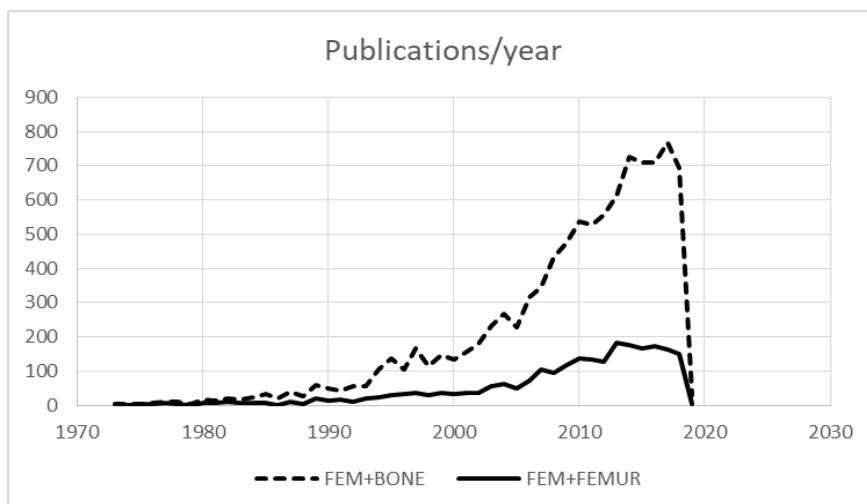


Figure 6.1 - Number of documents published through the years, in the subjects indicated. The data was obtained through a research on Scopus database (www.scopus.com) assuming as keywords the subjects indicated in the graph.

FEM was first used in orthopaedics in 1972 by Brekelmans [93]. In this study, in order to analyze the mechanical behavior of skeletal parts, a two-dimensional model of a femur was

developed and analyzed under a few load situations. The results obtained for the stresses and strains in the bone demonstrated that this method can be applied to a complex geometry and a variety of loading conditions without compromising the accuracy of the results.

6.1.1 - FEM and Bone

As mentioned in section 4.1, FEM can be applied in three areas of bone biomechanics: analysis of stress and strain, fracture prediction and study of bone remodeling process [86].

6.1.1.1 - Fracture Prediction

According to the Wolf's law, the human femur adopts an optimal structure in function of the normal loads of daily life. However, the bones are more vulnerable to non-habitual loads present in accidents and physical exercises [94]. In the cases where the loads exceed the maximum bone strength, bone structure failure occurs. Hip fracture is currently a common health problem among the elderly that results in increased morbidity and mortality, as well as high medical care costs. It is estimated that the number of hip fractures will rise from 1,7 million in 1990 to 6,3 million in 2050 [95]. Also, recent clinical studies have shown that the majority of hip fractures occurred at one of the three locations, the femoral neck (37%), the trochanter region (49%) and the femoral shaft (14%) (Figure 6.2) [96]. Due to the high costs and disabling nature of this injury, it is important to assess the femoral fracture risk in order to prevent it. FEM is a numerical method capable of integrate the femoral risk factors based on well-established mechanical principles and governing equations, allowing to understand the fracture mechanism and, ultimately, to predict femoral fractures [95].

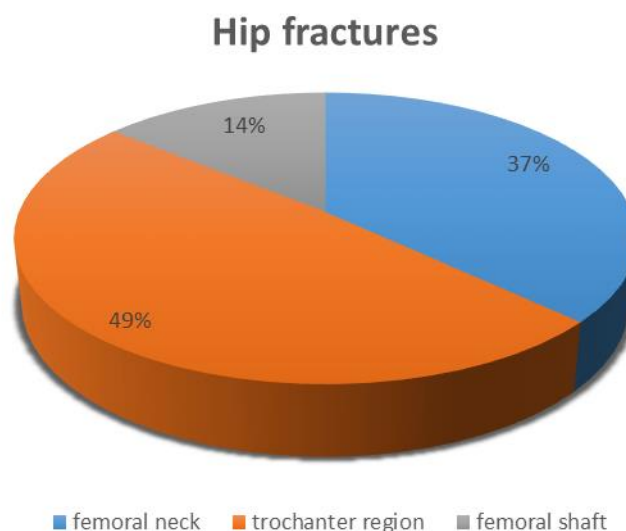


Figure 6.2 - Percentage of hip fracture in the femoral neck, trochanter region and femoral shaft.

The cause for femoral fractures is multifactorial. Early research focused on the loading conditions present in the bone [13]. Keyak et. al. developed an automated method for generating quantitative CT (QCT)-based femur models to predict femoral fracture load (Figure 6.3). Although the method produced a suboptimal representation of the bone surface, the results correlated well with experimental measurements on the same bone and can predict femoral fracture load within -40% to +60% with 95% [13].

Approximately 90% of femoral fractures are associated with a fall, with the descent and impact phases of a fall representing major etiologic importance. Several studies have been conducted to understand the importance of load direction as a fracture risk. In one of these studies, Pinilla et. al. study the influence of impact onto the lateral aspect of the greater trochanter on failure load of the proximal femur. Three different loading angles (angle between the neck axis and the femoral head load) were define, including 0° , 15° e 30° . The results obtained demonstrated a load reduction of 24% due to an increase in the loading angle from 0° to 30° . Also, the group observed that, independently of the femoral bone mineral density, the broad range of failure loads is explained by the impact direction of the fall [97]. Keyak et. al. also studied the impact of force direction on failure loads for two types of loading conditions, one representing impact from a fall and one similar to joint loading during daily activities. The results indicated that the greatest fracture risk was present in the fall configuration, particularly a fall onto the posterolateral aspect of the greater trochanter [98].

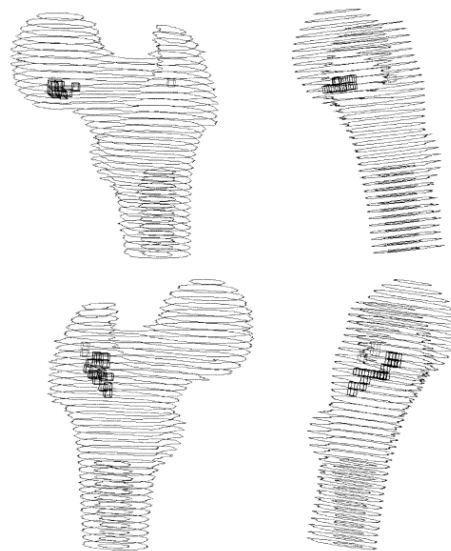


Figure 6.3 - Failure location computed for the stance loading condition (top) and fall condition (bottom) for a matched pair of femora. Adapted from [13].

Other studies have highlighted the importance of using multiple loading configurations in FE models to improve the prediction of fracture risk. Nishiyama *et. al.* developed a model that could estimate the bone stiffness and failure load under various loading conditions. They concluded that boundary conditions have a great impact on bone stiffness. The highest stiffness values were observe for 0° and -15° of internal rotation of the femoral neck, which corresponds to a fall impact anterolateral on the hip. The lowest stiffness value was found at 45° of internal rotation representing a fall on the hip where the impact is posterolateral [99]. On another study, Falcinelli et. al. simulated different loading configurations to identify the weakest structural condition of the proximal femur in order to improve the FE-models that predict femoral fractures. The model developed was able to identify fracture cases based on bone weakness, which, then, emphasizes the importance of the use of different loading conditions on FE models [100].

However, since less than 5% of falls result in fractures, other research groups believe to be important to consider other risk factors, such as bone strength, bone geometry and muscle activity [97]. Current methods for assessing bone fracture consider that reduced bone strength is related to fracture incidence and require two-dimensional or three-dimensional imaging techniques, such as dual-energy X-ray absorptiometry (DXA) or quantitative computed

tomography (QCT) to determine bone mineral density. Because bone strength is dependent, not only on bone mineral density, but also on three-dimensional shape, the mechanical properties and the loading conditions, these methods have only been partly successful in identifying patient with high fracture risk [13]. For that reason, FEM has been used to predict more accurately bone strength than densitometry measurements alone.

Orwoll et. al. developed the first QCT-FE models for proximal femurs of older men (Figure 6.4) and demonstrated the capacity of these models to predict bone fractures in men based on bone strength [1]. On another study, the group compared statistically three methods for predicting proximal femoral fracture loads: DXA, QCT and FEM. Three different models were developed: one model based on DXA images, another based on QCT images and an FE model based on QCT images. The results indicated that the FE model was able to explain 20% more of the variance in strength than the DXA models. Overall, the QCT-FE model proved to be a promising tool to predict femoral strength in vivo [101].

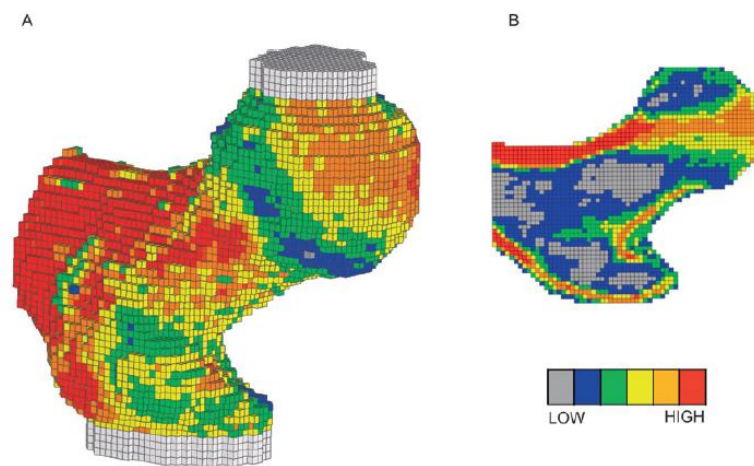


Figure 6.4 - Typical QCT-FE model of proximal femur, showing 3D (A) and 2D sectional (B) views. The color-coding shows the spatial variation of material strength assigned to the individual finite element. Adapted from [1].

Contrarily, Testi et. al. studied the risk of fracture in elderly patients based on DXA-FE models and the results were in agreement with the experimental results [102]. Ara et. al. also reported that DXA-FE models are able to predict up to 77% of femoral strength [103].

Langton et. al. performed a finite element analysis of 2D X-ray images and developed a 3D model derived from a single 2D radiographic image. When compared with the failure load prediction achieved with bone mineral density, the coefficient of determination to predict failure load was 54,5% for BMD and 80,4% for the model, which demonstrates that it has an increased accuracy of failure load assessment [104].

So far, the methods considered only used femora of cadavers or femoras of osteoporotic patients to analyze femoral strength. However, Bessho et. al. developed a CT-FE model based on the femora of ten patients with contralateral hip fracture in order to predict fracture load and fracture location. The group observed a markedly reduced structural strength in the femoral neck of the patients with hip fractures, which is in agreement with previous studies that reported a reduction of femoral neck strength by 50% less than that of normal femora. In conclusion, the model was capable to predict the fracture location and load. Thus, the group suggested that this is a valuable tool for clinical practice [105].

Age-related bone loss occurs due to a set of underlying structural changes that decreases proximal femoral strength, thus increasing the likelihood of structural failure in the case of a fall. The first study to document cross-sectional estimates of bone strength losses due to aging was conducted by Keaveny et. al. From a cohort of men and women with ages ranging from 20 to 80 years old, they observed a decline of 55% to 39% of proximal femoral bone strength of the greater trochanter over the lifetime of both men and women. However, this study had some limitations related to small number of elderly subjects. Lang et. al. evaluated the extent to which proximal femoral density, structure and strength change with age in function to gender. QCT-FE models were developed based on a cohort of elderly men and women and the results indicated bone loss between the genders is consistent with a higher fracture among elderly women. The deficits observed in women correlate with a period following the menopause [106]. In another study [107], the structural features of the proximal femur of women with the same age, with and without hip fracture, were compared in order to distinguish the women at higher risk for fracture. The results indicated a larger outer femoral neck in the women who sustain a fracture, which corresponds to a compensatory effect at the load-bearing inferior cortex. In conclusion, the group remarked that this deficit may be used as a biomarker for increased fracture risk.

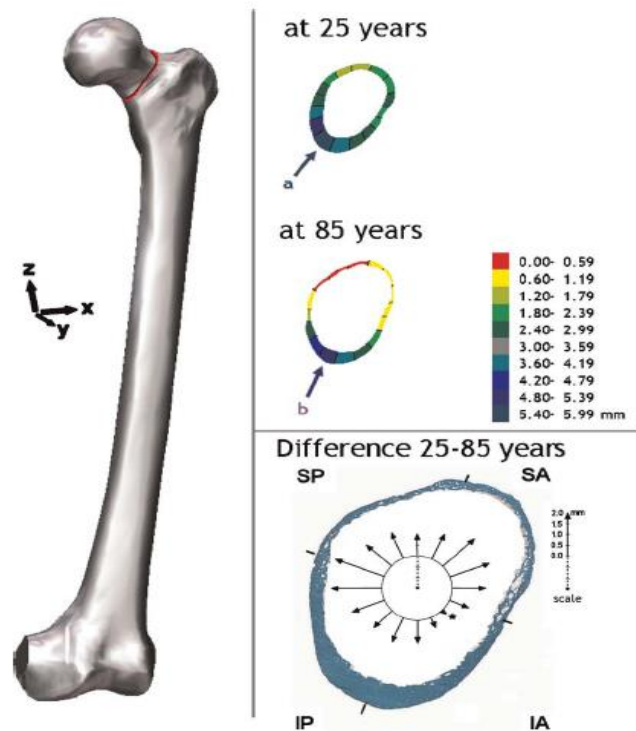


Figure 6.5 - (Left) Location of the midfemoral neck in stance; schematic diagram showing cortical thickness at the midfemoral neck at 25 and 85 years. Adapted from [19].

Femur bone strength can also be evaluated by its cortical thickness together with BMD, because cortical bone withstands greater loads than trabecular bone. Cortical thickness is not uniform throughout the bone due to the asymmetric mechanical loading present in daily bipedal locomotion. This loading condition results in a higher compressive stress at the inferior cortex and smaller tensile stress at the superior cortex of the femoral neck. As a result, cortical geometry of the proximal femur reflects a mechanically appropriate shape, with the cortical bone at the inferomedial side being thicker than at the superolateral side [95]. With aging, the cortical thinning becomes evident, with a decrease from 1,6 mm at the age of 25 to 0,3 mm at

the age of 85 years in females in the superoposterior cortex of the femoral neck (Figure 6.5) [19]. The cortical thinning of the femoral neck makes it more prone to fracture.

In order to assess the possibility of using cortical thickness as a bone fracture risk factor, Long et. al. analyzed DXA-FE simulations and demonstrated that cortical thickness has a better discriminative capacity for bone fracture than BMD and should, therefore, be used in FE models [95].

Recent studies have indicated that targeted exercises can help to prevent femoral fractures and that physical activity should be maintained with aging in order to preserve fracture resistance [108]. A study, represented in Figure 6.6, conducted based on 3D proximal femur FE models with young adult female athletes with distinct exercise loading patterns showed lower stresses at the femoral neck in the athletes that performed endurance running, soccer and squash [3]. Abe et. al. also observed that exercise loading history with high impacts or odd impacts, such as running and squash, can lower the risk of fall-induced femoral fracture [109].

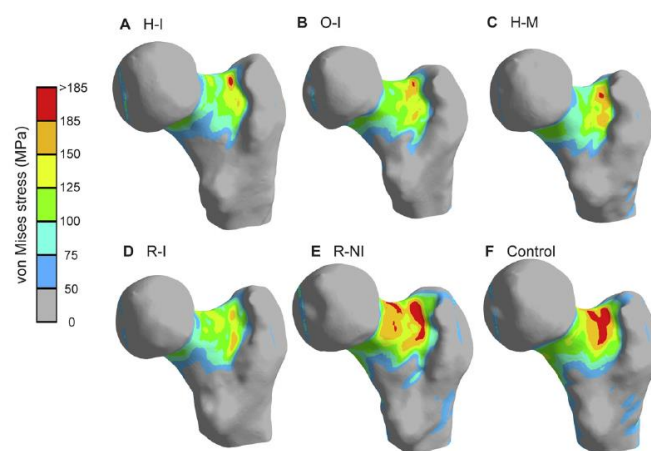


Figure 6.6 - Examples of typical Von Mises stress distribution from A, B, C, D, E, F and control group during fall simulation. H-I represents high-impact, O-I represents odd-impact, H-M represents high-magnitude, R-I represents repetitive-impact and R-NI represents repetitive non-impact. Adapted from [3].

Besides predicting the risk of bone fracture, FEM can also be used to determine the fracture location in the proximal femur. Keyak et. al. developed an automatically generated CT-FE model of the proximal femur to predict fracture location and type. For the stance configuration, the fracture location was predicted with an accuracy of 72% and 79% for the fall configuration. In conclusion, FE models can be used to predict the location of fractures with moderate accuracy and require, therefore, further studies for improvement of the models [110].

Patient-specific finite element (PSFE) models are the most recent method able to predict the biomechanical response of bones based on each individual anatomy. Several models have been developed so far. Trabelsi et. al. developed a PSFE model based on QCT and the numerical results obtained were in good correlation with the experimental results. This method has a high accuracy and can be used as a clinical decision-making tool [111].

However, despite all the models already developed, FEM has not yet been integrated in clinical routine procedure mainly because of its technical complexities.

6.1.1.2 - Analysis of Stress and Strain

The first studies conducted with FEM were concern with the stress and strain analysis of the femur. Valliappan et. al. developed a 3D-FE model and used isotropic mechanical properties for cortical and trabecular bone. The results demonstrated that the area with the higher stress levels was the femoral neck, which is the more fracture prone area of the femur, as mentioned before [42]. Aghili et. al. analyzed the stress patterns in the femur under different loading conditions. The results also evidenced a maximum stress at the inferior side of the femoral neck [112].

The stress and strain in the femur are influenced by the muscles activity. Some studies have confirmed the importance of the abductor muscles and ilio-tibial band to simulate femoral loading conditions. Duda et. al. developed an FE model based on a loading situation that included all thigh muscles and compared the results of strain distributions with those obtained from an FE model with simplified load regimes. The differences in the strains between the simplified model and the one with all thigh muscles included were as high as 26%. However, when the abductors are added to a loading situation of hip contact, the difference is reduced to 5% (Figure 6.7). In conclusion, FE simulations should include all thigh muscles to reproduce the physiological strain distribution in the human femur [15].

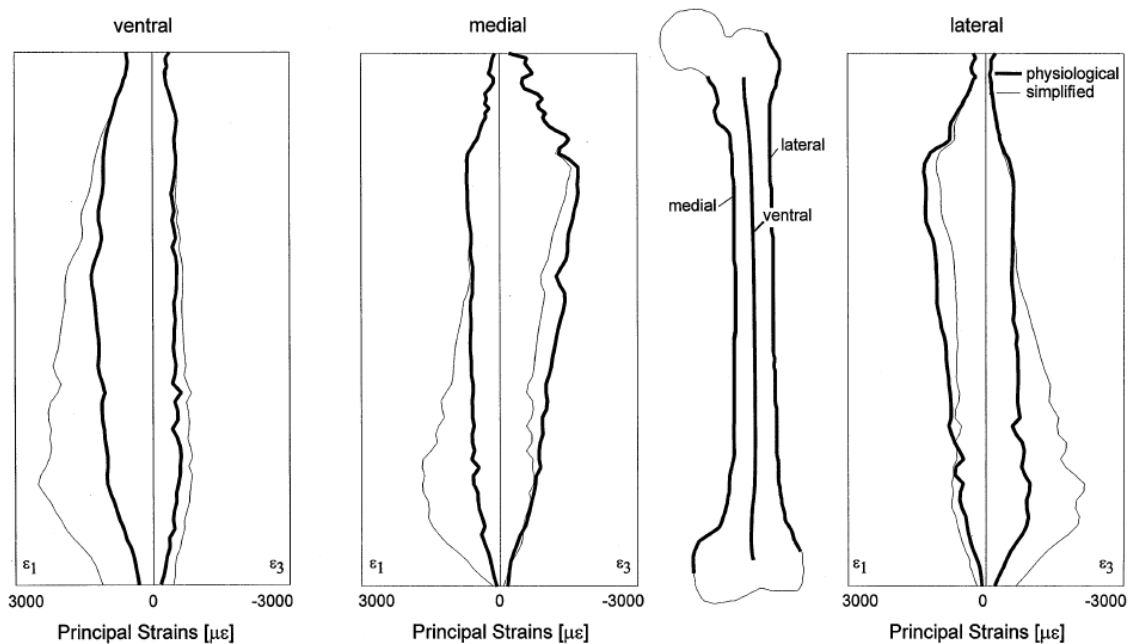


Figure 6.7 - Principal strains ϵ_1 (maximal) and ϵ_1 (minimal) along the human femur at 45% gait cycle with all thigh muscles included (dark lines). A representation for the simplified load regimes are also included (light lines). Adapted from [15].

The bone mechanical properties also influence the stress and strain patterns in the bone. Lotz et. al. determined the stress distribution in normal and osteoporotic proximal femora in a gait and fall configuration in order to understand the structural importance of cortical and trabecular bone. The results showed that the principal stresses were more concentrated in the cortical bone of the intertrochanteric region during gait configuration. Based on the stress distribution throughout the bone, the group observed that the cortical and trabecular bone carried approximately constant load cases but varied depending on location. The cortical bone supported 30% of the total load at the subcapital region, 50% at the mid-neck, 96% at the base

of the neck and 80% at the intertrochanteric region [113]. Nawathe et. al. also studied the influence of cortical and trabecular bone on the load sharing capacity in the femoral neck. The results demonstrated maximum stress levels in the cortical bone distally and proximally in the trabecular bone of the femoral neck [114]. Finally, Kachlík et. al. developed an FE model of the osteons in the proximal femur and observed that the cortical microstructure had influence on the stress distribution throughout the bone [115].

Stress fracture is a common type of fracture among athletes and military caused by repetitive skeletal loads during intense physical training. Voo et. al. evaluated the stress distribution in a human femur in order to assess the risk of stress fractures. They indicated that bone geometry has an influence on the stress distribution in the femur. The overall maximum stress was observed in the inferior aspect of the femoral neck. However, when they developed a FE model with a cortical thickness higher than the previous one, a reduced peak stress (35%) was observed in the inferior cortex of the neck with unchanged stress levels at the superior cortex [116].

6.1.1.3 - Study of Bone Remodeling Process

FEM is one of the numerical methods used to analyze the bone remodeling phenomena. As mentioned in section 2.12, several models of bone remodeling have been developed using FEM [63, 69, 70]. However, despite all the models already developed, bone remodeling is a complex process unable to be fully described at the present moment [5].

Bone remodeling is also important in implantology to estimate the changes in the stress fields in the bone created by implant insertion. Hip replacement surgery is a common surgical procedure required to treat femoral fractures where the femoral head is replaced by an implant [117]. Nowadays, there are many types of femoral implants with many shapes, materials and functionalities. Due to the adaptive remodeling effect induced in the bone by the implant, it is important to study the mass changes of the bone tissue after a hip replacement surgery [118]. Several studies have been performed to understand the influence of the prosthesis geometry, the material properties of the implant and the type of fixation [119, 120].

Musculoskeletal loading affects the patterns of stress and strain within the human femur and, thereby, influence the bone remodeling process. Some studies have already demonstrated that all thigh muscles should be included when simulating the bone remodeling process [15, 121]. Bitsakos et. al. performed an FE simulation with different muscle loading conditions and analyzed the effect on the outcome of the bone remodeling phenomena. The results obtained demonstrated that the model with simplified load regimes predicted more pronounced bone loss compared to those with all muscles included [122].

6.1.2 - FEM and Sarcoma

Sarcomas compromise the structural integrity of bone and soft tissues, as mentioned in section 3.3. of this manuscript. Through a search in the Scopus database, using the key words: finite element method, sarcomas, bone metastases and bone sarcomas, it was possible to notice that FEM has not yet been widely used in the study of sarcomas. In Figure 6.8, the search results are indicated as the total number of publications from the year 2003 to 2017, using the

combination of the keywords. From the total amount of publications concerning sarcomas, only 46% are related to bone sarcomas.

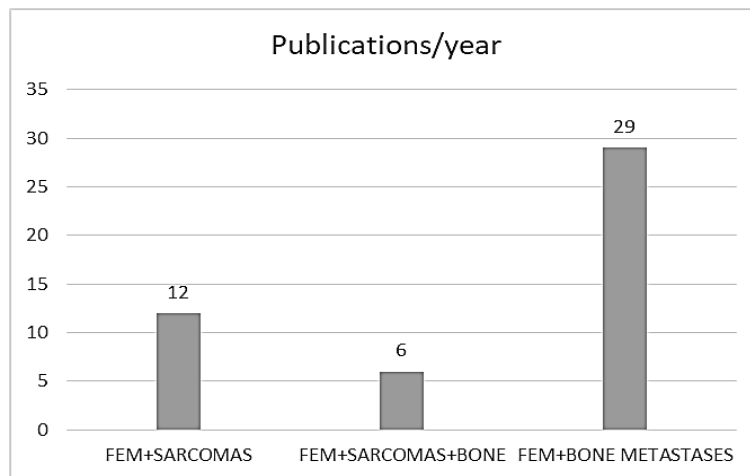


Figure 6.8 - Number of documents published through the years, in the subjects indicated. The data was obtained through a research on Scopus database (www.scopus.com) assuming as keywords the subjects indicated in the graph.

6.1.2.1 - FEM and Bone Sarcomas

As mentioned in section 3.5, bone sarcomas induce pathological changes in the bone that can increase the risk of fracture. Subject-specific finite element models have been created to analyze the long-term effects of limb reconstructions after the resection of bone tumors and to access the risk of bone fracture. One of these studies evaluated the fracture risk of a reconstructed proximal femur from a four-year-old child affected by Ewing's sarcoma, after three years of follow-up. The proximal femur was reconstructed using an allograft with a vascularized fibula autograft. The results demonstrated that the reconstructed femur had not recovered the whole mechanical strength when compared to the contralateral and healthy proximal femur. Higher stresses were also observed, particularly, in the neck and in the medial aspect of the allograft. As a result, these areas appeared weaker and had a higher fracture risk. However, no region in the model reached the fracture limit. In conclusion, this study demonstrated that subject-specific finite element models can be used to predict the fracture risk of a reconstructed femur after tumor resection [123].

Very few studies have considered the long-term biomechanical response of a reconstructed femur in response to different loading conditions. Valente *et. al.* developed a subject-specific finite element model of a reconstructed femur and combined it with a musculoskeletal model in order to study bone resorption under different mechanical stimulus induced by different loading conditions. The results obtained suggest that bone resorption occurs due to the effect of proximal metal screws and muscle loading, which affects the stress and strain conditions in the reconstructed femur. Therefore, the group suggested that the surgical treatment should be altered and physical therapy should be promoted to optimize bone adaptation [124].

However, no published papers dealing with the analysis of bone sarcomas and its effects, using finite element models, were found in the Scopus database. Several searches were conducted in Scopus, ScienceDirect and Elsevier database (with the keywords: "FEM" and "bone sarcomas") and no documents were found, revealing a gap in this research topic that this work intends to fulfill.

6.1.2.1 - FEM and Bone Metastatic Lesions

The total number of manuscripts dealing with bone sarcomas is very low when compared to the total amount of published works concerning bone metastatic lesions (Figure 6.8), which have been increasing recently (Figure 6.9) as a result of the growing incidence rates of bone metastatic disease.

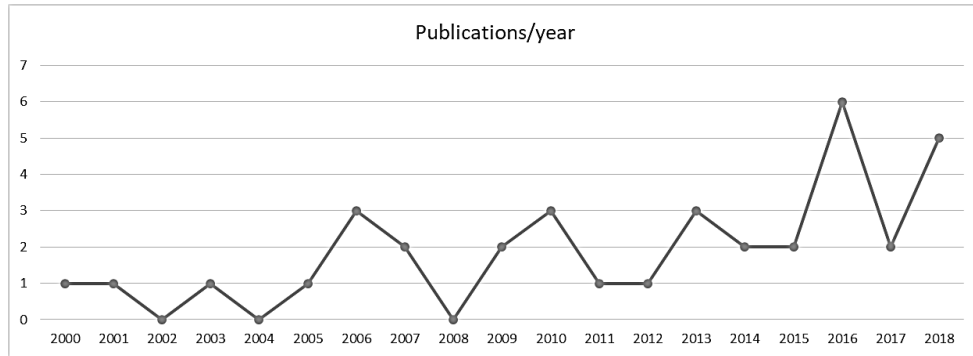


Figure 6.9 - Number of documents published through the years concerning bone metastatic lesions. The data was obtained through a research on Scopus database (www.scopus.com) assuming as keywords bone metastatic lesion and FEM.

As stated in section 3.1., osseous metastatic lesions in the femur are very common. Femoral metastases disrupt the bone remodeling process and may lead to pathological fractures. Surgical intervention is often required to treat these fractures, due to a poor healing of the bone. However, an increase in perioperative morbidity is often observed in the patients who suffer surgery as well as a higher risk for infection [124]. In some cases, some patients can be spared from unnecessary surgical procedures if at-risk lesions could be defined. For that reason, guidelines have been developed based on observational studies to predict the fracture risk [73]. Fidler studied the effect of metastases with different sizes in the fracture incidence of long bones. The results demonstrated that when more than 50% of the cortex was involved, the fracture incidence rate was approximately 60% and approximately 80% when more than 75% of the cortex was affected. Other authors assumed a certain size of lesion or a certain ratio of lesion width to bone width to be the main risk factors responsible for pathological fractures [125].

However, several authors concluded that these guidelines have a poor predictive power because they are based in a small sample size and are also associated with a large error in the estimation of the bone load-bearing capacity. Therefore, there are still no established clinical or radiological guidelines able to predict the fracture risk and validate fractures [73, 126].

Finite element analysis have been successfully used in fracture prediction of metastatic bone disease, but have not yet been applied in clinical practice. Most of past studies use healthy bones with artificially created defects as poor representations of actual metastatic tumors, in order to validate the FE model [127]. The results obtained are limited and do not accurately predict the fracture risk [28]. As such, recent studies simulate metastatic lesions in the femur and validate the results with actual metastatic bones. Yosibash *et. al.* created a patient-specific finite element model capable of predicting the risk of fractures in femurs with metastatic defects [28]. Also, Keyak *et. al.* developed an subject-specific FE model capable of predicting the proximal femoral strength and fractures in the subcapital region [128].

So far, the studies conducted do not take into consideration different sites of metastatic lesions within the bone. For that purpose, Keyak *et. al.* studied the effect of tumor location within the femur as a risk factor. To simulate the lesion, several defect sizes were considered for a preliminary studied: 10 mm, 15 mm and 20 mm in diameter. Defects smaller than 20 mm in diameter caused only minimal reductions in the proximal femoral strength. Hence, only a 20-mm-diameter spherical void was used to simulate a metastatic lesion in the neck and in the lesser trochanter. Within the femoral neck, the inferomedial defects had the greater effect on the proximal femoral strength. At the level of the lesser trochanter, the defect in the anteromedial surface of the bone resulted in the lowest proximal femoral strength. Defects located in the lateral or posterior corner led to consistently increasing proximal femoral strength (Figure 6.10). In conclusion, the percentage of intact bone strength is dependent on defect location, making these findings important to evaluate pathological fracture risk [18]. On another study, Benca *et. al.* demonstrated significant differences in the biomechanical behavior of metastatic femurs with lesions in superolateral or in the inferomedial neck. Also, different lesion locations lead to different magnitudes in failure load and stiffness. These results underline the importance of metastases location on current clinical guidelines for fracture prediction [73].

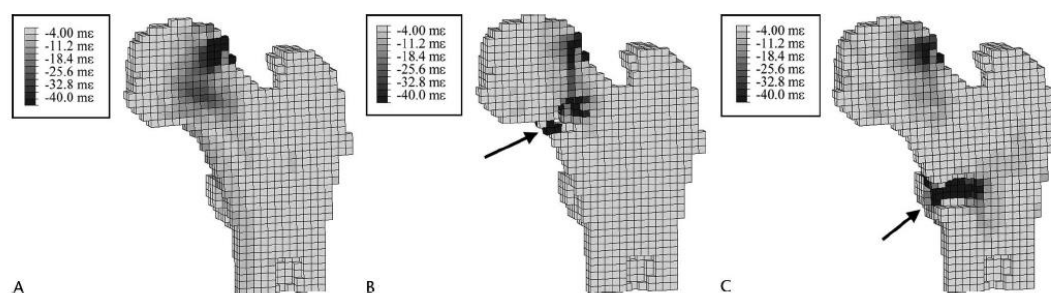


Figure 6.10 - Compressive principal strain illustrate different failure locations (shown in black) for the proximal femur (A) in the intact state, (B) with an inferomedial femoral neck defect, and (C) with a defect in the anteromedial corner at the level of the lesser trochanter. Adapted from [18].

6.2 - Meshless Methods

The FEM is the most commonly used discrete numerical method in bone mechanics. However, this method has some limitations due to mesh-based interpolation, such as low quality meshes with higher errors and unable to solve problems with discontinuities that do not align with elements edges [129]. Therefore, meshless methods were developed with the purpose to overcome the problems associated with FEM. A search through *Scopus* database (Figure 6.11) allowed to demonstrate that the number of published papers related to bone mechanics has been recently increasing. When the search is narrowed to the study of the femur, it was also possible to verify an increase in the number of published papers. However, because these methods have only been recently used in this area, the number of published papers is still lower than the ones related to FEM, which emphasizes the gap that exists concerning this topic, which this work intends to fulfill.

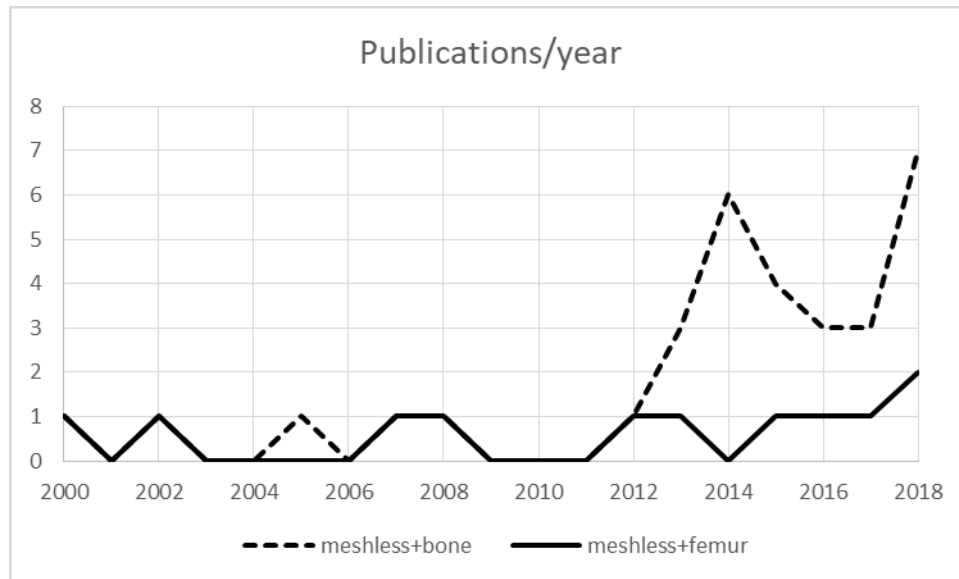


Figure 6.11 - Number of documents published through the years, in the subjects indicated. The data was obtained through a research on Scopus database (www.scopus.com) assuming as keywords the subjects indicated in the graph.

6.2.1 - Meshless Methods and Bone

Meshless methods have not yet been widely used in bone mechanics, as previously demonstrated in Figure 6.1. As a result, the majority of the work developed so far was to validate these methods and compared then to other numeric methods.

Several computational algorithms for bone remodeling process have been developed and implemented with FEM, as mentioned in section 5.1.1. Recently, meshless methods have been used to also analyze the bone remodeling process. Belinha *et. al.* presented a new algorithm for bone remodeling, based on a meshless method, the NNRPIM. The viability and efficiency of the algorithm was successfully tested, under multiple loading conditions, on a femur bone model and a calcaneus bone model [130-132]. On another work, Belinha *et. al.* also studied the bone tissue trabecular remodeling process with the meshless method NNRPIM [55]. Fernandez *et. al.* investigated the femoral cortical bone remodeling process based on the smooth particle hydrodynamics method (SPH). The results demonstrated that this is an effective method capable to predict the bone pore shapes and remodeling evolution overtime [133]. Doblaré *et. al.* considered that the natural element method (NEM) is the most appropriate method for biomechanics. For that reason, the group simulated the bone internal remodelling process on the femur and the results were compared with finite element models, demonstrating a good agreement and performance by the NEM [134].

More recently, meshless methods have been applied in implantology, namely in the study of femoral behavior after the insertion of a stem in the diaphysis. When compared with other numerical methods, the results obtained in this study allowed for a smoother and more accurate strain energy fields (SED) which means the remodeling predictions are more reliable [135].

Meshless methods can also predict bone fractures. Lee *et. al.* used the moving least square approximation technique to analyze the behavior of the trabecular femoral bone loaded in compression. The CT images of the trabecular bone were converted into a three-dimensional meshless model, which was used to simulate the osteoporotic process. Furthermore, a fracture

criterion was proposed and the process was simulated on the femur. The results demonstrated that trabecular bone is important in the prevention of progressive failure and that this method can be applied for the prognosis of osteoporosis [136]. On another work, Fernandez *et. al.* investigated the age-related changes in femoral cortical bone with the SPH method, in order to understand the mechanism for bone weakening and, subsequently, the increase in fracture vulnerability. The findings from this study proven that SPH can be successfully used to model pore shapes over time and, also, demonstrated that bone remodeling at the osteon level causes pore merging, which increases with aging. [137].

Finally, stress and strain distributions can be obtained with meshless methods. Liew *et. al.* was the first to apply the reproducing kernel particle approximate (RKPM) to the investigation of stress distribution within the proximal femur. The model was used to simulate the effects of aging and necrosis. However, the simplifications adopted to create the model limited the results and, furthermore, its clinical relevance [138]. Taddei *et. al.* developed a new approach for subject-specific strain prediction based on the cell method. The meshless implementation provided results with good accuracy, which demonstrates that meshless methods can have clinical applications [139].

6.2.2 - Meshless Methods and Sarcomas

In my best knowledge, there are no publications regarding the study of meshless methods and sarcomas. A search performed in the Scopus, ScienceDirect, Elsevier and Springer database, using the key words: meshless method, sarcomas, bone metastases and bone sarcomas, found no documents regarding these subjects, meaning that there is a gap in literature related to this topic, which this work intends to fulfill.

Chapter 7

Preliminary Work

Initially, a preliminary work was performed on a healthy proximal femur before the analysis of femoral bone sarcomas. This study allowed to introduce the basic software required for the development of the dissertation and to acquire a proficient level, as user, of the following software:

- 3D Slicer, a freeware capable to produce STL files from CT medical images, which allowed to understand the 3D anatomy of femur bones and to acquire the geometries from the DICOM files (CAT-scan files).
- FEMAP, (Siemens PLM Software, student version) - a software allowing the construction of meshes from STL files possessing drawing tools to create geometric models their respective meshes;
- FEMAS® (Finite Element and Meshless Analysis Software - cmech.webs.com) - a freeware academic software that allows the analysis of models using either the FEM or meshless methods combined with several linear and non-linear formulations.

In this chapter, the preliminary work is described and the results obtained from the analysis are presented with the main conclusions.

7.1 - The Structural Analysis of a Femur Bone Using a 2D FEM Approach

A two-dimensional (2D) model of the proximal femur was developed in order to achieve the proficient level in the previously mentioned software. The practical case study was conducted on a 2D model of a proximal femur based on an X-ray image in DICOM (Digital Imaging and Communications in Medicine) format. From the X-ray image, different points were extracted and designed in the FEMAP® software. The points were further connected, the boundary surfaces were established, and the triangle mesh was created. From FEMAP®, an INP file was generated and imported to FEMAS® software, where the two materials were defined (cortical bone and trabecular bone) represented with different colors (blue represents trabecular bone

and purple represents cortical bone). The final 2D model, represented in Figure 7.1, is composed by 7672 triangular elements (constant strain elements) and 4002 nodes.

In the present study, it was considered a Young's modulus (E) of $1,7 \times 10^4$ MPa and $2,13 \times 10^3$ MPa for cortical and trabecular bone, respectively. The Poisson's ratio (ν) was defined as 0,33 and 0,30 for cortical and trabecular bone respectively.

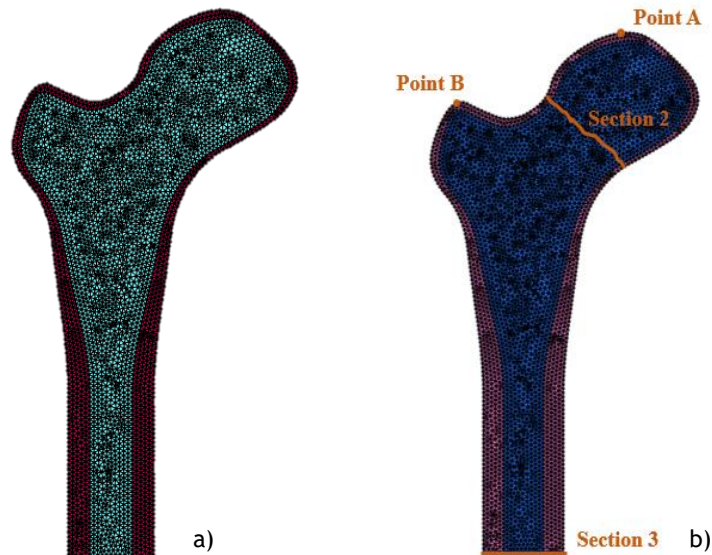


Figure 7.1 - (a) Final femur model with cortical (purple) and trabecular (blue) bone; (b) Points of interest selected for the study to analyze the strain and the von Mises stress.

In order to simplify and represent the model as close as possible to reality, the boundary conditions considered were applied in the distal section of the femur, preventing its movement. The loads applied can be divided into three different cases, each consisting of one parabolic distributed load over the joint surface and another parabolic distributed load on the trochanter, representing the abductor muscle attachment (Figure 7.2).

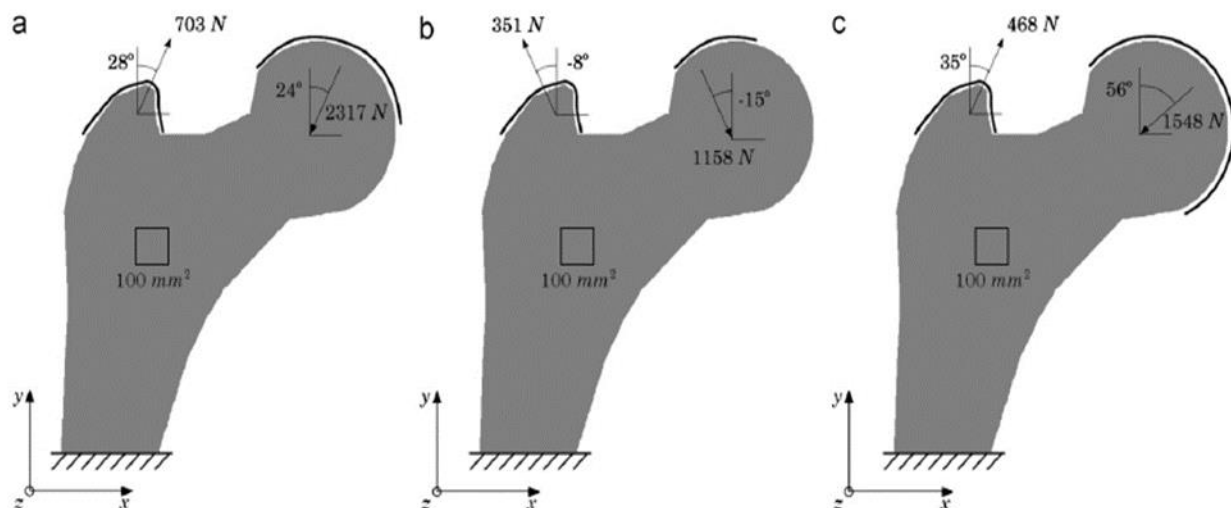


Figure 7.2 - Loads of the different cases. (a) First mechanical case, (b) Second mechanical case, (c) Third mechanical case.

The equivalent strain and the von Mises stresses distribution along the femur were obtained and are represented in Figure 7.3, respectively. Based on the results obtained, it was possible to determine some interest points, that is, nodes showing higher stress and strain. For that

reason, 2 points were selected, one in the femur head (PA) and the other in the trochanter (PB), respectively, as well as two different sections. Section 2 is composed by 25 nodes in the neck of the femur, while, in the distal segment, 20 nodes constitutes section 3 (Figure 7.1 (a)).

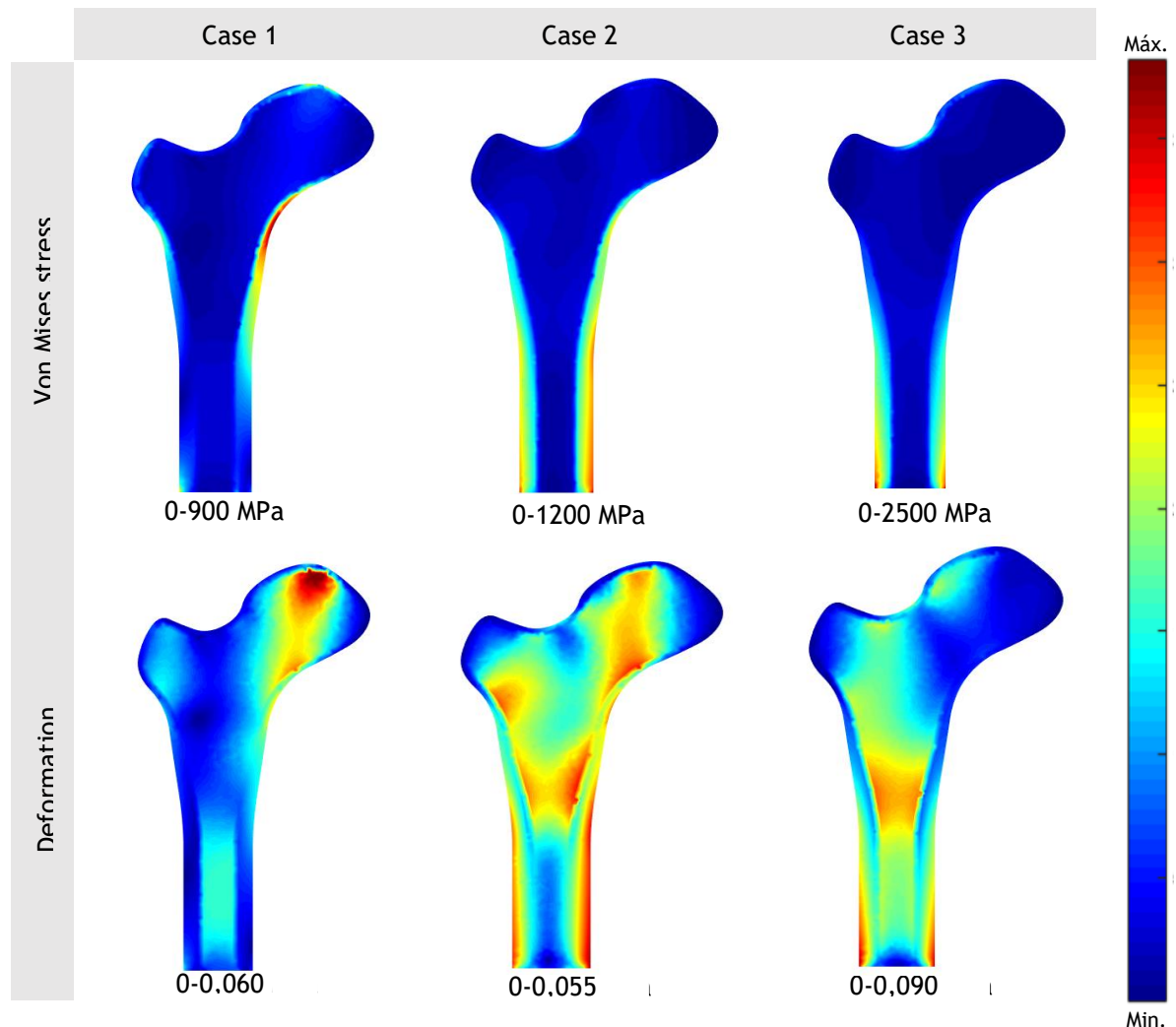


Figure 7.3 - Six numerical models resulting from the use of FEM in each load case. Three models present the equivalent von Mises stress and three others present the equivalent strain applied for the different load cases. Representation of the maximum stress and strain for each case.

The obtained results demonstrated that the highest stresses are concentrate in the cortical bone of the femur's shaft, particularly, in the lower portion of the femur. However, in case 1, despite existing higher stress levels in the cortical other than the trabecular bone, the highest stress is concentrated in the lower section of the femur's neck.

The cortical and trabecular bone have different behaviors and, therefore, different yield stress. In other words, the trabecular bone yields when the stresses are above 50 MPa, contrarily to the cortical bone, which can resist, approximately, to 170 MPa of stress. The results in Figure 7.3 demonstrates that in case 1, the stress varies between 0-900 MPa, with a higher stress being observed in the cortical bone. In this case, the stress exerted on the cortical bone exceeds the maximum stress, which means that the cortical bone begins to yield or undergo damages. The same can be observed in cases 2 and 3, especially because the range of stress is from 0-1200 MPa and 0-2500 MPa, respectively.

To better understand the stress applied both in the cortical and the trabecular bone, the equivalent von Mises stress was calculated for 2 sections (Figure 7.1 (b)) for each load cases and represented in graphs in Figure 7.4.

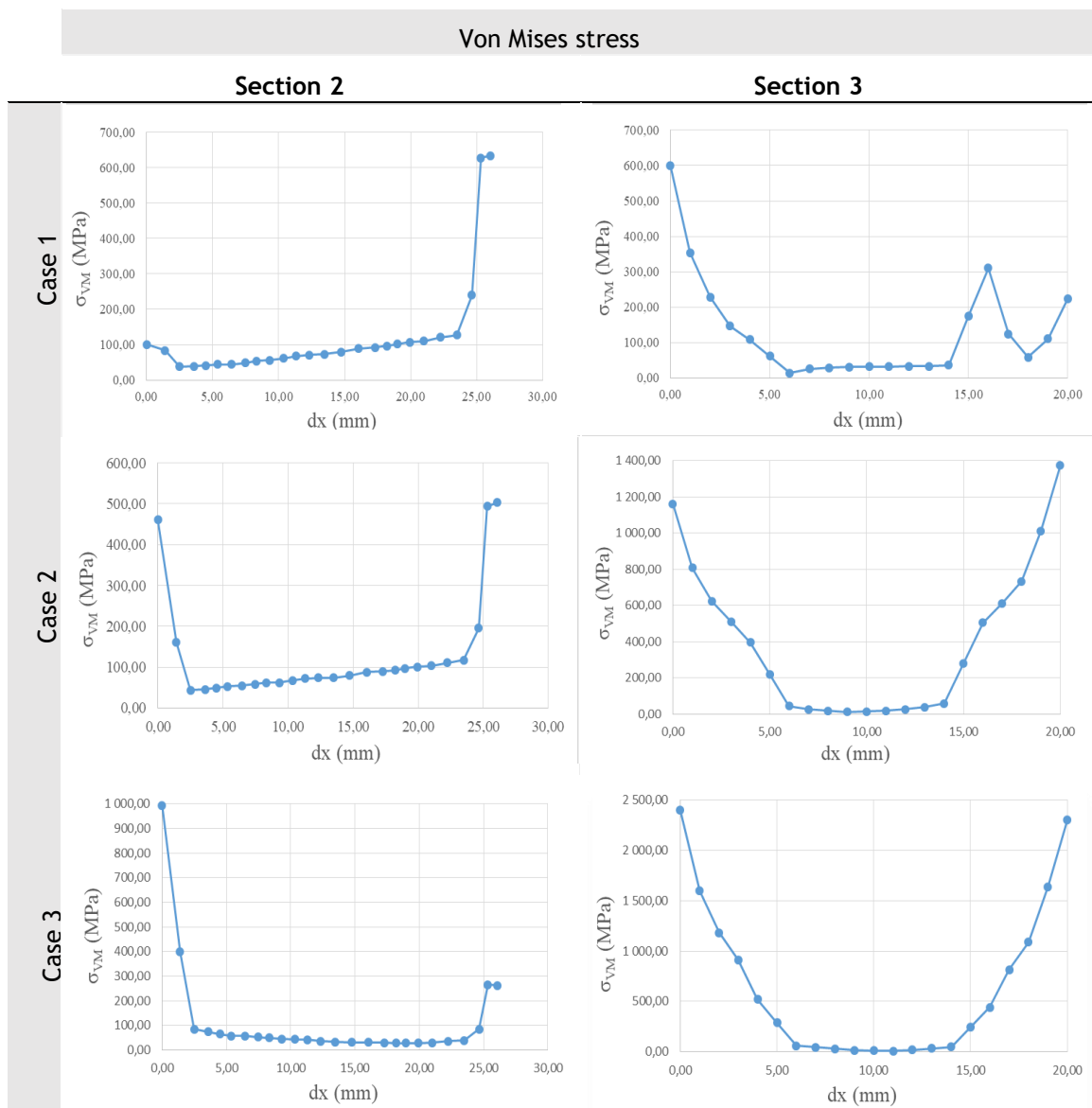


Figure 7.4 - Graphical representation of the values obtain for the equivalent von Mises stress, for each load case. The stress is represented in function of distance between nodes (dx), in millimeters (mm).

The cortical bone is represented in the graph's extremities, with the trabecular bone being represented in the middle of the graph. It is possible to observe that the distribution of stress increases in the cortical bone, decreasing when reaching trabecular bone, except in the case 1 of section 3, where it can notice an increase in stress in the right trabecular-cortical interface, followed by a decrease in stress in the cortical bone. In cases 2 and 3 of both sections, the stress present in the cortical bone are greater than 170 MPa, meaning that the bone enters in yield. However, in case 1 of section 2, the stress in the cortical bone on the left extremity of the section is smaller than the maximum stress of yield. The maximum values of stress are observed in case 2 and 3 of section 3, as it is expected, considering the color maps in Figure 7.3.

Notice that in this work, it was considered the 2D plane strain deformation theory. Thus, in fact only a thin slice of femur bone (with 1mm thick) was analyzed, in which the total force was applied. Therefore, the magnitude of the variable fields do not correspond to the real scenario. They are a qualitative representation of the real stress/strain distributions. In order to obtain a better approximation, one should divide the value of the obtained variable fields by the thickness of the femur bone (which is approximately 30mm to 35mm). After this dimensional correction, it is possible to observe that all stress values obtained are below the yield/ultimate stress of bone tissue.

The equivalent strain of the femur bone for each of the load cases is represented in Figure 7.3. Despite being denser, the cortical bone is capable of supporting lower levels of strain, before fracturing, contrarily to the trabecular bone. In case 1, the higher strain is visible in the trabecular bone on the femur's head and neck. In case 2, both trabecular and cortical bone experiment high levels of strain, particularly in the shaft and neck of the femur. Also affected, the trabecular and cortical bone in case 3 experiment the highest strain mainly in the shaft of the femur.

The results in Figure 7.5.5 shown significant values of displacement in the x component of the vector, particularly in point A. In conclusion, the femur experiments the higher displacement in case 2, both in the head (Point A) and trochanter (Point B) of the femur.

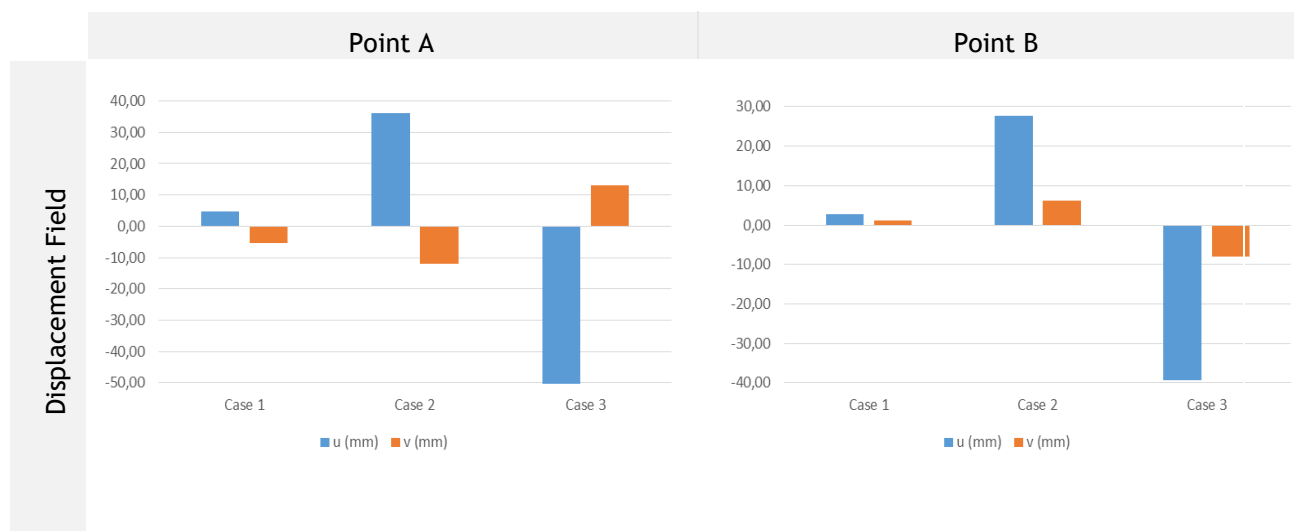


Figure 7.5 - Bar graphs for displacement field, in millimeters (mm), of point A and point B, for each load case. The u represents the x component of the displacement vector and v represents y component of displacement field.

Chapter 8

Numerical Analysis of Bone Sarcomas in the Proximal Femur

In this chapter, the numerical analysis performed with femoral bone sarcomas will be presented. For that reason, a 2D and 3D model of a cancerous femur bone were developed based on X-ray images and CT scan, respectively. The aim of this work is to study the influence of this type of malignancy in the bone structure, both on a global and local scale. Moreover, three numerical methods were used (FEM, NNRPIM and RPIM) not only to compare them and understand the level of performance of meshless methods, but also to expand the state-of-art of meshless methods.

8.1 - Numerical Analysis of Two-dimensional Femur Models with Bone Sarcomas

In this section, 12 two-dimensional models of bone sarcomas in the proximal femur were developed, in order to understand the effect of size and location of the tumor on the bone structure. The generic geometry of model, represented in Figure 8.1(b), was created based on radiographs provided by the Hospital Center of Porto (Figure 8.1(a)).

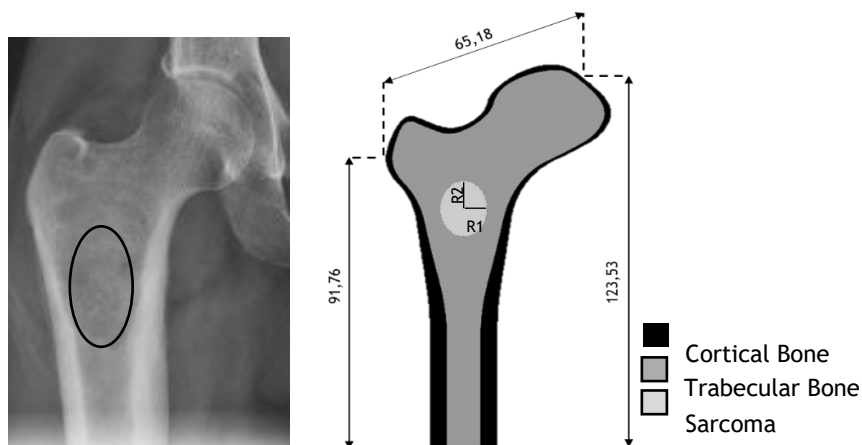


Figure 8.1 - (a) Anteroposterior radiograph of the femur on the right side of the patient; (b) Representation of the geometric femur model with a bone sarcoma located on the shaft.

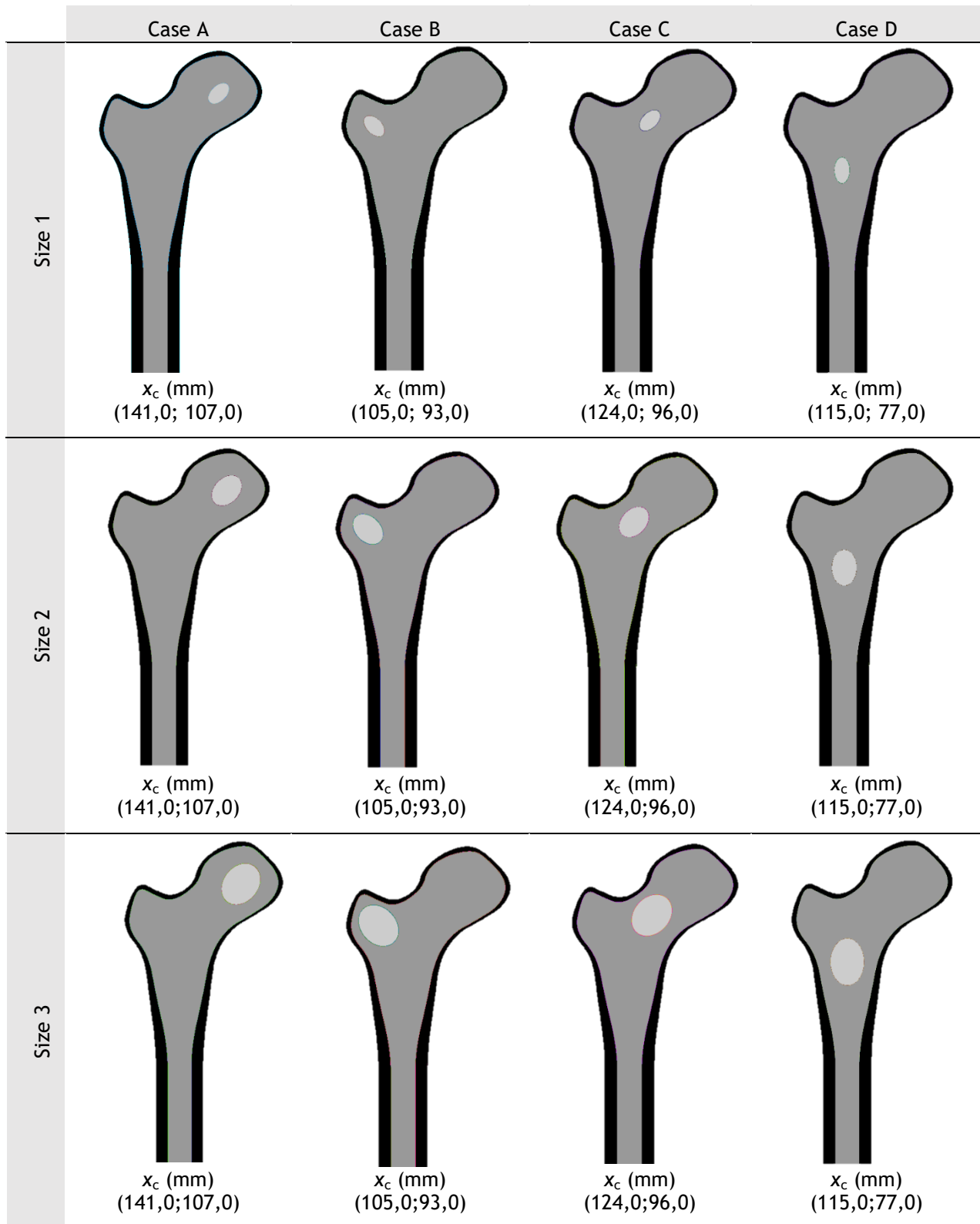


Figure 8.2 - Representation of the 12 two-dimensional models of bone sarcomas in the proximal femur.

Four different clinical cases of bone sarcomas were analyzed. The tumors assumed an elliptical shape and are located in four different areas of the proximal femur, x_c , namely, head, neck, greater trochanter and body. The 12 two-dimensional models are represented in Figure 8.2. In the bone sarcomas of each clinical case, the rays R_1 and R_2 of the ellipse vary, where $R_1=3$ mm and $R_2=5$ mm correspond to size 1; $R_1=5$ mm and $R_2=7$ mm correspond to size 2; and

$R_1=7$ mm and $R_2=9$ mm correspond to size 3. Therefore, the defects with a size 1 occupy an area of approximately 47 mm^2 , the ones with a size 2 occupy an area of 110 mm^2 and the ones with a size 3 have an area of 198 mm^2 . Finally, the domain of the 12 geometric models was discretized into a mesh of 4010 nodes and 7640 triangular elements with an irregular nodal distribution, as represented in Figure 8.3(a) and (b).

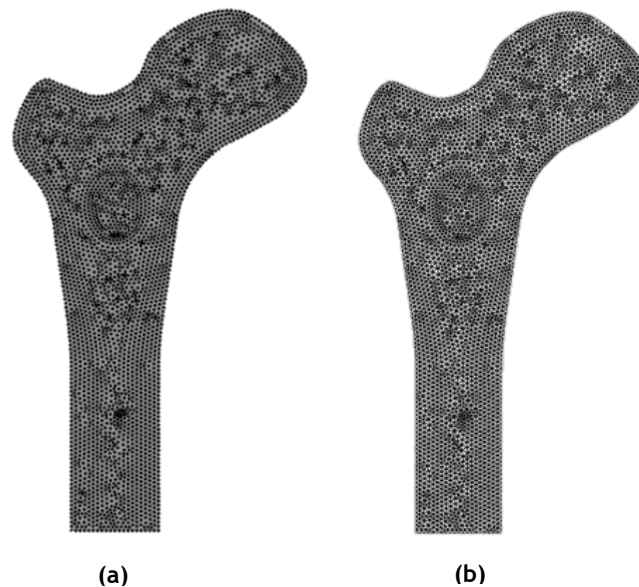


Figure 8.3 - Discretization of the problem domain: (a) nodal mesh; (b) element mesh.

The numerical models are constituted by three different materials: cortical bone tissue, trabecular bone tissue and bone sarcoma, as observed in Figure 8.3(c). The layer of cortical bone presents a maximum thickness of 5 mm. The materials considered have a linear elastic, homogenous and isotropic behavior and its mechanical properties are summarized in Table 8.1.

Table 8.1 - Mechanical Properties of the materials [14, 24].

Materials	Young's Modulus (E) (MPa)	Poisson's coefficient (ν)
Cortical Bone	$1,70 \times 10^4$	0,33
Trabecular Bone	$2,13 \times 10^3$	0,30
Sarcoma	$5,84 \times 10^2$	0,30

In this work, a 2D plane strain deformation theory was considered and only a thin slice of femur bone (with 1 mm thick) was analyzed, in which the forces were applied. For that reason, a representative load case was assumed for a patient weighting 100 kg, based on the first load case proposed by Beaupré *et. al.* [14] and the load case proposed by Kersh *et. al.* [25] and Lutz *et. al.* [16]. The load case proposed by Beaupré *et. al.* [14] consists on one parabolic distributed load over the joint surface and another parabolic distributed load on the trochanter, representing the abductor muscle attachment. On the other hand, the load case proposed by Lutz *et.al* [16] and Kersh *et. al.* [25] includes the same forces described by Beaupré *et. al.* [14] plus the force exerted by the iliopsoas muscle, with an insertion point in the lesser trochanter. Thus, the loads represented in Figure 8.4(c) were later normalized to account for the thickness of the femur model. Therefore, each of the forces were divided by the total thickness of the femur (which is approximately 30 mm [41]), which results in a more accurate representation of the real stress/strain distribution in the bone. An essential boundary condition was also imposed, in which all degrees of freedom were constrain at the base of the model, preventing

its movement. In Figure 8.4(a), (b) and (c) is represented the resultant of each force applied and the corresponding direction, as well as the essential boundary condition.

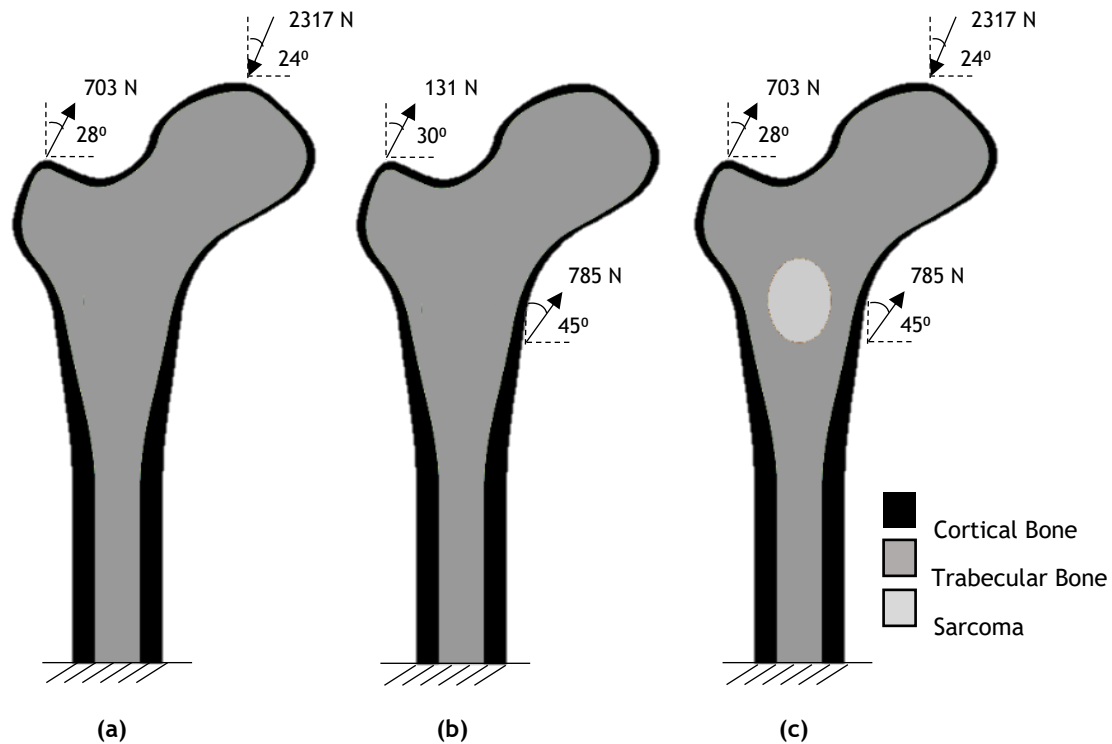


Figure 8.4 - Representation of the natural and essential boundary conditions: (a) load case described by Beaupré *et. al.* [14]; (b) load case described by Lutz *et. al.* [16] and Kersh *et. al.* [25]; (c) loads applied to the femur models with bone sarcomas.

The results obtained from the computational analysis for the 12 two-dimensional models, using three numerical methods, FEM, RPIM and NNRPIM, are presented. In Figure 8.5, Figure 8.6 and Figure 8.7, it is possible to observe the dispersion color maps of the von Mises effective stress (σ_{sef}) for FEM, RPIM and NNRPIM, respectively. In Figure 8.8, Figure 8.9 and Figure 8.10, the dispersion color maps of the principal stress 1 (σ_{11}) for FEM, RPIM and NNRPIM are represented, respectively. Finally, in Figure 8.11, Figure 8.12 and Figure 8.13, it is presented the color maps of the principal stress 2 (σ_{22}) for FEM, RPIM and NNRPIM, respectively.

Through a qualitative analysis, it is possible to observe that, for all clinical cases, the highest stress concentrations are present in the cortical bone on the upper right side of the femoral diaphysis and upper femoral head. In case A for size 3, the stress levels is higher on the upper side of the femoral head. However, contrarily to what was expected, the von Mises effective stress presents a tendency to increase with the increase in size of the bone sarcoma, regardless of the numerical method used. According to Keyak *et. al.*, a simulated spherical lytic lesion in the proximal femur with a diameter smaller than 20 mm will only cause minimal reductions in femoral strength [18]. Therefore, considering that all bone sarcomas simulated in this work have a diameter smaller than 20 mm, it could explain the tendency of the effective stress to increase as the tumor grows in size.

Nevertheless, it can be noticed that case C, located in the neck of the femur, is the most critical due to higher levels of stress, indicating that this case could lead to the fracture of the femoral neck. These results are in agreement with other studies [18, 73], where lesions located in the femoral neck, particularly inferomedial defects, compromised the bone mechanical properties, which may result in transcervical neck fractures of the proximal femur.

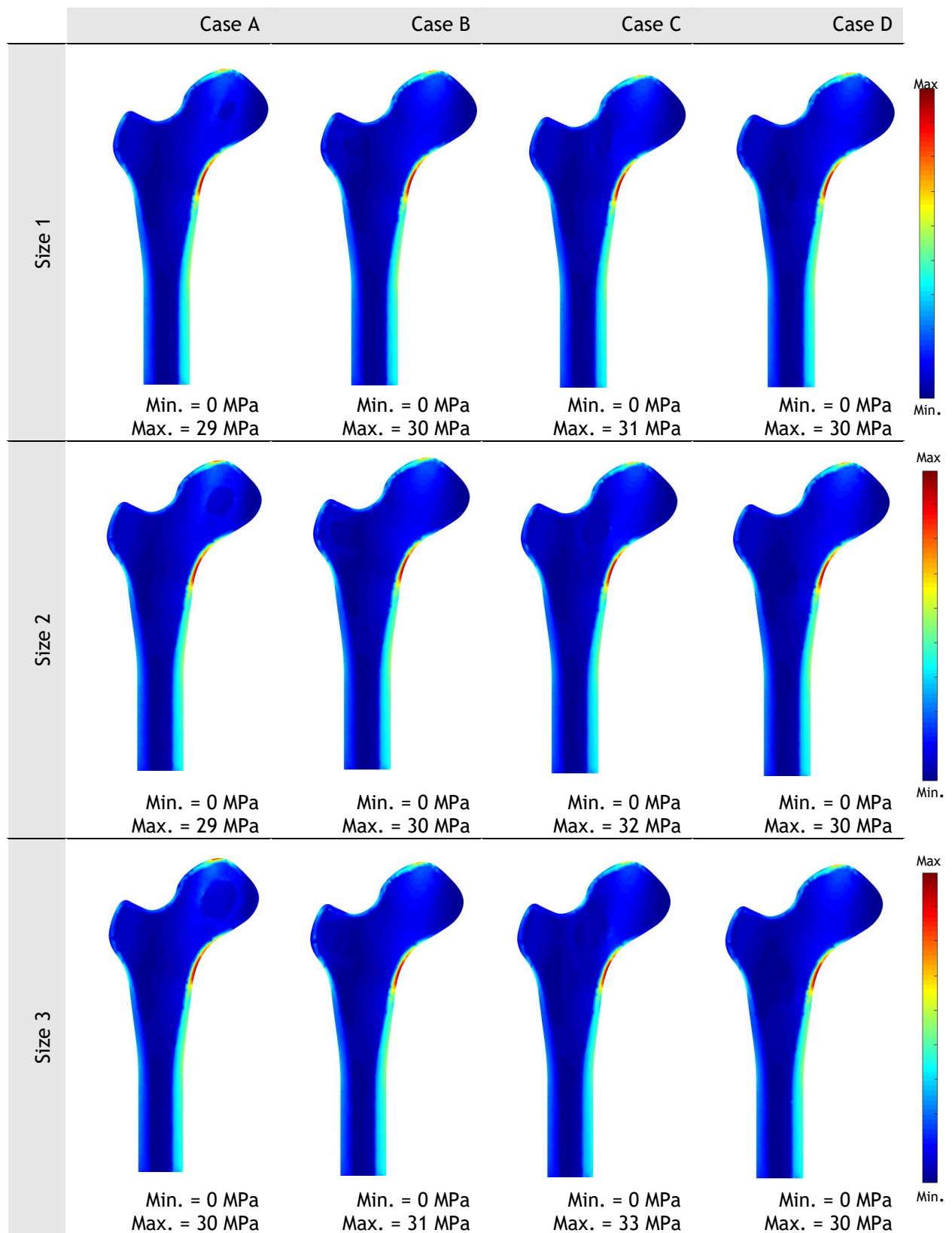


Figure 8.5 - Color maps of the von Mises effective stress (σ_{sef}) of the 12 two-dimensional models, using FEM.

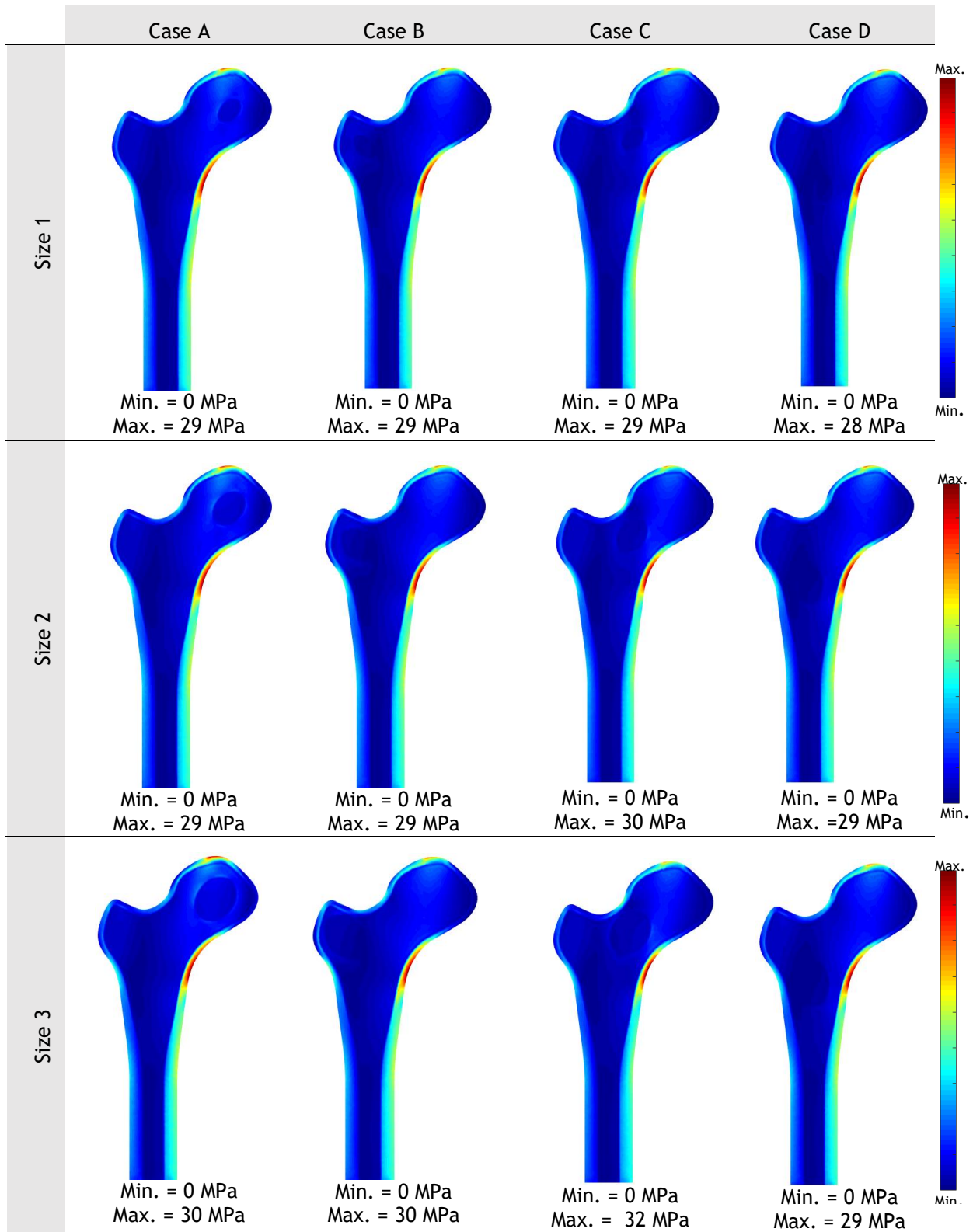


Figure 8.6 - Color maps of the von Mises effective stress (σ_{set}) of the 12 two-dimensional models, using RPIM.

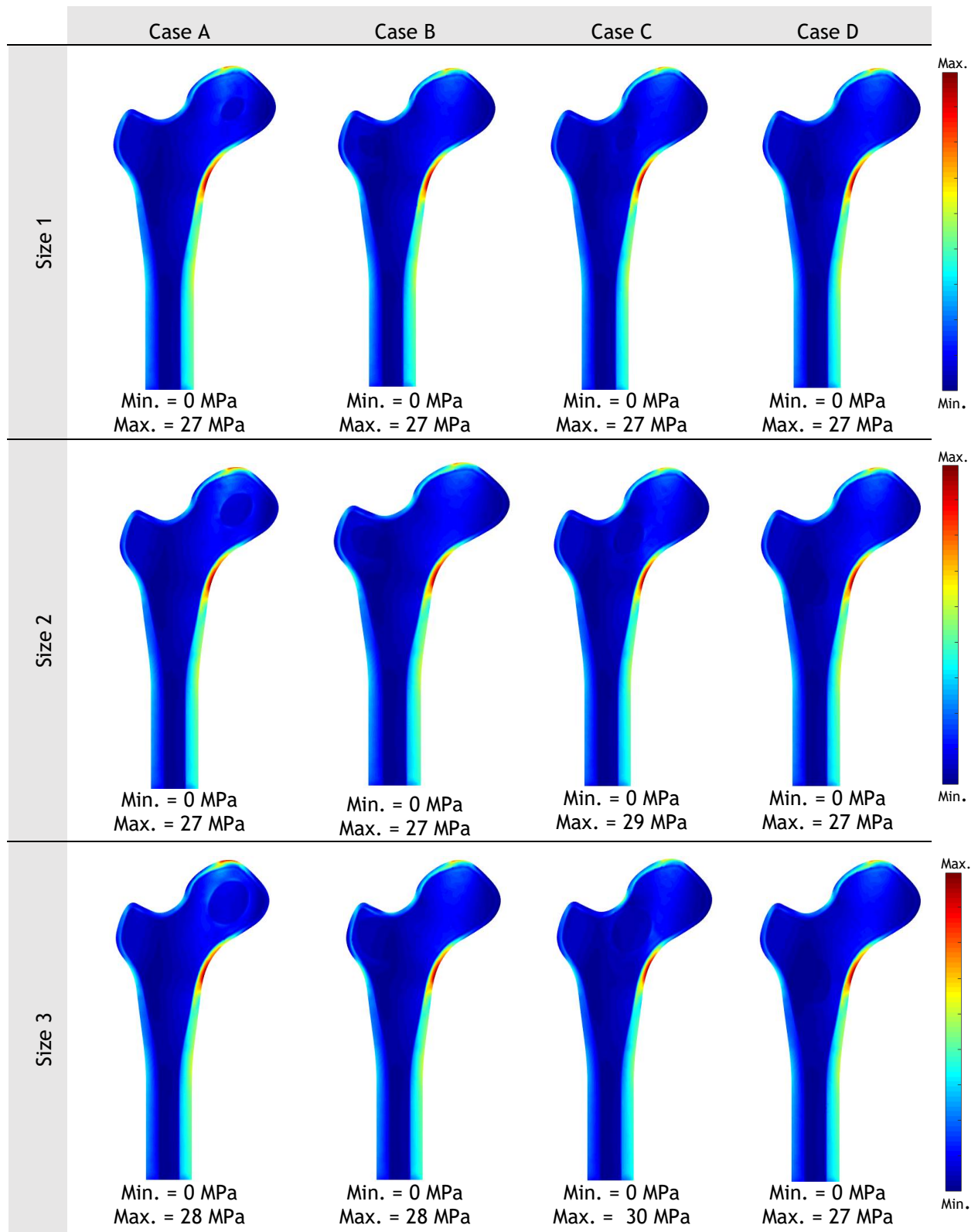


Figure 8.7 - Color maps of the von Mises effective stress (σ_{sef}) of the 12 two-dimensional models, using NNRPIM.

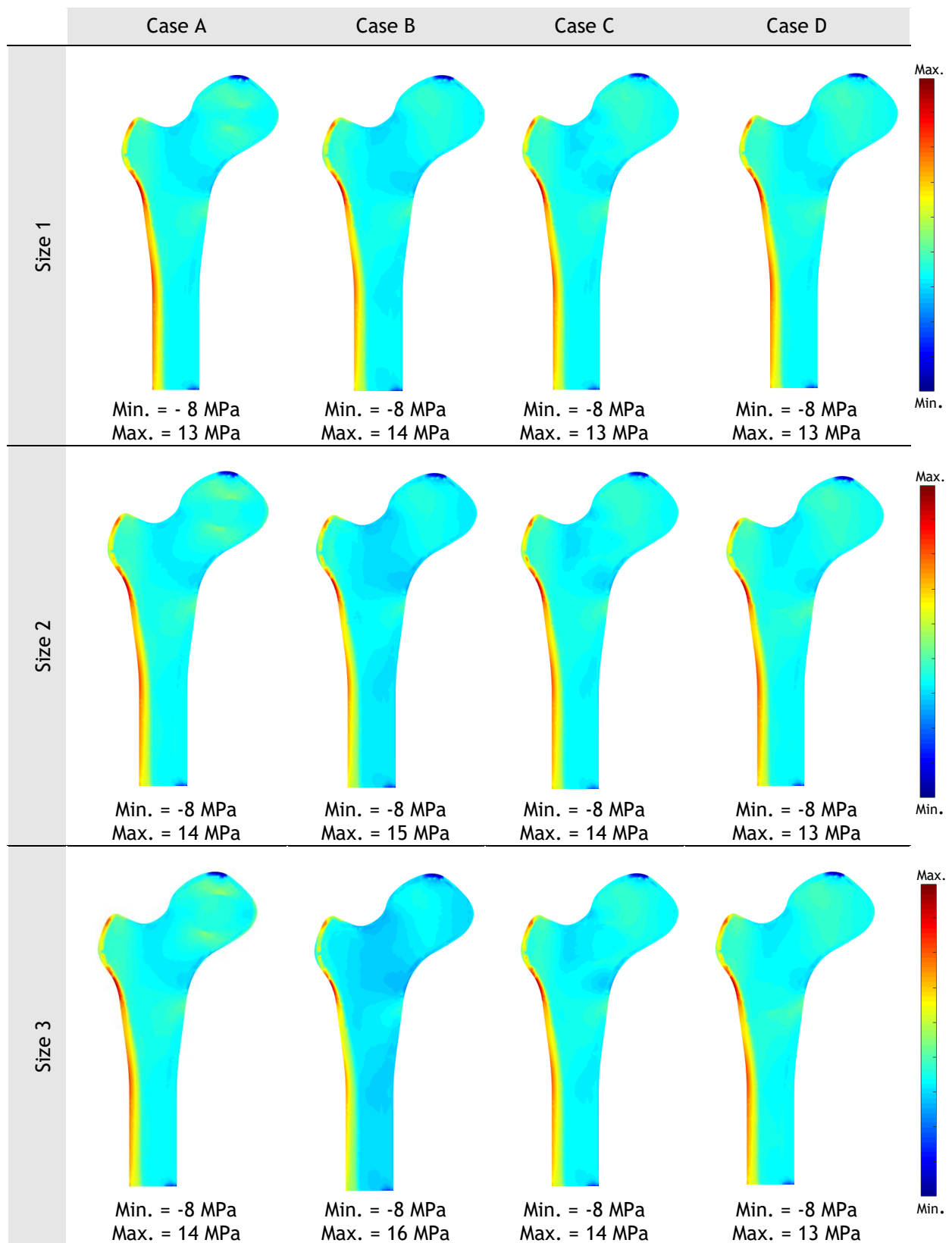


Figure 8.8 - Color maps of the principal stress 1 (σ_{11}) of the 12 two-dimensional models, using FEM.

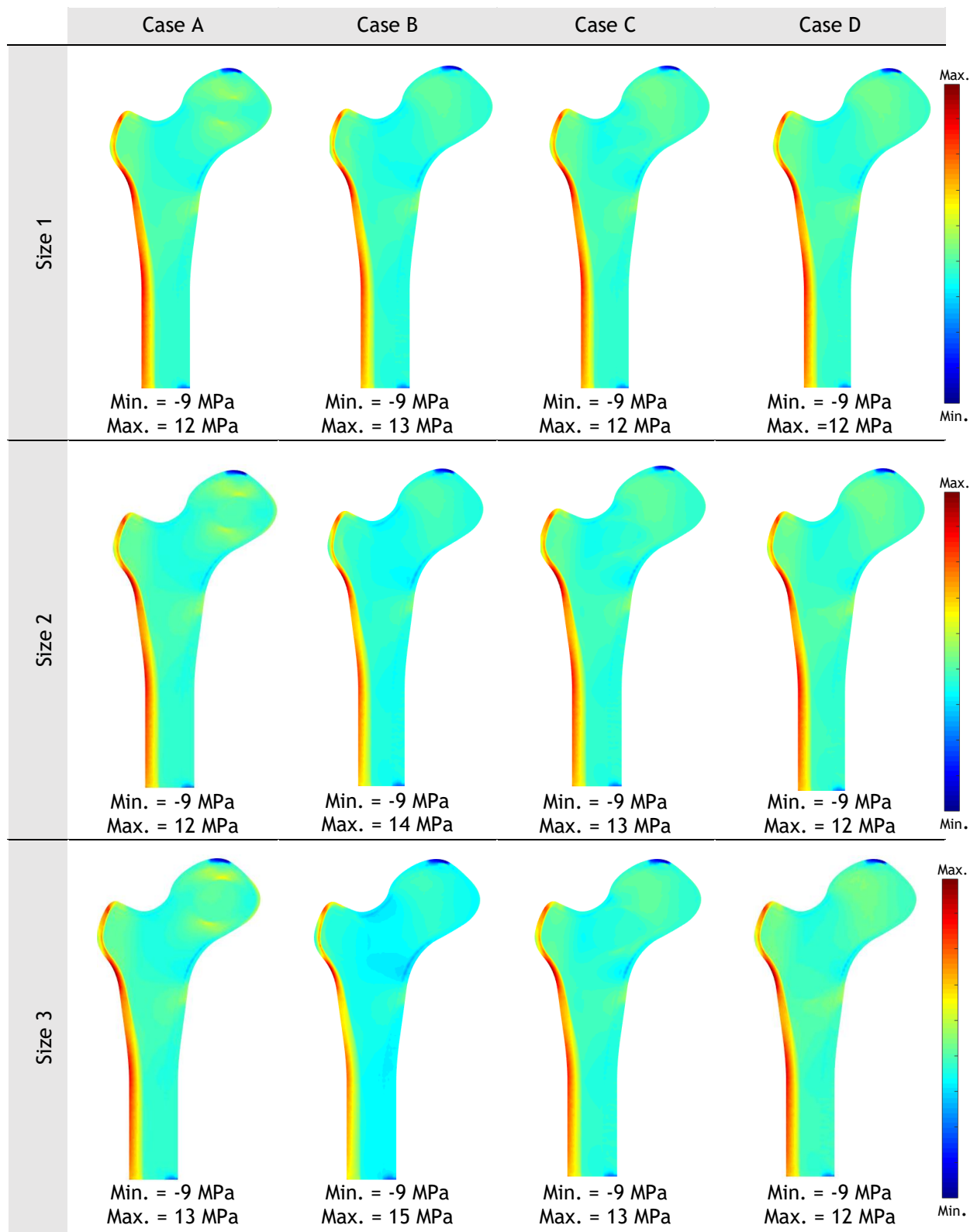


Figure 8.9 - Color maps of the principal stress 1 (σ_{11}) of the 12 two-dimensional models, using RPIM.

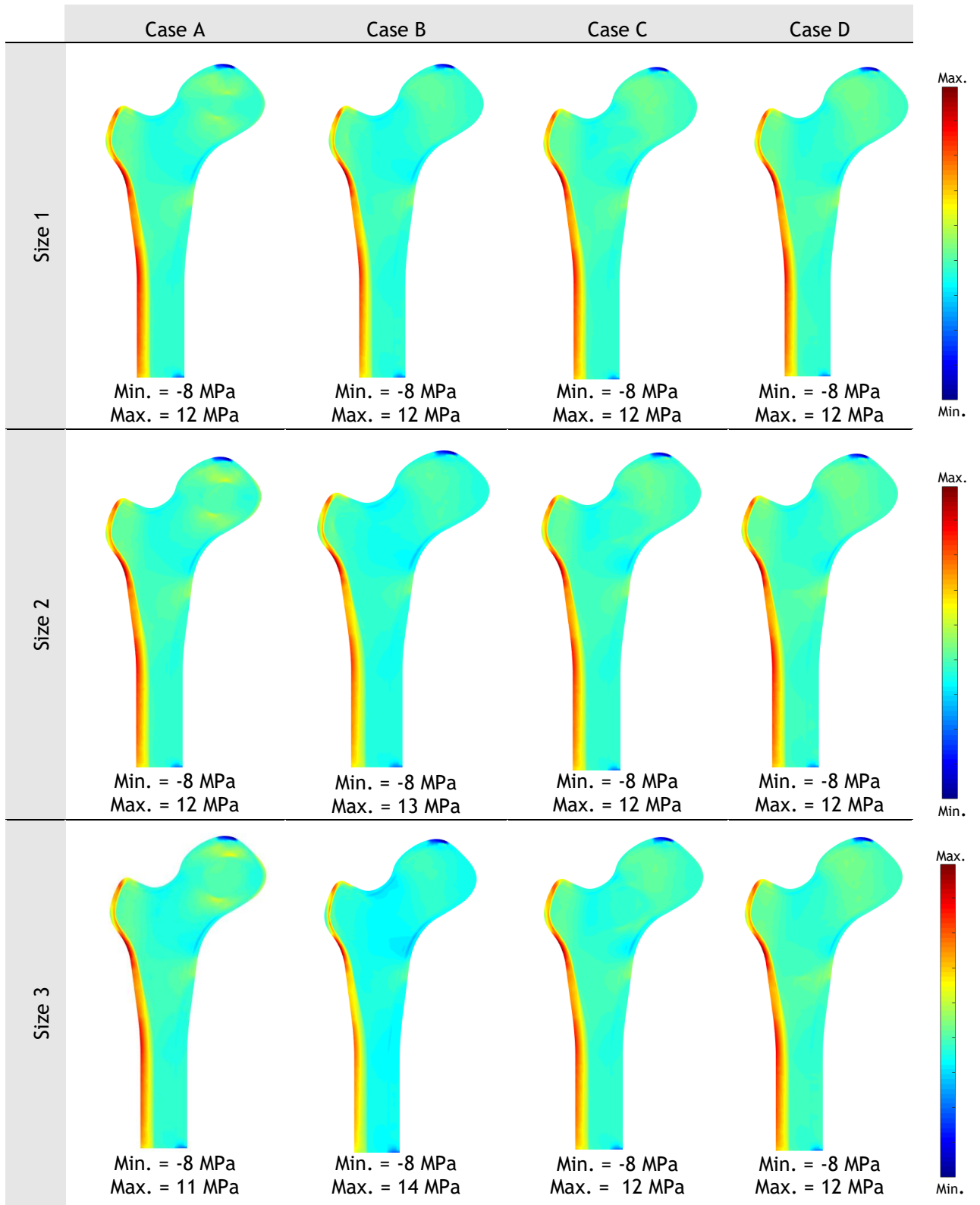


Figure 8.10 - Color maps of the principal stress 1 (σ_{11}) of the 12 two-dimensional models, using NNRPIM.

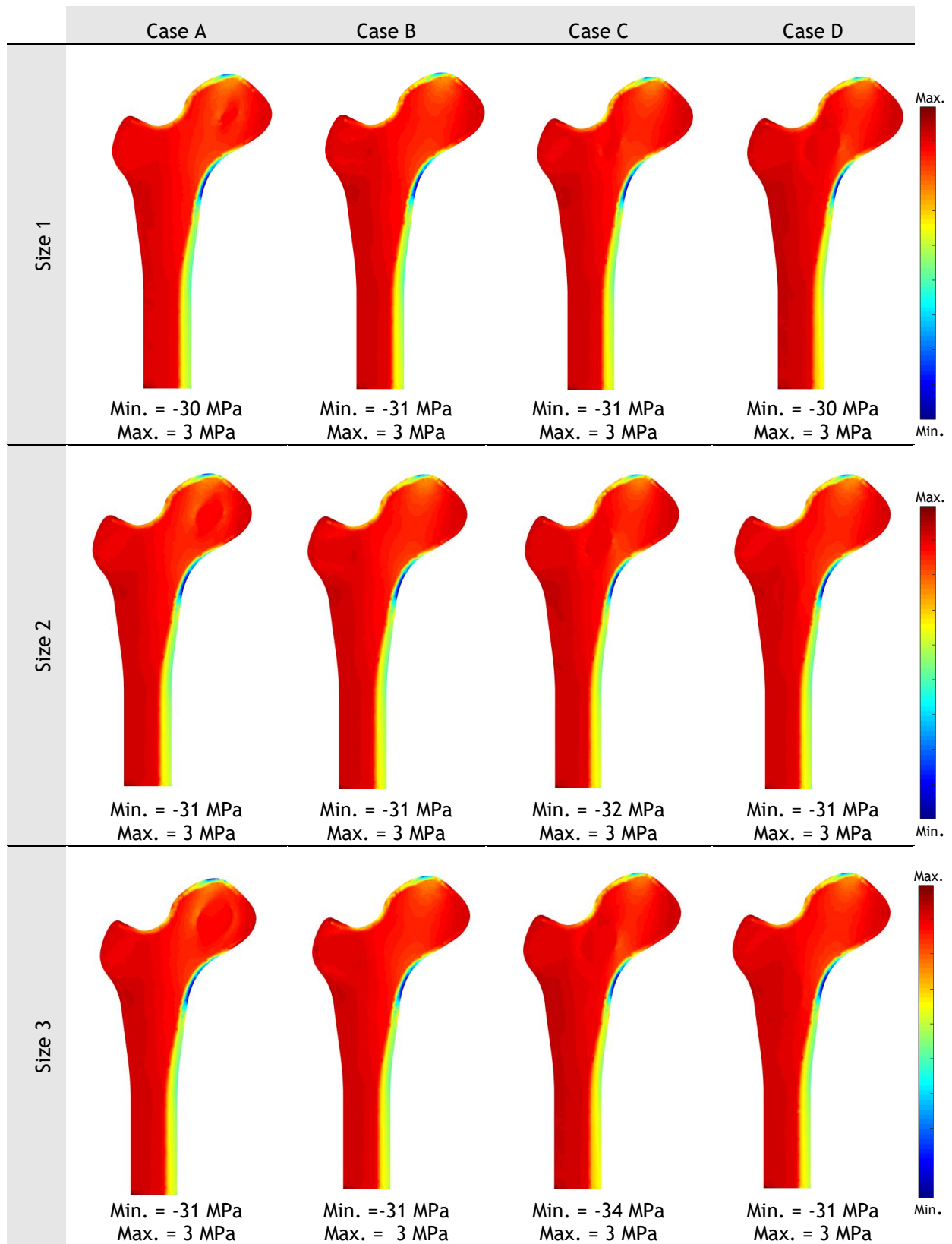


Figure 8.11 - Color maps of the principal stress 2 (σ_{22}) of the 12 two-dimensional models, using FEM.

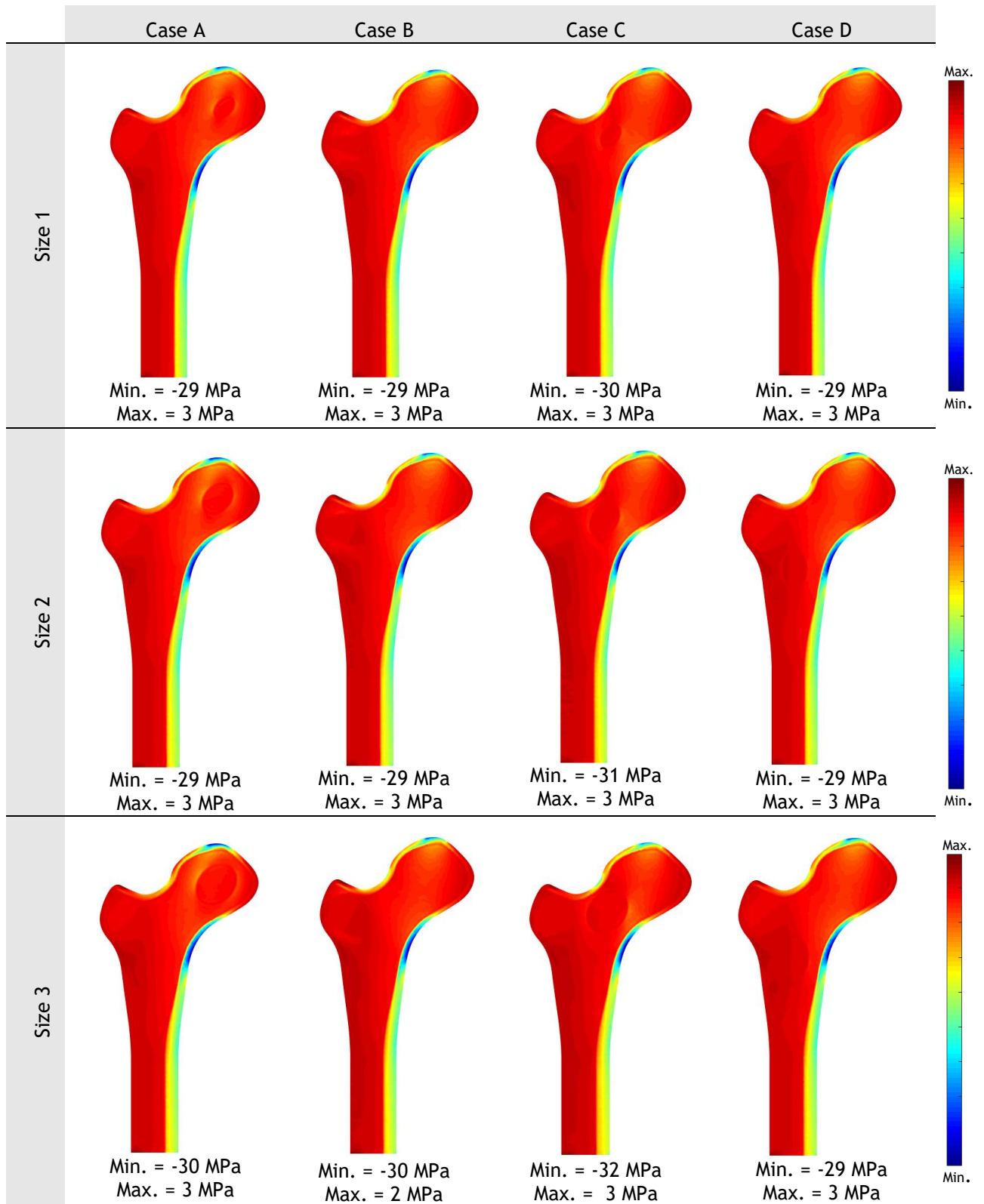


Figure 8.12 - Color maps of the principal stress 2 (σ_{22}) of the 12 two-dimensional models, using RPIM.

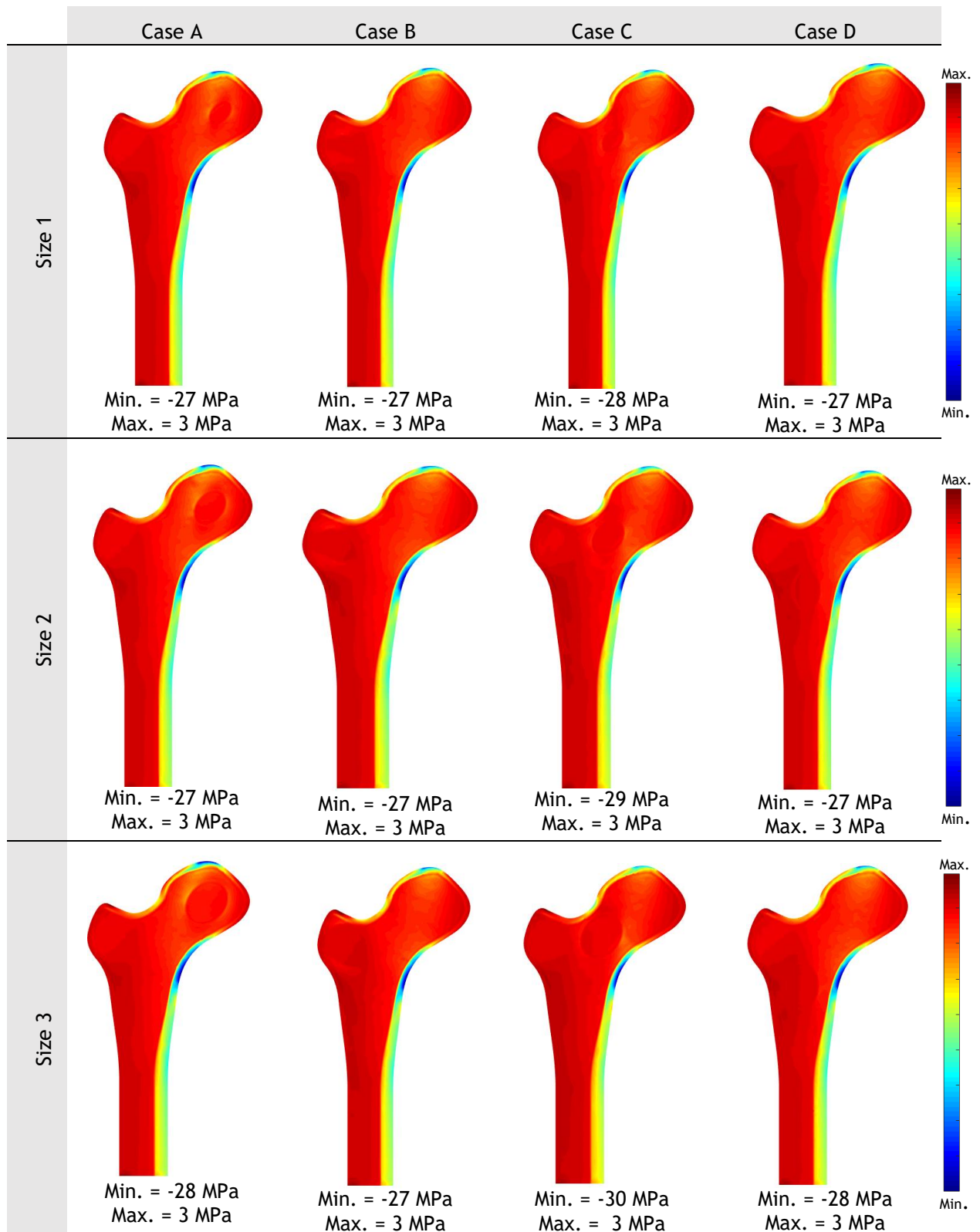


Figure 8.13 - Color maps of the principal stress 2 (σ_{22}) of the 12 two-dimensional models, using NNRPIM.

Regarding the dispersion color maps of principal stress 1 and 2, it is possible to observe which type of stress (traction and compression) are present in the different areas of the proximal femur in each clinical case. In the cortical bone present on the left side of the femoral shaft, the highest tensile stresses can be found, as well as in the cortical bone present in the left side of the greater trochanter. These regions of traction are mainly due to the tensile force applied to the greater trochanter, which translates the force exerted by the abductor muscles at the stage when the foot touches the ground during the cycle of the human gait. With regard to compressive stresses, these are present in the cortical bone on the right side of the femoral diaphysis and in the superior region of the femoral head. This is mainly due to the compressive force exerted on the femoral head caused by the hip joint.

The tensile stresses (positive stresses) are similar in all clinical cases, regarding the size of the bone sarcoma. Except for case B, where the bone sarcoma is located in the greater trochanter, which demonstrates an increasing trend of tensile stresses with the increase of the size of the bone sarcoma. As with tensile stresses, the compressive stresses (negative stresses) are similar in all the clinical cases. The clinical case C, with the sarcoma located on the femoral neck, is the case where the highest compressive stresses are observed, as would be expected considering the von Mises effective stresses, previously observed.

In all models, it is also possible to observe tensile and compressive zones in the bone tissue surrounding the sarcomas. Ergo, in order to understand the influence of the location of the bone sarcoma in the adjacent bone tissue, a set of nodes around the tumor was selected. In Figure 8.14 is possible to observe a generic representation of the selected nodes. In Figure 8.15, Figure 8.16 and Figure 8.17 are graphically presented the results obtained from the von Mises effective stress, using FEM, RPIM and NNRPIM, for each of the four areas of interest mentioned above. These results demonstrate the stress level along the curved line represented in Figure 8.14, starting in point P1 and following the anti-clock direction, P2, P3, P4 and finishing in P1. In order to allow a better comparison between the analysis, the length of the curve was normalized between 0 and 1, with the expression $\bar{x} = x/L$, being \bar{x} the normalized position on the curve, x the real position on the curve and L the length of the curve. All the graphs similar with Figure 8.15, Figure 8.16 and Figure 8.17 from this point forward, respect this normalization scheme.

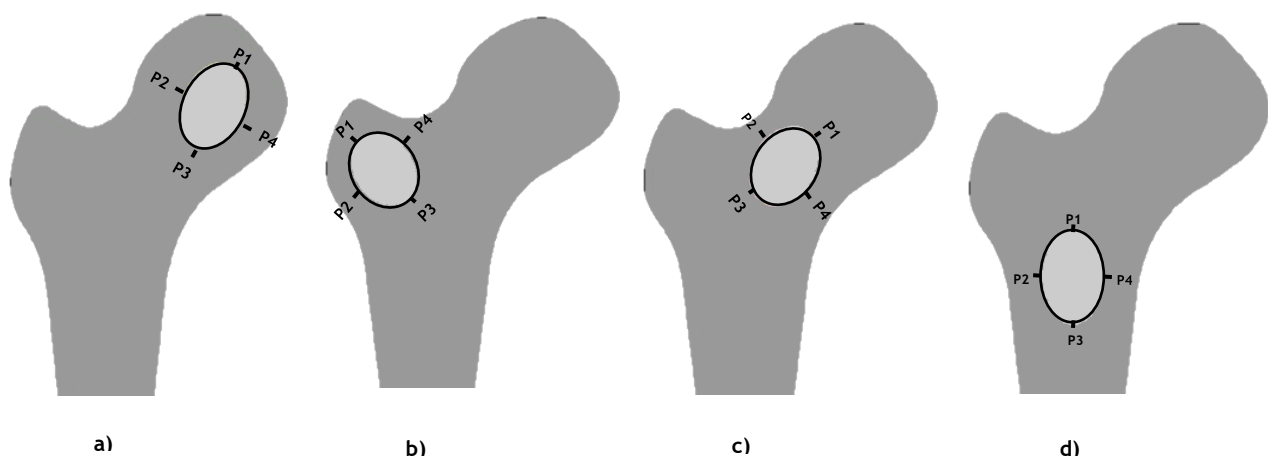


Figure 8.14 - Generic representation of the selected nodes (black line) for all clinical cases: (a) Case A; (B) case B; (c) Case C and (d) Case D.

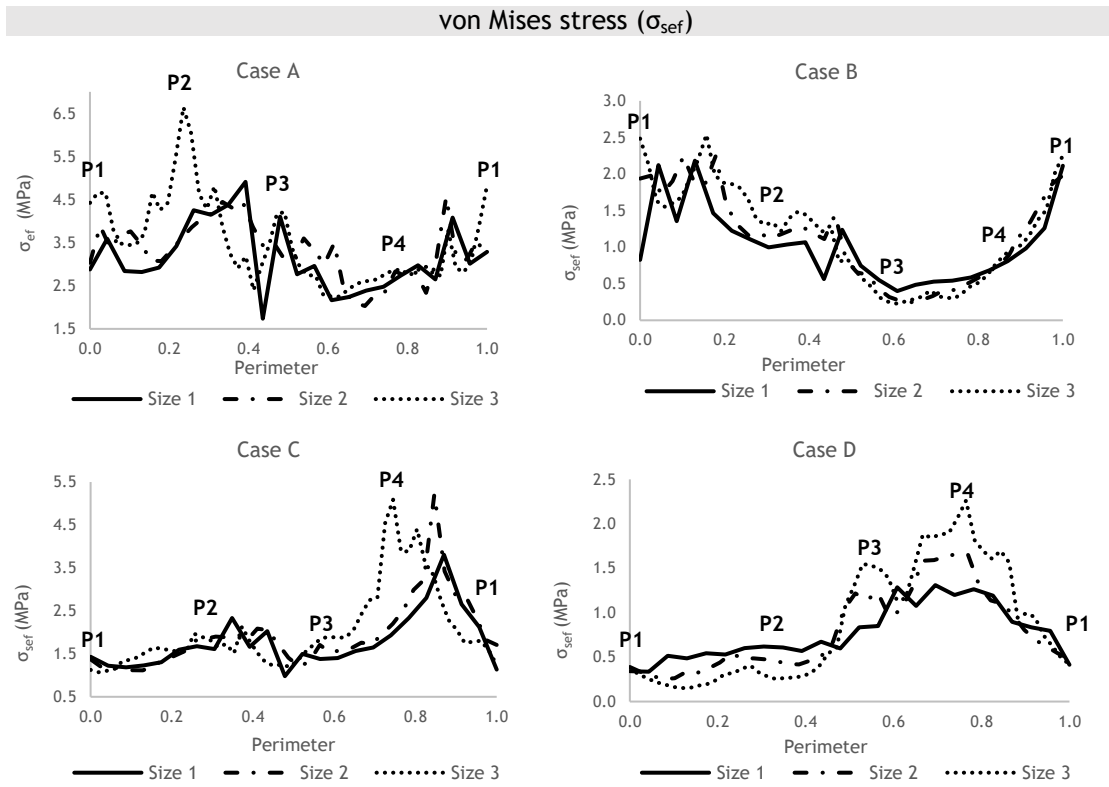


Figure 8.15 - Graphical representation of the von Mises stress distribution obtained through FEM for the cases of bone sarcomas studied in the four areas of interest.

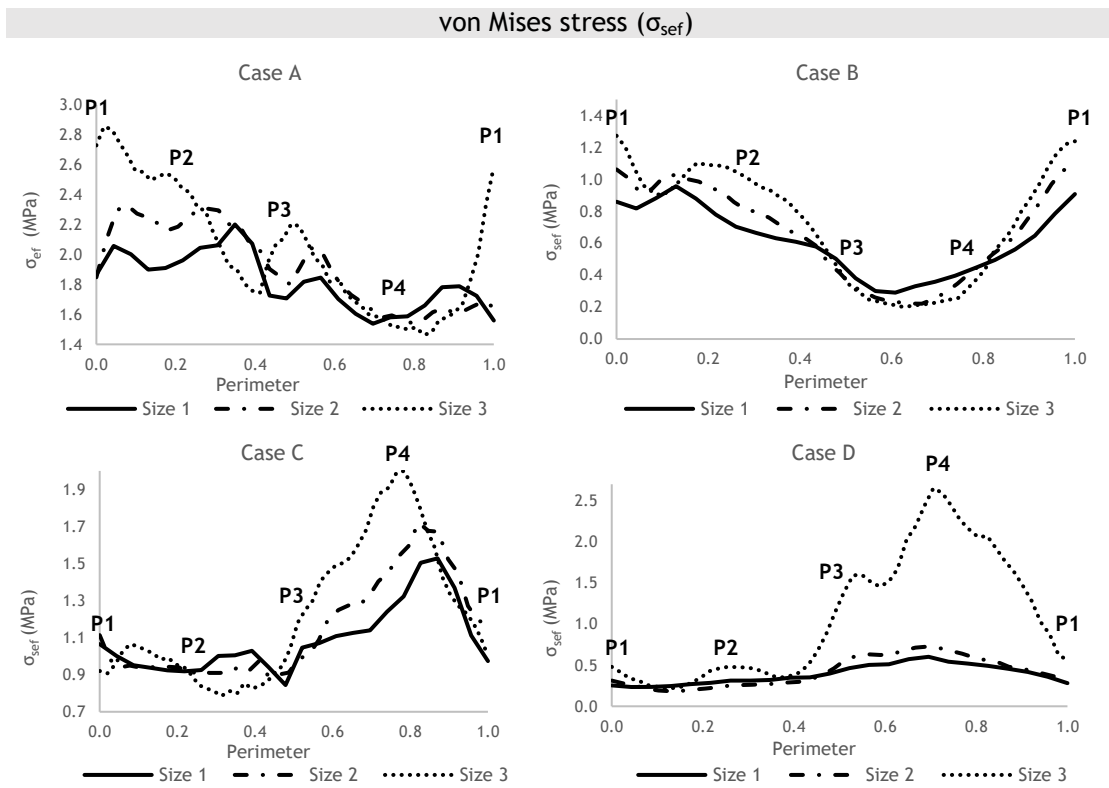


Figure 8.16 - Graphical representation of the von Mises stress distribution obtained through RPIM for the cases of bone sarcomas studied in the four areas of interest.

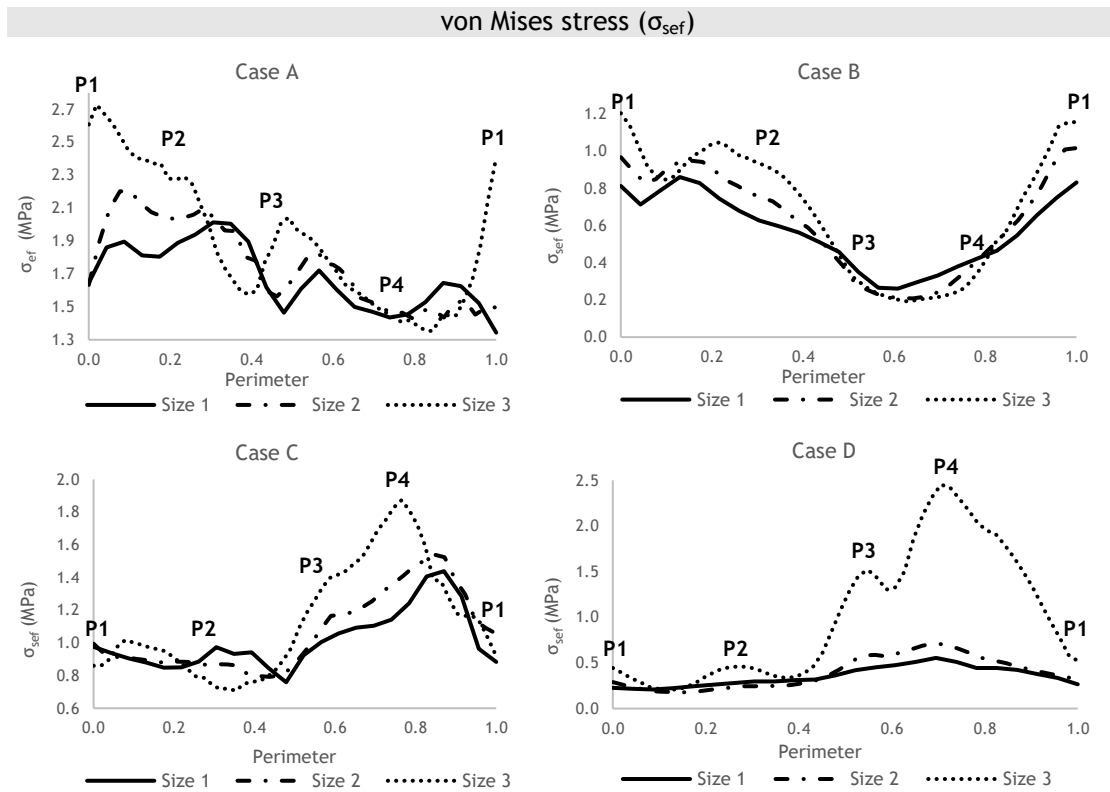


Figure 8.17 - Graphical representation of the von Mises stress distribution obtained through NNRPIM for the cases of bone sarcomas studied in the four areas of interest.

The quantitative analysis of the von Mises effective stress demonstrates a similar graphical distribution in all sizes of sarcomas, 1, 2 and 3, with RPIM and NNRPIM. However, the graphics obtained through FEM present higher values of stress than the ones obtained with meshless methods. Nevertheless, a tendency to an increase of stress with the increase of size of the bone sarcoma can be observed in all clinical cases. For that reason, the effect of the tumor size in adjacent bone tissue will be further discussed later in this subsection.

Moreover, case A demonstrates the highest levels of effective stress, which vary between 2,7 (NNRPIM) to 6,5 MPa (FEM). The area of bone tissue most affected is in P1, located in the upper side of the femoral head, except in the case using FEM, which demonstrates higher stresses near P2. Nonetheless, an agreement can be observed between these results and the previous dispersion color maps. Contrarily to case A, the lowest levels of stress are observed in case B, particularly between P3 and P4. In this case, the bone tissue in the left side of the greater trochanter (P1) is the most affected area. Finally, in case C and D, the effective stress increases between P3 to P4, with P4 demonstrating higher values of stress that vary between 2,5 MPa (RPIM and NNRPIM) to 5,5 MPa (FEM). In both cases, the inferomedial neck and upper right side of the diaphysis present high levels of stress, which is in agreement with the dispersion color maps observed previously.

The graphics regarding the principal stress 1 and 2, using FEM, RPIM and NNRPIM, for each clinical case are represented in Figure 8.18, Figure 8.19 and Figure 8.20, respectively. Overall, meshless methods assume the same graphical distribution, contrarily to FEM, as previously observed. The areas with higher tensile stresses occur in P1 (case A) and P3 (case D), indicating that these are regions of traction. Also, regarding compressive stresses, P4 is a region of compression in case D, while P1 also presents high levels of compressive stresses in case A. In case C, the tensile stresses are low, contrarily to compressive stresses which are higher in P4

(region of compression). Finally, case B presents the lowest levels of tensile and compressive stresses, as previously observed.

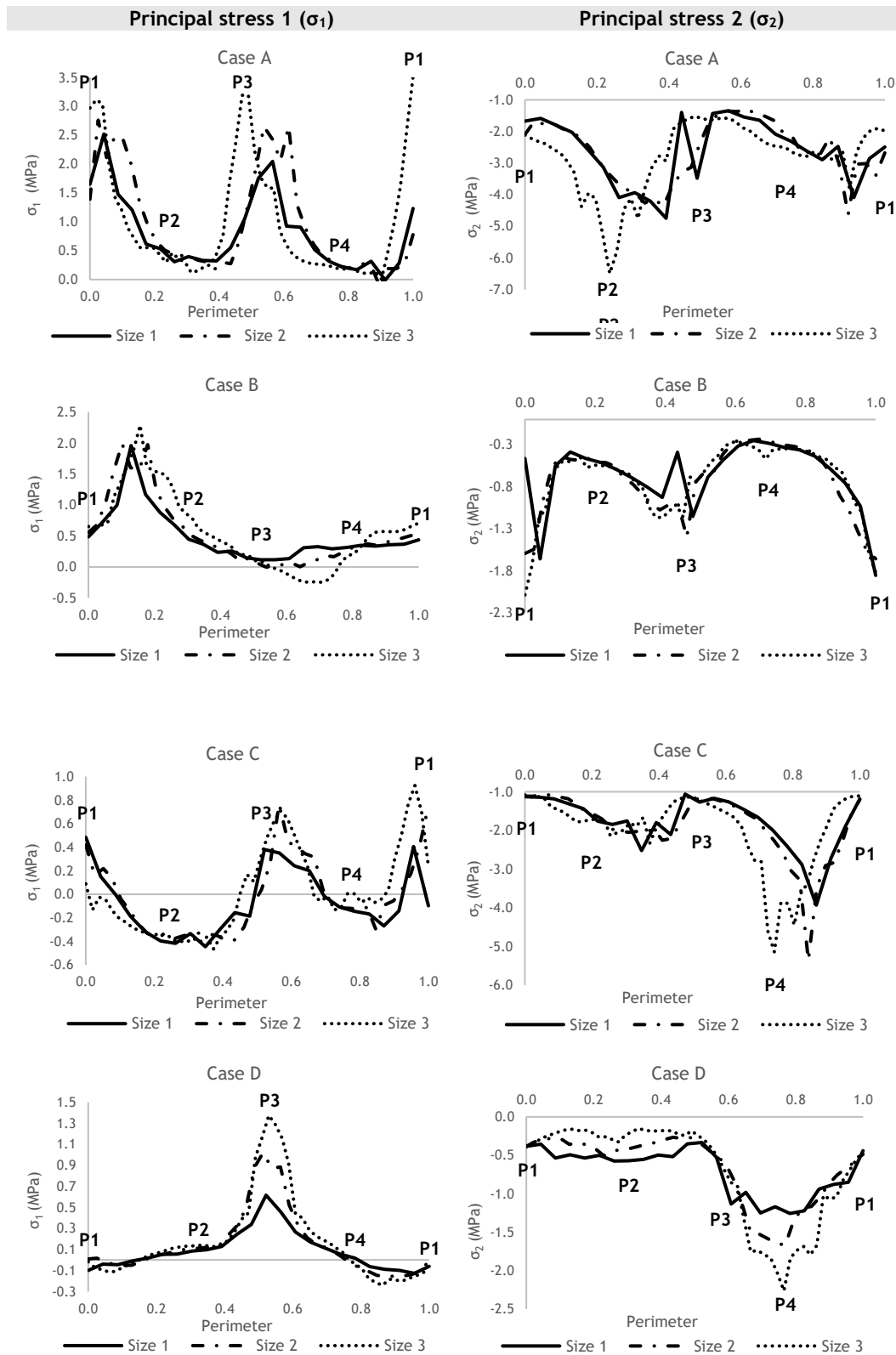


Figure 8.18 - Graphical representation of the principal stress 1 and 2 obtained through FEM for the cases of bone sarcomas studied in the four areas of interest.

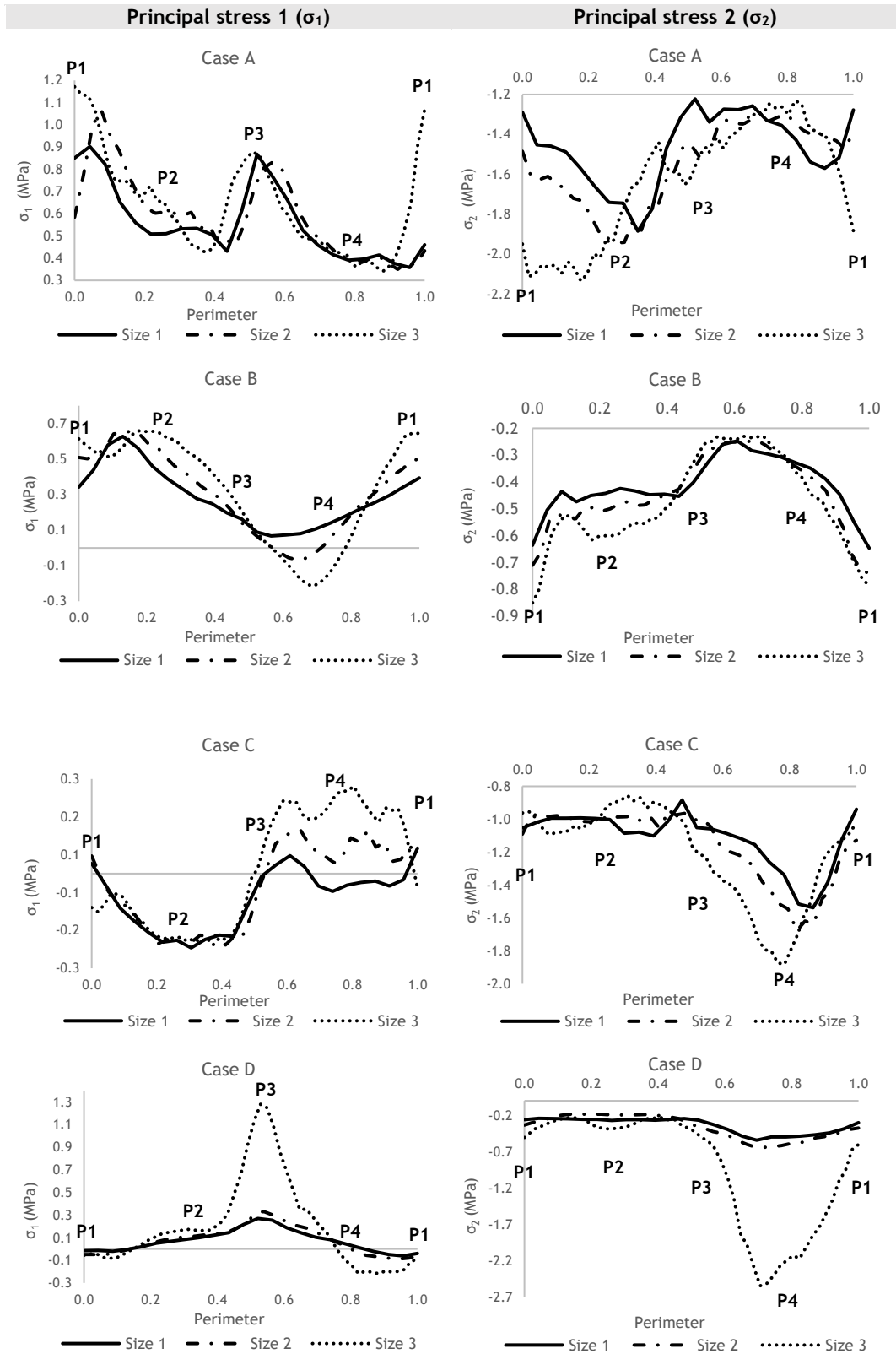


Figure 8.19 - Graphical representation of the principal stress 1 and 2 obtained through RPIM for the cases of bone sarcomas studied in the four areas of interest.

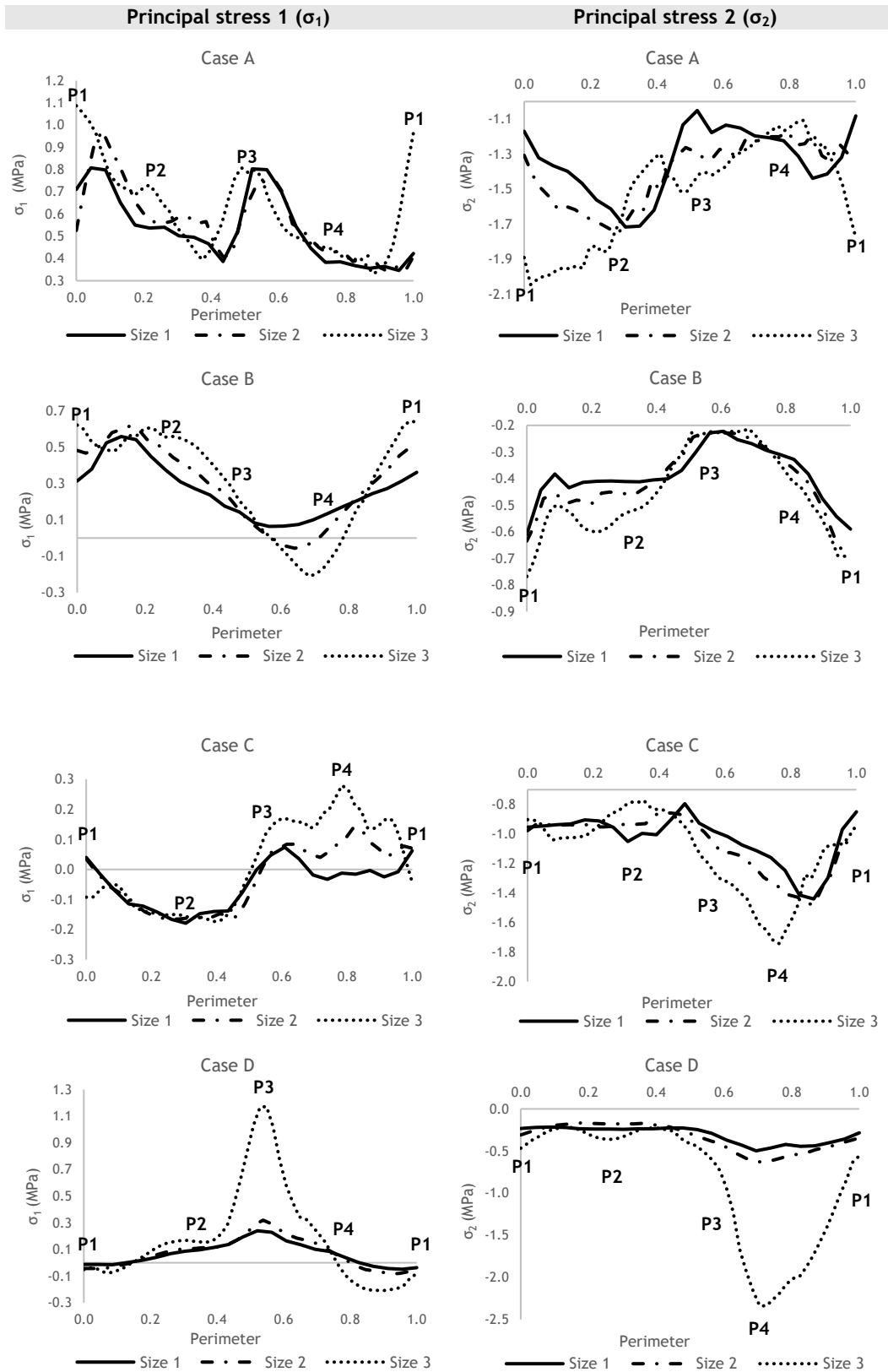


Figure 8.20 - Graphical representation of the principal stress 1 and 2 obtained through NNRPIM for the cases of bone sarcomas studied in the four areas of interest.

Lastly, to better understand the effect of the sarcoma size in the adjacent bone tissue, the maximum values of the von Mises effective stress and principal stress 1, as well as the minimum values of the principal stress 2, obtained from the previous graphics, were represented in Figure 8.21, Figure 8.22 and Figure 8.23, respectively.

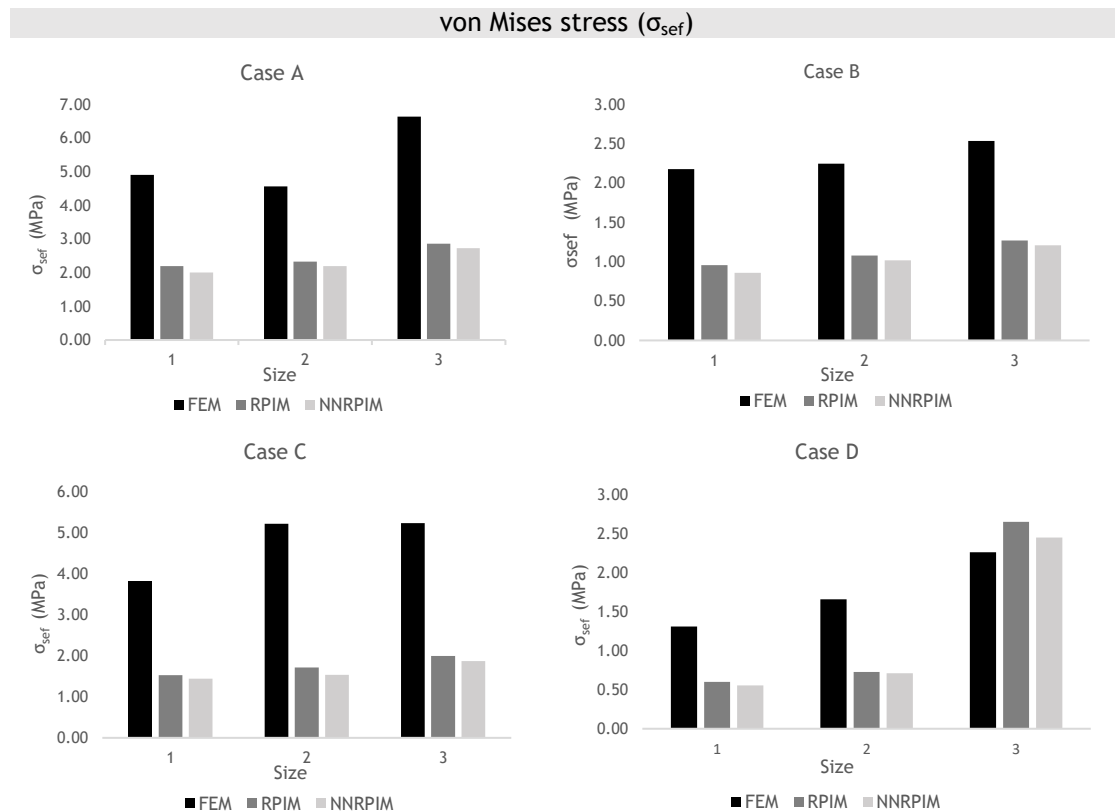


Figure 8.21 - Graphical representation of the maximum von Mises effective stress obtained through FEM, RPIM and NNRPIM for all clinical cases of bone sarcomas.

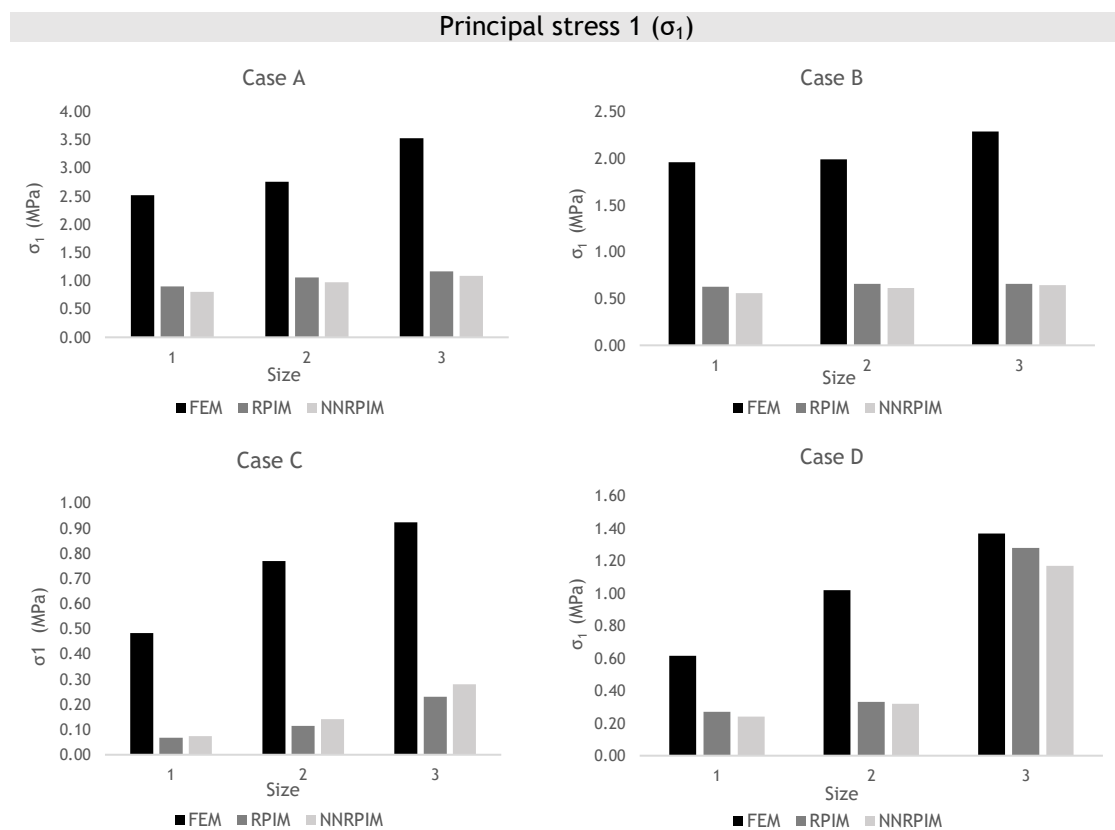


Figure 8.22 - Graphical representation of the maximum principal stress 1 obtained through FEM, RPIM and NNRPIM for all clinical cases of bone sarcomas.

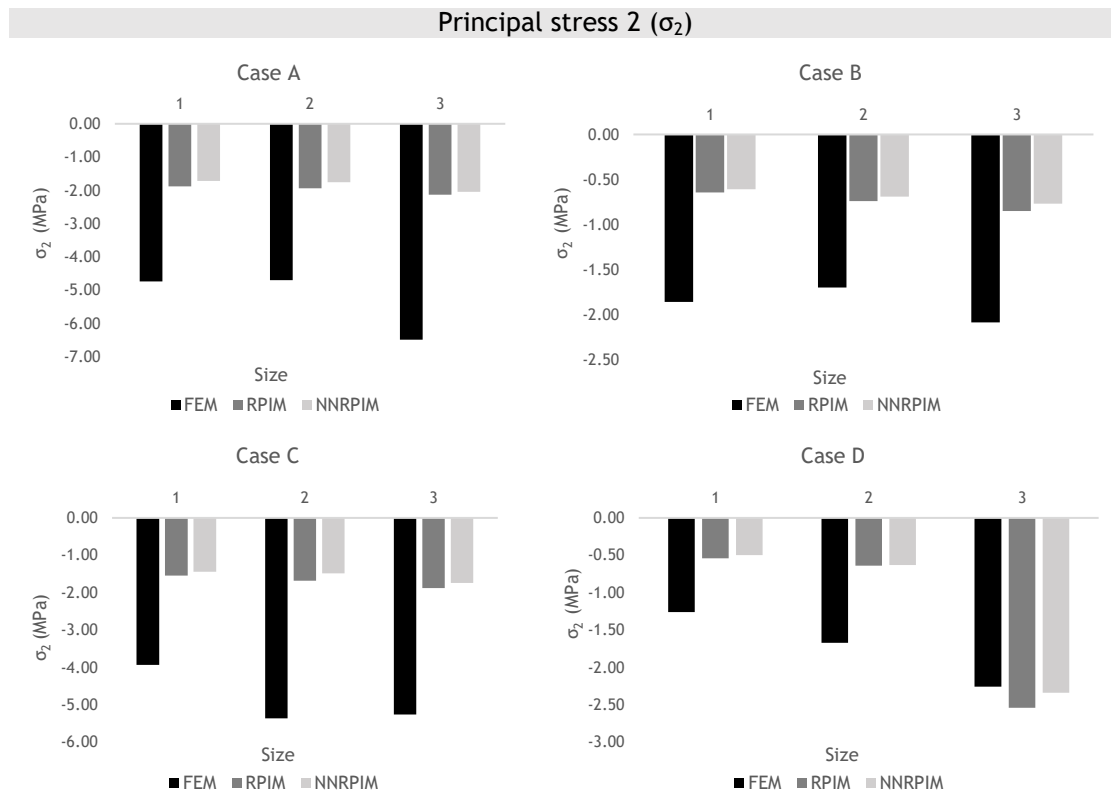


Figure 8.23 - Graphical representation of the maximum principal stress 2 obtained through FEM, RPIM and NNRPIM for all clinical cases of bone sarcomas.

A difference can be observed in the stress, as the tumor grows, on the results obtained with FEM. For meshless methods, the difference is higher for case D.

Therefore, the location of the maximum effective stresses, principal stress 1 and 2 for each clinical case, considering the three different methods used, are represented in Figure 8.24, Figure 8.26 and Figure 8.25, respectively.

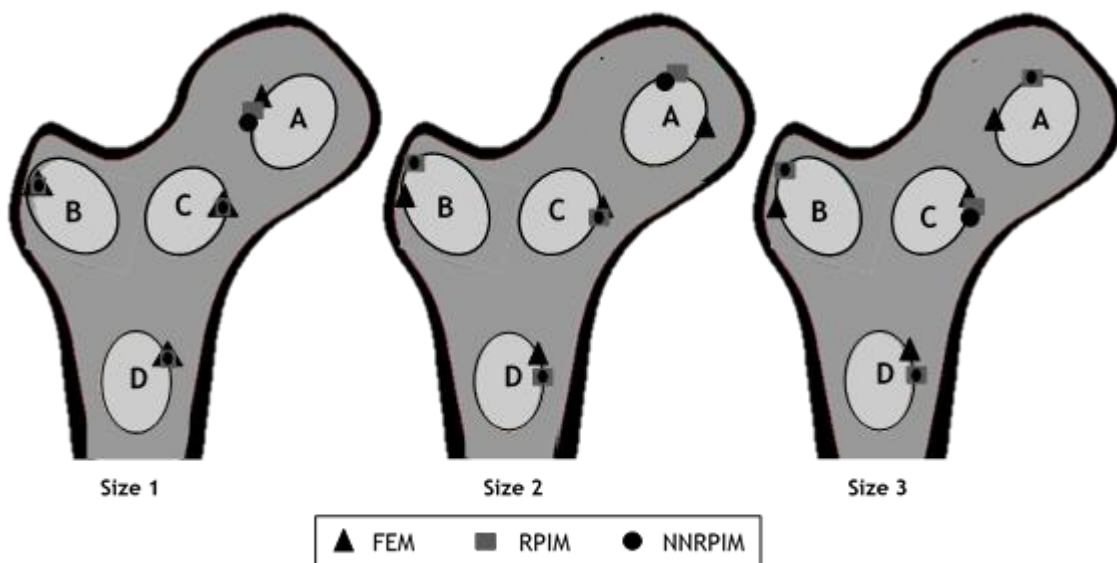


Figure 8.24 - Generic representation of the location of maximum values of the von Mises effective stress obtained through FEM, RPIM and NNRPIM, for size 1, 2 and 3 of all clinical cases analyzed.

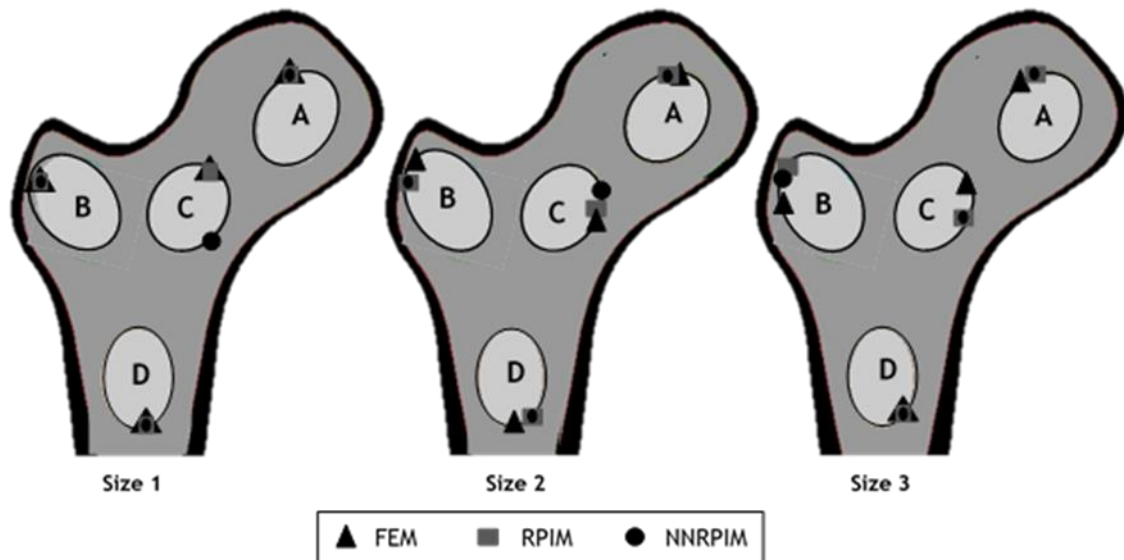


Figure 8.26 - Generic representation of the location of maximum values of the principal stress 1 obtained through FEM, RPIM and NNRPIM, for size 1, 2 and 3 of all clinical cases analyzed.

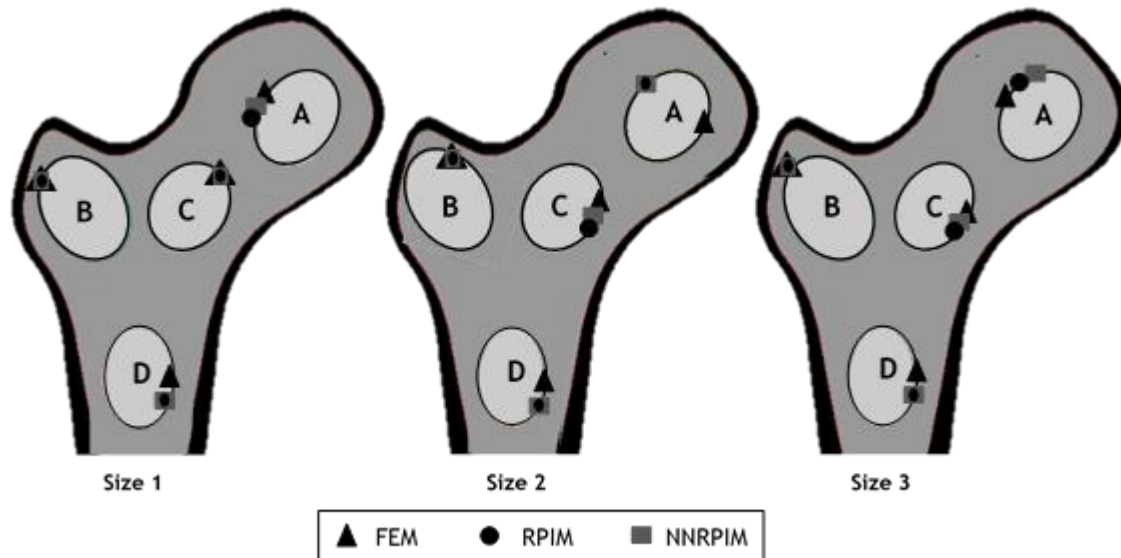


Figure 8.25 - Generic representation of the location of maximum values of the principal stress 2 obtained through FEM, RPIM and NNRPIM, for size 1, 2 and 3 of all clinical cases analyzed.

Overall, a similarity between all numerical methods can be perceived. Additionally, in case A, the upper side of the femoral head, particularly in the left side of the tumor, occurs the highest effective stresses and both compressive and tensile stresses. In case B, the upper left side of the trochanter is the area most affected and presents both regions of compression and traction. In case C, the inferomedial side of neck is the area most affected by the stresses created by the tumor in the femoral neck. Finally, in case D, the region of compression occurs on the right side of the shaft for all sizes of the sarcomas, while the region of traction is verified in the middle area of the femoral shaft. All these results are in agreement with the ones previously observed.

In conclusion, there is a increasing trend of stresses with the growth of the tumor. However, an increase can be seen locally in the bone tissue adjacent to the sarcomas, particularly in the inferomedial side of the neck and upper right side of the shaft. Therefore, micro-damages will start to form in these areas, as a result of the tumors, and continue to propagate throughout the bone, increasing its fragility and possibly creating fractures. Considering the overall effect

caused by the sarcomas demonstrated in the dispersion color maps, it is possible to speculate that the microdamages will most likely lead to the fracture of the femoral neck, as indicated in the literature [18, 73, 123].

Lastly, a qualitative comparison between the solutions obtained using FEM and meshless methods can be done, which denotes a relative similarity between the results obtained, particularly in the graphical distributions and dispersion color maps. However, the stress values are higher using FEM than RPIM and NNNRPIM. The inequalities between the different numerical methods can be justified by differences in the formulations, particularly in the creation of the nodal mesh. As previously demonstrated in subsection 4.2, in meshless methods, the nodes are randomly distributed, since shape functions are approximated by influence-domains rather than elements (FEM), which results in more homogeneous solutions than the ones obtained with FEM. Also, the use of tetrahedral elements in FEM creates low quality meshes, negatively impacting the final solutions. These results validate the information obtained in literature [5].

8.2 - Numerical Analysis of Three-dimensional Femur Models with Bone Sarcomas

The numerical analysis conducted previously only considered a simplified 2D analysis assuming plain strain assumptions. Consequently, to better understand the effect of bone sarcomas in the overall volume of the femur, it is required to analyze a three-dimensional model of a femur with bone sarcomas. Thus, in this next subsection, 8 three-dimensional models of bone sarcomas in the proximal femur were developed based on CT scans provided by the Hospital Center of Porto. The generic 3D model, composed by 2172 nodes and 2030 tetrahedral elements, is represented in Figure 8.27(a).

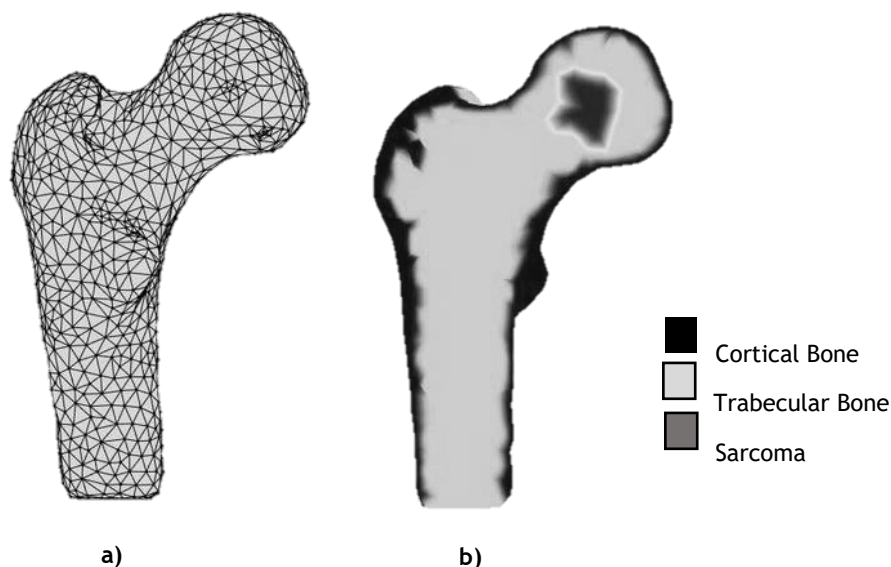


Figure 8.27 - (a) Element mesh (b) Representation of the geometric three-dimensional femur model with a bone sarcoma located on the femoral head.

The same clinical cases used for the numerical analysis of the 2D models were, also, analyzed in the 3D models. Based on a Matlab routine, the bone sarcomas were developed with a circular shape and located in four different areas of the proximal femur, x_c , namely head, neck, greater trochanter and shaft. In each clinical case, the ray $R1$ varies, where $R1=10$ mm corresponds to size 1, while size 2 corresponds to $R1=20$ mm. Therefore, the defects with a

size 1 occupy an area of approximately 314 mm² and the ones with a size 2 occupy an area of approximately 1256 mm². The 8 three-dimensional models are represented in Figure 8.28.

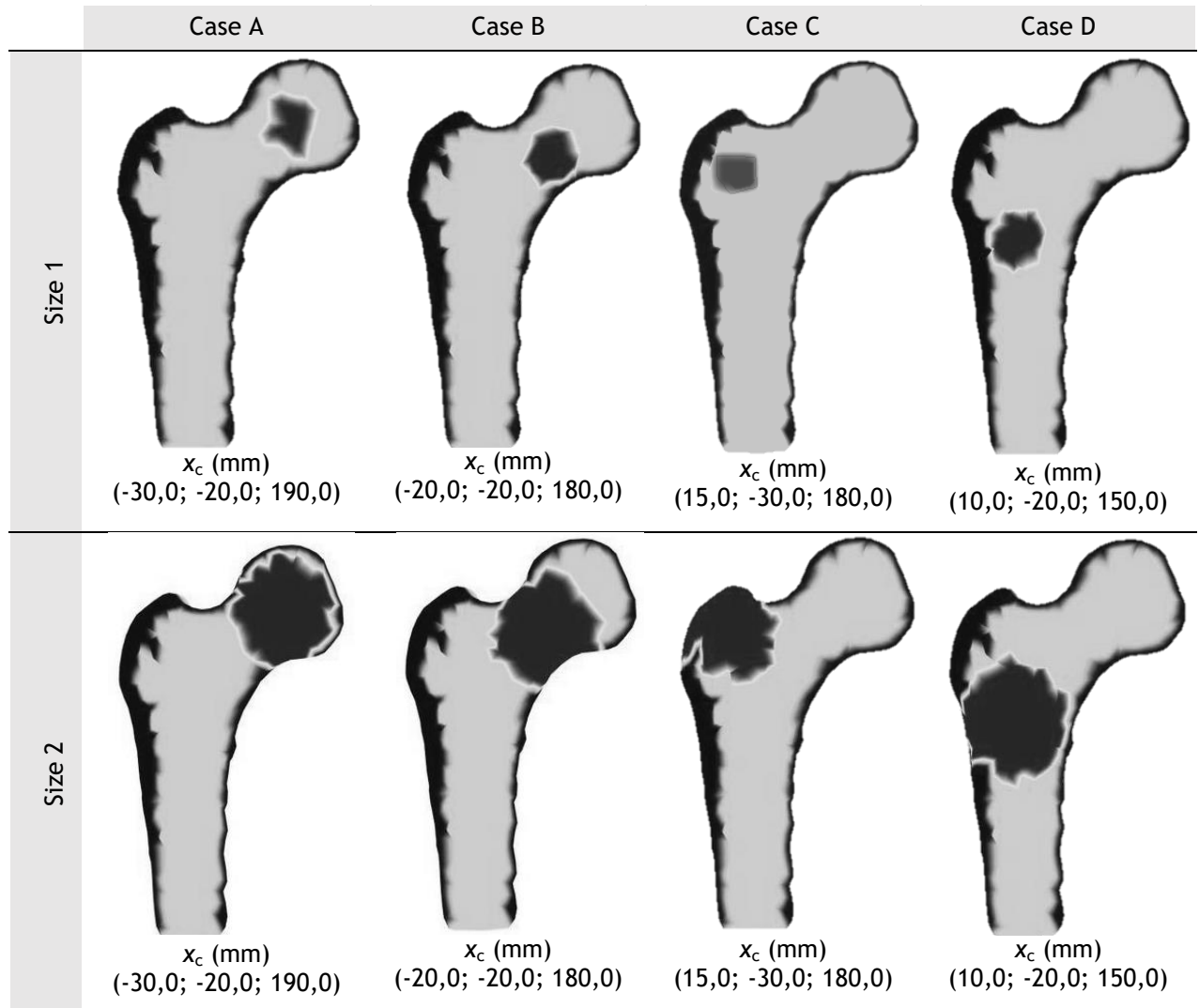


Figure 8.28 - Representation of the 8 three-dimensional models of bone sarcomas in the proximal femur.

Regarding the materials, the models are constituted by a layer of cortical bone tissue, a layer of trabecular tissue and bone sarcoma, as observed in Figure 8.27(b). The layer of cortical bone presents a maximum thickness of 1 mm. The materials considered have a linear elastic, homogenous and isotropic behavior and its mechanical properties are summarized in Table 8.2.

Table 8.2 - Mechanical Properties of the materials [14, 24].

Materials	Young's Modulus (E) (MPa)	Poisson's coefficient (ν)
Cortical Bone	$1,70 \times 10^4$	0,33
Trabecular Bone	$2,13 \times 10^3$	0,30
Sarcoma	$5,84 \times 10^2$	0,30

The essential and natural boundary conditions applied in the 3D models are also the same as the ones described previously for the 2D models. However, in this case, the forces were not normalized because it is a three-dimensional model of a proximal femur. Therefore, a representative load case was assumed for a patient weighting 100 kg, based on the first load case proposed by Beaupré *et. al.* [14] and the load case proposed by Kersh *et. al.* [25] and Lutz

et. al. [16], described previously in subsection 8.1. An essential boundary condition was also imposed, in which all degrees of freedom were constrain at the base of the model, preventing its movement. In Figure 8.29(a), (b) and (c) is represented the resultant of each force applied and the corresponding direction, as well as the essential boundary condition.

The results obtained from the computational analysis of the four 3D models, using three

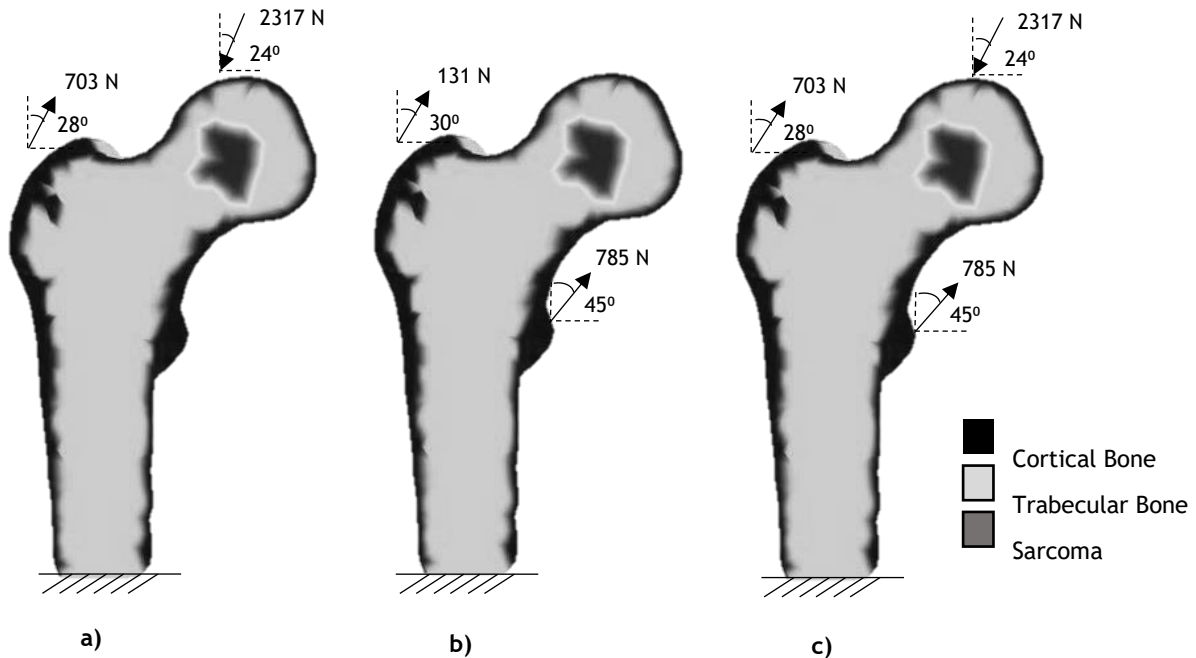


Figure 8.29 - Representation of the natural and essential boundary conditions: (a) load case described by Beaupré *et.al.* [14]; (b) load case described by Lutz *et. al.* [16] and Kersh *et. al.* [25]; (c) loads applied to the femur models with bone sarcomas.

numerical methods, FEM, RPIM and NNRPIM, are presented. In Figure 8.30, Figure 8.31 and Figure 8.32, it is possible to observe the dispersion color maps of the von Mises effective stress (σ_{ef}) for FEM, RPIM and NNRPIM, respectively. In Figure 8.33, Figure 8.34 and Figure 8.35, the dispersion color maps of the principal stress 1 (σ_{11}) for FEM, RPIM and NNRPIM are represented, respectively. Finally, in Figure 8.36, Figure 8.37 and Figure 8.38, it is presented the color maps of the principal stress 3 (σ_{33}) for FEM, RPIM and NNRPIM, respectively.

A qualitative analysis of the color maps demonstrates that bone sarcomas have a higher impact on cortical bone, as evidenced by the higher values of stress present in it. The trabecular bone, however, presents the same stress distribution and values, regardless of the tumor size.

On the other hand, the growth of the sarcoma does not interfere with the stress values in case A and C. For case B, a minimal increase of stress can be observed, with the increase of tumor size. For case D, it is possible to observe an increase in stress values between size 1 and size 2, with the highest stress values being present in the femoral neck and diaphysis for size 2. However, for all clinical cases, a difference in the stress pattern can be observed with the growth of the bone sarcoma, which indicates that this malignancy does affect the femoral bone structure. In all cases, the femoral diaphysis and neck are the areas most significantly affected.

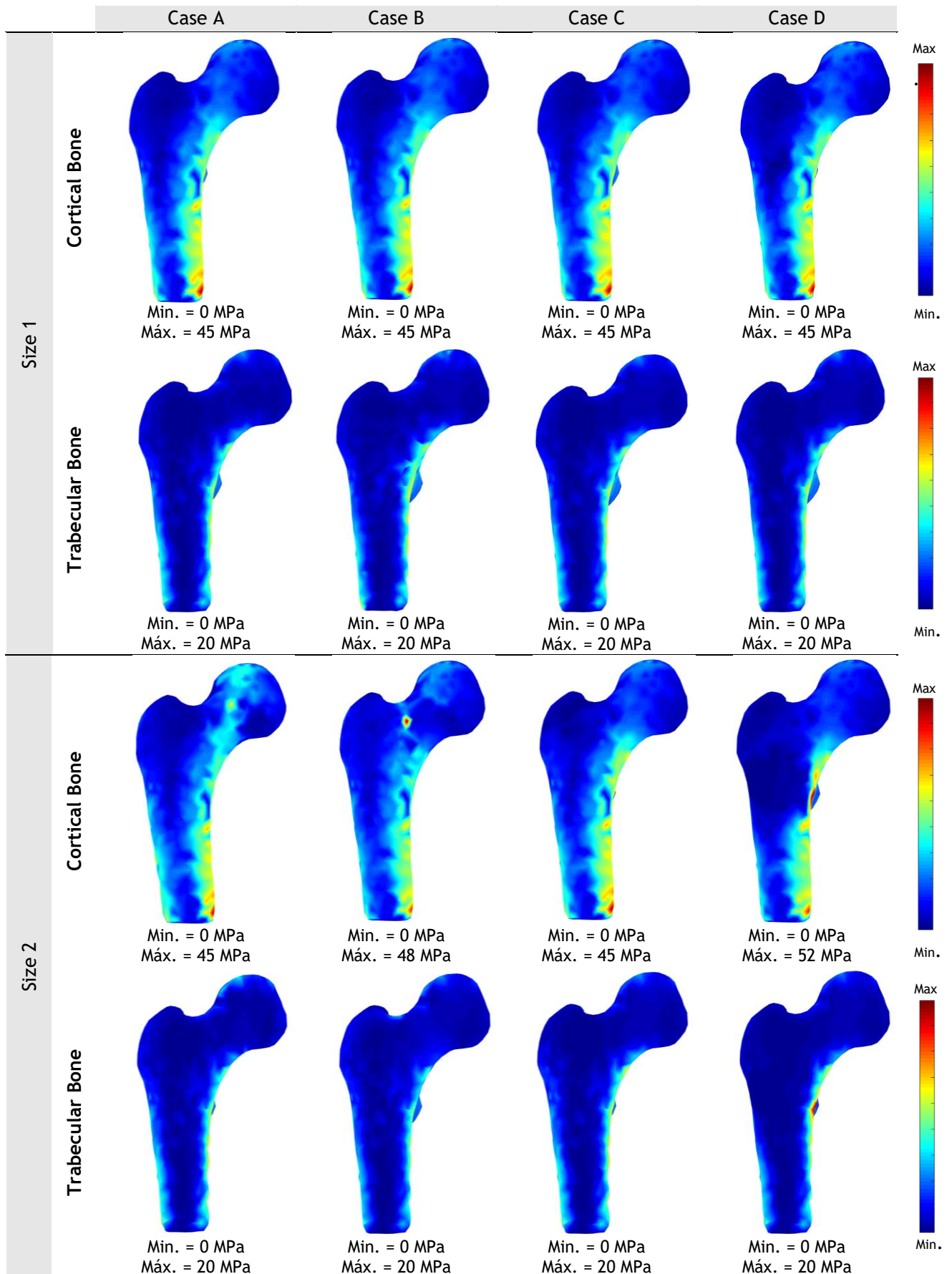


Figure 8.30 - Color maps of the von Mises effective stress (σ_{sef}) in the cortical and trabecular bone of the 8 three-dimensional models, using FEM.

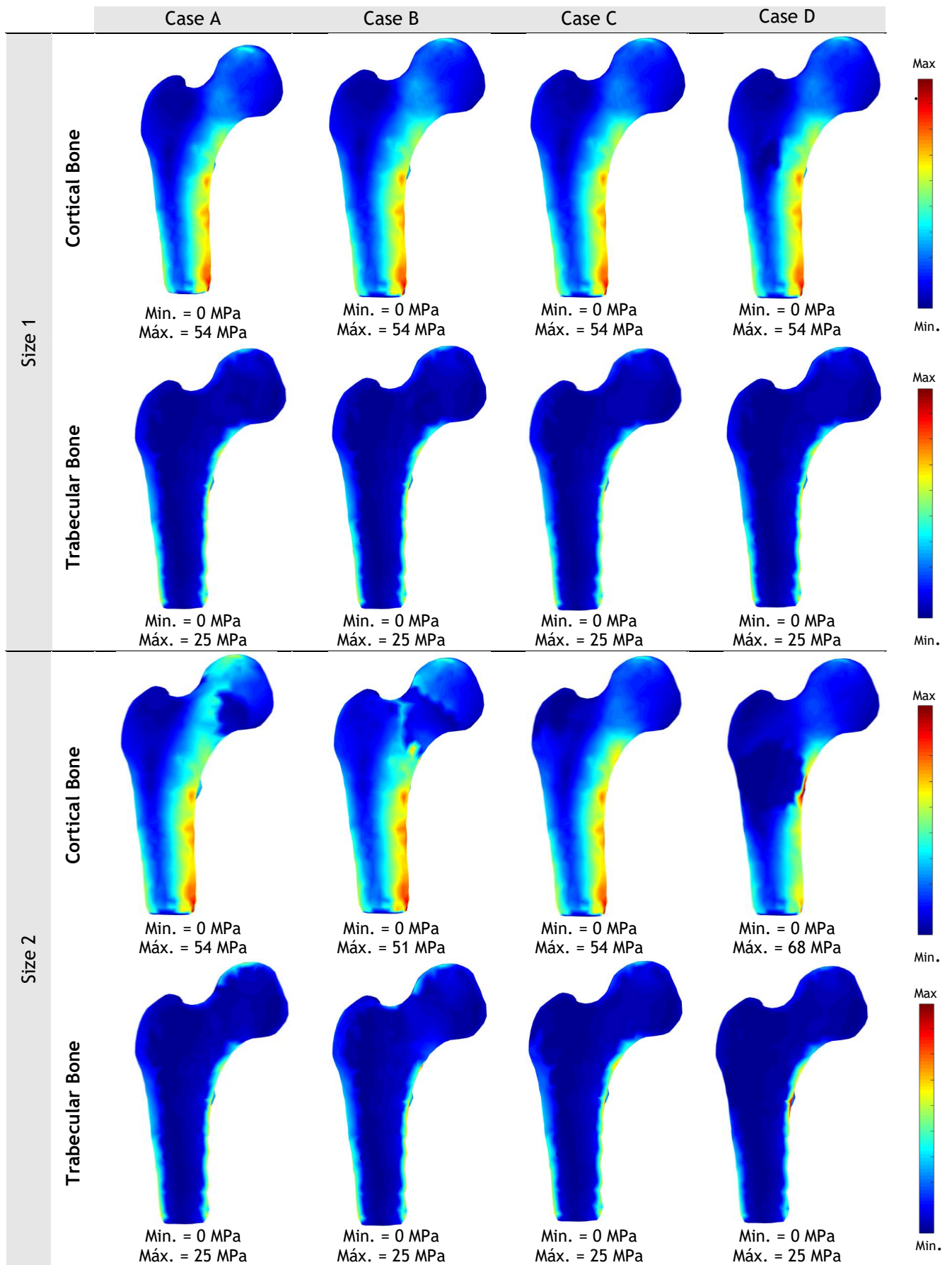


Figure 8.31 - Color maps of the von Mises effective stress (σ_{sef}) in the cortical and trabecular bone of the 8 three-dimensional models, using RPIM.

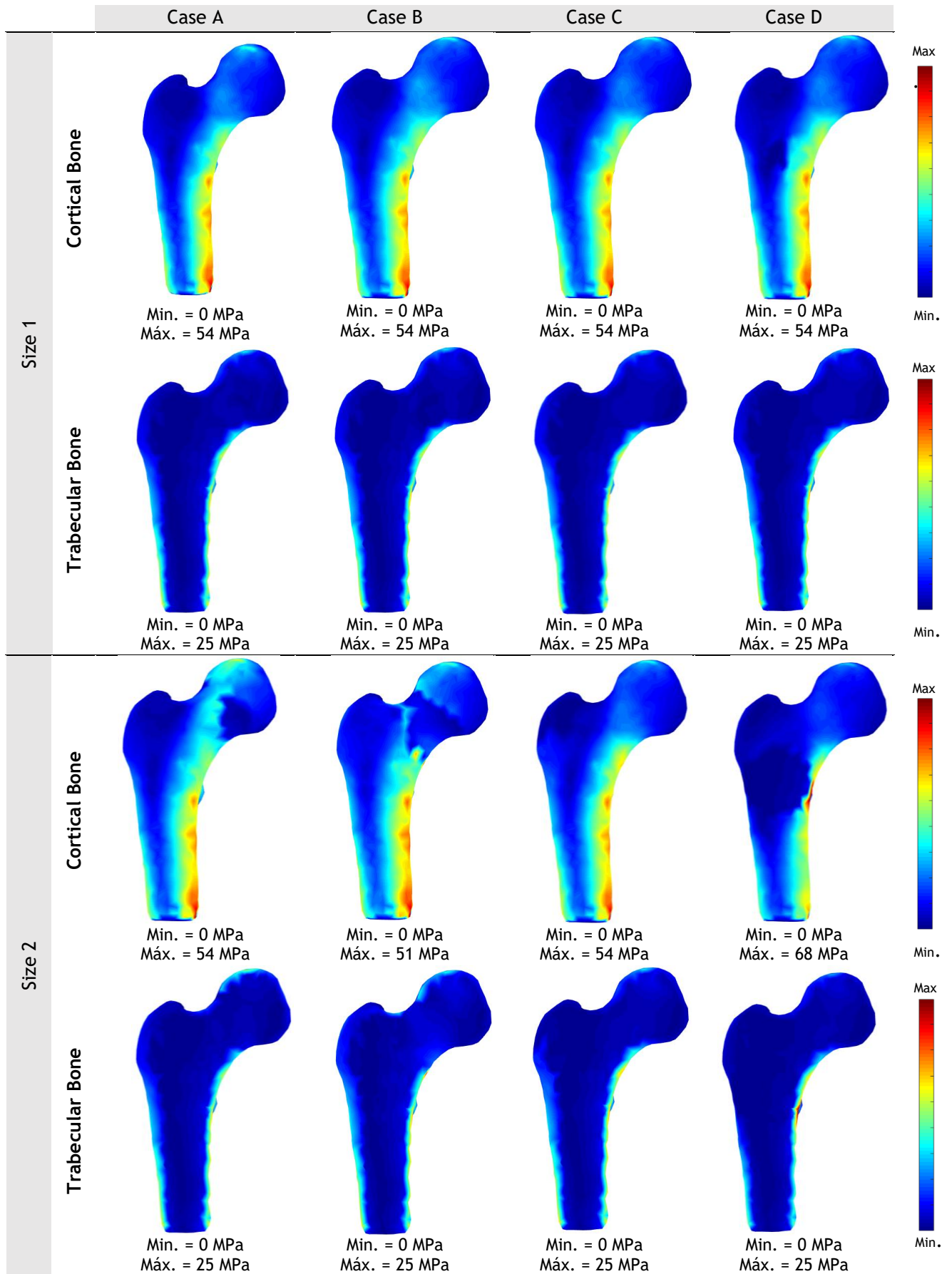


Figure 8.32 - Color maps of the von Mises effective stress (σ_{sef}) in the cortical and trabecular bone of the 8 three-dimensional models, using NNRPIM.

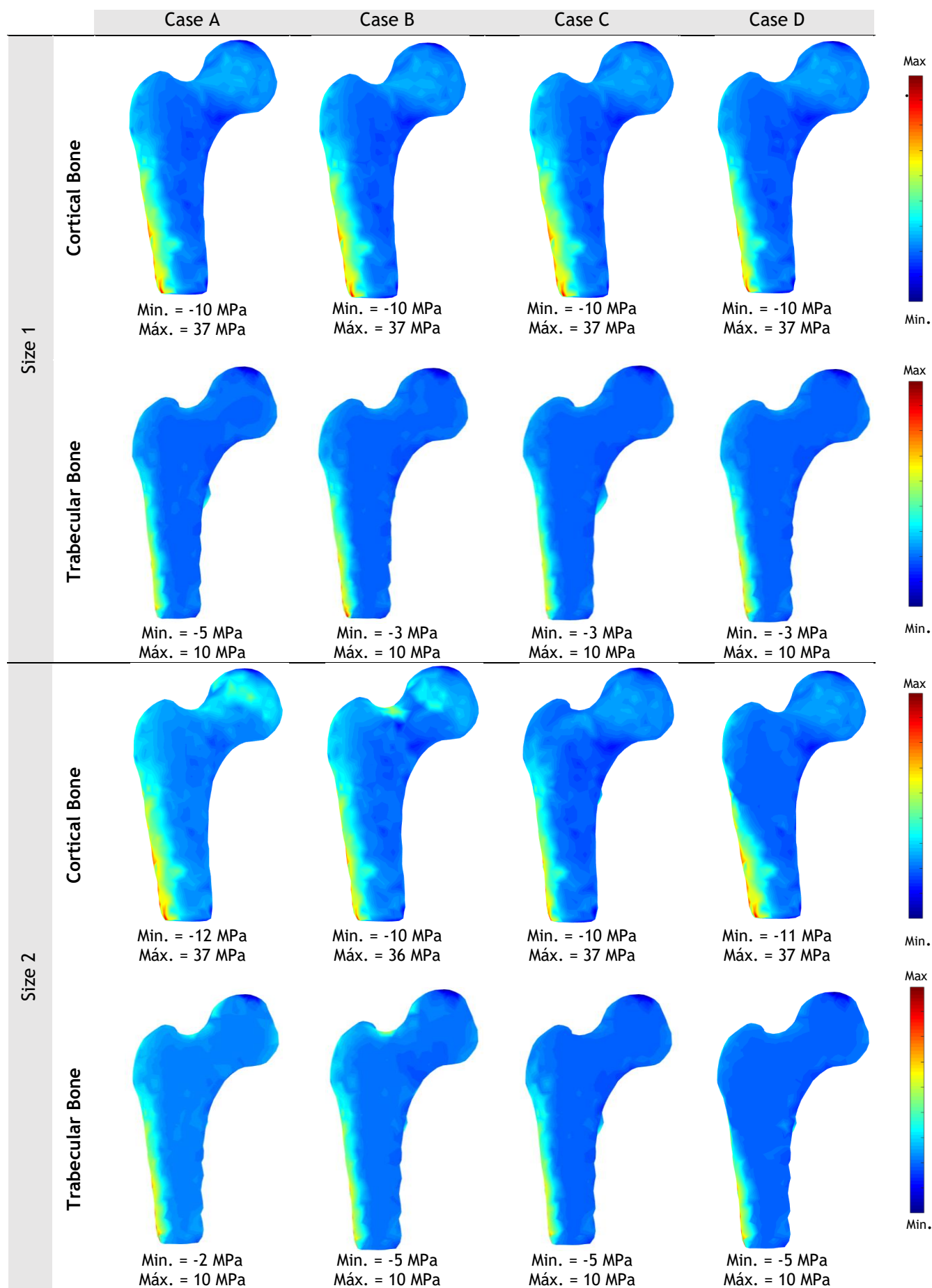


Figure 8.33 - Color maps of the principal stress 1 (σ_{11}) in the cortical and trabecular bone of the 8 three-dimensional models, using FEM.

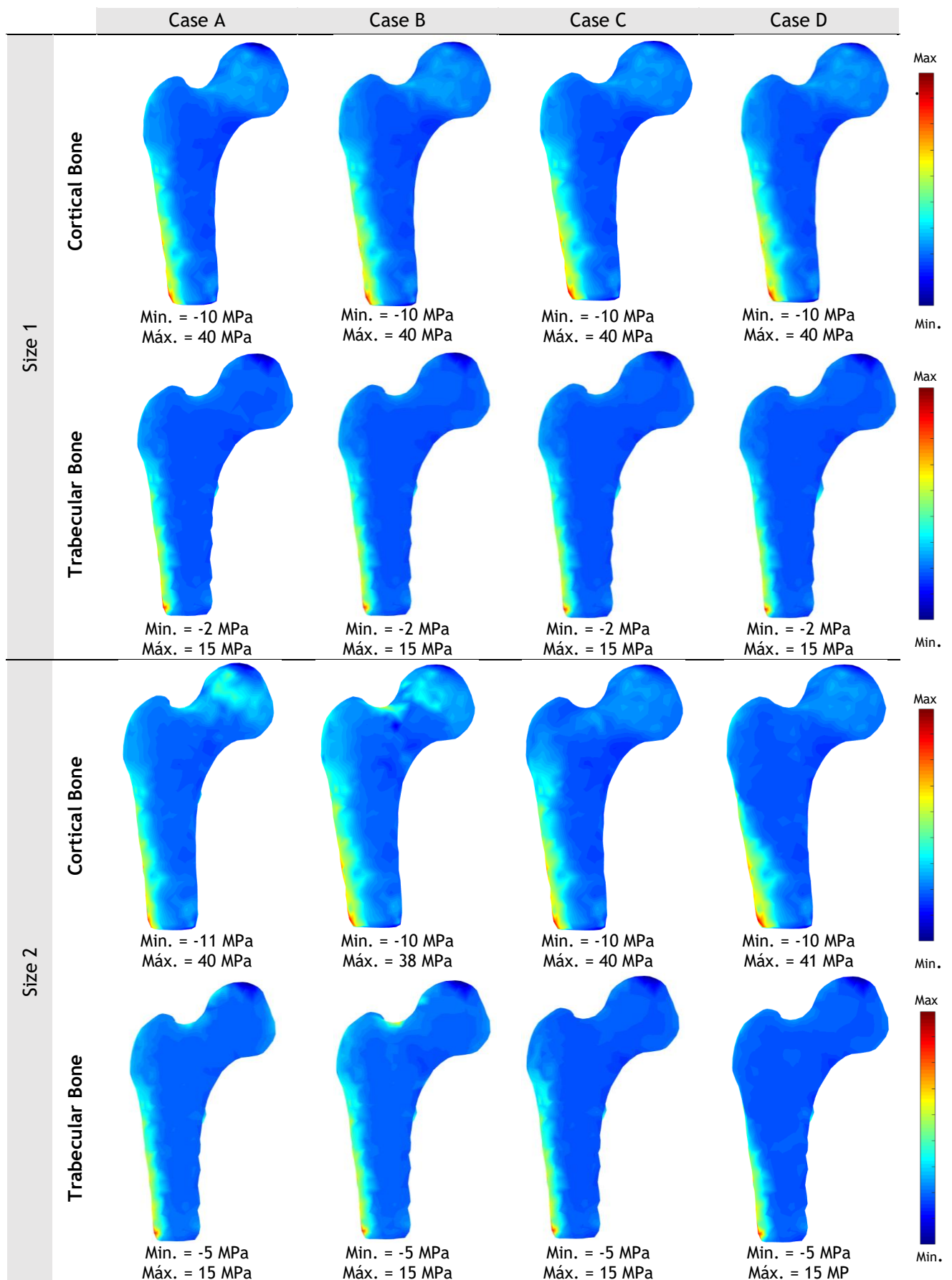


Figure 8.34 - Color maps of the principal stress 1 (σ_{11}) in the cortical and trabecular bone of the 8 three-dimensional models, using RPIM.

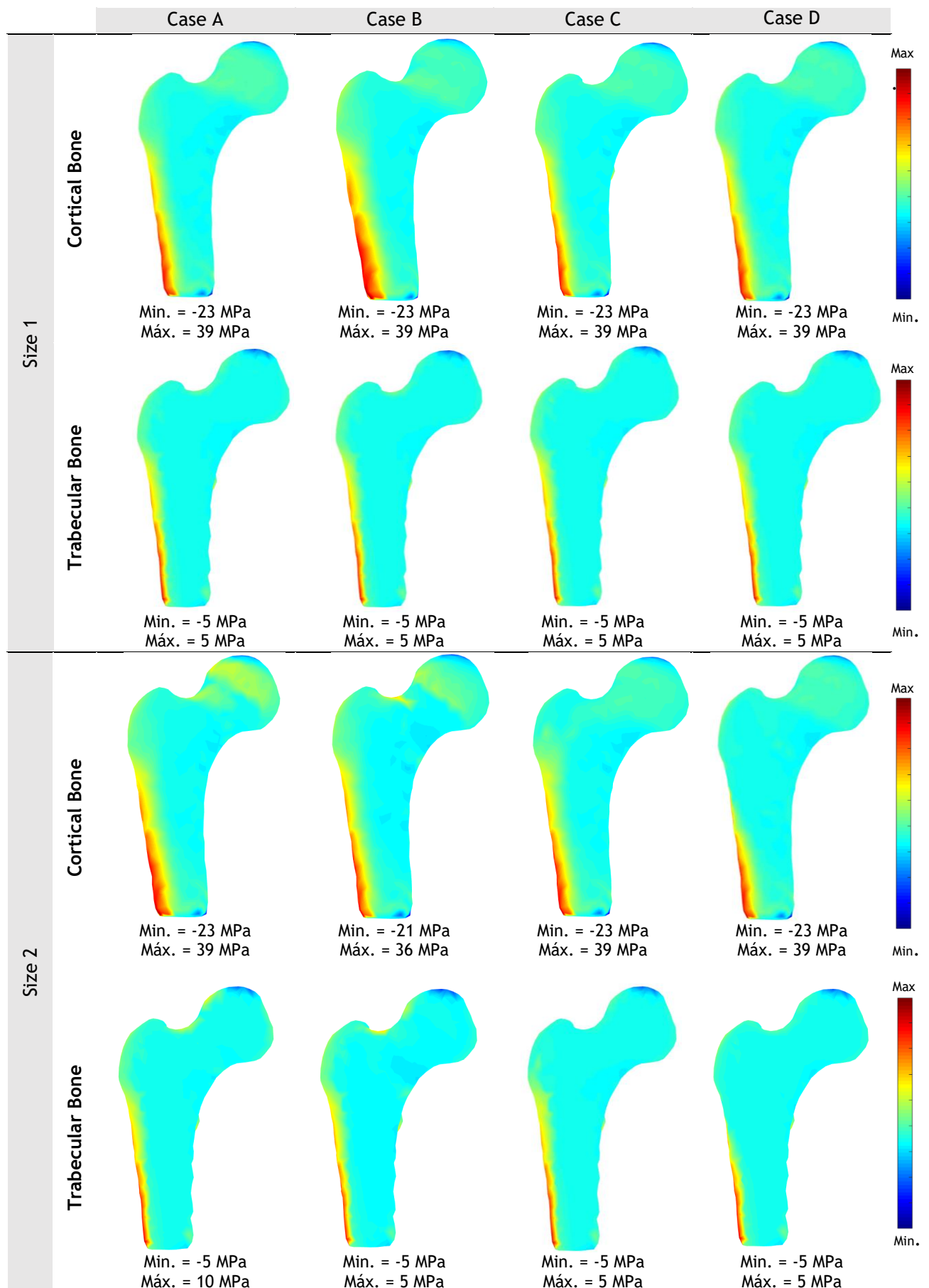


Figure 8.35 - Color maps of the principal stress 1 (σ_{11}) in the cortical and trabecular bone of the 8 three-dimensional models, using NNRPIM.

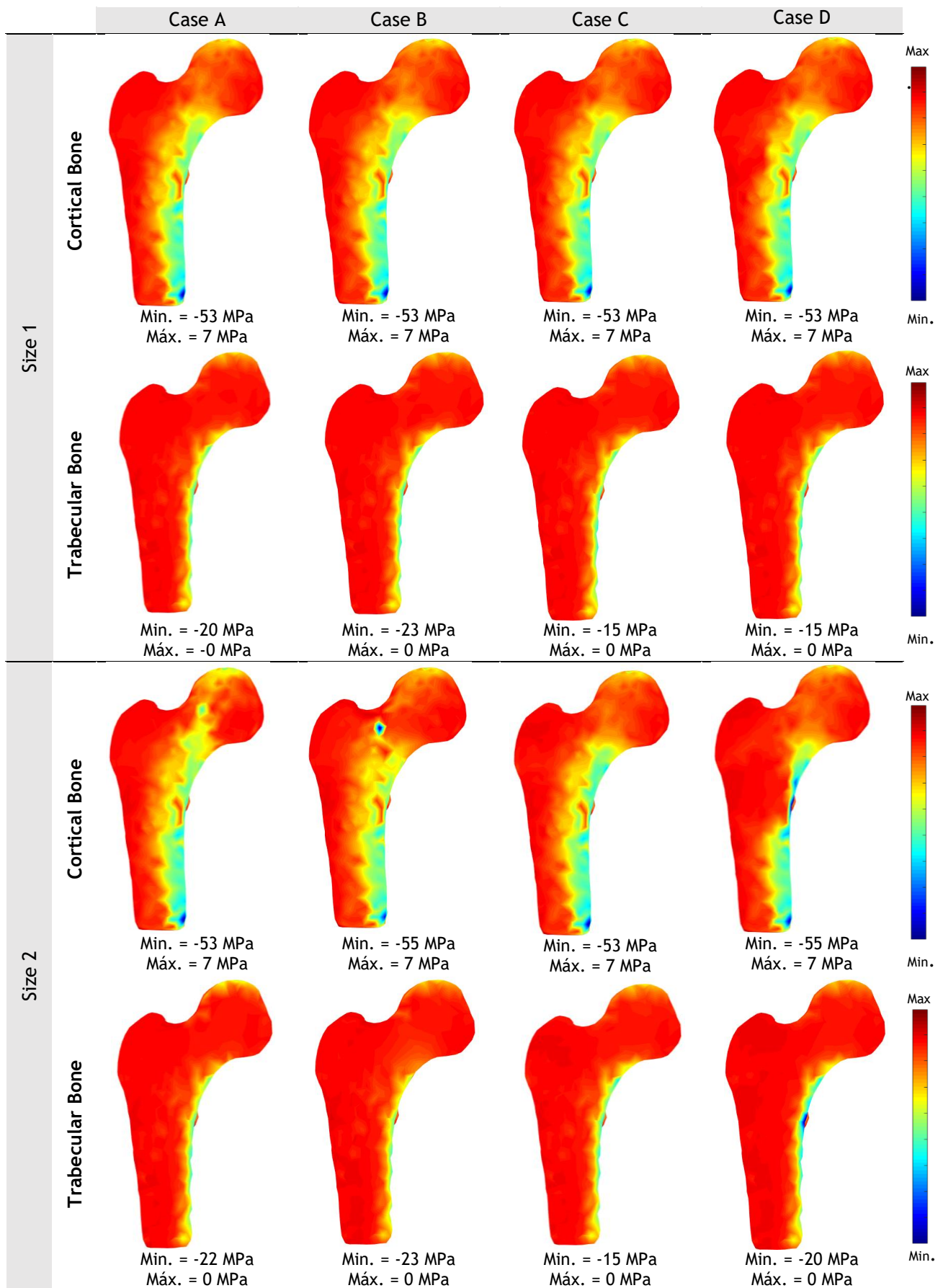


Figure 8.36 - Color maps of the principal stress 3 (σ_{33}) in the cortical and trabecular bone of the 8 three-dimensional models, using FEM.

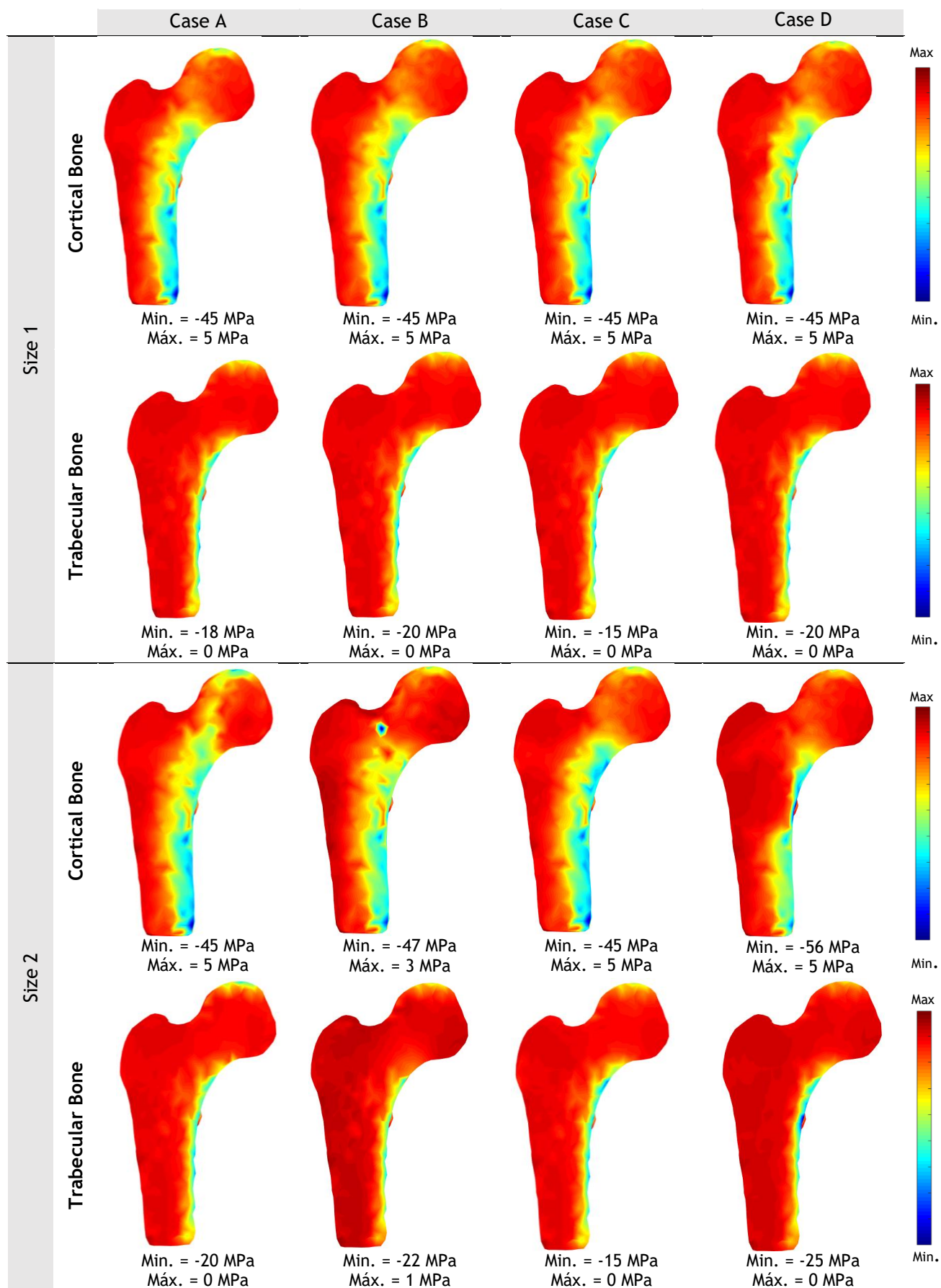


Figure 8.37 - Color maps of the principal stress 3 (σ_{33}) in the cortical and trabecular bone of the 8 three-dimensional models, using RPIM.

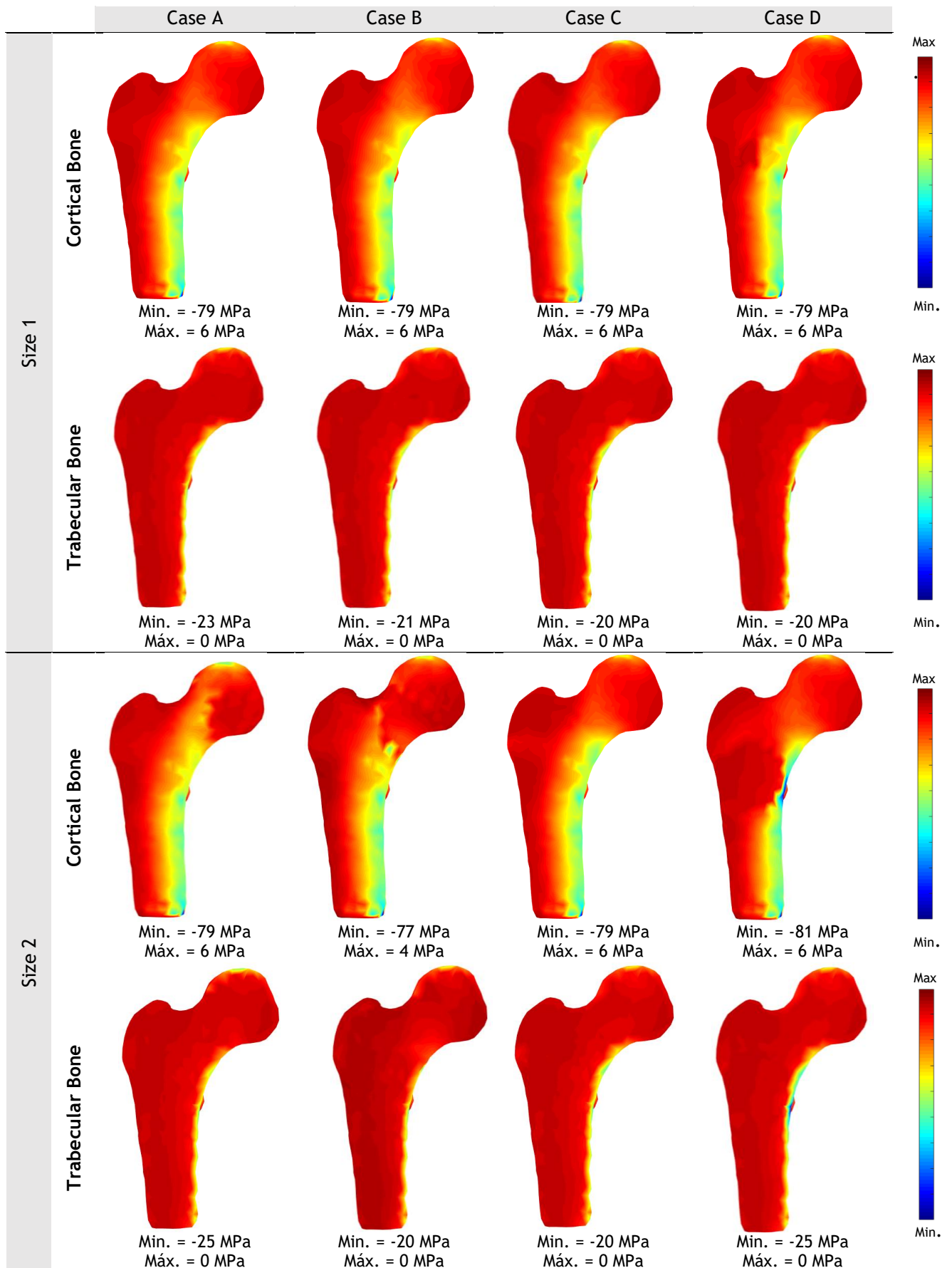


Figure 8.38 - Color maps of the principal stress 3 (σ_{33}) in the cortical and trabecular bone of the 8 three-dimensional models, using NNRPIM.

Therefore, it can be concluded that case D, where the tumor is located in the femoral shaft, is the most critical case and the one that could lead to the fracture of the femoral neck or diaphysis. These results are in agreement with the analysis conducted previously with 2D models, which evidenced a higher fracture risk for the femoral neck.

In the dispersion color maps of principal stress 1 and 2, it is possible to observe that the greatest tensile stresses can be found in the cortical bone on the left side of the femoral shaft. These regions of traction are mainly due to the tensile force applied to the greater trochanter, which translates the force exerted by the abductor muscles at the stage when the foot touches the ground during the cycle of the human gait. On the other hand, the compressive stresses are present in the cortical bone on the right side of the femoral diaphysis up to the inferomedial neck as well as in the upper region of the femoral head. This is mainly due to the compressive force exerted on the femoral head caused by the hip joint.

As previously demonstrated in the 2D models, the tensile stresses (positive stresses) are similar in all clinical cases, regardless of the size of the bone sarcoma. Contrarily, the compressive stresses (negative stresses) are similar in case A and C. However, in case B and D, the compressive stresses increase with the tumor size, with case D demonstrating the highest compressive stresses, as would be expected considering the von Mises effective stresses, previously observed. Relatively to the bone tissue surrounding the bone sarcoma, it can be noticed a minimal effect, which will be further detailed.

After the qualitative analysis, 4 areas of interest were selected and are represented in Figure 8.39. Thus, five points of interest were selected in these zones to perceive which is the most affected in each clinical case. It was analyzed the von Mises effective tension, the principal tension 1 and principal tension 3 for each point of interest, using different methods: FEM, RPIM and NNRPIM. In Figure 8.40, Figure 8.41, Figure 8.42 and Figure 8.43 are graphically presented the results obtained from the von Mises effective stress for all clinical cases studied.

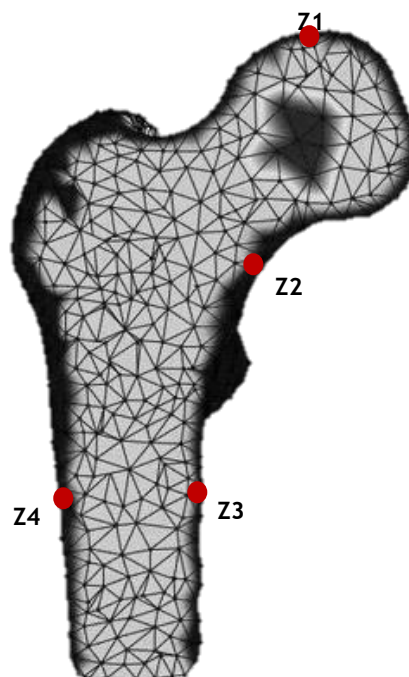


Figure 8.39 - Representation of the zones (red circles) where the points of interest were selected.

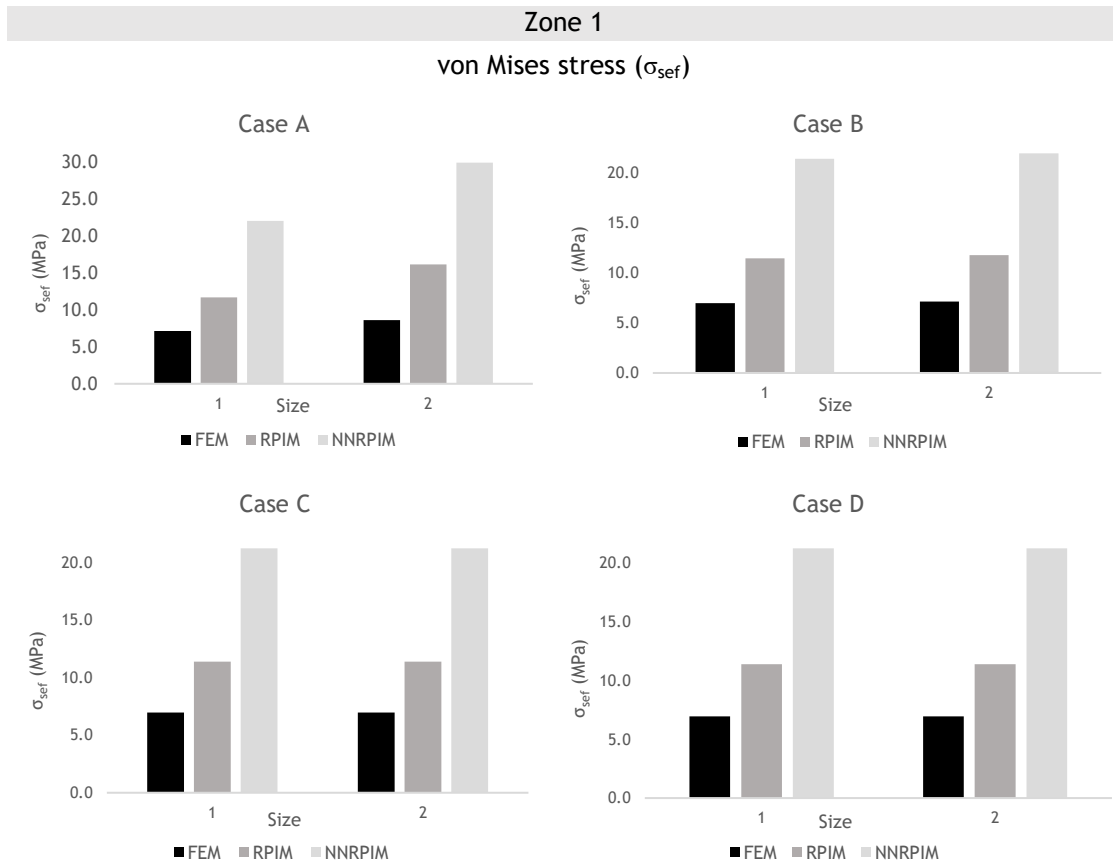


Figure 8.40 - Graphic representation of the von Mises effective stress obtained through FEM, RPIM and NNRPIM, for all clinical cases studied in zone of interest 1.

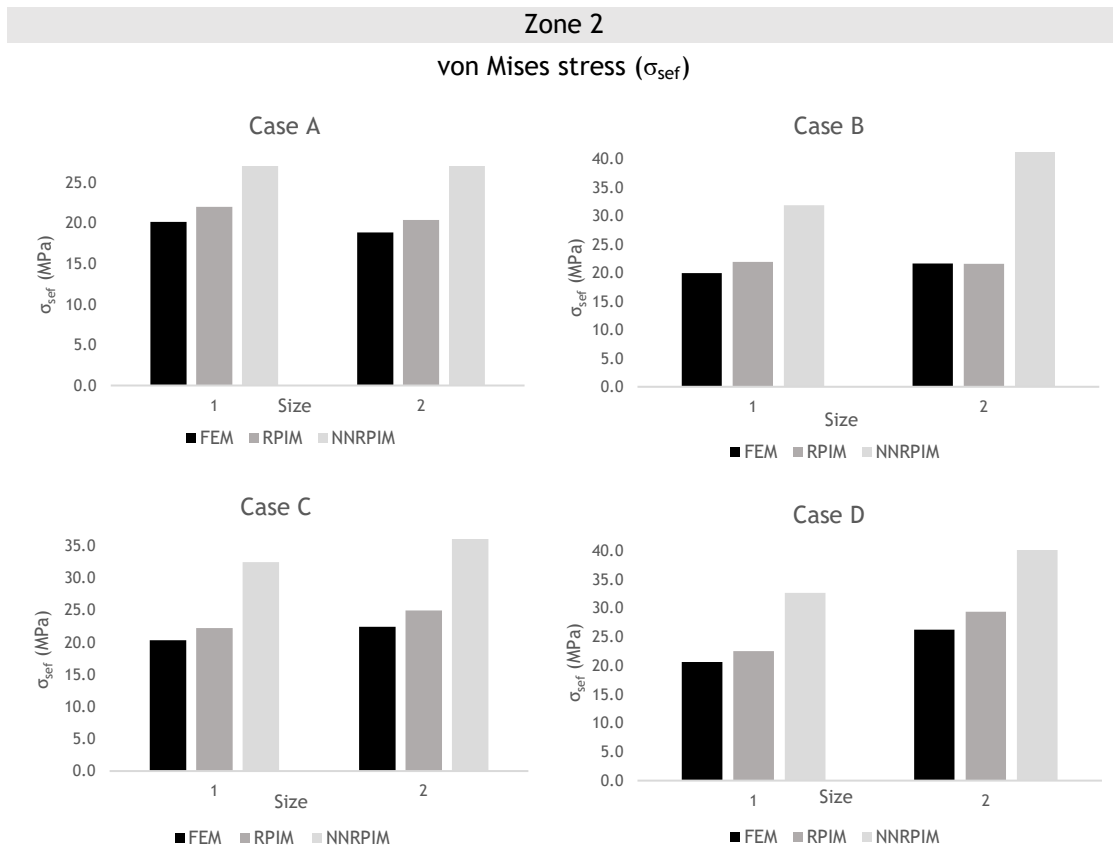


Figure 8.41 - Graphic representation of the von Mises effective stress obtained through FEM, RPIM and NNRPIM, for all clinical cases studied in zone of interest 2.

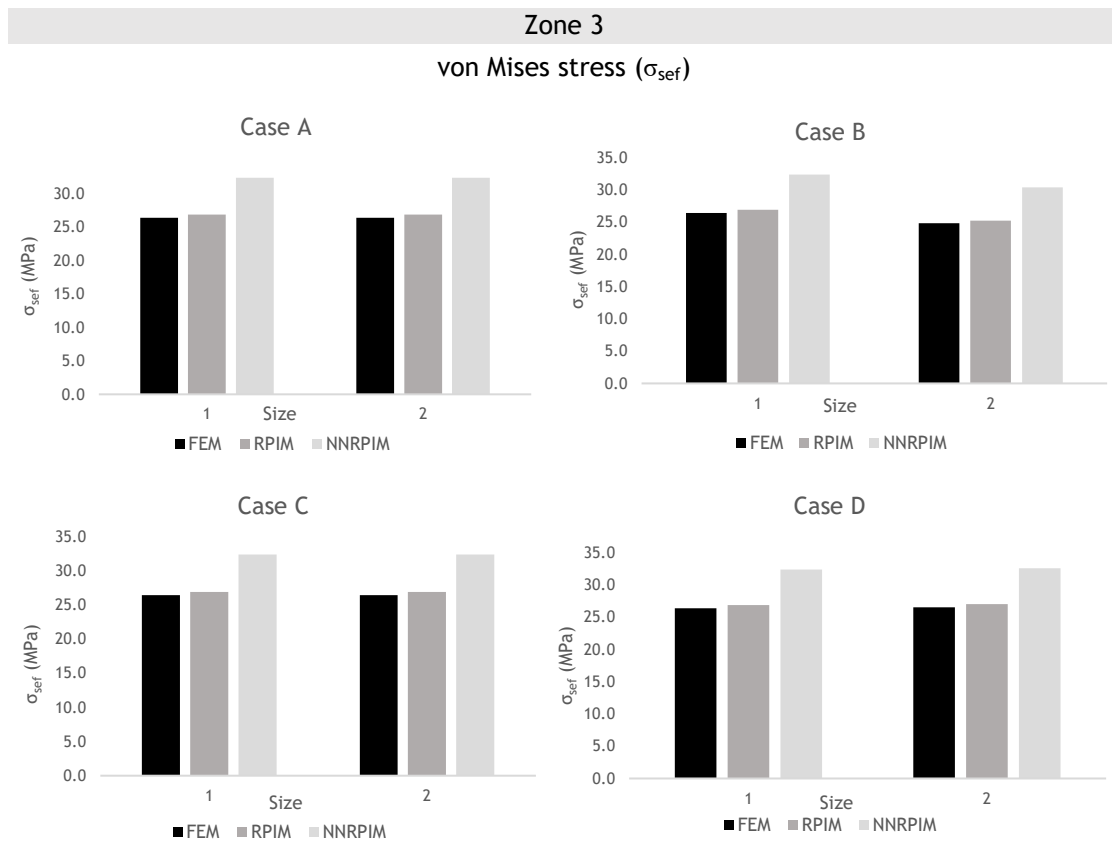


Figure 8.42 - Graphic representation of the von Mises effective stress obtained through FEM, RPIM and NNRPIM, for all clinical cases studied in zone of interest 3.

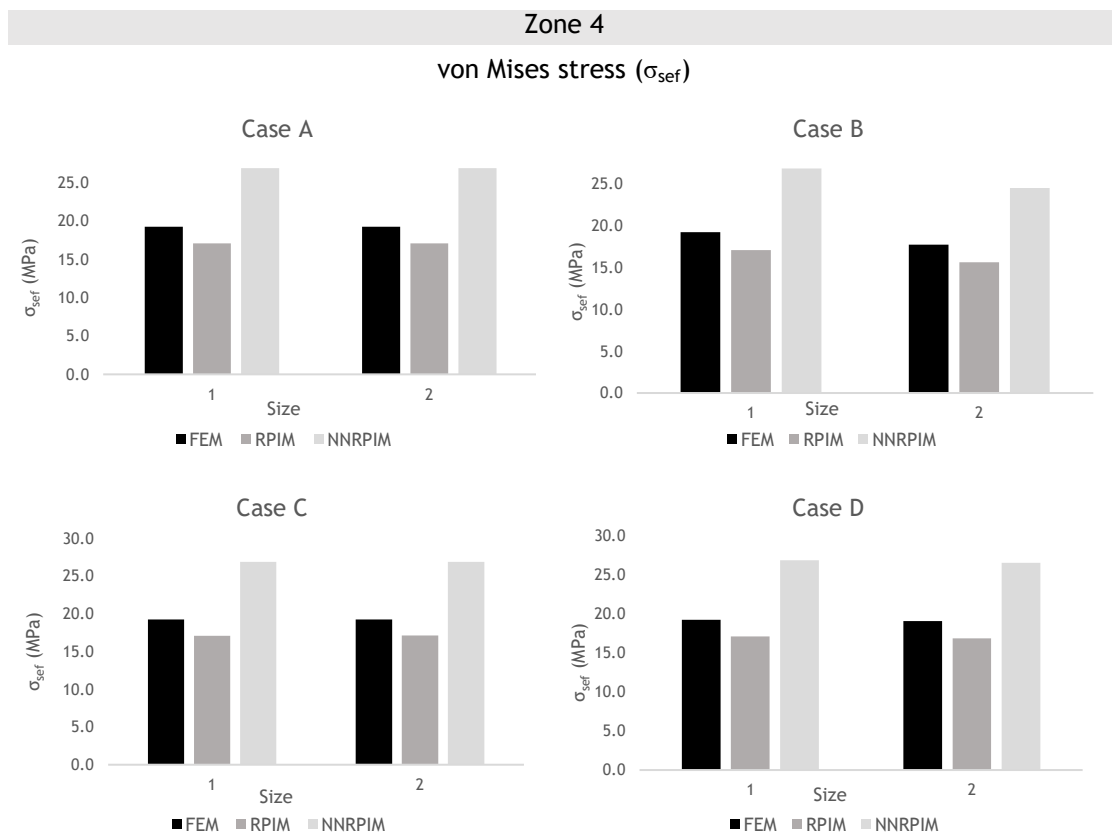


Figure 8.43- Graphic representation of the von Mises effective stress obtained through FEM, RPIM and NNRPIM, for all clinical cases studied in zone of interest 4.

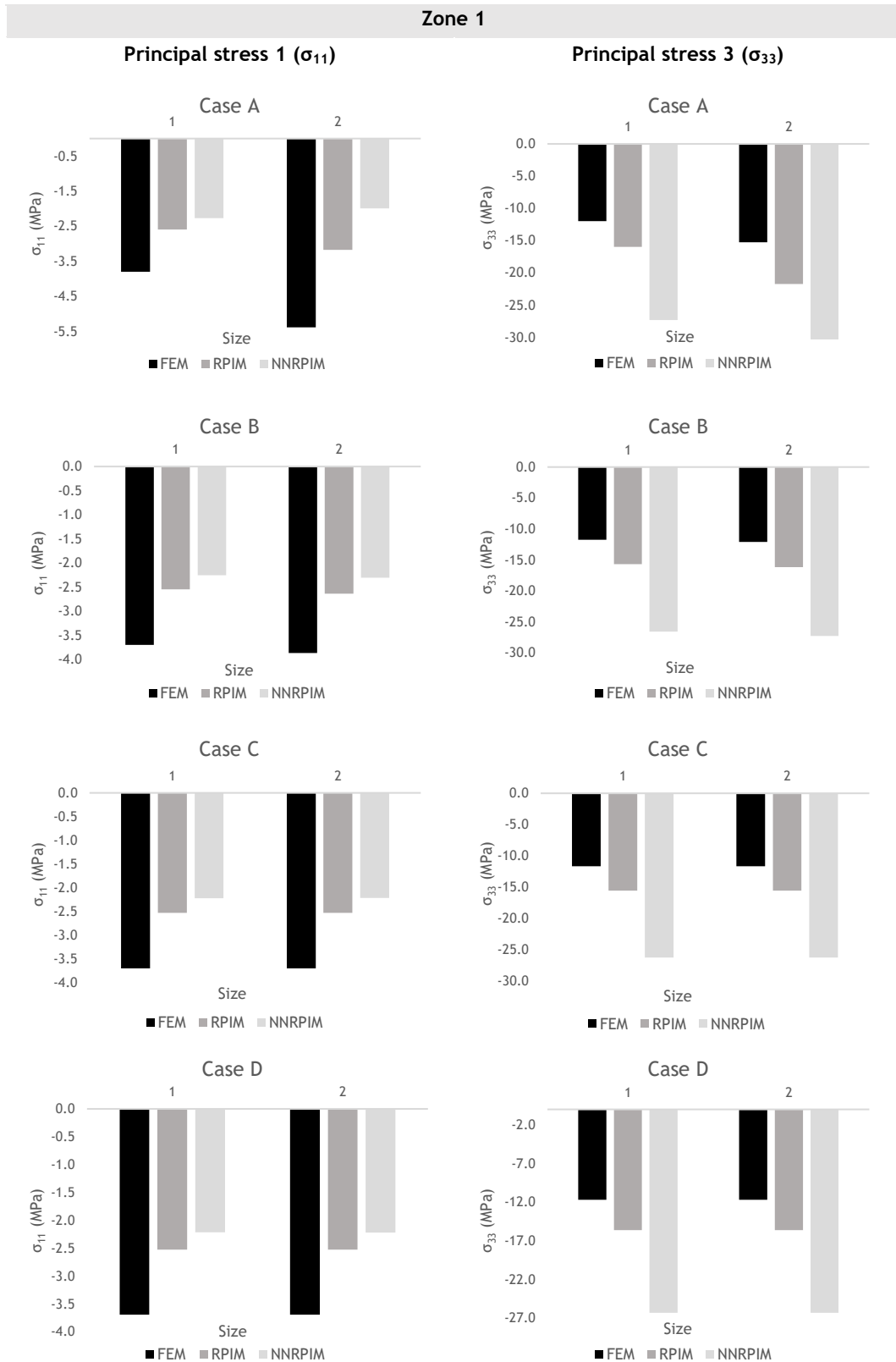


Figure 8.44 - Graphic representation of the principal stress 1 and 3 obtained through FEM, RPIM and NNRPIM, for all clinical cases studied in zone of interest 1.

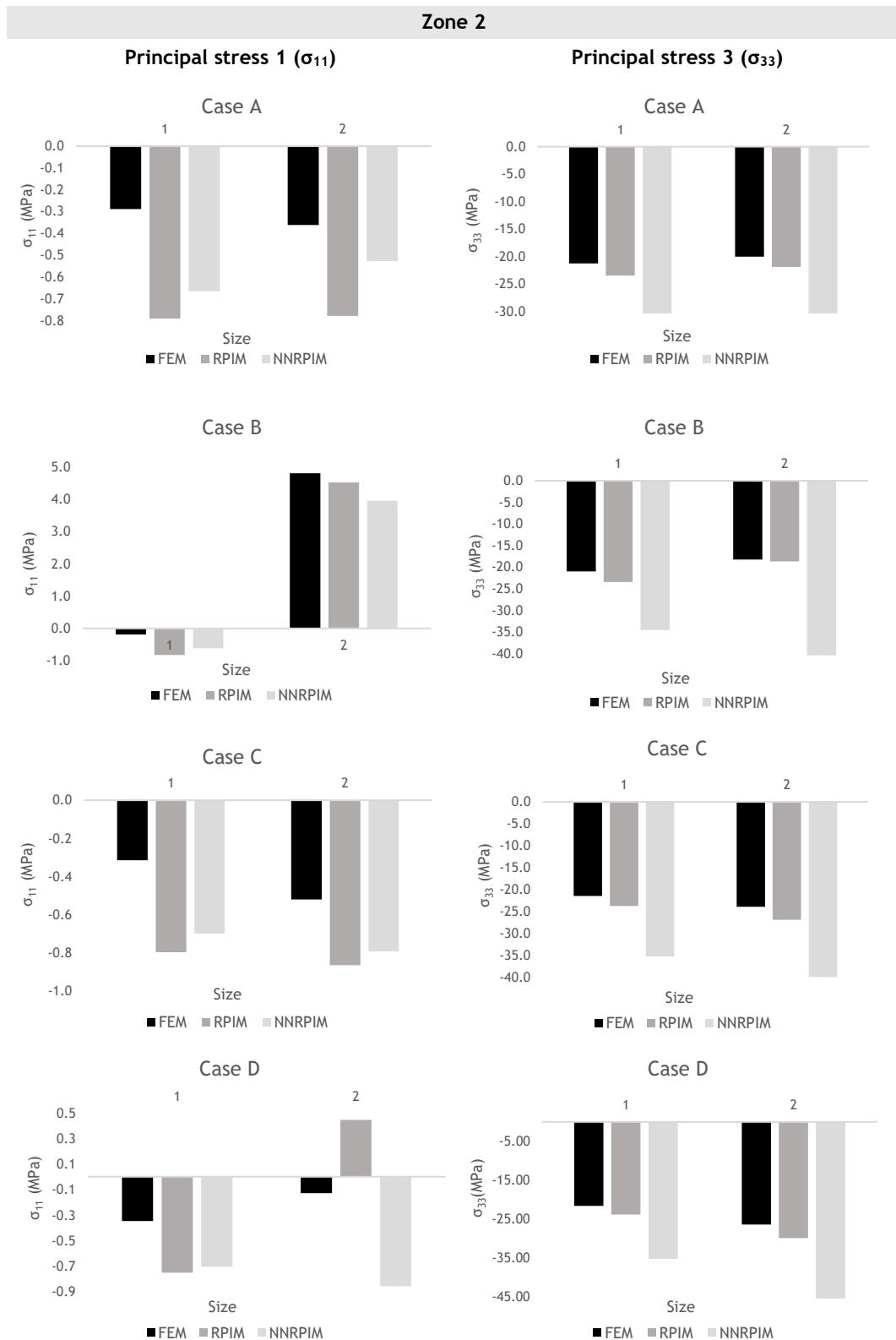


Figure 8.45 - Graphic representation of the principal stress 1 and 3 obtained through FEM, RPIM and NNRPIM, for all clinical cases studied in zone of interest 2.

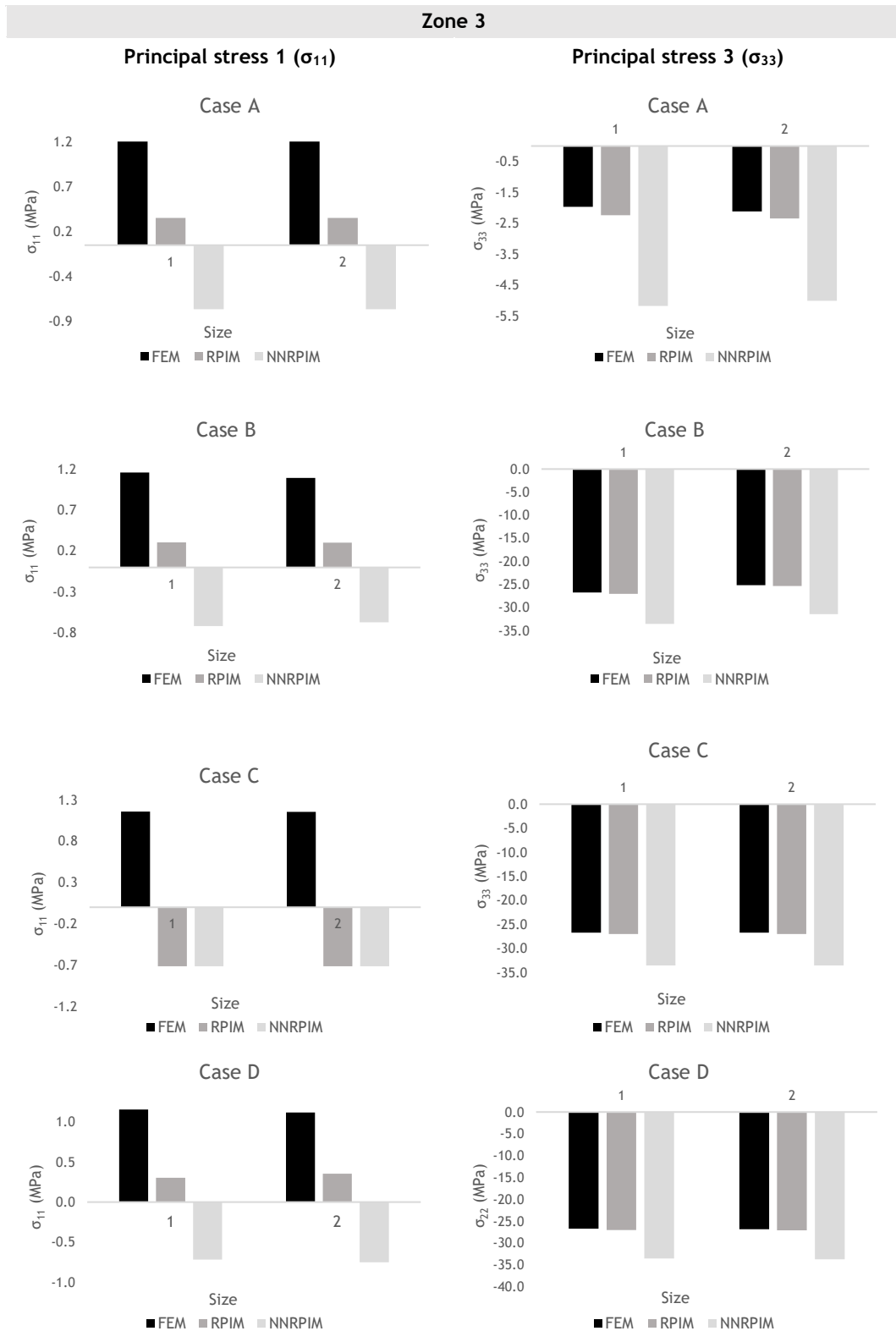


Figure 8.46 - Graphic representation of the principal stress 1 and 3 obtained through FEM, RPIM and NNRPIM, for all clinical cases studied in zone of interest 3.

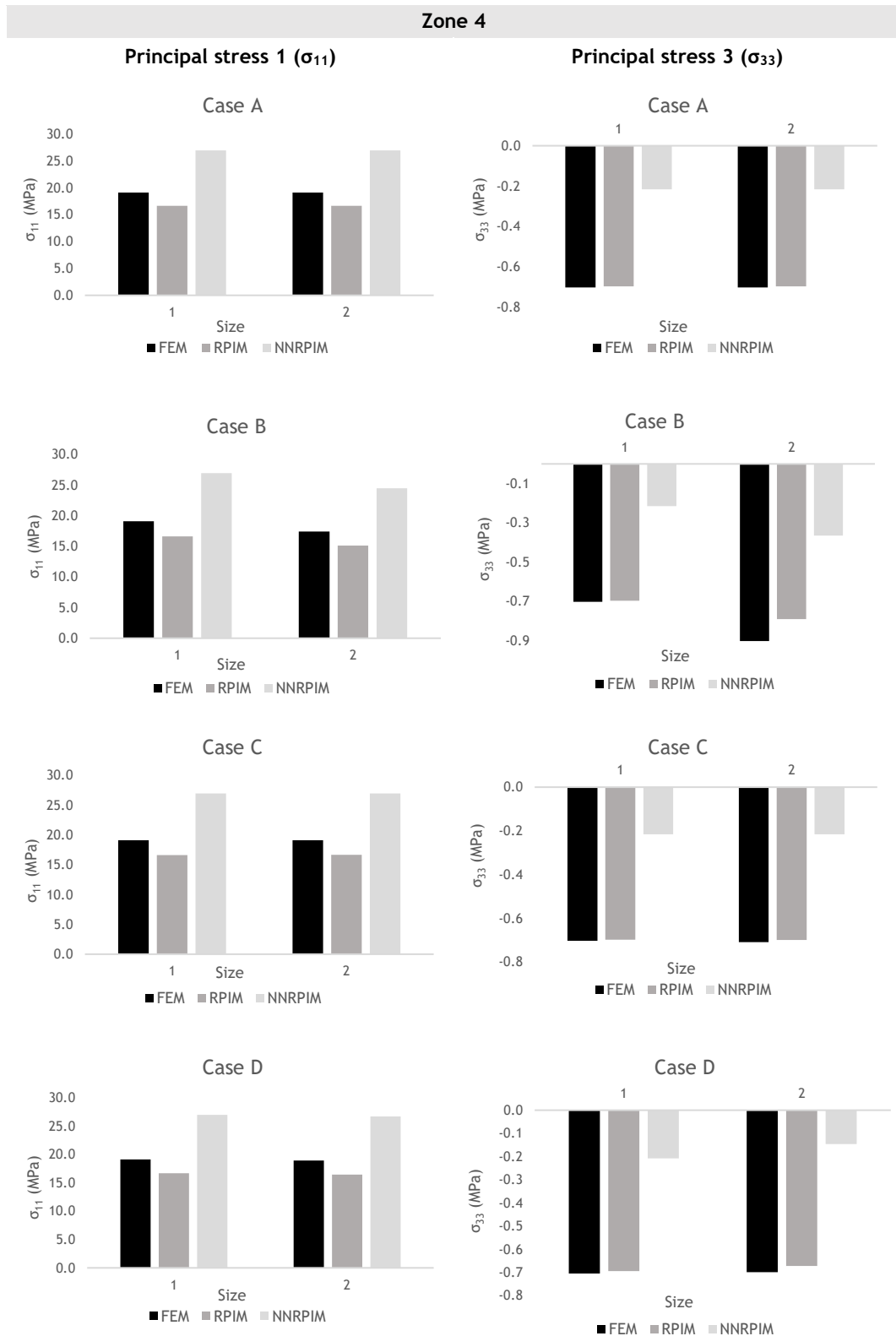


Figure 8.47 - Graphic representation of the principal stress 1 and 3 obtained through FEM, RPIM and NNRPIM, for all clinical cases studied in zone of interest 4.

In zone 1, 3 and 4, it is possible to notice that, for all clinical cases, the size of the sarcoma does not influence the increase in stress. When comparing these zones, the highest stresses are present in zone 3 and vary between 30-35 MPa in all clinical cases. However, all the cases studied for this area have an identical stress that is not significantly affected by the increase in size of the bone sarcoma. The zone 1, located in the femoral head, demonstrates the lowest values of stress, which vary between 20-30 MPa. Nevertheless, a tendency to an increase in stress is observed for case A with the increase in the tumor size (in this area of interest). In zone 4, case C and D have the highest stress values, but the stress is identical regardless of the tumor size. Finally, the maximum stress values, of approximately 40 MPa, are present in zone 2 of case B, size 2, where an increase in stress can be noticed with the growth of the sarcoma. The same can be observed for case D (also in zone 2), where the tumor size induces an increase in stress, demonstrating the highest stress value, of approximately 38 MPa, in size 2.

In Figure 8.44, Figure 8.45, Figure 8.46 and Figure 8.47, the results obtained for principal stress 1 and principal stress 3 can be observed. Overall, it is possible to observe that zone 1, 2 and 3 are regions of compression (higher negative values of principal stress 3) and zone 4 is a region of traction (higher values of principal stress 1), which is in agreement with the literature [140]. In zone 1, 3 and 4, it can be verified that for all cases, the compression stresses are identical, independently of the tumor size. Contrarily, in zone 2, an increase in stress with the increase of the sarcoma size can be observed, with the exception of case A.

In order to understand the effect of the bone sarcoma in the surrounding bone tissue, a set of nodes around the tumors were selected. In Figure 8.48 is possible to observe a generic representation of the selected nodes. For each clinical case, it was analyzed the von Mises effective stress, the principal stress 1 and principal stress 2 for each of the four areas of interest, using different methods: FEM, RPIM and NNRPIM. In Figure 8.49, Figure 8.50, Figure 8.51 and Figure 8.52 are graphically presented the results obtained from the von Mises effective stress for all clinical cases studied, for each of the four areas of interest mentioned above.

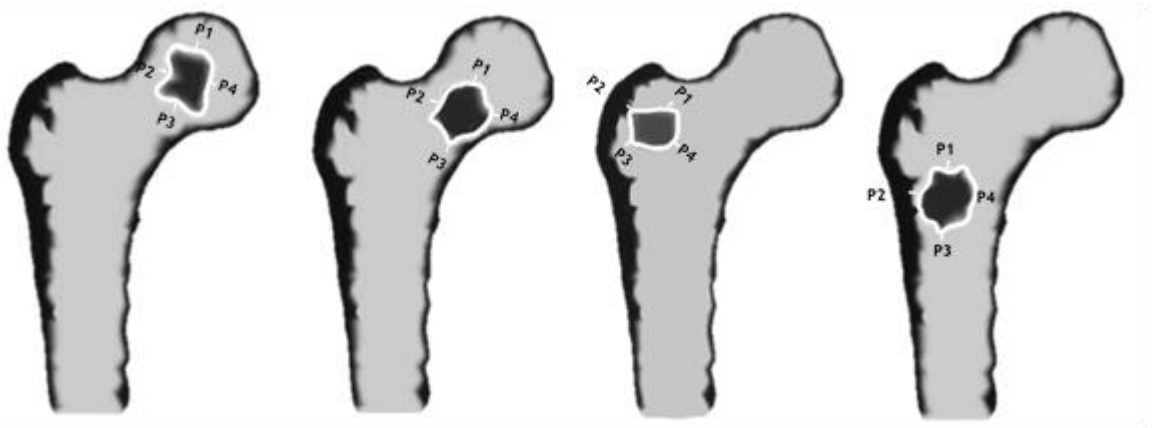


Figure 8.48 - Generic representation of the selected nodes (black line) for all clinical cases: (a) Case A; (b) case B; (c) Case C and (d) Case D.

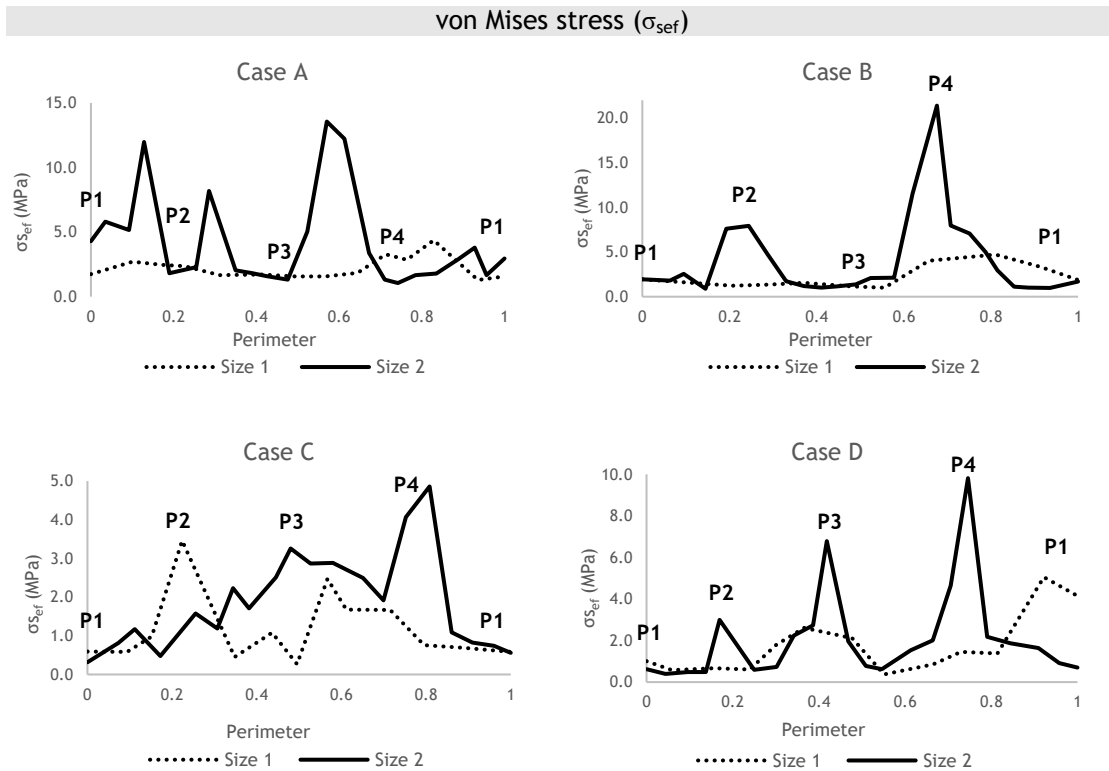


Figure 8.49 - Graphical representation of the von Mises effective stress obtained through FEM for the cases of bone sarcomas studied in the four areas of interest.

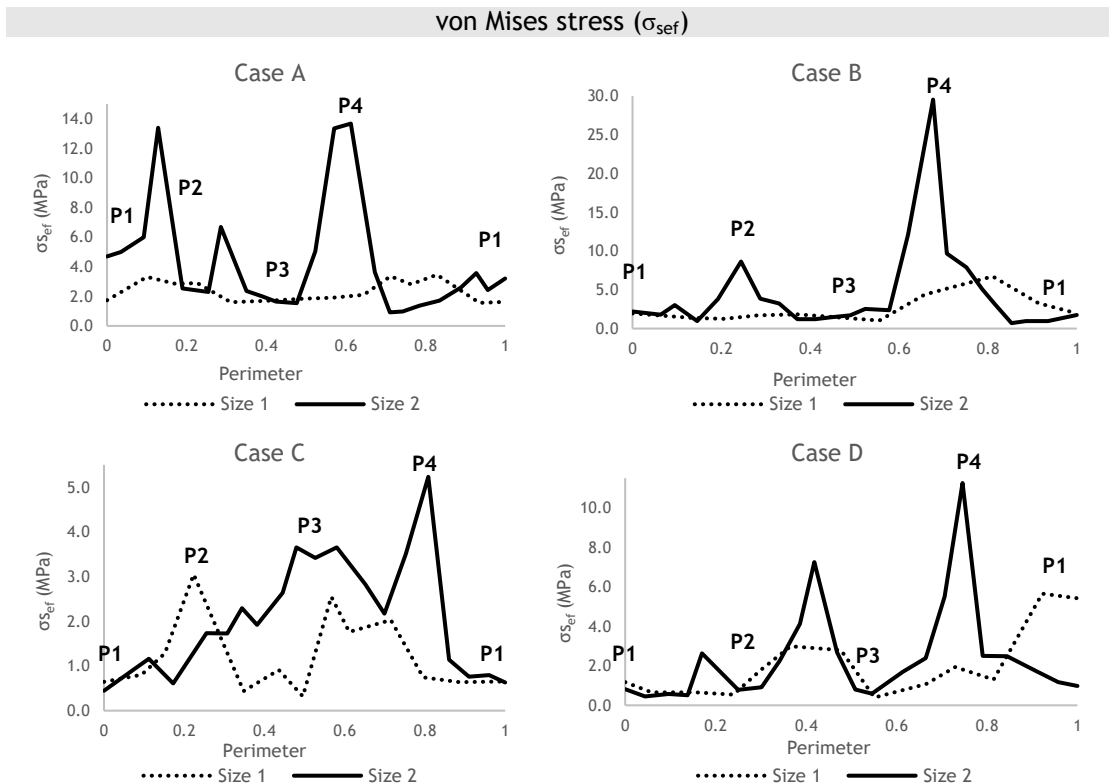


Figure 8.50 - Graphical representation of the von Mises effective stress obtained through RPIM for the cases of bone sarcomas studied in the four areas of interest.

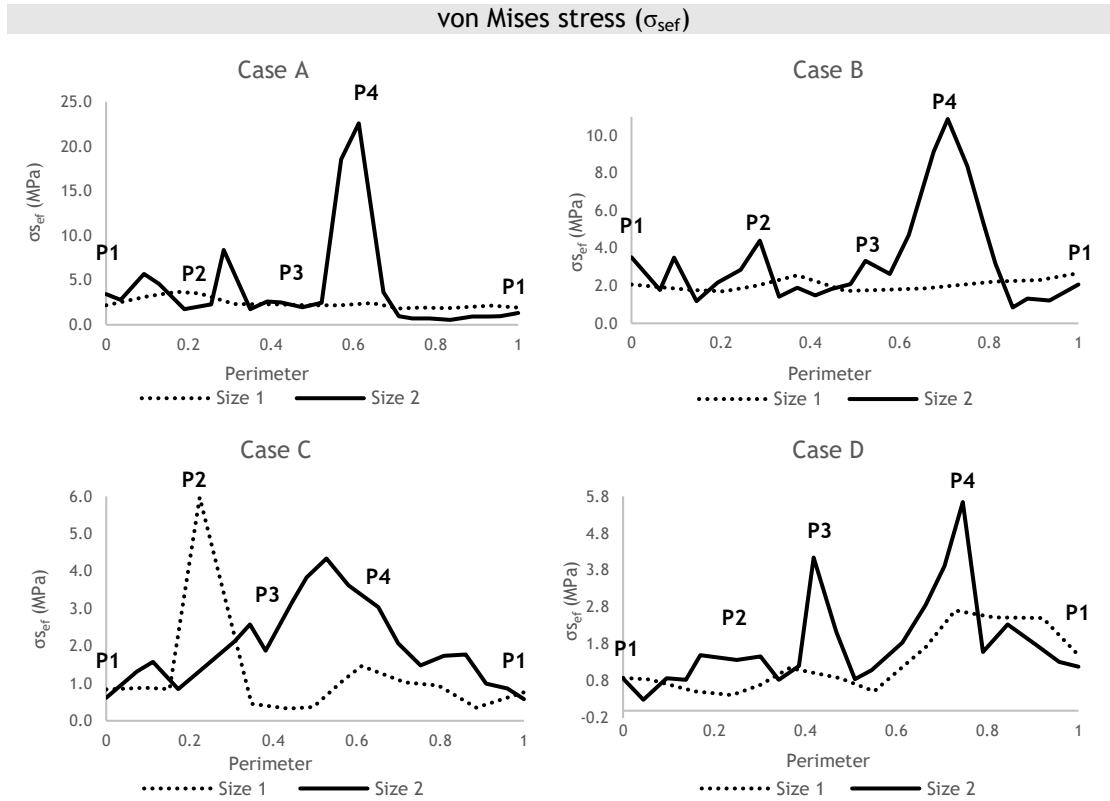


Figure 8.51 - Graphical representation of the von Mises effective stress obtained through NNRPIM for the cases of bone sarcomas studied in the four areas of interest.

The quantitative analysis of the von Mises effective stress demonstrates a similar graphical distribution in all sizes of sarcomas, with FEM and meshless methods. An increase of stress with the increase of size of the bone sarcoma can be observed in all clinical cases.

Moreover, case B demonstrates the highest levels of effective stress, which vary between 20 MPa (FEM) to 30 MPa (RPIM), except for case A, using NNRPIM, which demonstrates higher values of stress than case B. The area of bone tissue most affected is P4, which is near the femoral neck. The lowest levels of stress are observed in case C, particularly in P1. In this case, the bone tissue in the greater trochanter is the most affected area (area between P3 and P4 for size 2 and P2 for size 1). Finally, in case D, the effective stress increases in P4, demonstrating higher values of stress of approximately 10 MPa. These results are in agreement with the previous color maps, which demonstrates that the femoral neck and right side of the diaphysis are the areas most affected by the bone sarcomas.

The graphics regarding the principal stress 1 and 3, using FEM, RPIM and NNRPIM, for each clinical case are represented in Figure 8.52, Figure 8.53 and Figure 8.54, respectively. Overall, meshless methods and FEM assume the same graphical distribution. The areas with higher tensile stresses occur in P2 (case A) and P3 (case D), indicating that these are regions of traction. Also, regarding compressive stresses, P4 is a region of compression in case A, B and D (size 2), while P2 presents high levels of compressive stresses in case C, for size 1. Finally, case B presents the lowest levels of tensile stresses, while case C demonstrates lower levels of compressive stresses.

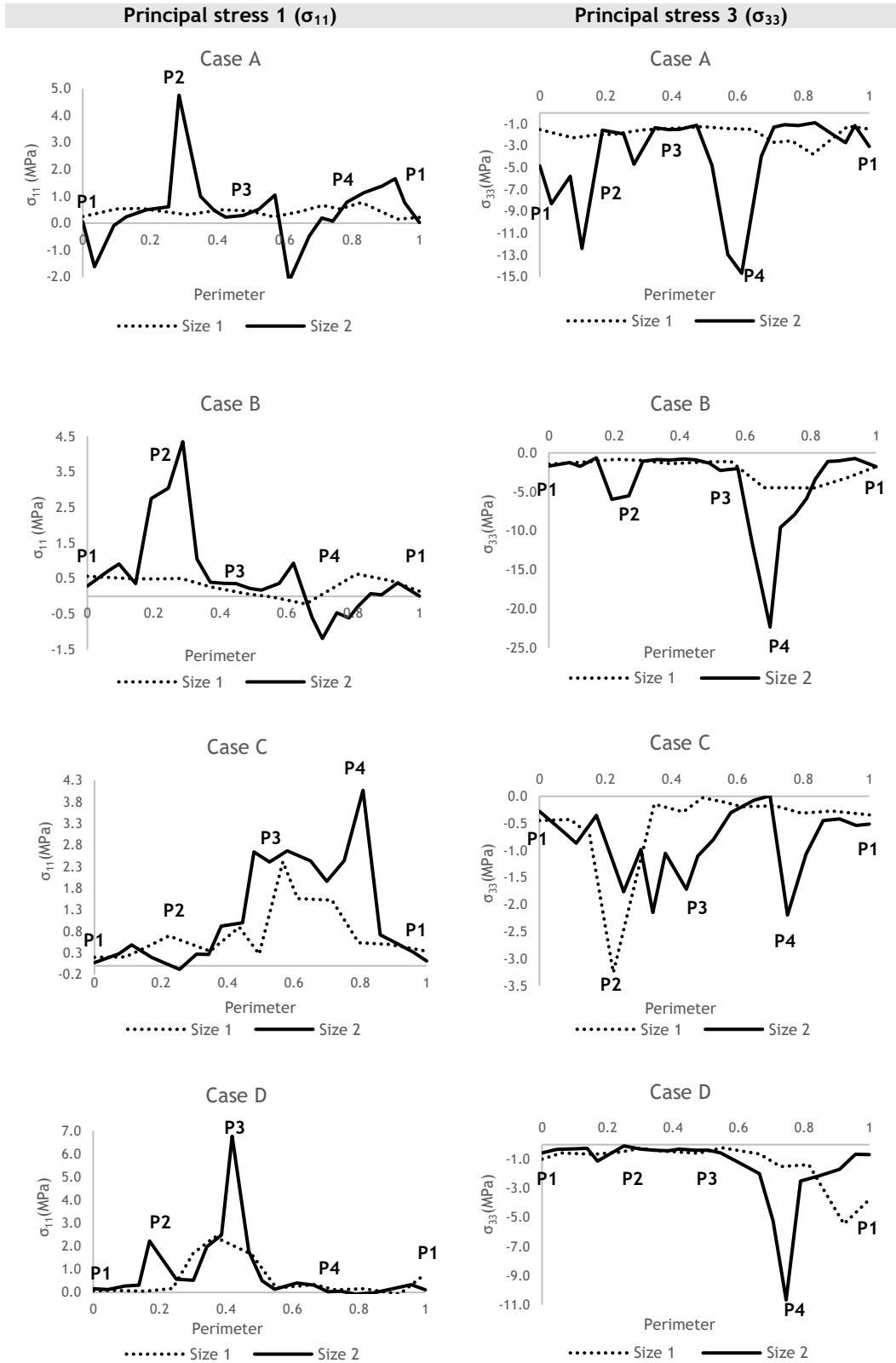


Figure 8.52 - Graphical representation of the principal stress 1 and 3 obtained through FEM for the cases of bone sarcomas studied in the four areas of interest.

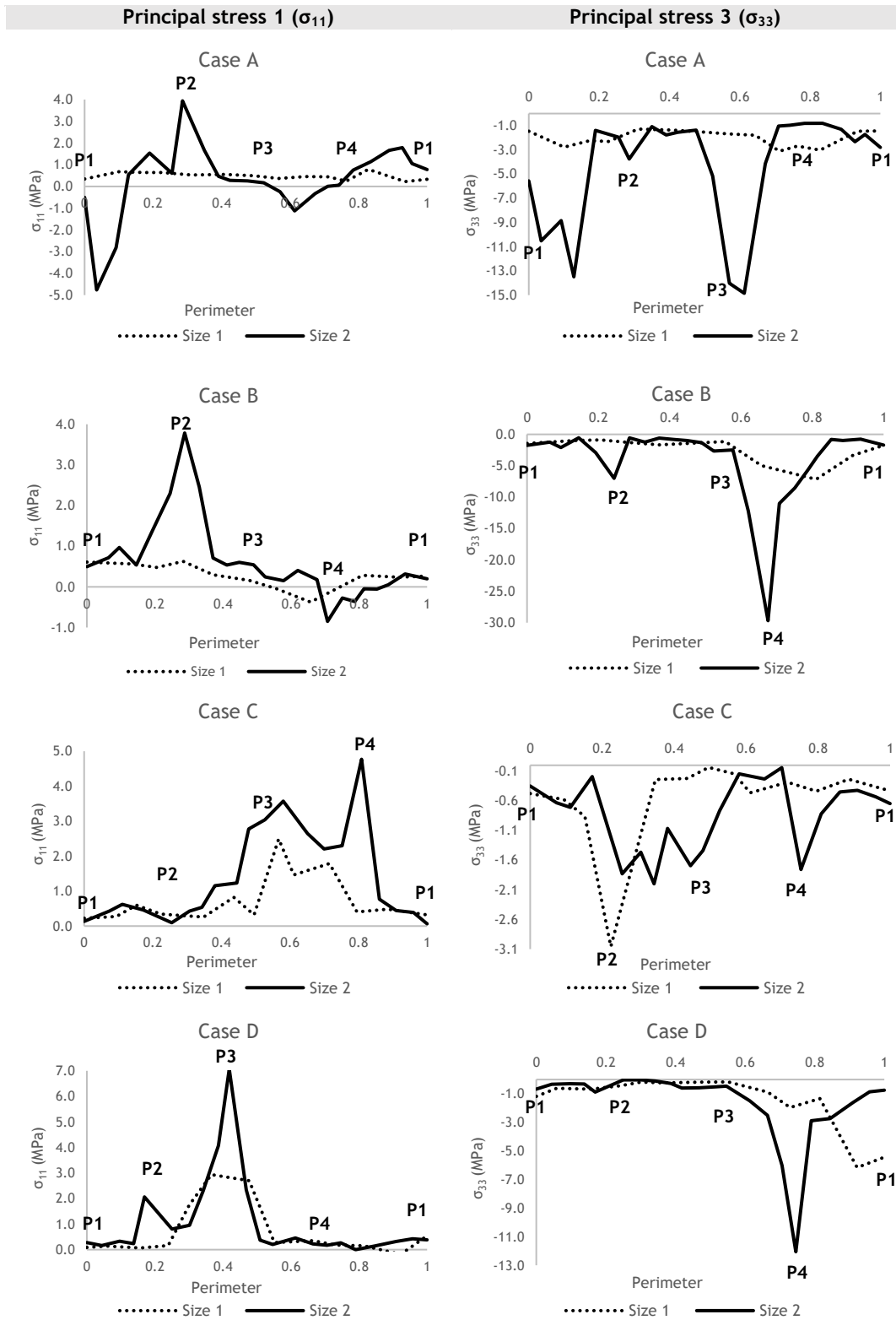


Figure 8.53 - Graphical representation of the principal stress 1 and 3 obtained through RPIM for the cases of bone sarcomas studied in the four areas of interest.

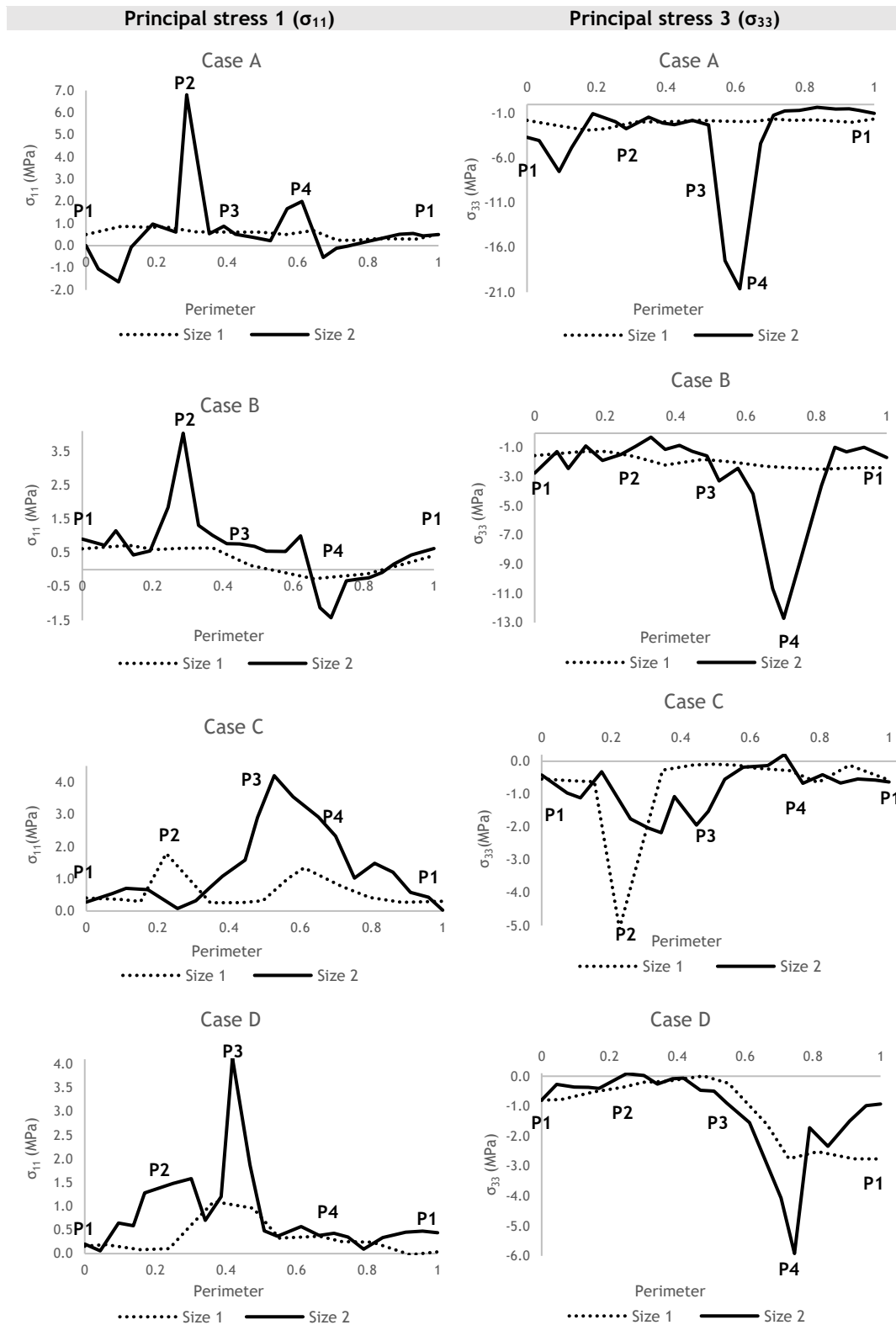


Figure 8.54 - Graphical representation of the principal stress 1 and 3 obtained through NNRPIM for the cases of bone sarcomas studied in the four areas of interest.

In conclusion, case A and C demonstrate minimal changes in stress with the increase of the sarcoma size. However, there is an increase of stress with the growth of the tumor in case B and D, both on a local and global scale, particularly in the inferomedial side of the neck and upper right side of the shaft. Therefore, these areas are more likely to occur micro-damages, as a result of the tumors, and continue to propagate throughout the bone, increasing its fragility and possibly creating fractures. These results are in agreement with the ones obtained for the 2D model, which evidence the formation of microdamages and possible fracture of the femoral neck.

At last, when comparing the numerical methods, it is possible to observe that a relative similarity between the results obtained, particularly in the graphical distributions and dispersion color maps. However, as previously explained, differences in formulations and the type of elements used can cause inequalities between the different numerical methods, which validate the information obtained in literature [5].

Chapter 9

Conclusions and Future Work

The bone is a dynamic tissue in constant remodeling in response to biological and mechanical stimulus. However, pathological changes can occur to its structure as a result of a disease, such as bone sarcomas, which increases its susceptibility to fracture.

Bone sarcomas are rare primary malignant tumors that originate in the bone and affect, mainly, children and young adults. The most common types are osteosarcoma, chondrosarcoma and Ewing's sarcoma. However, despite being a rare condition, the incidence rate for these type of tumors is rising as life expectancy becomes higher in developed countries. Another important factor is the bone growth rate. Long bones, such as the femur, are more likely to develop this type of malignancy, particularly in the metaphyses, where the growth rate is maximum during adolescence. Nevertheless, recent improvements in treatments have increased the survival rates, but the late effects have a negative impact in the health of the patient. As a result, the bone cancer survivals report several physical limitations that compromise its social and economic environment. In the literature, the majority of studies considers bone metastatic cancer instead of bone sarcomas, reporting reduced bone strength and changes in its mechanical properties. Thus, a review of the literature demonstrate that there are still several unanswered questions related to the effect of bone sarcomas, in this case, in the proximal femur, which makes it crucial to understand the biomechanical effect of these tumors on the bone.

Therefore, the main purpose of this work is to simulate and analyze the effect of bone sarcomas in the proximal femur using advanced discretization techniques, such as FEM and meshless methods (RPIM and NNRPIM). Another goal is to validate the meshless methods as a way of simulating and studying the effect of bone sarcomas on the proximal femur.

Thus, a preliminary work was initially developed, where a proximal femur model was used to evaluate the biomechanical behavior of the bone in a healthy condition. For that reason, a linear elastic two-dimensional analysis was performed, where the stress and strain distribution throughout the bone was evaluated. Overall, the results demonstrate higher stresses in the shaft of the femur, particularly in the cortical bone. Relatively to the deformation, the cortical and trabecular bone in the shaft and neck of the femur presented significant deformations.

This preliminary work allowed to acquire the necessary competences in computational tools, namely image processing and numerical simulation software using advanced discretization techniques (finite element methods and meshless methods).

Additionally, the effect of bone sarcomas on the proximal femoral structure was evaluated with a 2D and 3D model. In the two numerical studies, four different clinical cases of bone sarcomas were simulated with different sizes. In the two-dimensional approach, the sarcomas were simulated on the femoral head, neck, greater trochanter and shaft and assumed an elliptical shape with three different sizes. In the three-dimensional approach, the same clinical cases were analyzed but only two sizes were considered. However, in both cases, the biomechanical analysis was conducted using FEM, RPIM and NNRPIM, in order to compare these methods and validate the use of meshless methods to simulate bone sarcomas. The results obtained demonstrated a local influence of the sarcoma in the surrounding bone tissue, with the tumor growth, particularly in the inferomedial side of the neck and upper right side of the shaft. When considering the global effect of these tumors, the results demonstrated higher stresses in the femoral neck which may result in the formation of microdamages and possible fracture. In the future, it would be interesting to test a real femur with bone sarcomas and compare the results with the ones obtained in this study.

Finally, the results obtained allowed to conclude that meshless methods can be used to simulate bone sarcomas and result in smoother stress fields than FEM. However, this study presented some significant limitations. The most evident is the simplification of the two-dimensional and three-dimensional models in order to reduce the number of nodes and elements. Although, it is possible to analyze models with more nodes using FEM and meshless methods, RPIM and NNRPIM, the computational power that would be required to obtain the same level of discretization would be increased considerably. In addition, as an essential boundary condition, the femoral bone was fixed in the middle shaft, which causes increasing artificial stiffness as it approaches the attachment region. This work used mechanical properties for metastatic bone cancer instead of bone sarcomas. However, the literature did not report the mechanical conditions for bone sarcomas. Therefore, the mechanical properties of metastatic bone cancer were approximated to bone sarcomas, despite having different physiologies.

References

- [1] E. S. Orwoll *et al.*, "Finite element analysis of the proximal femur and hip fracture risk in older men," *J Bone Miner Res*, vol. 24, no. 3, pp. 475-83, Mar 2009.
- [2] A. H. Behzadi *et al.*, "Applications of PET/CT and PET/MR Imaging in Primary Bone Malignancies," *PET Clin*, vol. 13, no. 4, pp. 623-634, Oct 2018.
- [3] S. Abe, N. Narra, R. Nikander, J. Hyttinen, R. Kouhia, and H. Sievanen, "Exercise loading history and femoral neck strength in a sideways fall: A three-dimensional finite element modeling study," *Bone*, vol. 92, pp. 9-17, Nov 2016.
- [4] H. Gray, *Anatomy of the human body*. Bartleby, 1918.
- [5] J. Belinha, *Meshless Methods in Biomechanics*. Springer, 2014.
- [6] G. J. Tortora and B. Derrickson, *Introduction to the Human body*. 2010.
- [7] F. H. Martini;, R. B. Tallitsch;, and J. L. Nath, N. Pearson, Ed. *Human Anatomy*, 9th edition ed. 2018.
- [8] M. N. Pathria, C. B. Chung, and D. L. Resnick, "Acute and Stress-related Injuries of Bone and Cartilage," vol. 280, no. 1, pp. 21-38, 2016.
- [9] C. VanPutte, J. Regan, R. Seeley, T. Stephens, and P. Tate, *Seeley's Anatomy and Physiology*, Eleventh Edition ed. McGraw Hill Education: McGraw Hill Education, 2014.
- [10] E. Y. S. Chao, "A Survey of Finite Element Analysis in Orthopedic Biomechanics: The First Decade," *J. Biomechanics*, vol. 16, no. 6, pp. 385-409, 1983.
- [11] N. Kumar and B. Gupta, "Global Incidence of Primary Malignant Bone Tumors," *Current Orthopaedic Practice*, vol. 27, pp. 530-535, 2016.
- [12] Z. Bumingham, M. Hashibe, L. Spector, and J. D. Schiffman, "The Epidemiology of Sarcome," *Clinical Sarcoma Research*, vol. 2, no. 14, pp. 1-16, 2012.
- [13] J. H. Keyak, S. A. Rossi, K. A. Jones, and H. B. Skinner, "Prediction of Femoral Fracture Load using Automated Finite Element Modeling," *J Biomech*, vol. 31, pp. 125-133, 1998.
- [14] G. S. Beaupré, T. E. Orr, and D. R. Carter, "An Approach for Time Dependt Bone Modeling and Remodeling-Application: A Preliminary Remodeling Simulation," *Journal of Orthopaedic Research*, vol. 8, no. 5, pp. 662-670, 1990.
- [15] G. N. Duda, M. Heller, J. Albinger, O. Schulz, E. Schneider, and L. CLaes, "Influence of Muscle Forces on Femoral Strain Distribution," *J Biomech*, vol. 31, pp. 841-846, 1998.

- [16] F. Lutz *et al.*, "Calculation of muscle forces during normal gait under consideration of femoral bending moments," *Med Eng Phys*, vol. 38, no. 9, pp. 1008-15, Sep 2016.
- [17] T. S. Kaneko, M. R. Pejicic, J. Tehranzadeh, and J. H. Keyak, "Relationships between material properties and CT scan data of cortical bone with and without metastatic lesions," *Medical Engineering & Physics*, vol. 25, no. 6, pp. 445-454, 2003.
- [18] J. H. Keyak, T. S. Kaneko, H. B. Skinner, and B. H. Hoang, "The Effect of Simulated Metastatic Lytic Lesions on Proximal Femoral Strength," *Clinical orthopaedics and related research*, no. 450, pp. 139-145, 2007.
- [19] K. E. S. Poole *et al.*, "Changing structure of the femoral neck across the adult female lifespan," *Journal of Bone and Mineral Research*, vol. 25, no. 3, pp. 482-491, 2010.
- [20] F. A. Sabet, A. Raeisi Najafi, E. Hamed, and I. Jasiuk, "Modelling of bone fracture and strength at different length scales: a review," *Interface Focus*, vol. 6, no. 1, p. 20150055, Feb 6 2016.
- [21] H. T. Ta, C. R. Dass, P. F. Choong, and D. E. Dunstan, "Osteosarcoma treatment: state of the art," *Cancer Metastasis Rev*, vol. 28, no. 1-2, pp. 247-63, Jun 2009.
- [22] C. A. Stiller *et al.*, "Descriptive epidemiology of sarcomas in Europe: report from the RARECARE project," *Eur J Cancer*, vol. 49, no. 3, pp. 684-95, Feb 2013.
- [23] F. Bray, J. Ferlay, I. Soerjomataram, R. L. Siegel, L. A. Torre, and A. Jemal, "Global cancer statistics 2018: GLOBOCAN estimates of incidence and mortality worldwide for 36 cancers in 185 countries," *CA Cancer J Clin*, vol. 68, no. 6, pp. 394-424, Nov 2018.
- [24] A. Nazarian, D. von Stechow, D. Zurakowski, R. Muller, and B. D. Snyder, "Bone volume fraction explains the variation in strength and stiffness of cancellous bone affected by metastatic cancer and osteoporosis," *Calcif Tissue Int*, vol. 83, no. 6, pp. 368-79, Dec 2008.
- [25] M. E. Kersh, S. Martelli, R. Zebaze, E. Seeman, and M. G. Pandy, "Mechanical Loading of the Femoral Neck in Human Locomotion," *J Bone Miner Res*, vol. 33, no. 11, pp. 1999-2006, Nov 2018.
- [26] S. Partovi, L. Zipp, P. Faulhaber, C. Kosmas, and P. R. Rios, "Hybrid PET/MRI Imaging in two Sarcoma Patients- Clinical Benefits and Implications for Future Trials," *Int J Clin Exp Med*, vol. 7, no. 3, pp. 640-648, 2014.
- [27] F. Zarin, T. Kazemi, and P. Vakili, "A Review of Malignant Bone Tumors," *Research Journal of Pharmaceutical, Biological and Chemical Sciences*, vol. 6, no. 2, pp. 884-893, 2015.
- [28] Z. Yosibash, R. Plitman Mayo, G. Dahan, N. Trabelsi, G. Amir, and C. Milgrom, "Predicting the stiffness and strength of human femurs with real metastatic tumors," *Bone*, vol. 69, pp. 180-90, Dec 2014.
- [29] N. C. I. network, "Bone Sarcomas: incidence and Survival Rates in England," 2010.
- [30] K. K. Ness, A. C. Mertens, M. M. Hudson, W. M. Leisenring, and K. C. Oeffinger, "Limitations on Physical Performance and Daily Activities among Long-Term Survivors of Childhood Cancer," *Annals of Internal Medicine*, vol. 143, no. 9, pp. 639-648, 2005.
- [31] B. Widhe and T. Widhe, "Initial Symptoms and Clinical Features in Osteosarcoma and Ewing Sarcoma," *The Journal of Bone and Joint Research*, vol. 82, no. 5, pp. 667-674, 2000.
- [32] A. K. Freeman, V. P. Sumathi, and L. Jeys, "Primary malignant tumours of the bone," *Surgery (Oxford)*, vol. 36, no. 1, pp. 27-34, 2018.
- [33] J. C. Clark, C. R. Dass, and P. F. Choong, "A review of clinical and molecular prognostic factors in osteosarcoma," *J Cancer Res Clin Oncol*, vol. 134, no. 3, pp. 281-97, Mar 2008.
- [34] A. Srejekha, "Infinite to finite: An overview of finite element analysis," *Indian Journal of Dental Research*, vol. 21, no. 3, pp. 425-432, 2010.
- [35] G. Iolascon, G. Resmini, and U. Tarantino, "Mechanobiology of bone," *Aging Clin Exp Res*, vol. 25 Suppl 1, pp. S3-7, Oct 2013.
- [36] B. Clarke, "Normal bone anatomy and physiology," *Clin J Am Soc Nephrol*, vol. 3 Suppl 3, pp. S131-9, Nov 2008.
- [37] L. C. Junqueira; and J. Carneiro; , *Histologia Básica*. Guanabara Koogan, 2004.
- [38] D. J. Hadjidakis and Androulakis, II, "Bone remodeling," *Ann N Y Acad Sci*, vol. 1092, pp. 385-96, Dec 2006.

- [39] R. Florencio-Silva, G. R. Sasso, E. Sasso-Cerri, M. J. Simoes, and P. S. Cerri, "Biology of Bone Tissue: Structure, Function, and Factors That Influence Bone Cells," *Biomed Res Int*, vol. 2015, p. 421746, 2015.
- [40] U. H. Lerner, "Bone Remodeling in Post-menopausal Osteoporosis," *J Dent Res*, vol. 85, no. 7, pp. 584-595, 2006.
- [41] D. W. Huang, C. H. Chang, S. Wang, and Y. C. Tsai, "Dynamic Characteristics of a Hollow Femur," *Life Science Journal*, vol. 9, no. 1, pp. 723-726, 2012.
- [42] S. Valliappan, N. L. Svensson, and R. D. Wood, "Three Dimensional Stress Analysis of the Human Femur," *Comput. Biol. Med*, vol. 7, pp. 253-264, 1977.
- [43] H. Fonseca, D. Moreira-Goncalves, H. J. Coriolano, and J. A. Duarte, "Bone quality: the determinants of bone strength and fragility," *Sports Med*, vol. 44, no. 1, pp. 37-53, Jan 2014.
- [44] C. M. Schnitzler, "Bone Quality: A Determinant for Certain Risk Factors for Bone Fragility," *Calcif Tissue Int*, vol. 53, pp. 27-31, 1993.
- [45] J. Compston, "Bone Quality: What is it and How is it Measured?," *Arq Bras Endocrinol Metab*, vol. 50, no. 4, pp. 579-585, 2006.
- [46] L. D. Dorr, M. Faugere, A. M. Mackel, T. A. Gruen, B. Bogner, and H. H. Malluche, "Structural and Cellular Assessment of Bone Quality of Proximal Femur," *Bone*, vol. 14, pp. 231-242, 1993.
- [47] W. C. Li, C. H. Shih, S. W. Ueng, H. N. Shih, M. S. Lee, and P. H. Hsieh, "Uncemented total hip arthroplasty in chronic hemodialysis patients," *Acta Orthop*, vol. 81, no. 2, pp. 178-82, Apr 2010.
- [48] E. F. Morgan and M. L. Buxsein, "Biomechanics of Bone and Age-Related Fractures," in *Principles of Bone Biology*, A. Press, Ed., 2008.
- [49] A. Krauze and M. Kaczmarek, "Numerical Analysis of Femur in Living and Dead Phase," *Journal of Achievements in Materials and Manufacturing Engineering*, vol. 26, no. 2, pp. 163-166, 2008.
- [50] J. C. Rice, "On the Dependence of the Elasticity and Strength of Cancellous Bone on Apparent Density," *J Biomech*, vol. 21, no. 2, pp. 155-168, 1988.
- [51] M. B. Schaffler and D. B. Burr, "Stiffness of Compact Bone: Effect of Porosity and Density," *J Biomech*, vol. 21, no. 1, pp. 13-16, 1988.
- [52] L. Peng, J. Bai, X. Zeng, and Y. Zhou, "Comparison of isotropic and orthotropic material property assignments on femoral finite element models under two loading conditions," 2006.
- [53] D. R. Carter and W. C. Hayes, "The Compressive Behavior of Bone as a Two-Phase Porous Structure," *The Journal of Bone and Joint Surgery*, vol. 59, pp. 954-962, 1977.
- [54] J. C. Lotz, T. N. Gerhart, and W. C. Hayes, "Mechanical Properties of Metaphyseal Bone in the Proximal Femur," *J Biomech*, vol. 24, no. 5, pp. 317-329, 1991.
- [55] J. Belinha, R. M. Jorge, and L. M. Dinis, "A meshless microscale bone tissue trabecular remodelling analysis considering a new anisotropic bone tissue material law," *Comput Methods Biomech Biomed Engin*, vol. 16, no. 11, pp. 1170-84, 2013.
- [56] P. Zioupos, R. B. Cook, and J. R. Hutchinson, "Some basic relationships between density values in cancellous and cortical bone," *J Biomech*, vol. 41, no. 9, pp. 1961-8, 2008.
- [57] S. C. Cowin and D. H. Hegedus, "Bone remodeling I: theory of adaptive elasticity," *Journal of Elasticity*, vol. 6, no. 3, pp. 313-326, 1976.
- [58] S. C. Cowin, A. M. Sadegh, and G. M. Luo, "An Evolutionary Wolff's Law for Trabecular Architecture," *Journal of Biomechanical Engineering*, vol. 114, pp. 129-136, 1992.
- [59] D. P. Fyhrie and D. R. Carter, "A Unifying Principle Relating Stress to Trabecular Bone Morphology," *Journal of Orthopaedic Research*, vol. 4, pp. 304-317, 1986.
- [60] D. R. Carter, T. E. Orr, and D. P. Fyrie, "Relationships Between Loading History and Femoral Cancellous Bone Architecture," *J Biomech*, vol. 22, no. 5, pp. 231-244, 1989.
- [61] G. S. Beaupré, T. E. Orr, and D. R. Carter, "An Approach for Time-Dependent Bone Modeling and Remodeling-Theoretical Development," *Journal of Orthopaedic Research*, vol. 8, no. 5, pp. 651-661, 1990.
- [62] H. E. Pitterman, T. J. Reiter, and F. G. Rammerstorfer, "Computational Simulation of Internal Bone Remodeling," *Computational Methods in Engineering*, vol. 4, no. 4, pp. 296-323, 1997.

- [63] M. Doblaré and J. M. Garcia, "Anisotropic bone remodelling model based on a continuum damage-repair theory," *J Biomech*, vol. 35, pp. 1-17, 2002.
- [64] C. Rattanakul, Y. Lenbury, N. Krishnamara, and D. J. Wollkind, "Modeling of bone formation and resorption mediated by parathyroid hormone: response to estrogen/PTH therapy," *Biosystems*, vol. 70, no. 1, pp. 55-72, 2003.
- [65] S. V. Komarova, "Mathematical model of paracrine interactions between osteoclasts and osteoblasts predicts anabolic action of parathyroid hormone on bone," *Endocrinology*, vol. 146, no. 8, pp. 3589-95, Aug 2005.
- [66] M. D. Ryser, N. Nigam, and S. V. Komarova, "Mathematical modeling of spatio-temporal dynamics of a single bone multicellular unit," *J Bone Miner Res*, vol. 24, no. 5, pp. 860-70, May 2009.
- [67] S. V. Komarova, R. J. Smith, S. J. Dixon, S. M. Sims, and L. M. Wahl, "Mathematical model predicts a critical role for osteoclast autocrine regulation in the control of bone remodeling," *Bone*, vol. 33, no. 2, pp. 206-215, 2003.
- [68] B. P. Ayati, C. M. Edwards, G. F. Webb, and J. P. Wikswo, "A Mathematical Model of Bone Remodeling Dynamics for Normal Bone Cell Populations and Myeloma Bone Disease," *Biology Direct*, vol. 5, no. 28, pp. 1-17, 2010.
- [69] R. Hambli, "Connecting Mechanics and Bone Cell Activities in the Bone Remodeling Process: An Integrated Finite Element Modeling," *Frontiers in Bioengineering and Biotechnology*, vol. 2, 2014.
- [70] E. G. Mercuri, A. L. Daniel, M. B. Hecke, and L. Carvalho, "Influence of different mechanical stimuli in a multi-scale mechanobiological isotropic model for bone remodelling," *Med Eng Phys*, vol. 38, no. 9, pp. 904-10, Sep 2016.
- [71] J. Hardin, G. Bertoni, and L. J. Kleinsmith, *World of the Cell*, eighth edition ed. Pearson Benjamin Cummings, 2012.
- [72] A. Luetke, P. A. Meyers, I. Lewis, and H. Juergens, "Osteosarcoma treatment - where do we stand? A state of the art review," *Cancer Treat Rev*, vol. 40, no. 4, pp. 523-32, May 2014.
- [73] E. Benca *et al.*, "Effect of simulated metastatic lesions on the biomechanical behavior of the proximal femur," *J Orthop Res*, vol. 35, no. 11, pp. 2407-2414, Nov 2017.
- [74] G. D. Roodman, "Mechanisms of Bone Metastasis," *The New England Journal of Medicine*, vol. 350, no. 16, pp. 1655-1664, 2004.
- [75] L. L. Robison *et al.*, "Long-term outcomes of adult survivors of childhood cancer," *Cancer*, vol. 104, no. 11 Suppl, pp. 2557-64, Dec 1 2005.
- [76] M. Barrera, T. Teall, R. Barr, M. Silva, and M. Greenberg, "Health related quality of life in adolescent and young adult survivors of lower extremity bone tumors," *Pediatr Blood Cancer*, vol. 58, no. 2, pp. 265-73, Feb 2012.
- [77] S. Dadia and R. Grimer, "Characteristics, Diagnosis and Treatment of Bone and Soft Tissue Sarcomas," *British Journal of Hospital Medicine*, vol. 68, no. 11, pp. 589-593, 2007.
- [78] CanTeen, "The Economic Cost of Cancer in Adolescents and Young Adults " CanTeen2016.
- [79] K. L. Schulman and J. Kohles, "Economic burden of metastatic bone disease in the U.S.," *Cancer*, vol. 109, no. 11, pp. 2334-42, Jun 1 2007.
- [80] G. J. O'Sullivan, F. L. Carty, and C. G. Cronin, "Imaging of bone metastasis: An update," *World J Radiol*, vol. 7, no. 8, pp. 202-11, Aug 28 2015.
- [81] R. Grimer, N. Athanasou, C. Gerrand, and I. Judson, "UK Guidelines for the Management of Bone Sarcomas," *Hindawl Publishing Corporation*, vol. 10, pp. 1-15, 2010.
- [82] W. Brenner, K. H. Bohuslavizki, and J. F. Eary, "PET Imaging of Osteosarcoma," *The Journal of Nuclear Medicine*, vol. 44, no. 6, pp. 930-942, 2003.
- [83] K. Strobel *et al.*, "The additional value of CT images interpretation in the differential diagnosis of benign vs. malignant primary bone lesions with 18F-FDG-PET/CT," *Eur J Nucl Med Mol Imaging*, vol. 35, no. 11, pp. 2000-8, Nov 2008.
- [84] T. S. Kaneko, J. S. Bell, M. R. Pejicic, J. Tehranzadeh, and J. H. Keyak, "Mechanical properties, density and quantitative CT scan data of trabecular bone with and without metastases," *J Biomech*, vol. 37, no. 4, pp. 523-30, Apr 2004.

- [85] P.-A. Abrahamsson, "Pathophysiology of Bone Metastases in Prostate Cancer," *European Urology Supplements*, vol. 3, no. 5, pp. 3-9, 2004.
- [86] S. K. Parashar and J. K. Sharma, "A review on application of finite element modelling in bone biomechanics," *Perspectives in Science*, vol. 8, pp. 696-698, 2016.
- [87] A. Boccaccio, A. Ballini, C. Pappalettere, D. Tullo, and S. Cantore, "Finite Element Method (FEM), Mechanobiology and Biomimetic Scaffolds in Bone Tissue Engineering," *Int J. Biol. Sci.*, vol. 7, pp. 122-132, 2011.
- [88] S. P. Vaananen, L. Grassi, G. Flivik, J. S. Jurvelin, and H. Isaksson, "Generation of 3D shape, density, cortical thickness and finite element mesh of proximal femur from a DXA image," *Med Image Anal*, vol. 24, no. 1, pp. 125-134, Aug 2015.
- [89] Y. T. Gu, "Meshfree Methods and Their Comparisons," *International Journal of Computational Methods*, vol. 2, no. 4, pp. 477-515, 2005.
- [90] C. S. S. Tavares, J. Belinha, L. M. J. S. Dinis, and R. M. N. Jorge, "The Elasto-plastic Response of the Bone Tissue Due to the Insertion of Dental Implants," *Procedia Engineering*, vol. 110, pp. 37-44, 2015.
- [91] L. M. J. S. Dinis, R. M. Natal Jorge, and J. Belinha, "Analysis of 3D solids using the natural neighbour radial point interpolation method," *Computer Methods in Applied Mechanics and Engineering*, vol. 196, no. 13-16, pp. 2009-2028, 2007.
- [92] G. R. Liu and S. S. Quek, *The Finite Element Method: A Practical Course*. Butterworth Heinemann, 2003.
- [93] W. A. M. Brekelmans, H. W. Poort, and T. J. J. H. Slooff, "A New Method to Analyse the Mechanical Behaviour of Skeletal Parts," *Acta Orthopaedica Scandinavica*, vol. 43, no. 5, pp. 301-317, 1972.
- [94] E. Verhulp, B. van Rietbergen, and R. Huiskes, "Load distribution in the healthy and osteoporotic human proximal femur during a fall to the side," *Bone*, vol. 42, no. 1, pp. 30-5, Jan 2008.
- [95] Y. Long, W. D. Leslie, and Y. Luo, "Study of DXA-derived lateral-medial cortical bone thickness in assessing hip fracture risk," *Bone Rep*, vol. 2, pp. 44-51, Jun 2015.
- [96] J. D. Michelson, A. M. Myers, R. Jinnah, Q. Cox, and M. v. Natta, "Epidemiology of Hip Fractures Among the Elderly," *Clinical orthopaedics and related research*, no. 311, pp. 129-135, 1995.
- [97] T. P. Pinilla, J. C. Boardman, M. L. Bouxsein, E. R. Myers, and W. C. Hayes, "Impact Direction from a Fall influences the Failure Load of the Proximal Femur as much as Age-Related Bone Loss," *Calcif Tissue Int*, no. 58, pp. 231-235, 1996.
- [98] J. H. Keyak, H. B. Skinner, and J. A. Fleming, "Effect of Force Direction on Femoral Fracture Load for Two Types of Loading Conditions," *Journal of Orthopaedic Research*, vol. 19, pp. 539-544, 2001.
- [99] K. K. Nishiyama, S. Gilchrist, P. Guy, P. Crompton, and S. K. Boyd, "Proximal femur bone strength estimated by a computationally fast finite element analysis in a sideways fall configuration," *J Biomech*, vol. 46, no. 7, pp. 1231-6, Apr 26 2013.
- [100] C. Falcinelli *et al.*, "Multiple loading conditions analysis can improve the association between finite element bone strength estimates and proximal femur fractures: a preliminary study in elderly women," *Bone*, vol. 67, pp. 71-80, Oct 2014.
- [101] D. D. Cody, G. J. Gross, F. J. Hou, H. J. Spencer, S. A. Goldstein, and D. P. Fyhrie, "Femoral Strength is Better Predicted by Finite Element Models than QCT and DXA," *J Biomech*, vol. 32, pp. 1013-1020, 1999.
- [102] D. Testi, M. Viceconti, F. Baruffaldi, and A. Capello, "Risk of Fracture in Elderly Patients: a New Predictive Index Based on Bone mineral Density and Finite Element Analysis," *Computer Methods and Programs in Biomedicine*, vol. 60, pp. 23-33, 1999.
- [103] E. Dall'Ara, R. Eastell, M. Viceconti, D. Pahr, and L. Yang, "Experimental validation of DXA-based finite element models for prediction of femoral strength," *J Mech Behav Biomed Mater*, vol. 63, pp. 17-25, Oct 2016.
- [104] C. M. Langton, S. Pisharody, and J. H. Keyak, "Comparison of 3D finite element analysis derived stiffness and BMD to determine the failure load of the excised proximal femur," *Med Eng Phys*, vol. 31, no. 6, pp. 668-72, Jul 2009.
- [105] M. Bessho *et al.*, "Prediction of the strength and fracture location of the femoral neck by CT-based finite-element method: a preliminary study on patients with hip fracture," *J Orthop Sci*, vol. 9, no. 6, pp. 545-50, 2004.

- [106] T. F. Lang *et al.*, "Age-related loss of proximal femoral strength in elderly men and women: the Age Gene/Environment Susceptibility Study--Reykjavik," *Bone*, vol. 50, no. 3, pp. 743-8, Mar 2012.
- [107] J. Carballido-Gamio *et al.*, "Proximal femoral density distribution and structure in relation to age and hip fracture risk in women," *Journal of Bone and Mineral Research*, vol. 28, no. 3, pp. 537-546, 2013.
- [108] S. Kaptoge *et al.*, "Effects of physical activity on evolution of proximal femur structure in a younger elderly population," *Bone*, vol. 40, no. 2, pp. 506-515, 2007.
- [109] S. Abe, N. Narra, R. Nikander, J. Hyttinen, R. Kouhia, and H. Sievänen, "Impact loading history modulates hip fracture load and location: A finite element simulation study of the proximal femur in female athletes," *Journal of Biomechanics*, vol. 76, pp. 136-143, 2018.
- [110] J. H. Keyak, S. A. Rossi, K. A. Jones, C. M. Les, and H. B. Skinner, "Prediction of Fracture Location in the Proximal Femur using Finite Element Models," *Medical Engineering & Physics*, vol. 23, pp. 657-664, 2001.
- [111] N. Trabelsi, Z. Yosibash, C. Wutte, P. Augat, and S. Eberle, "Patient-specific finite element analysis of the human femur--a double-blinded biomechanical validation," *J Biomech*, vol. 44, no. 9, pp. 1666-72, Jun 3 2011.
- [112] A. L. Aghili *et al.*, "Stress Analysis of Human Femur under Different Loadings," pp. 518-522, 2011.
- [113] J. C. Lotz and W. C. Hayes, "Stress Distributions within the Proximal Femur during Gait and Falls: Implications for Osteoporotic Fracture," *Osteoporosis Int*, vol. 5, pp. 252-261, 1995.
- [114] S. Nawathe, B. P. Nguyen, N. Barzanian, H. Akhlaghpour, M. L. Bouxsein, and T. M. Keaveny, "Cortical and trabecular load sharing in the human femoral neck," *J Biomech*, vol. 48, no. 5, pp. 816-22, Mar 18 2015.
- [115] V. Baca, D. Kachlik, Z. Horak, and J. Stingl, "The course of osteons in the compact bone of the human proximal femur with clinical and biomechanical significance," *Surg Radiol Anat*, vol. 29, no. 3, pp. 201-7, Apr 2007.
- [116] L. Voo, M. Armand, and M. Kleinberger, "Stress Fracture Risk Analysis of the Human Femur based on Computational Biomechanics," *Johns Hopkins APL Technical Digest*, vol. 25, no. 3, pp. 223-230, 2004.
- [117] Z. Yosibash, A. Katz, and C. Milgrom, "Toward verified and validated FE simulations of a femur with a cemented hip prosthesis," *Med Eng Phys*, vol. 35, no. 7, pp. 978-87, Jul 2013.
- [118] R. Mittal and S. Banerjee, "Proximal femoral fractures: Principles of management and review of literature," *J Clin Orthop Trauma*, vol. 3, no. 1, pp. 15-23, Jun 2012.
- [119] H. Weinans and R. Huiskes, "Effects of Fit and Bonding Characteristics of Femoral Stems on Adaptive Bone Remodeling," *Journal of Biomechanical Engineering*, vol. 116, pp. 393-400, 1994.
- [120] B. van Rietbergen and R. Huiskes, "Load transfer and stress shielding of the hydroxyapatite-ABG hip: A study of stem length and proximal fixation," *The Journal of Arthroplasty*, vol. 16, no. 8, pp. 55-63, 2001.
- [121] K. Polgár, H. S. Gill, D. W. Murray, and J. J. O'Connor, "Strain Distribution within the Human Femur due to Physiological and Simplified loading: Finite Element Analysis using the Muscle Standardized Femur Model" vol. 217, 2003.
- [122] C. Bitsakos, J. Kerner, I. Fisher, and A. A. Amis, "The effect of muscle loading on the simulation of bone remodelling in the proximal femur," *J Biomech*, vol. 38, no. 1, pp. 133-9, Jan 2005.
- [123] F. Taddei, M. Viceconti, M. Manfrini, and A. Toni, "Mechanical strength of a Femoral Reconstruction in Paediatric Oncology: a Finite Element Study," *Journal of Engineering in Medicine*, vol. 217, no. 111-119, 2003.
- [124] G. Valente *et al.*, "Relationship between bone adaptation and in-vivo mechanical stimulus in biological reconstructions after bone tumor: A biomechanical modeling analysis," *Clin Biomech (Bristol, Avon)*, vol. 42, pp. 99-107, Feb 2017.
- [125] M. Fidler, "Incidence of Fracture Through Metastases in Long Bones," *Acta Orthopaedica Scandinavica*, vol. 52, no. 6, pp. 623-627, 1981.

- [126] J. A. Hipp, D. S. Springfield, and W. C. Hayes, "Predicting Pathological Fracture Risk in the Management of Metastatic Bone," *Clinical orthopaedics and related research*, no. 312, pp. 120-135, 1995.
- [127] L. C. Derikx, J. B. v. Aken, D. Janssen, and Y. M. v. d. Linden, "The Assessment of the Risk of Fracture in Femora with Metastatic Lesions," *The Journal of Bone and Joint Research*, vol. 94, no. 8, pp. 1135-1142, 2012.
- [128] J. H. Keyak, T. S. Kaneko, J. Tehranzadeh, and H. B. Skinner, "Predicting Proximal Femoral Strength Using Structural Engineering Models," *Clinical Orthopaedics and Related Research*, vol. &NA;, no. 437, pp. 219-228, 2005.
- [129] V. P. Nguyen, T. Rabczuk, S. Bordas, and M. Dufloy, "Meshless methods: A review and computer implementation aspects," *Mathematics and Computers in Simulation*, vol. 79, no. 3, pp. 763-813, 2008.
- [130] J. Belinha, R. M. Natal Jorge, and L. M. J. S. Dinis, "Bone tissue remodelling analysis considering a radial point interpolator meshless method," *Engineering Analysis with Boundary Elements*, vol. 36, no. 11, pp. 1660-1670, 2012.
- [131] J. Belinha, L. M. J. S. Dinis, and R. M. N. Jorge, "The Meshless Methods in the Bone Tissue Remodelling Analysis," *Procedia Engineering*, vol. 110, pp. 51-58, 2015.
- [132] M. M. A. Peyroteo, J. Belinha, S. Vinga, L. M. J. S. Dinis, and R. M. Natal Jorge, "Mechanical bone remodelling: Comparative study of distinct numerical approaches," *Engineering Analysis with Boundary Elements*, 2018.
- [133] J. W. Fernandez, R. Das, P. W. Cleary, P. J. Hunter, C. D. Thomas, and J. G. Clement, "Using smooth particle hydrodynamics to investigate femoral cortical bone remodelling at the Haversian level," *Int J Numer Method Biomed Eng*, vol. 29, no. 1, pp. 129-43, Jan 2013.
- [134] M. Doblaré, E. Cueto, B. Calvo, M. A. Martínez, J. M. Garcia, and J. Cegoñino, "On the employ of meshless methods in biomechanics," *Computer Methods in Applied Mechanics and Engineering*, vol. 194, no. 6-8, pp. 801-821, 2005.
- [135] J. Belinha, L. M. J. S. Dinis, and R. M. Natal Jorge, "The analysis of the bone remodelling around femoral stems: A meshless approach," *Mathematics and Computers in Simulation*, vol. 121, pp. 64-94, 2016.
- [136] J. D. Lee, Y. Chen, X. Zeng, A. Eskandarian, and M. Oskard, "Modeling and simulation of osteoporosis and fracture of trabecular bone by meshless method," *International Journal of Engineering Science*, vol. 45, no. 2-8, pp. 329-338, 2007.
- [137] J. W. Fernandez, R. Das, C. D. L. Thomas, P. W. Cleary, M. D. Sinnott, and J. Clement, "Strain Reduction between Cortical Pore Structure Leads to Bone Weakening and Fracture Susceptibility: An Investigation Using Smooth Particle Hydrodynamics," *IFBMBE Proceedings*, vol. 31, no. 784-787, 2010.
- [138] K. M. Liew, H. Y. Wu, and T. Y. Ng, "Meshless method for modeling of human proximal femur: treatment of nonconvex boundaries and stress analysis," *Computational Mechanics*, vol. 28, no. 5, pp. 390-400, 2002.
- [139] F. Taddei, M. Pani, L. Zovatto, E. Tonti, and M. Viceconti, "A new meshless approach for subject-specific strain prediction in long bones: Evaluation of accuracy," *Clin Biomech (Bristol, Avon)*, vol. 23, no. 9, pp. 1192-9, Nov 2008.
- [140] E. F. Rybicki, F. A. Simonen, and E. B. Weis, "On the mathematical analysis of stress in the human femur," *J Biomech*, vol. 5, pp. 203-215, 1972.